The Mechanics of Extreme Water Waves

by

David John Skyner

Doctor of Philosophy

The University of Edinburgh

1992

Abstract

The design and construction of a versatile new wave flume is described along with associated apparatus and experimental methods. In particular, the practices developed for the use of Particle Image Velocimetry (PIV) for the measurement of the internal kinematics of waves are detailed. Two studies are then described, both of which make use of the PIV technique. In the first, a deep-water long-crested breaking wave is generated in a time-stepping numerical model, then replicated in the wave flume. Measurements of the internal kinematics are made throughout the breaking process, including measurements into the plunging spout. After a small shift of the numerical data to match the surface profiles, the predicted and measured kinematics are shown to agree within about 2%. In the second study, steep steady waves are combined with sheared currents. The resulting kinematics are found to be reasonably predicted in the crest region by adding the results of irrotational computations to the stretched current profile. However, calculation of the vorticity of the measured flow fields indicates that the conditions were not steady, and that the shear of the current was reducing with time.

Declaration

This thesis has been composed by myself and, except where stated, the work contained is my own.

David Skyner

August, 1992

Acknowledgments

I would like to thank the following people for their advice and assistance during the work: my supervisor, Clive Greated, for his encouragement and guidance, along with Bill Easson; Callum Gray, who first implemented the PIV system at Edinburgh; Tom Bruce and Paul Quinn in the lab; Peter Woodhead, who provided invaluable advice on software; Laird Parker, who made most of the parts for the flume, along with Frank Morris and the rest of the technicians.

The research projects from which this thesis has grown were fund by the SERC, the Department of Energy and the EC MAST programme, and their support is gratefully acknowledged.

Contents

Chapter 1

Introduction

1.1 Subject Background

Knowledge of the mechanics of the oceans has always been sought, particularly the motions of the waves, currents and tides. Historically, the main interest has been for the safe navigation of ships. Recently, coastal and offshore engineering industries have developed, and the interest in understanding the mechanics of waves has been taken up with renewed rigour.

The dynamic loading on a fixed or moving structure depends on the internal kinematics of the waves. In the design of offshore oil rigs, a good estimate of the kinematics of the largest storm waves is needed to determine the loadings which the legs of the platform will have to be able to withstand [45, 37, 53]. Offshore wave energy devices must be able to survive extreme conditions in order to be economic, and this has to be considered at an early stage of their design [50, 6].

The building of coastal defences is a necessity in many places, and, given the huge cost of such projects, small increases in the understanding of the impact and erosion process can lead to substantial savings. With the prospect of the sea level rising, this aspect will take on an increasing urgency.

The importance of extreme waves goes beyond engineering design: processes such as mixing of the surface layers of the oceans and aeration depend strongly on wave breaking, the strength of which correlates with the biggest waves. Similarly, the estimation of the spread of pollutants in the presence of a storm requires consideration of the extreme mechanics.

Ocean waves are mainly driven by the wind, which in turn is powered by the sun. The waves generated in this way are essentially random, and a probabilistic element must be included in their full description. Most often a given sea state can be reasonably described by a spectral distribution over frequency and direction, with random phase [44].

Extreme waves — waves which are substantially bigger or energetic than the average — can occur in a number of ways. In a random spectrum, there will be a corresponding distribution of wave heights, and the larger of these will have a relatively low occurrence. These large waves can be thought of as being due to the random focussing of wave frequencies and of wave angles, and are likely to be breaking if the overall sea state is high, when they are often known as *freak* waves. As the waves approach the shore, the decreasing water depth will at some point induce extreme velocities in the crest, leading to breaking and a loss of energy.

There are other, related mechanisms which contribute to the formation of extreme waves. Refraction of waves around an island can lead to constructive interference, and hence large waves, beyond the island. When the waves from two storms generated in different locations cross, the confused sea may contain some very large individual waves. If the depth of the sea is shallow enough, then the topography of the bottom can result in focussing of the waves into *hot spots* of height and energy.

Finally, any of the mentioned mechanisms can also be further affected by the presence of currents. These can be due to a number of causes, including the tides, the large scale motions of the oceans, and those induced by the wind. There is some limited evidence for a strongly sheared, wind-driven current near the surface,

during storms [23, 47]. As high winds and high sea states invariably coincide, it is important to study the combined kinematics of such cases.

1.2 Scientific Study of Extreme Waves

While a full description of the ocean might appear desirable, this can never be achieved practically and would have only a limited value anyway. In the scientific study of the ocean waves, one of the main aims is to understand the trends which are present and then to be able to make good estimates in cases which are representative of important circumstances. The most common means to this end is to identify some significant mechanism from the overall problem, to isolate it and to study it from a number of angles.

The approaches which are available in scientific study can be divided, arbitrarily, into the experimental, numerical and theoretical. The interplay between these approaches is crucial to the advancement of science and has been discussed in this subject area by Peregrine [41] and others. Some aspects of the experimental and numerical approaches are discussed here, to put the present work into context.

1.2.1 Experimentation and its Limitations

Experimentation has a number of virtues, not least of which is that the processes can often be observed directly, especially by eye. The experimental approach is sometimes more flexible than the numerical, in the way that new physical aspects can be introduced to the system, and common 'bugs' are often easier to detect. For example, a leak in the flume may be more easily spotted than the non-conservation of mass in a numerical simulation.

However, there are significant limitations to the experimental approach. It is often difficult or impossible to eliminate unwanted effects, such as the energy loss at the

side walls as a wave travels down a flume. It may be impractical to conduct the experiments at the most suitable scale, and scale effects will have to be ignored or dealt with. The experimental apparatus can never be perfect, and any inaccuracies may subtly affect the processes being modelled. Finally, measurements may have to be restricted, for practical reasons, to a few discrete locations, despite qualitative information of the process being available everywhere.

1.2.2 Numerical/Mathematical Models and Their Limitations

In contrast to experimentation, in numerical simulations it is generally possible to extract the value of a selected quantity at any chosen location, and to obtain arrays of these values over the coordinate space, if desired. Simulations can be perfectly repeatable and highly accurate, allowing numerical investigations which look at the effect of small parameter changes on the process being studied. Experimentally, such sensitivity analyses are often swamped by noise.

Numerical modelling also has its limitations, most often because the assumptions in the model leave out some physical effect which becomes desirable. For example, wave models often have assumptions that the flow is inviscid, irrotational and incompressible. If these effects are not negligible and can't be easily included, the modelling may be inappropriate. Finally, there are some fundamental numerical problems, such as those associated with discretisation and numerical stability. As with experiments, these problems can often be reduced by an increase in resources, for instance using a bigger computer, but they remain as the ultimate limitation on the approach.

1.2.3 New Experimental Techniques

Experimentation relies on the existence of suitable measuring techniques, and often advances are made when new techniques become available. Recently, Particle Image Velocimetry (PIV) has become an reliable method [1, 43], allowing velocity fields to be measured experimentally in much greater detail — offering possibilities for renewed insight, and validation of empirical and numerical models.

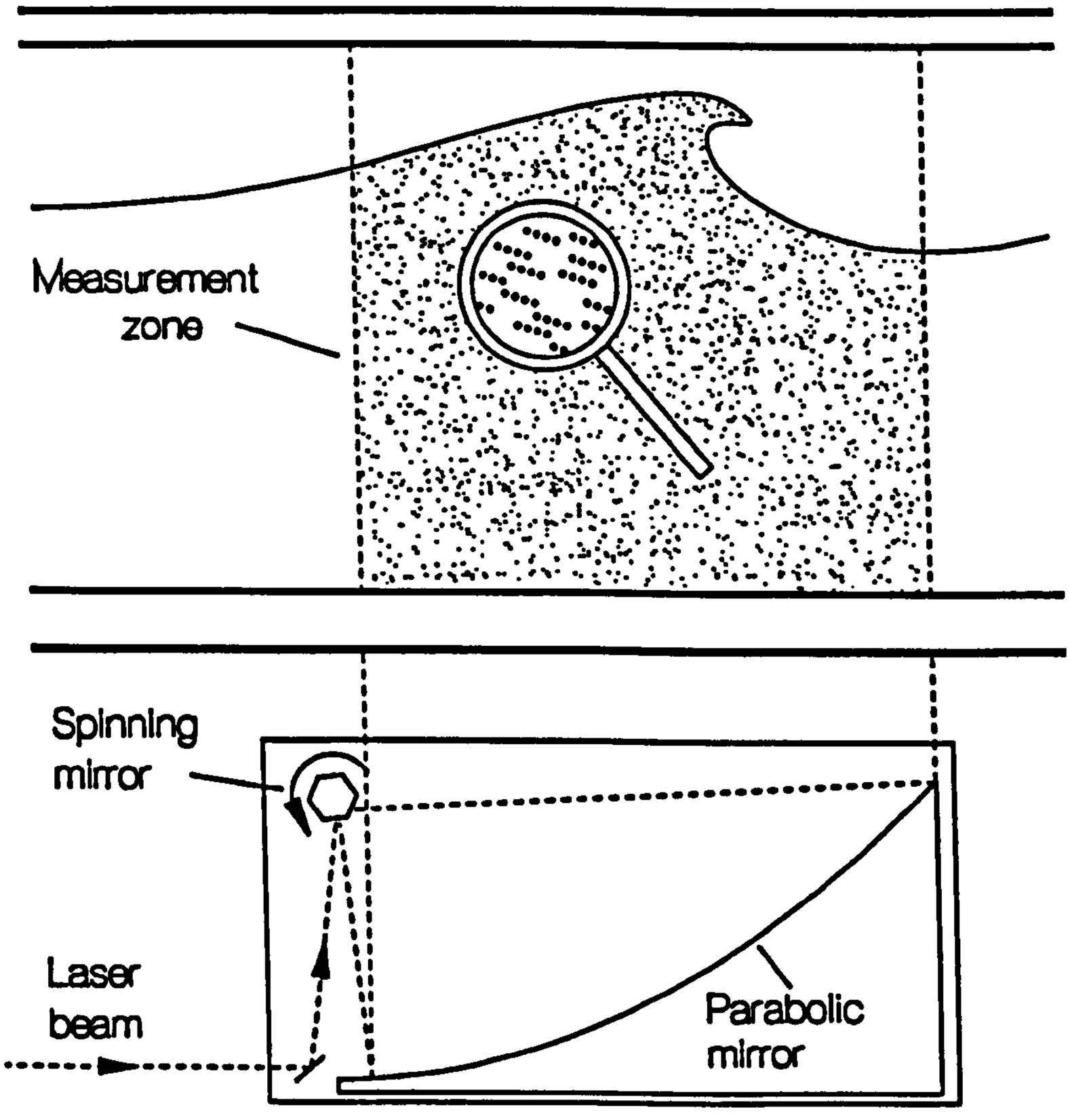

Figure 1.1: Schematic diagram of PIV measurements of a breaking wave

PIV is a measurement technique which can yield very accurate, simultaneous velocity measurements over a wide area of a flow-field. In PIV, multiple images of small tracer particles are recorded onto film (see figure 1.1), which is subsequently analysed to discover the particle motions and hence the velocity field.

Since the early experiments [3, 55, 26], the PIV method has received much research

attention, aided by the increased availability of high-powered lasers to illuminate the flow and the advance in the speed of computers, making automated analysis of the photographs possible. A good review of the technique has been given by Gray [20]. While the principles of method are well established in general, each application requires particular implementations and practices. For the study of the kinematics of water waves, PIV has only recently been developed [19], and is now at the stage where it can be used to yield reliable velocity measurements [57, 60].

1.3 Thesis Focus and Context

In the present study two generic types of extreme wave have been selected and their mechanics investigated experimentally: a long-crested, deep-water breaking wave; and the combination of steep, steady waves with sheared currents. The internal kinematics have been measured with PIV, and, where possible, the results compared with numerical prediction.

1.3.1 The Evolution of a Long-Crested Deep-Water Breaking Wave

In the breaking wave study, a particular deep-water, plunging, breaking wave was chosen and investigated in great detail. The wave selected was arbitrary, but it was considered more important that similar waves could be generated numerically and experimentally, than that the chosen wave should have any particular parameters, other than being very extreme. The study concentrates on extracting the most information with the PIV measurement technique of this particular flow, and on the careful comparison between the measurements and the numerical predictions. The design of the wave flume built for this project allowed the same wave to be followed through all phases of its evolution, from its initial steepening, until after

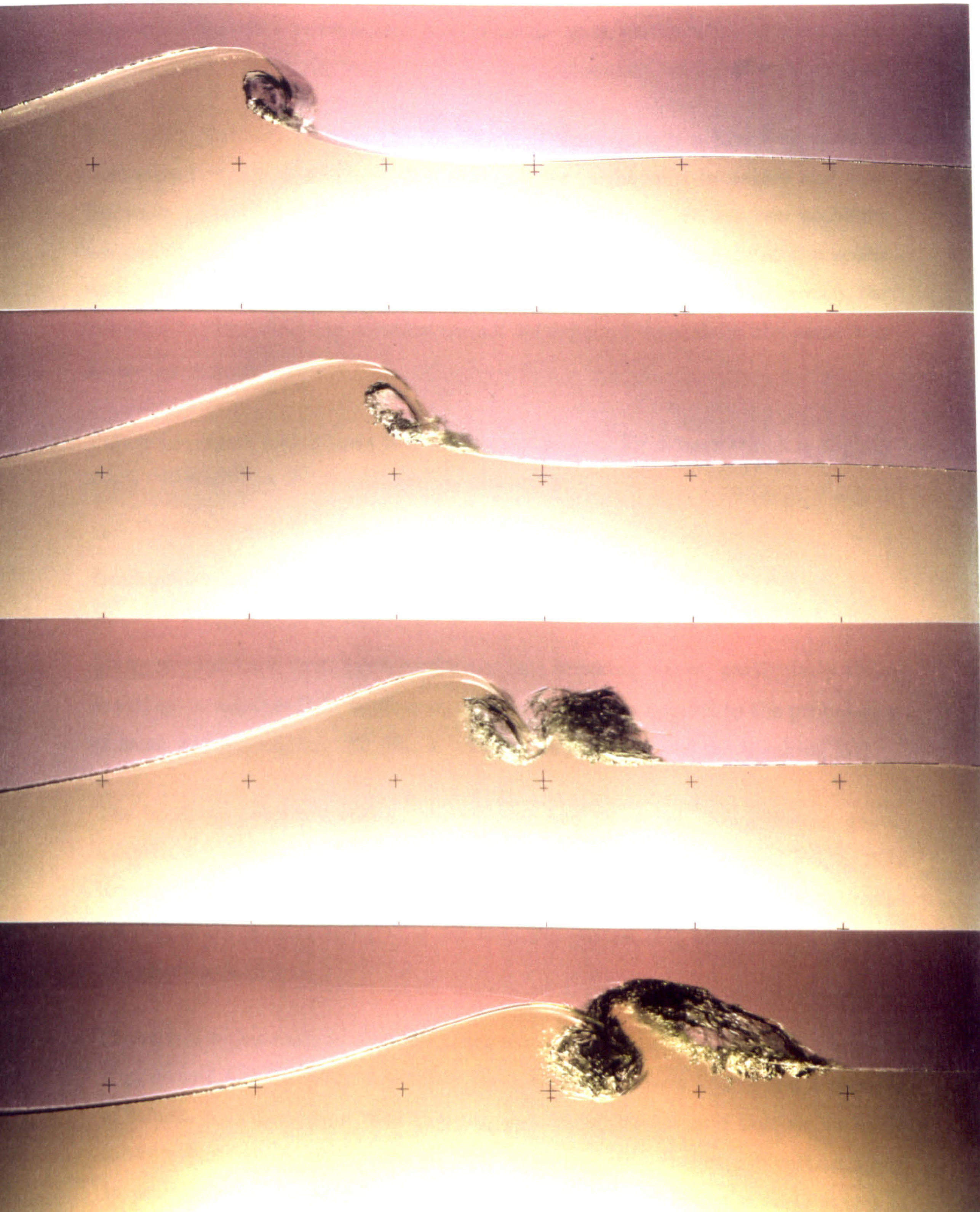

Figure 1.2: The breaking of a long-crested deep-water wave

breaking. The work consolidates and expands upon earlier work of the author [59, 57].

The study does not address the likelihood of finding such a breaking wave in the real sea, but it is assumed that such a wave might exist in nature and that the main properties would scale with Froude scaling. There are two problems associated with this assumption: surface tension is not negligible at the scales used [66], but can be considered a small effect; and after the wave has broken, the behaviour of the resulting aeration cannot be expected to scale in the same way as the kinematics.

Figure 1.2 shows four phases of the breaking process for a wave which is slightly more extreme than the one chosen for the study.

Background to the Breaking Wave Study

Many studies have been performed regarding breaking waves, particularly those breaking on beaches [39]. In deep water, effort has been applied to the probability of freak waves occurring [32, 52], as well as the mechanics of the breaking [31].

The breaking process is difficult to measure and to model. Nevertheless, good, quantitative descriptions of the breaking process have been reported [63, 5, 36]. Recently, measurements have been made of the crest kinematics just before breaking [24], of the aeration induced by the breaking process [34], and of the turbulence left afterwards [38].

Numerical computations of overturning waves were first performed by Longuet-Higgins and Cokelet [35]. Since then refinements have been made, and a number of robust, fully non-linear time-stepping numerical models have become available for two dimensional waves [14, 25, 54]. However, they can be difficult to apply to practical situations and are limited in their application to the early stages of breaking. A good review of numerical computations is given by Peregrine [40].

Experimental studies have been undertaken for comparison with numerical predictions, most notably at MIT[15]. Here, good agreement was obtained between point measurements of the internal kinematics and the prediction of a numerical model, for a deep water breaking wave. However, such comparative studies are rare, perhaps because of the difficulties encountered in trying to arrange the same experimental and numerical conditions.

1.3.2 Steep, Steady Waves on Sheared Currents

The wave/current study was concerned with the laboratory measurement of steep regular waves on strongly sheared currents, with parameters representative of those which might be found in the real sea. Suitable current profiles were established in the flume, waves generated, and the combined kinematics measured with PIV. The initial work [58] was funded by the UK Department of Energy.

Background to the Wave/Current Study

The combined kinematics of waves and currents have been approached theoretically, numerically and experimentally. A good review of recent work has been published by the UK Department of Energy [12]. A complete treatment for regular waves travelling on uniform currents has been given by Fenton [17].

Recently, numerical and analytical approaches have accommodated non-uniform currents to varying degrees. Uniform vorticity (constant shear) has been include in fully-nonlinear time-stepping models [64]. The combination of steady waves with linear and bi-linear currents has been tackled numerically [10, 16]. Steady wave computations have been extended to include currents of arbitrary profile [8] [65].

Experimental studies have been few and limited, with notable exceptions [61]. In that study, measurements were made of the combined kinematics of medium

amplitude waves on extremely sheared currents. The measurements were made using Laser Doppler Anemometry (LDA), extending up to the trough level only. The range of velocities due to the current was one or two times that due to the wave kinematics, in all cases, and fair agreement was obtained with the predictions from Chaplin's model [8].

Other experimental work includes that of Thomas [65], where good agreement was obtained between laboratory measurements and numerical predictions for weakly sheared currents. Good experimental measurements have been reported [30] on the interaction of waves and non-uniform current. In that study, which concentrated on the effects near the bed, it was noted that the mean shear in the wave zone was reduced in the opposite direction from the wave propagation. Particle Image Velocimetry (PIV) has previously been used to measure the combined kinematics of small waves and currents [18], but the PIV measurements were disappointing compared with those obtained with LDA, and the study inconclusive.

The UK Department of Energy has produced Guidance Notes on the ways of including currents into design [13]. This document gives methods for obtaining the best estimates for different currents in a variety of circumstances. At present, all current combinations are simplified to bi-linear profiles, whose parameters are given by empirical rules.

Chapter 2

Wave Theories and Modelling

2.1 Summary

This chapter contains no new results, but serves to outline the mathematical modelling approaches made use of in the subsequent chapters. Theoretical and numerical modelling methods are mentioned, along with some commonly used engineering approximations.

2.2 Wave Theory

Much theoretical work has been done on water waves. For many experimental studies, linear theory is a very useful tool, and covers most needs. However, there are also some more general theoretical approaches, some specifically non-linear, which have been used to support the present experimental work. These are outlined along with the aspects of linear theory made use of in later chapters.

2.2.1 Linear Theory

If the motion within a wave is irrotational, inviscid and incompressible, then the velocity potential satisfies Laplace's equation. In order to find solutions for the flow, boundary conditions must first be satisfied. On the surface, Bernoulli's equation is used. For monochromatic two-dimensional waves travelling on constant depth, linear solutions can be found for the velocity gradient and other quantities after suitable approximations have been made. The relationships arrived at are summarised below, for a wave travelling in the positive x direction.

For sinusoidal waves, the surface elevation is given by

$$\eta(x,t) = Re\left\{ae^{-ikx+i\omega t}\right\} \tag{2.1}$$

and the velocity potential ϕ by

$$\phi(x,z,t) = Re\left\{ia\frac{\omega}{k}\frac{\cosh k(z+h)}{\sinh kh}e^{-ikx+i\omega t}\right\} \tag{2.2}$$

where ω is given by the dispersion relationship

$$\omega^2 = gk\tanh kh \tag{2.3}$$

From equation 2.2 the horizontal and vertical velocity components can be determined as

$$u = Re\left\{a\omega\frac{\cosh k(z+h)}{\sinh kh}e^{-ikx+i\omega t}\right\} \tag{2.4}$$

$$v = Re\left\{ia\omega\frac{\sinh k(z+h)}{\sinh kh}e^{-ikx+i\omega t}\right\} \tag{2.5}$$

From equation 2.1 the waves travel with phase velocity

$$c_p = \frac{\omega}{k} \tag{2.6}$$

and it can be shown that the group velocity is given by

$$c_g = \frac{\omega}{2k}\left[1 + \frac{2kd}{\sinh 2kd}\right] \tag{2.7}$$

Implicit in any linear theory is the assumption that different solutions can be superimposed to yield another solution, providing the resulting amplitude is not too large. This can be made use of in the generation of spectra and the estimation of the evolution of wave groups. If the frequencies components are equally spaced then the wavefield can be described by

$$A(x,t) = Re\left\{\sum_{n=N_0}^{N_1} A_n e^{-ik_n x + i\omega_n t + i\alpha_n}\right\} \tag{2.8}$$

where A_n and ω_n are the amplitude and angular frequency of the nth component, with

$$\omega_n = 2\pi n\,\delta\omega \tag{2.9}$$

Linear theory is only strictly correct for very small waves, but its range of applicability is surprisingly large. For many purposes, linear theory provides a very good first estimate of values.

2.2.2 General Theory

Doppler Theory

If waves travel on a uniform, non-turbulent current, or if waves on otherwise still water are viewed by a moving observer, then their frequency is modified according to Doppler theory.

Consider a steady wave with wavelength λ. If this wave has frequency f_1 when observed in a given frame of reference S_1, then an observer in a second frame of

reference S_2, moving with velocity u, measured in the direction of wave propagation and relative to S_1, will measure an apparent frequency f_2, given by the Doppler formula

$$f_2 = f_1 - \frac{u}{\lambda} \tag{2.10}$$

In the frame of reference where there is no underlying flow, the frequency and wavelength are related by the appropriate dispersion relationship, such as that given in equation 2.3, for small waves.

2.2.3 Non-linear Theory

Theoretical considerations have led to some important results concerning the steepest, stable waves. The development of these approaches is well covered in the literature and books such as Sarpkaya and Isaacson [53]. Of most interest for offshore design is the result [9] concerning the limiting steepness in deep water.

$$H/L = .141 \tag{2.11}$$

For a given period, as the waveheight increases the wavelength also lengthens. For the limiting wave steepness, on deep water, the wavelength is related to that obtained from the linear dispersion relationship (equation 2.3) by

$$\lambda = 1.22\lambda_0 \tag{2.12}$$

2.3 Numerical Modelling Methods

Numerical modelling takes advantage of theoretical considerations, mathematical methods and computing resources to solve problems in situations which are analytically intractable. Of interest for the present studies are expansion methods

used to obtain solutions for steady waves and boundary integral methods used to propagate time-evolving wave groups. These methods generally assume the flow to be inviscid, incompressible and irrotational.

The expansion methods are based on the use of the velocity potential or the stream function, and there are two basic approaches, known widely as Stokes's method and Dean's stream function. Dean's stream function and related methods are more suited to the calculation of very steep waves. Many refinements of these methods have been proposed [7, 48].

In the boundary integral method, it is assumed that the starting boundary conditions are known, for example by calculation with an expansion method. Computational points are positioned along all boundaries, each with a coordinate and velocity potential. Points on the free surface are allowed to move, while points on other boundaries are either fixed, or move with prescribed motions. If the flow is two-dimensional, use can be made of Cauchy's integral theorem to solve Laplace's equation for the time derivatives of the surface motion. All of the computational points are then updated to their predicted values at the next time step, and the process repeated.

2.4 Numerical Models Used in the Studies

The author was fortunate enough to be given copies of programs written by Klopman, Chaplin and Dold et Al., and to run these at Edinburgh.

2.4.1 Two-Dimensional Steady-state Models

Three programs were available for the calculation of steep, steady waves. Klopman's program was used to calculate wave parameters, Chaplin's to obtain the internal flow field, and Dold's when vorticity was required.

Klopman's Program

Klopman's program is based on the Fourier approximation method of Rienecker and Fenton [48]. The main input parameters for the program are the height of the wave, the frequency or wavelength, and the mean water depth. A value for the current can be specified and this is flagged to either be the mean mass transport velocity or the mean, Eulerian current velocity averaged below the trough, as required. The program computes the surface elevation and the stream function, given the required number of Fourier components. An extensive table of wave parameters is output, including such quantities as the wavelength or frequency and the mean Eulerian velocity. Horizontal velocity components can be calculated under the crest and trough.

Chaplin's Stream Function Program

Chaplin's Program is based on stream function theory [11, 7], and can calculate the velocities under steady waves to a given order. The main input parameters are the wave height and frequency. The wave surface is calculated along with the velocities at specified points, allowing a grid of velocity vectors to be constructed. The program is available commercially as *MSTR56*.

Bristol Constant Vorticity Program

The Bristol Constant Vorticity Program, *STCHY*, takes the water depth, wave height and wavelength in dimensionless form, along with a constant value of vorticity and control parameters. The elevation and velocity potential are calculated along the free surface and output to a file. This file serves as the input to an extensive set of processing programs.

2.4.2 Two-Dimensional Time-stepping Model

The time-stepping program was provided by the University of Bristol [14]. The main program *WCHY* takes an array of surface computational points ($z(x_n)$ and $\phi(x_n)$), and time-steps the flow until a specified time, or until the calculations become unstable if the wave is overturning. It is implicit in the formulation that the end boundary conditions are periodic. An important feature of the numerical scheme is the use of higher order derivatives in the time-stepping, resulting in a computationally efficient scheme.

Input to the program can be generated by the steady wave program *STCHY* or by other means. Resulting data is processed by other programs to obtain quantities such as the internal velocity field.

2.5 Engineering Approximations

While sophisticated numerical models exists which would be suitable in many circumstances, they are not always used in current engineering practice. This is perhaps due to a combination of availability of the models and the difficulties sometimes experienced matching the required input parameters to the particular circumstances. An example of a typical engineering approximation is the estimation of the internal kinematics of steep waves by arbitrary stretching of the results of linear theory to the free surface [68]

2.5.1 Current stretching

The present recommendation for obtaining the combined wave/current kinematics in offshore design given by UK Department of Energy [13] is to estimate a bi-linear current, then to use a suitable, complete wave/current theory to calculate the

kinematics. Alternatively, a method of stretching the current to the free surface is given, which is then added to the kinematics generated by an irrotational model.

The current value at a given height above the bed is moved to a new location by multiplying the distance from the bed by the factor $(1 + C_N/h)$, where C_N is the crest elevation, obtained numerically, and h the water depth. The recommendation is that no attempt be made to conserved the total mass flux of the current when stretching.

Variations on the current stretching methods have been discussed by Baltrop [4]. Applying conservation of mass flux at each phase of the wave is clearly wrong, as this incorrectly predicts the kinematics for a wave riding on a uniform, non-turbulent current. In this case the kinematics can be correctly obtained by Doppler shifting the frequency to the current frame, calculating the internal kinematics in this frame, then adding the constant current to all velocities.

Chapter 3

Experimental Facilities and Techniques

3.1 Summary

The requirements for the experimental projects are discussed, and the actual facilities built and used detailed. Especially developed experimental practices are described, in particular those needed in the taking of Particle Image Velocimetry photographs. Methods of analysing the photographs and other measurements are covered, and associated errors and limitations mentioned.

3.2 Experimental Requirements

In the process of transforming the idea for an experimental research project to a completed study a full assessment has to be made, preferably at an early stage, of the experimental facilities that will be required. Most often in scientific research the details of the work being undertaken only become apparent once the study is under way, so that it may not be possible to fully specify the requirements for the experimental facilities at the start. Even when the experimental needs are fully understood, they may prove impossible to fulfill and must be modified accordingly. In most experimental studies there is an interplay between what is desirable and

what is practicable.

Given that the requirements from the experiments can be specified, the first task is to decide whether they can be met by using existing facilities, whether modifications are necessary or whether completely new apparatus should be built. Such decisions rest on the balance between the suitability of the different options with the difficulties which might be encountered in implementing them. In some circumstances the requirements may be very impracticable due to physical constraints, such as the resolution limits of recording media. In other cases the ideal apparatus may be too expensive to buy or too time-consuming to build. The necessary technical expertise might be lacking, or the desired apparatus might be too big for the laboratory. There are many constraints which limit the scope of any experimental study, and the goals must be modified as necessary.

For the kinematic studies covered in the present work, a number of experimental requirements were identified. These were fixed upon at a point before most the apparatus for the main experiments was built, and were identified as a result of experience already gained measuring breaking waves with PIV, as well as from other research projects previously undertaken.

The experiments needed a wave flume, which had to be dimensionally accurate, if straightforward comparisons were to be made with numerical simulations. The flume had to have very good optical access and the PIV illumination system had to be easily moved to different parts of the tank, so that kinematic measurements could be made at any position required by experimental considerations, such as the desirability of following a breaking wave through the whole of its evolution. The wave generator needed to be of a very high quality. For the study of wave/current interaction, the current inlets had to be able to shape the current close to a specified profile. An estimation of the number of PIV photographs which would need to be analysed meant that the speed of PIV analysis had to be increased by at least an order of magnitude. Finally, a decision was also made to make the experimentation as automated as possible, to the degree that the current PIV process would allow.

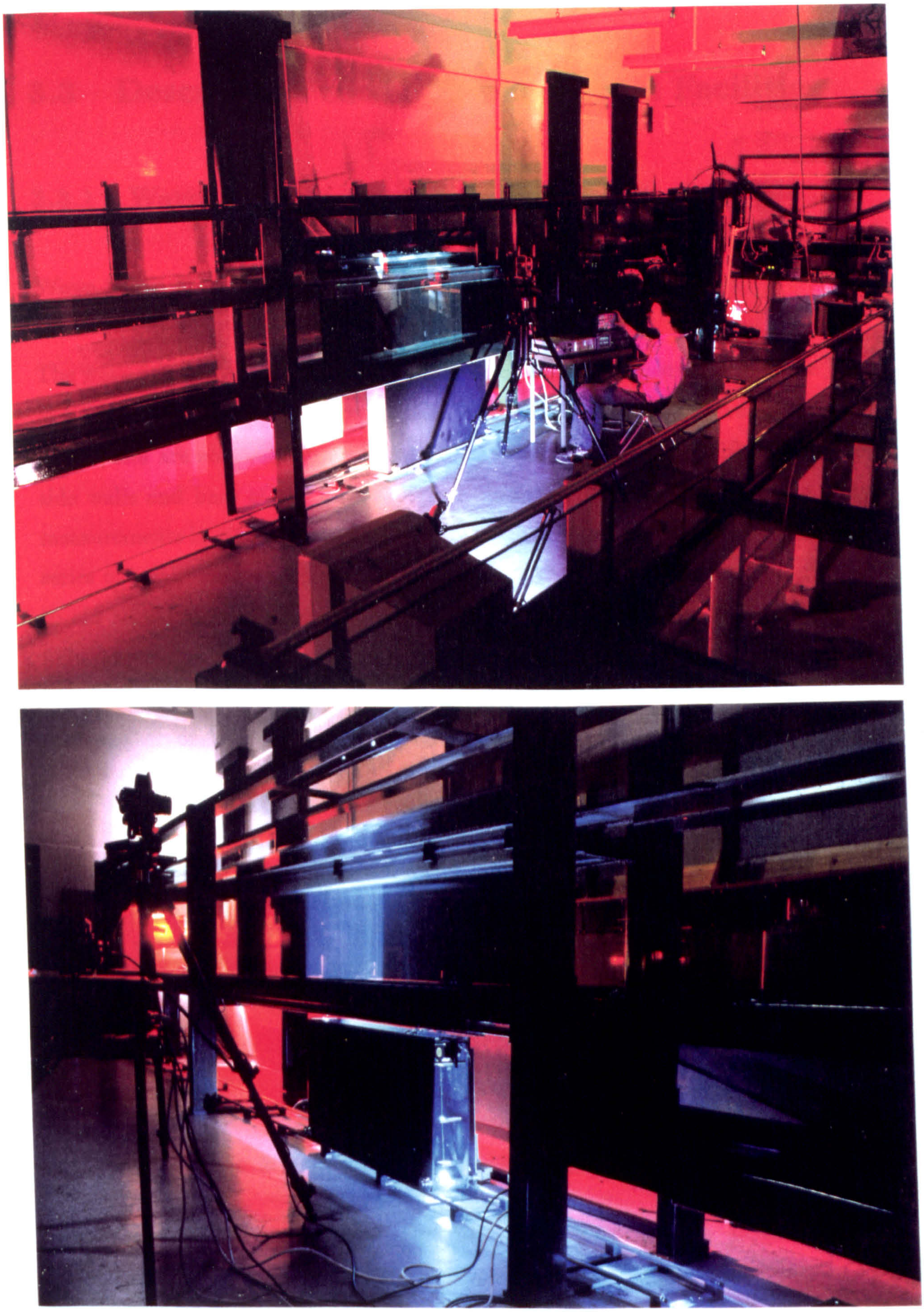

Figure 3.1: Photographs of the laboratory, showing the wave flume (above), and the arrangement for PIV measurements of the wave kinematics (below)

3.3 Description of the Experimental Facilities

3.3.1 Wave Flume

Wave Flume Description

The wave flume used for the main experimental studies is illustrated in figure 3.2. Waves are generated by a hinged-paddle, absorbing wavemaker, travel from right to left, and are normally absorbed by a mesh beach at the end of the flume. The side walls and base of the tank are glass, allowing good optical access for PIV measurements in either of the two bays furthest from the wavemaker. There is a series of small crosses at regular intervals along the glass wall of the second bay to aid registration of photographs. The illumination system which provides the pulsed light sheet for the PIV photography is mounted on rails and can be moved anywhere beneath the two measurement bays. Current can be injected below the wave-maker, or from the end of the tank.

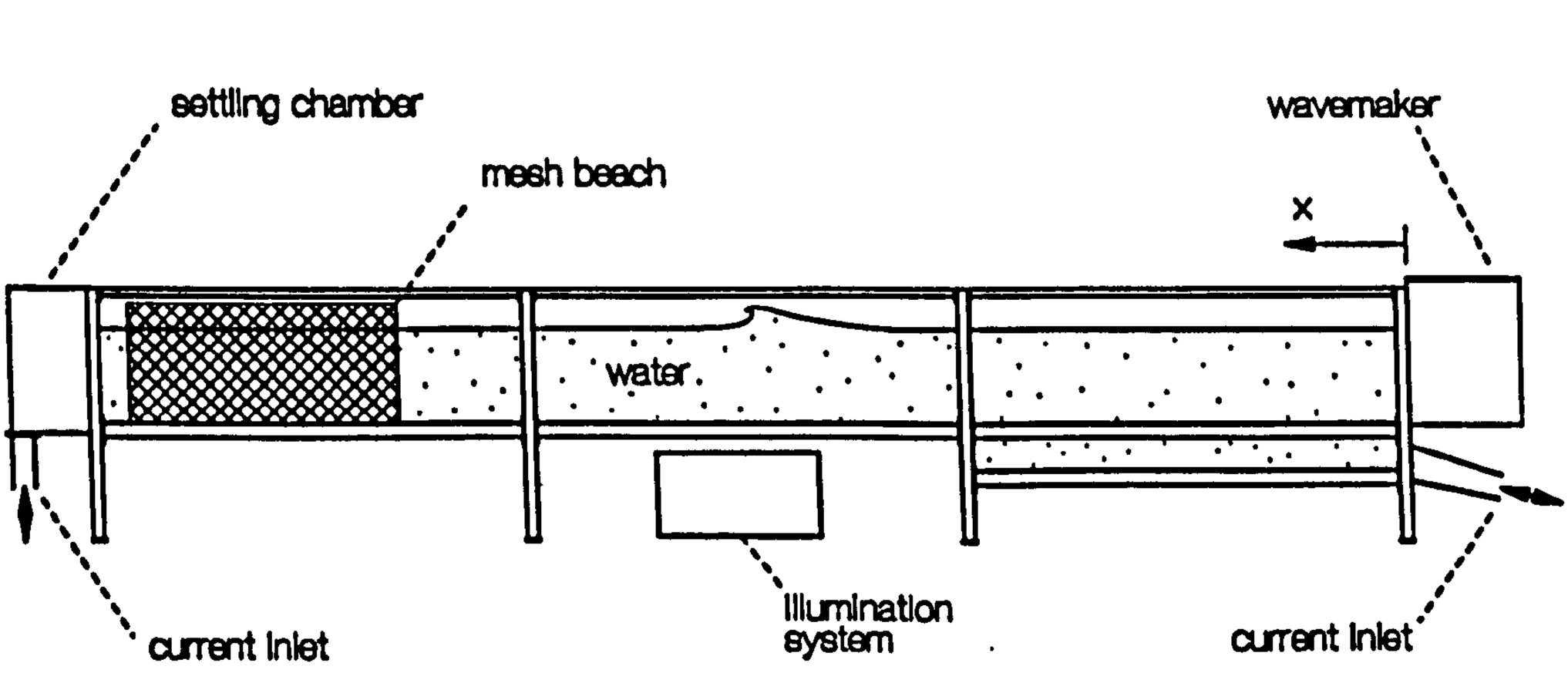

Figure 3.2: 9.770m wave flume used for the experimental studies

The flume is 9.770m long and .400m wide. The normal water depth is .750m. x is measured along the flume from the wavemaker end, and z upwards from the water surface. In this chapter, the flume and associated apparatus is shown as normally viewed in the laboratory. In the subsequent chapters, describing the

experimental studies, the flume is shown reversed so that waves travel left to right, and x increases in the usual direction.

Wave Flume Construction

The wave flume was designed with the requirements mentioned in section 3.2 in mind, particularly those relating to PIV measurements. In the design of the flume the main concern was to balance the need for very large glass bays with a desire for dimensional accuracy and rigidity. The path which lead to the final design consisted of selecting the largest panes of the thickest glass which were readily available and ensuring that the metal frame to support them would be adequate to within some specified criterion. The available glass panes were of 25mm float glass, with dimensions 3210 × 1050mm.

Earlier experience with wave flumes indicated that maximum rigidity of the wave flume along with the highest possible dimensional accuracy is very desirable. High rigidity minimises problems with vibration, whether in connection with wave or current generation, or during measurements of, for example, wave impact forces. Ensuring good dimensional accuracy eliminates the need to worry about the effects of varying flume width and makes the design of apparatus to fit in all parts of the flume much easier. The criterion judging the structural qualities of the flume was chosen, arbitrarily, to be that the individual static deflections at five key points in each bay should be .5mm when the flume was filled to its normal water depth. An additional requirement was also imposed that if the flume was overfilled that the maximum stress in the glass should be within the manufacturer's recommendations.

The key points for which deflection calculations were undertaken are marked in figure 3.3. The calculations were made to determine the stiffness required of the structural members, and appropriate formulae were taken from [49]. The maximum deflection of the glass, at (a), depends only on the glass thickness and water depth if the bay length is long compared to its height. Deflections (a), (b)

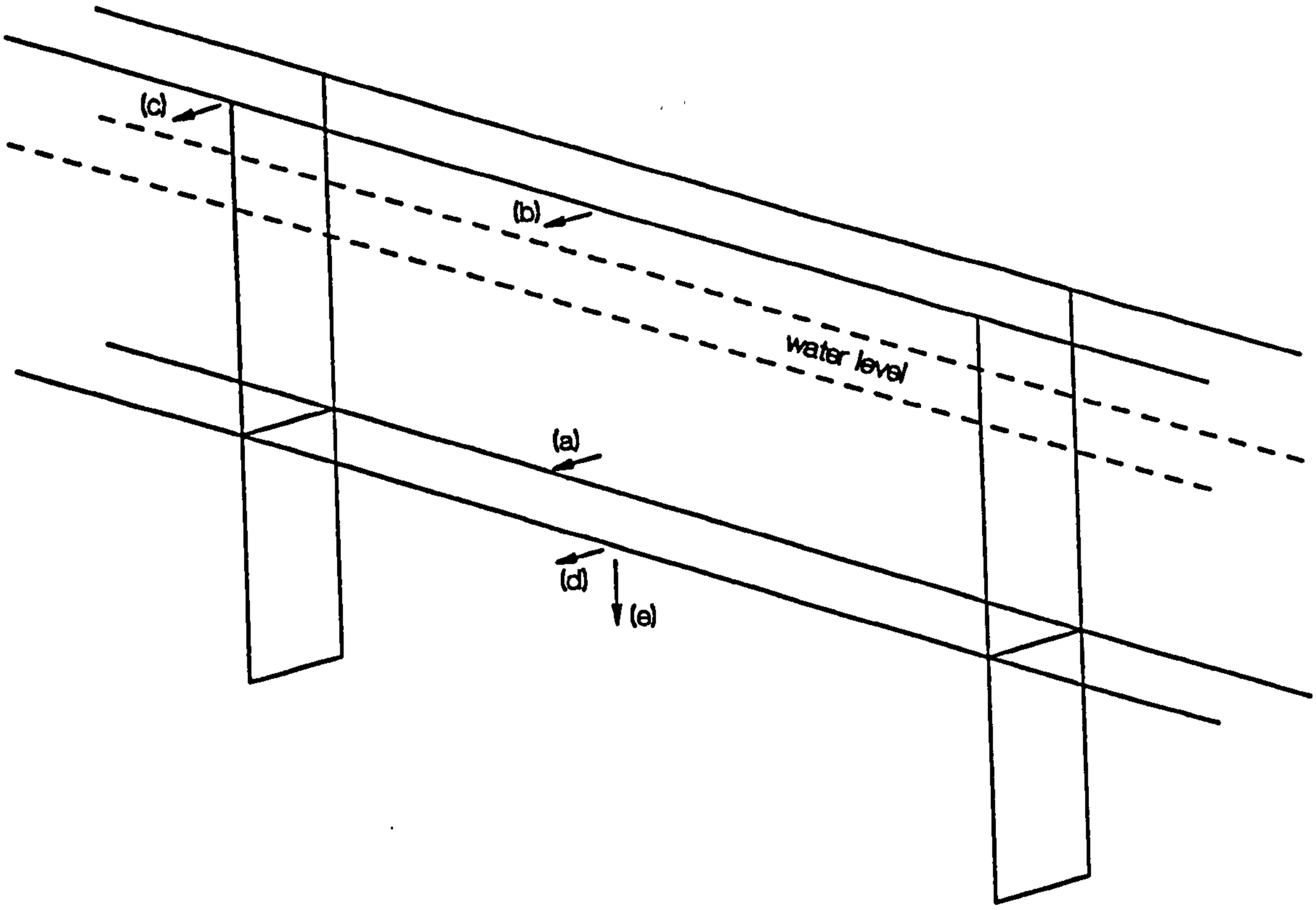

Figure 3.3: Metal frame of the wave flume

and (c) all contribute to the widening of the flume at the still water level when filled with water. Deflections (d) and (e) are less important in relation to the dimensional accuracy of the flume when filled, but must be kept small if the gap to be sealed between the bottom and side walls is to remain reasonably constant when the flume is filled and emptied.

Having determined the second moment of area required of each of the structural elements, appropriate material was selected. This was hollow, rectangular box section steel with 1/4" thick walls. The cross-sectional dimensions of each beam was selected from the stiffness criterion.

The construction of the tank frame was by a combination of welding and bolting. The vertical and cross members were welded into *H* frames, with an additional tie across the feet, and the longitudinal member had flanges welded to their ends in order to allow their bolting to the *H* frames. This arrangement is shown in

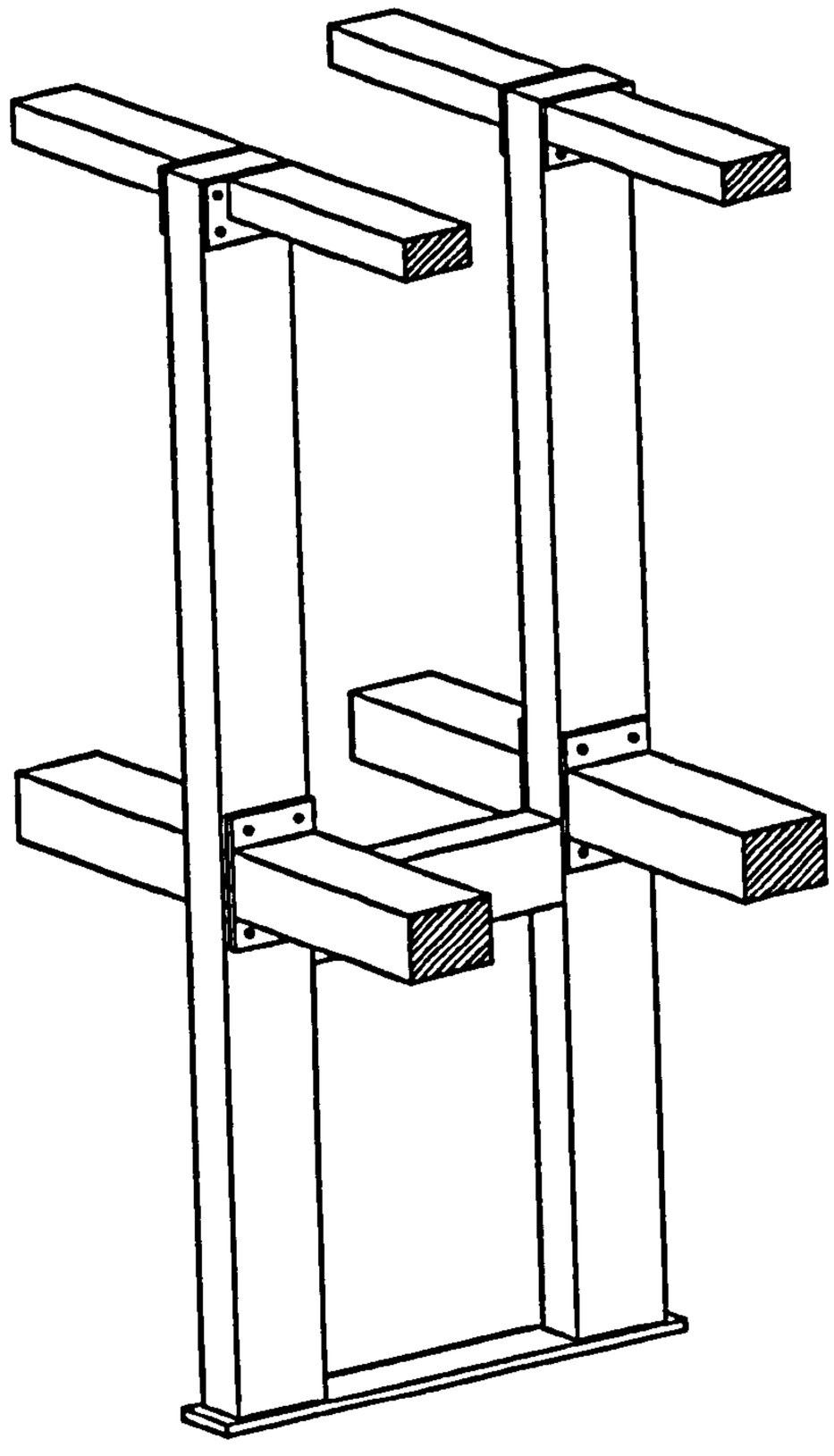

Figure 3.4: Structural members of the wave flume

figure 3.4. The steel frame was bolted up and overall levelling and straightening achieved by placing *shim* under the feet and beneath the flanges, as necessary..

The requirement for the glass to be held within the frame was that it should be fully supported, and that the supporting forces should be as spread out as possible and not too close to the edges of the panes. This was achieved by the use of $\frac{1}{4} inch$ aluminium angled section and strips bolted to the steelwork, with continuous pads of double sided tape between the aluminium and the glass. The arrangement of these materials is shown in figure 3.5.

While the dimensional accuracy of the welding was everywhere higher than had been hoped for, some of the steel beams were found to be bent and the frame was not sufficiently accurate for the glass as it stood. This was rectified by placing *shimming* material between the steelwork and the aluminium, until the internal

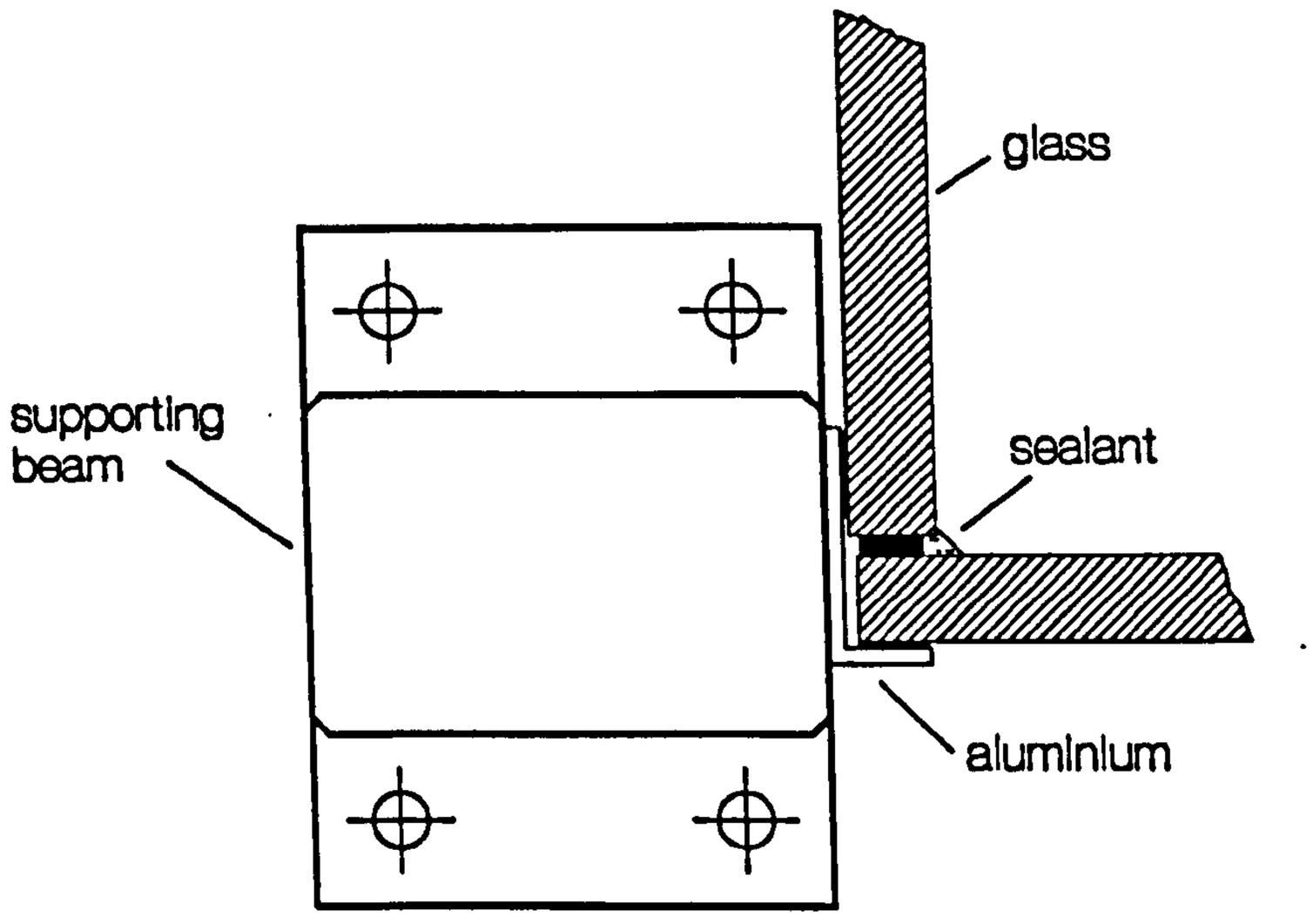

Figure 3.5: Constructional detail of the wave flume

aluminium frame was deemed to be sufficiently accurate. This process was somewhat time consuming. It may generally be better when designing a wave flume to reduce the dimensional accuracy requirement for the structurally frame and to position the glass very accurately by bedding it onto the metal frame with a few mm of a setting material such as *Silastic* silicon rubber. This technique has been successfully used at Delft Hydraulics. However, in the case of the Edinburgh flume the choice of double-sided tape supported by a metal frame made dimensionally accurate was somewhat fortuitous as the glass panes were all badly warped, requiring up to 60kgf of static force to hold them flat, which could be provided by the adhesive tape.

In order that the glass panes should remain sealed together on filling the tank, the gaps between them should be sufficiently large so that the sealant does not have to stretch too much. This was achieved by allowing 5mm gaps between the elements along the flume, and standing the side walls on $\frac{1}{4} inch$ rubber strip. Unfortunately, the supplied glass panes were not within the dimensional tolerance specified, and the gaps, in some places, were smaller than desired. The other important consideration when creating sealing gaps is that the sealant should be supported on

the outside, so that it cannot fail catastrophically, and any minor leaks should be squeezed closed. The joints were sealed with *Silastic* silicon rubber, and despite all the thought given to effective sealing, a number of leaks still occurred.

Figure 3.6: Construction of the wave flume

As well as needing to possess characteristics already described, the wave flume was designed to allow the easy fitting of other pieces of apparatus. The glass walls of the flume were terminated with metal sealing surfaces, and the end *H* sections had suitable fixing attached to allow the wavemaker and current inlets not only to be clamped up and sealed, but also to be easily removed if necessary. 1 inch circular stainless steel rails were provided along the top of the flume to allow easy positioning of apparatus and clamping, if necessary.

3.3.2 Wave Generation Hardware

The most essential piece of equipment in a wave flume is the wave generator. If the experimental studies are to be of a high quality then the wavemaker must be able to produce waves which are of a similar quality. The generated waves must be highly repeatable and steady, if specified as such. The amount of cross waves should be small and spurious distortion of steep waves minimal. The wavemaker

should be able to produce big enough waves suitable both for the wave flume and the wave studies to be performed. Finally, the wavemaker should be able to provide good absorption of any reflections.

These requirements fulfilled by a wave generator manufactured by *Edinburgh Designs Ltd.* This design has evolved from the original absorbing wave paddle first described by Salter [51].

Wave Paddle Description

The wave generator is illustrated in figure 3.7. Its principal features are the triangular shaped paddle, hinged at the bottom; a rolling gusset which prevents water from entering behind the paddle; and a motor which rocks the paddle backwards and forwards via a drive belt. The motor is aided against the hydrostatic forces of the water by springs which also pull on the drive belt.

The drive belt is attached to the back of a circular sector mounted on the top of the paddle. The point at which the belt meets this sector is constant in space and independent of the angle of the paddle, to avoid any non-linearity being introduced by the mechanics. All torques about the hinge applied to the paddle from the sector pass through a piezo-electric force transducer. In addition there is a tachometer in line with the torque motor which measures the angular velocity of the paddle.

The wavemaker is effectively controlled by two control loops. The lowest level loop is between the torque motor and the torque transducer, in order that any torque demanded of the motor is actually achieved at the paddle. This loop has a very high gain, possible as a result of the stiffness and short effective length of the drive belt, and the motor can be regarded as delivering exactly the torque required, so long as it is not too great. In a second control loop the torque demand is calculated from the sum of the externally requested torque and terms proportional to a filtered signal of the angular velocity and to the angular position squared. The

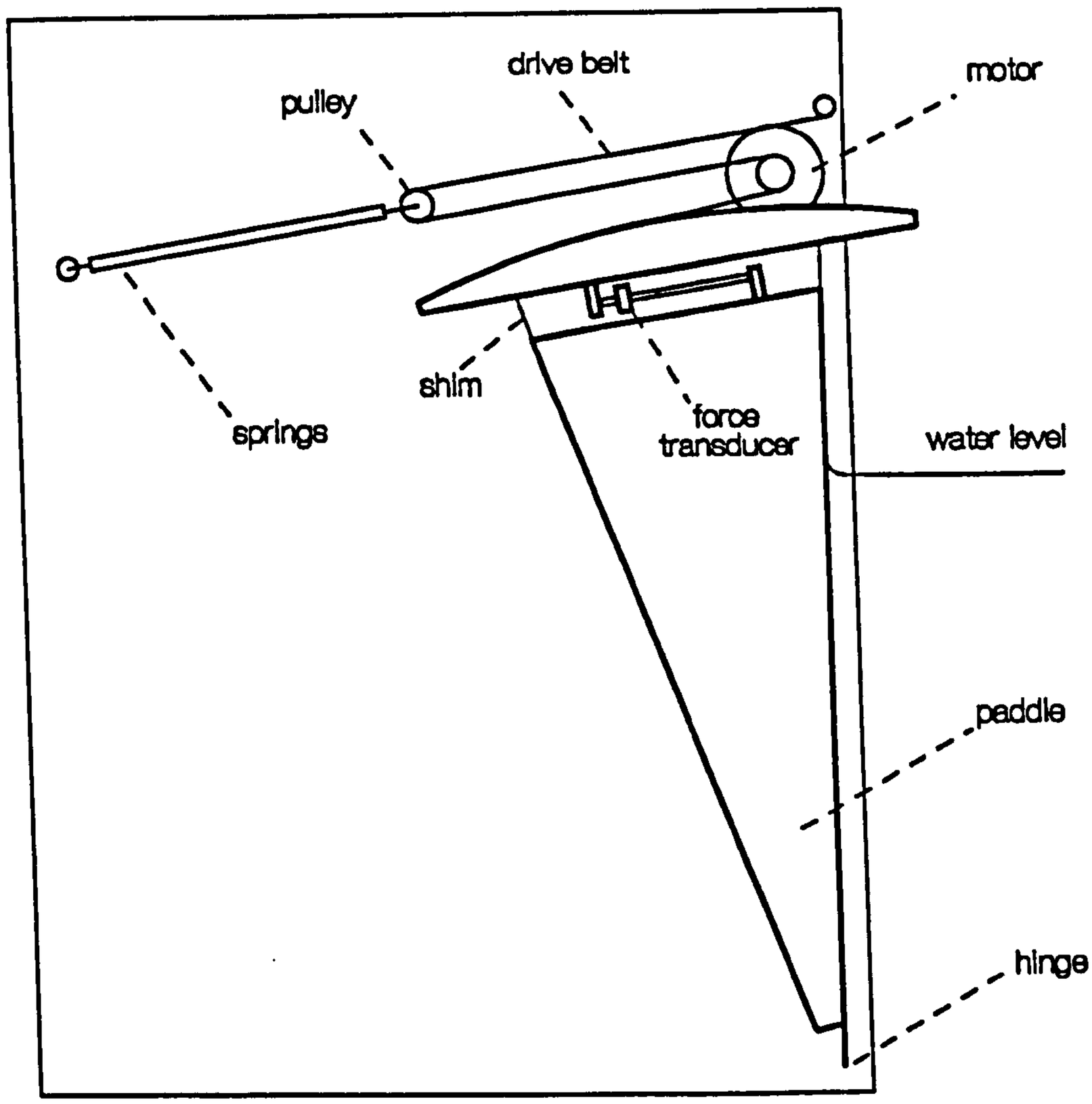

Figure 3.7: Absorbing wave generator

externally requested torque is responsible for the generation of waves. The filtered velocity term is present to provide absorption of reflected waves and the squared angular position term is included to remove the hydrostatic non-linear term which otherwise tends to push the wavemaker back.

The width of the paddle of the wavemaker is chosen in such a way that the gap between its edge and the walls of the tank is half the width of the water surrounded by the rolling gusset. As a result, water which jets through this gap as the gusset moves, travels at about the same speed as the front of the paddle, minimising the generation of cross waves.

Wave Paddle Characteristics

The maximum possible wave elevation that can be generated by the paddle depends on its maximum travel at low frequencies and on the theoretical limiting wave height, mentioned in section 2.2.3, at higher frequencies. The heights calculated in this way are plotted in figure 3.8, along with measurements from the flume. The maximum generated waves will always be smaller than the limiting values, because of instabilities and non-linearities of the wavemaker.

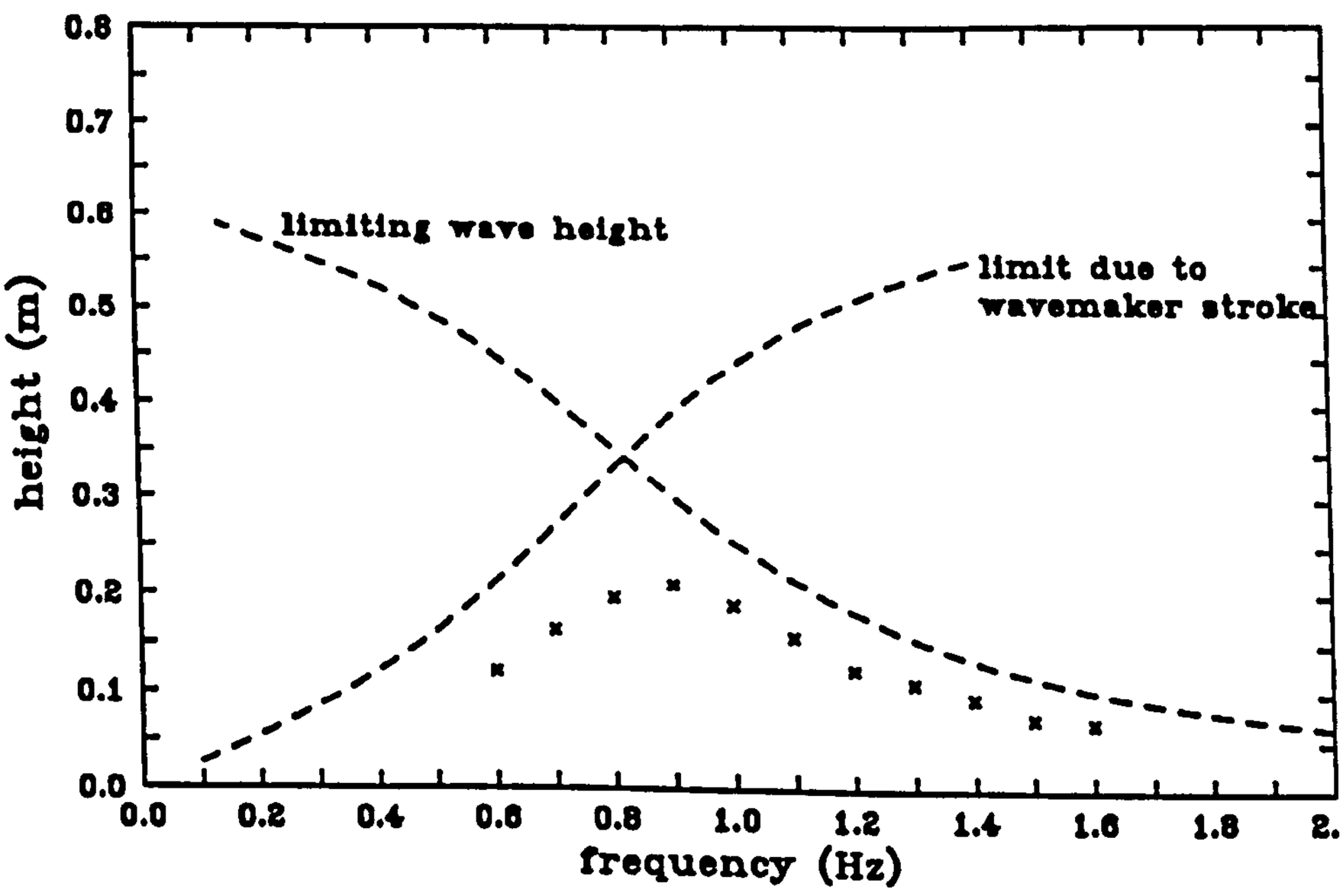

Figure 3.8: Maximum possible wave heights from the wave generator

At lower and intermediate frequencies, the wavemaker was not able to generate wave as high as the available stroke would suggest, because the power amplifiers driving the motor were found to be current-limiting.

3.3.3 Wave Gauges

The gauges used to measure wave height in the studies were wire wave gauges of the conductive type, provided courtesy of the Edinburgh University Wave Power Project (EUWPP).

Wave Gauge Description

The wire wave gauge consists of two parallel metal rods which are partially immersed in the water. The circuitry shown in figure 3.9 is designed to measure the conduction between the rods. The conductance of the water is measured through a third wire and a compensation made for it.

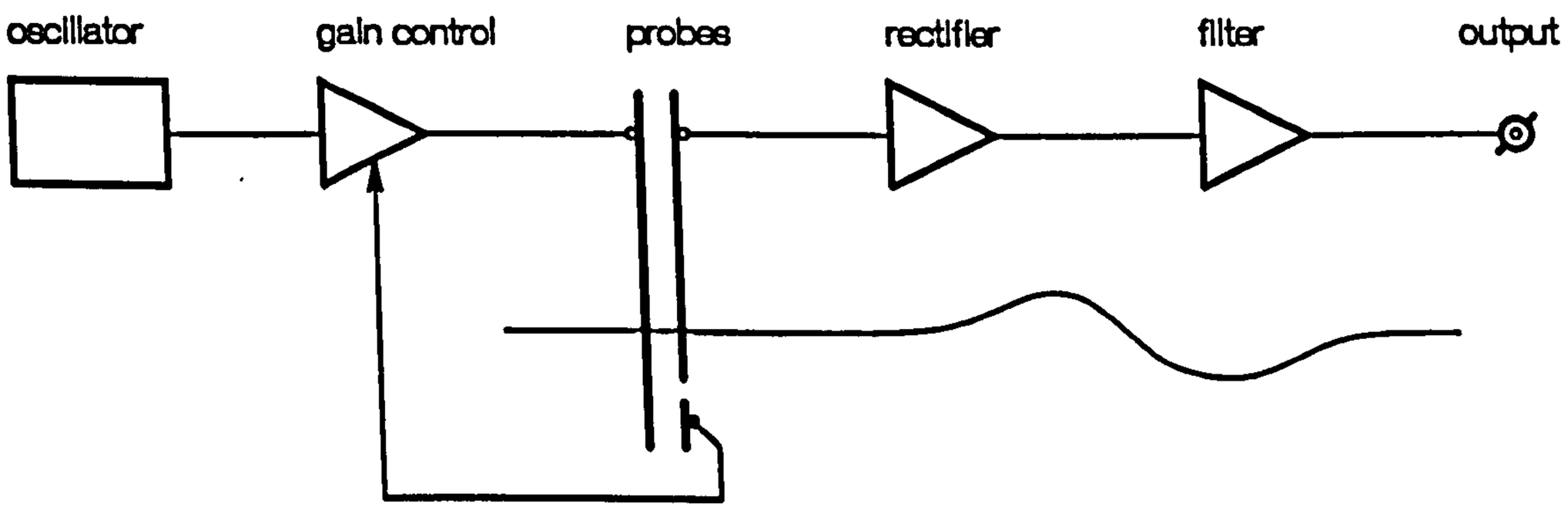

Figure 3.9: Wire wave gauge

Wave Gauge Characteristics

The important characteristics of a wave gauge are its linearity of response with wave height, the drift of its calibration value with time and the limits of wave-heights which can be accurately measured. Due to meniscus effects, the gauges have been found to be inaccurate when the wave amplitude is less than 1mm [56], but this is much smaller than the waves used in the present studies. The drift of the calibration value can be checked periodically.

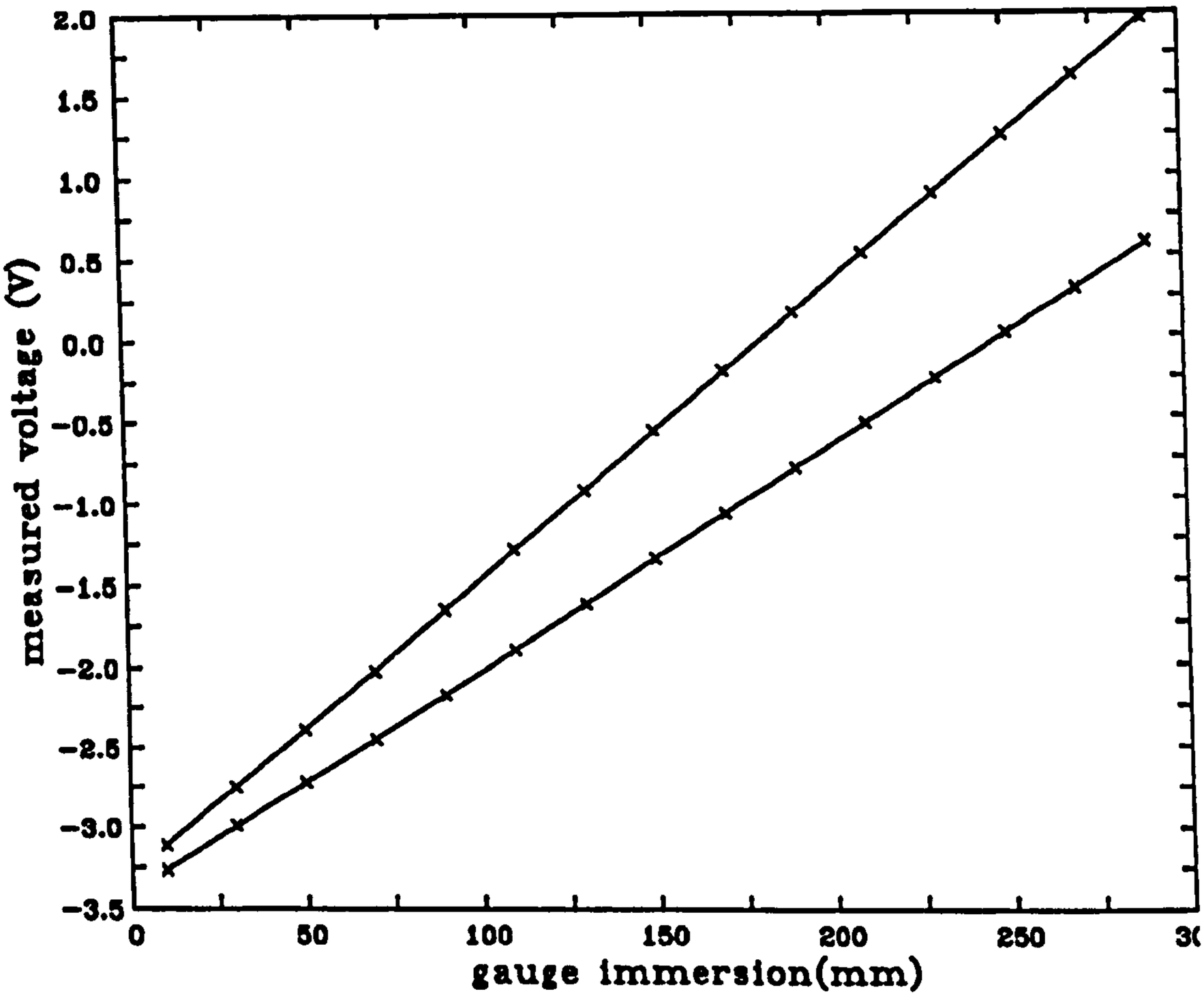

Figure 3.10: Wave gauge measurements against water surface height, for each of two gauges

While the linearity of the gauges can be expected to be very good, due to their design, it is particularly important when attempting comparisons between experiments and numerical predictions to be sure of this assumption's correctness. This was checked in an experiment in which the voltage response was measured against immersion distance into still water. The response is plotted in figure 3.10, for each of two gauges, and was found to be very linear.

3.3.4 Current Generation

The requirement for current generation in the flume was for flow in either direction, with a variable delivery up to a maximum total flux of about $.3ms^{-1}$ and control of the current profile.

General Layout

The overall flow rate and the direction of current is controlled by four valves in a piping network which joins the wave flume to a centrifugal pump. The layout of the piping network is shown in figure 3.11. The pump was chosen to be able to deliver up to 85 litres/s, which corresponds to a bulk flow in the tank of around .28m/s, but the presence of the valves in the network restricted this maximum flow rate to about .25m/s. The pipework connects to the flume at two places — beneath the wavemaker and at the far end of the tank, see figure 3.2 — and by setting the appropriate valves the direction of the flow is selected.

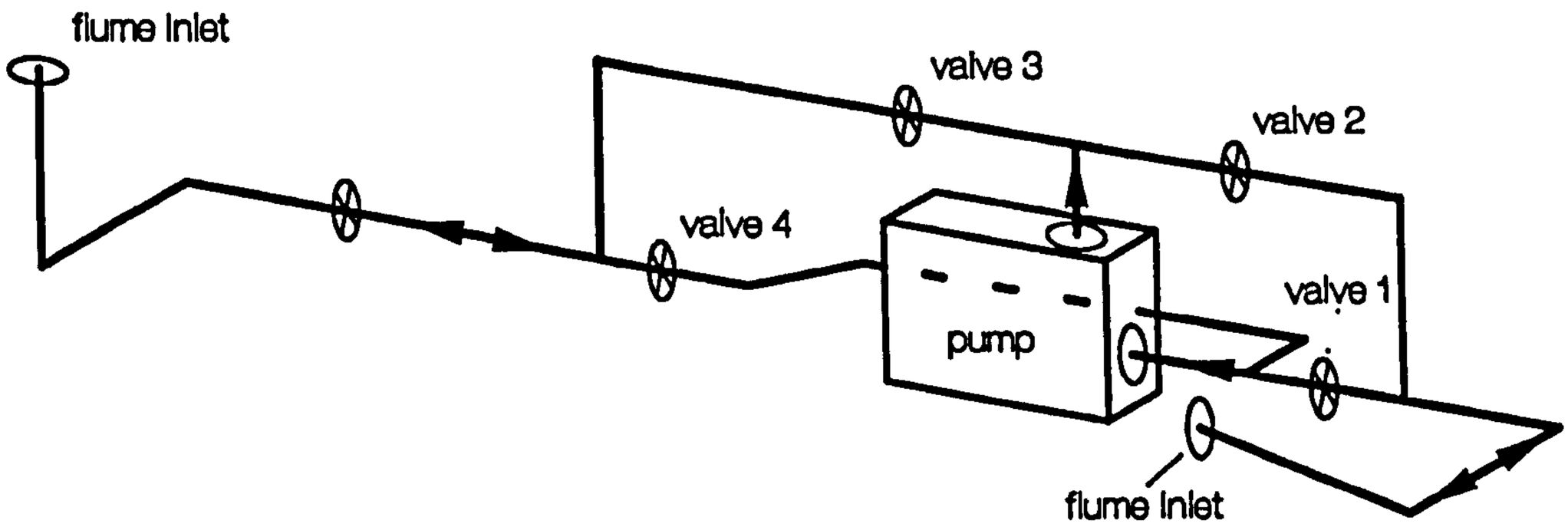

Figure 3.11: Layout of the recirculating current system

Current Inlets and Outlets

When the flow is introduced beneath the wavemaker it first encounters a volume filled with plasticised *chicken wire*, which breaks up the large scale turbulence. The current then diffuses through a 2m long porous lid which is positioned flush with the bed of the flume, and immediately in front of the wavemaker. This arrangement is shown in figure 3.12.

In most of the tests the current entered the tank at the end away from the wavemaker. Here, the inlet is arranged so that the flow enters a settling chamber

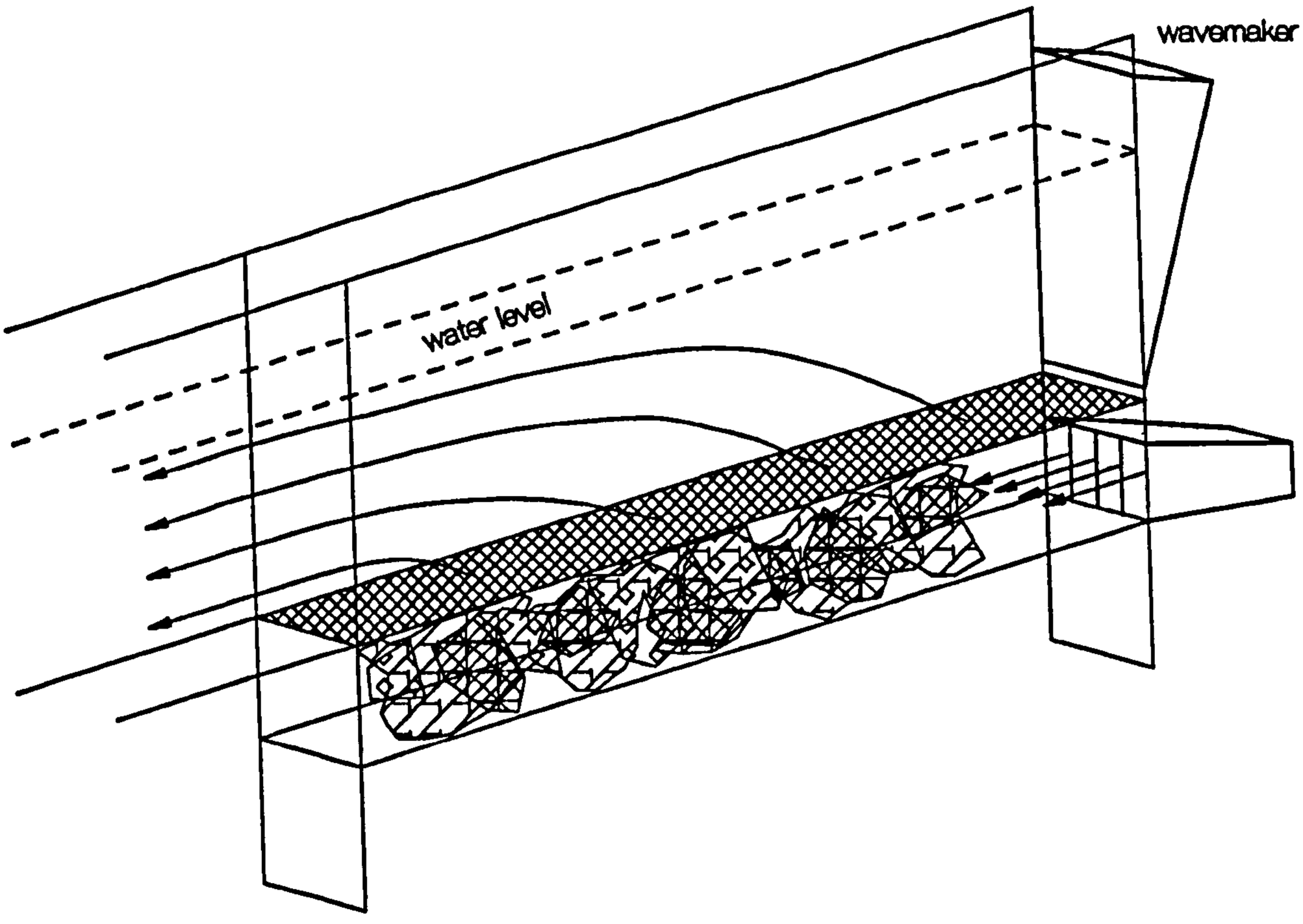

Figure 3.12: Current inlet beneath the wavemaker, showing the current flow and the mesh to reduce the large scale turbulence

vertically, at the bed level of the rest of the tank. Due to space constraints, the settling chamber could not be very large and having a contraction, while desirable, was impractical. As well as reducing the overall level of turbulence of the current, the chamber needed to shape the current profile.

The elements in the settling chamber are shown in figure 3.13. On entry to the chamber the flow first encounters a number of levels of thick plastic mesh (skeletal foam, 10 pores/inch) held horizontally by a rigid frame at five levels up to the water surface. These have the effect of breaking up the flow and forcing it to become horizontal in the direction of the wave generator. Next in that direction, there is another mesh, 50mm thick, held vertically and reaching from the bed to above the water surface. There follows a 90mm gap, then a final vertical mesh. Before the final mesh, baffles can be placed to shape the profiles to a desired form.

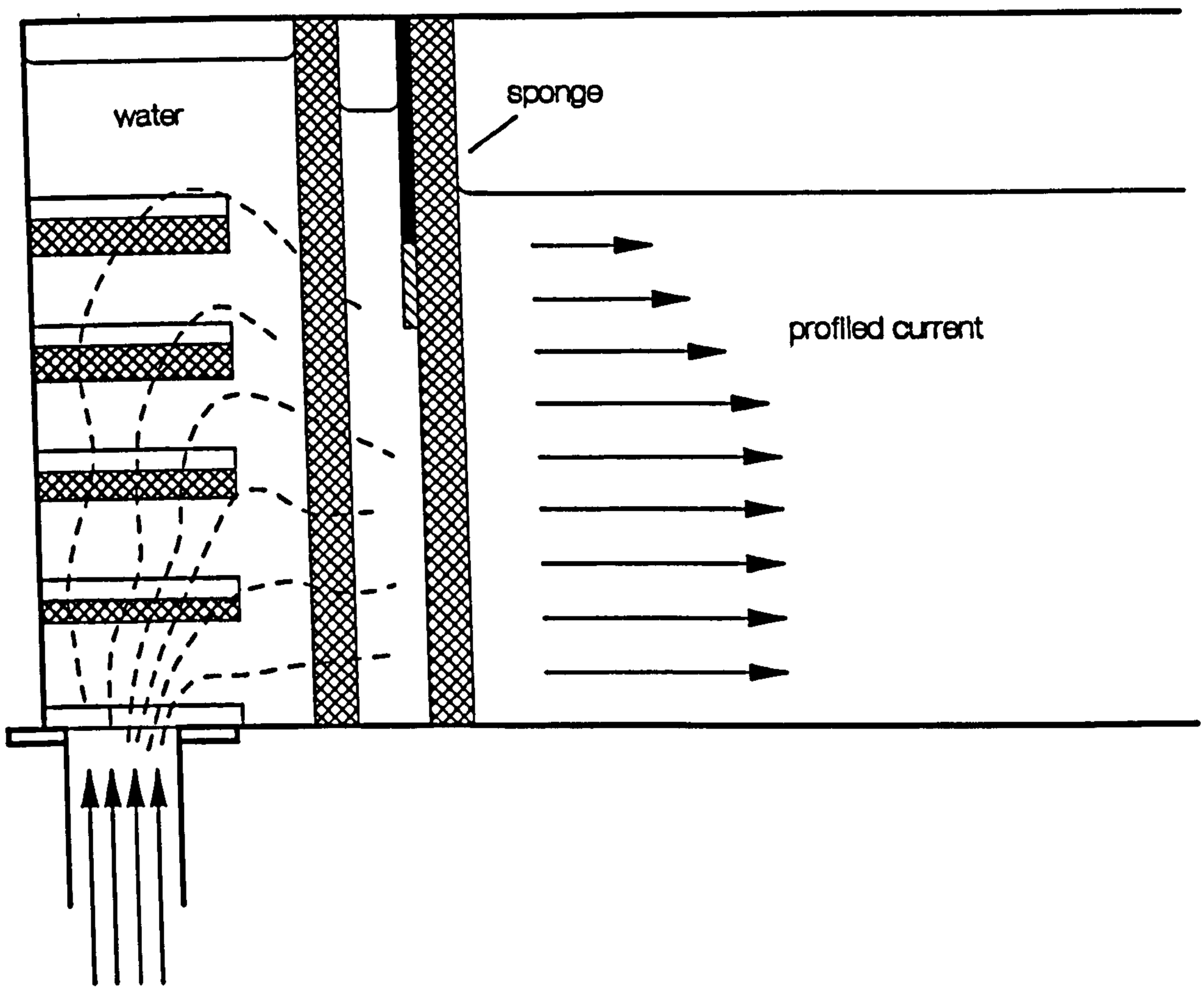

Figure 3.13: Settling chamber used to reduce the current's turbulence and to shape its profile

3.3.5 PIV Acquisition Hardware

The essential elements of the method of Particle Image Velocimetry (PIV) have been noted in section 1.2.3. The implementation of the technique for water wave and other studies at the University of Edinburgh was achieved by Gray [19], and the apparatus used in the present study was, in essence, the same. However, an number of re-implementations and refinements have been made by the author and others.

In photographic, two-dimensional PIV the first requirement is to capture multiple images of seeding particles in a chosen plane of the flow onto film. This requirement can be subdivided into the need for an illumination system capa-

ble of pulsing the measurement plane, a suitable camera and film, and seeding material to accurately follow the flow.

PIV Illumination System

The illumination system consists of a high power laser, beam transmission optics and an optical system to produce the pulsed illumination sheet. All aspects of this system were implemented by Paul Quinn, in consultation with the author.

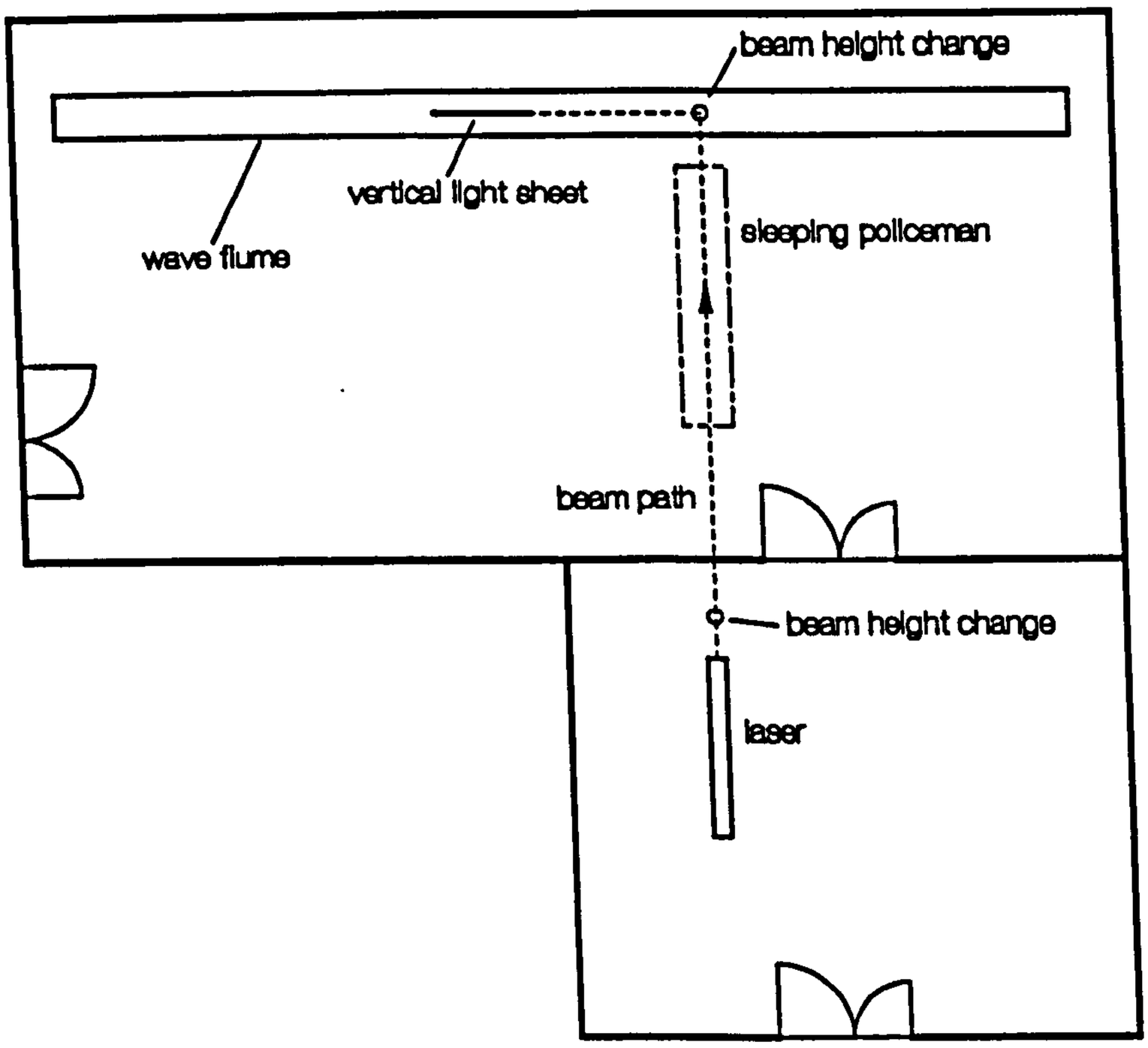

Figure 3.14: Laboratory layout, showing the laser beam path

The light source for illuminating the particles is a 15W Continuous Wave Argon-Ion laser. This is mounted on a rigid table, bolted to the concrete floor, in a small room beside the laboratory containing the wave flume. The resulting beam path length to the measurement area is quite long, up to 16m, but the problems associated with this are outweighed by the advantages of having the laser out of the way. The arrangement is safer, and all of the noisy, heat-producing accessories which go along with such a high powered laser can be conveniently hidden behind

the door. The arrangement of the laser, the beam path and the flume are shown in figure 3.14.

The laser beam is steered via four steering mirrors until it is running along and underneath the wave flume. The beam path is fully enclosed, for safety reasons, and crosses the laboratory inside a *sleeping policeman.* A telescopic enclosure surrounds the beam as it travels down the wave flume so that the box containing the sheet forming optics can be conveniently moved to different positions along the flume. The beam path is routinely realigned several times a year. The procedure starts at the laser and each mirror is adjusted so that the beam hits the centre of the next. In the final section, with the telescopic enclosure, all four degrees of freedom of the beam have to be set correctly.

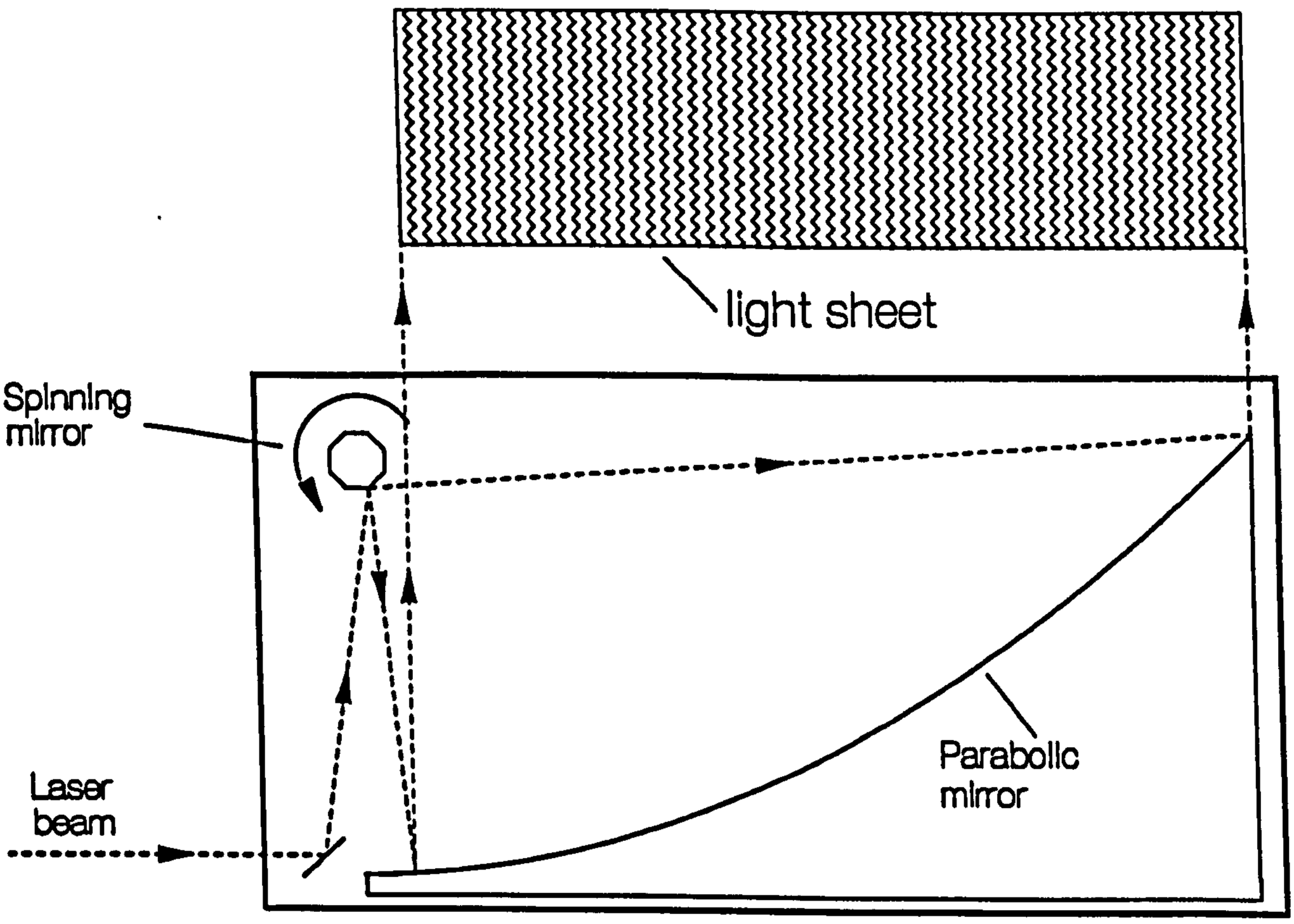

Figure 3.15: The *scanning-beam* illumination system

The pulse light sheet is produced by the *scanning-beam* method [21]. The *scanning-beam* system is illustrated in figure 3.15, and comprises two parallel ver-

tical metal plates, with various optical components mounted internally between them. As the beam enters the box, it is first deflected upwards, through two matched lenses, which narrow the beam. The beam then reflects off an eight-sided precision rotating mirror, each facet of which scans it through 90 degrees. A suitably positioned parabolic mirror recollimates the beam so that it is travelling vertically, independent of the rotating mirror angle. The scanning beam enters the wave tank through the glass base. The scan rate of the system is controlled by electronics and is continuously variable in the range 0.5-8ms.

The *scanning-beam* illuminates a plane in the flume which extends from the bed to the water surface, is 1 metre wide, and about 2mm thick. The measurement zone lies half way between the side walls of the flume and can be positioned beneath the flume in the second or third bays. This is achieved by mounting the illumination system on rails for ease of movement and accuracy of location. The light sheet can be regarded as flat, to within about 3mm.

Inevitably there are light losses between the laser and the measuring zone. These are important to consider as high-powered lasers are very expensive and each loss increases the size of laser required, if it is to be used at its maximum power rating. An intensity meter was used to measure the light levels at each stage of the beam path, and the deduced reflection coefficients for each of the components is given in table 3.1.

Optical Component	Reflection Coefficient
Beam steering Mirror	95%
Beam collimating Lenses	1% & 6%
Rotating Octagonal Mirror	80%
Parabolic Mirror	73%
Tank Wall	20%

Table 3.1: Reflection coefficients of the components along the optical beam path

The losses associated with the rotating mirror, the parabolic mirror and the base of the wave flume are quite large. However, it is hard to see how these values can

be improved.

Camera

The choice of photographic equipment is of some importance in PIV. The camera should have a flat-field lens if image plane distortions are not to be a great problem. The choice of the focal length of the lens can reduce the effect of out-of-plane motions and improve the imaged region of the flow.

A Hasselblad 500 *EL/M* camera was used for all of the PIV measurements. The lens used was of focal length 80mm or 150mm, depending on experimental considerations, and in some of the tests extra lenses were used to enable the measurement plane to be focussed at a closer distance. Lens distortion was measured [19] to be 1.5% at the edge of the field of view.

The two timing aspects of the camera's operation rely on mechanical devices and were checked. An accurate knowledge of the delay between triggering the camera and its shutter opening is essential, and an idea of the actual shutter times is important if the number of particle exposures is to be reasonably well predicted.

The trigger and shutter times were measured by detecting the signal from a photodiode placed on the path of a low-powered laser beam passing through the lens. From the time of the start of the signal, relative to the triggering time, the camera trigger delay was found to be 33ms if the lens was already cocked and 78ms if it was not. From the duration of the signal the actual shutter times were determined for the 80mm lens, which houses the timing mechanism, and these are given in table 3.2. There are some large departures from the nominal speeds, but the consequence of this is only a small change in the number of exposures recorded.

Nominal speed (seconds)	Nominal speed (ms)	Actual speed (ms)	Error
1	1000	780.0	-22%
1/2	500	564.0	13%
1/4	250	322.0	29%
1/8	125	148.0	18%
1/15	67	94.0	40%
1/30	33	32.2	-2%
1/60	17	18.2	7%
1/125	8	12.2	52%
1/250	4	5.2	30%
1/500	2	3.2	60%

Table 3.2: Shutter times for the Hasselblad 80mm lens

Film

The resolution of the film is central to the performance of the whole method, and must be considered carefully. Kodak Tmax, a high contrast, high resolution, black and white, negative film, gives good results.

Seeding

The seeding used in all of the experiments was conifer pollen. This is almost exactly neutrally buoyant, quite reflective, and, at about 70μm, small enough to follow the flows being studied sufficiently accurately. If anything, the pollen has a small tendency to float, with rise velocities of the order of 0.25mms^{-1} [46].

3.3.6 Experimental Control System

The number of elements which required integration into the experimental control system was quite small. The minimum requirement for the system is to simultaneously drive the wavemaker while sampling signals from the wavegauges or triggering the camera.

Hardware Interface

The schematic layout of the experimental control system is shown in figure 3.16. The computer controlling the hardware is an Archimedes 310. Up to eight channels can be sampled almost simultaneously by a 12-bit multiplexed Analogue-to-Digital converter resident in an expansion port within the computer. Output to the wavemaker is generated by an 8-bit Digital-to-Analogue converter present in a separate control box. This box also contains a switched relay connection which was used to close the contacts to trigger the camera, and is connected to the computer via the 1MHz bus interface. While some of the hardware elements were considered only just sufficient for the present studies, and likely to be inadequate for studies requiring more controlled or sampled elements, time constraints meant that they had to suffice. Ideally, the output interface would be replaced, particularly to improve the resolution of the DtoA converter.

Experimental Control Software

The control software was designed at an earlier stage, and is not tied to any particular hardware interface, except at the lowest level. All communication with the experimental apparatus is regarded as analogue/digital output/input to/from numbered channels and follows the practice evolved at the EUWPP. The software can be regarded as existing at three distinct levels, each of which is available as a programming interface. At the lowest level, a clock controls output and input events on a regular basis. Before each event the appropriate output values are

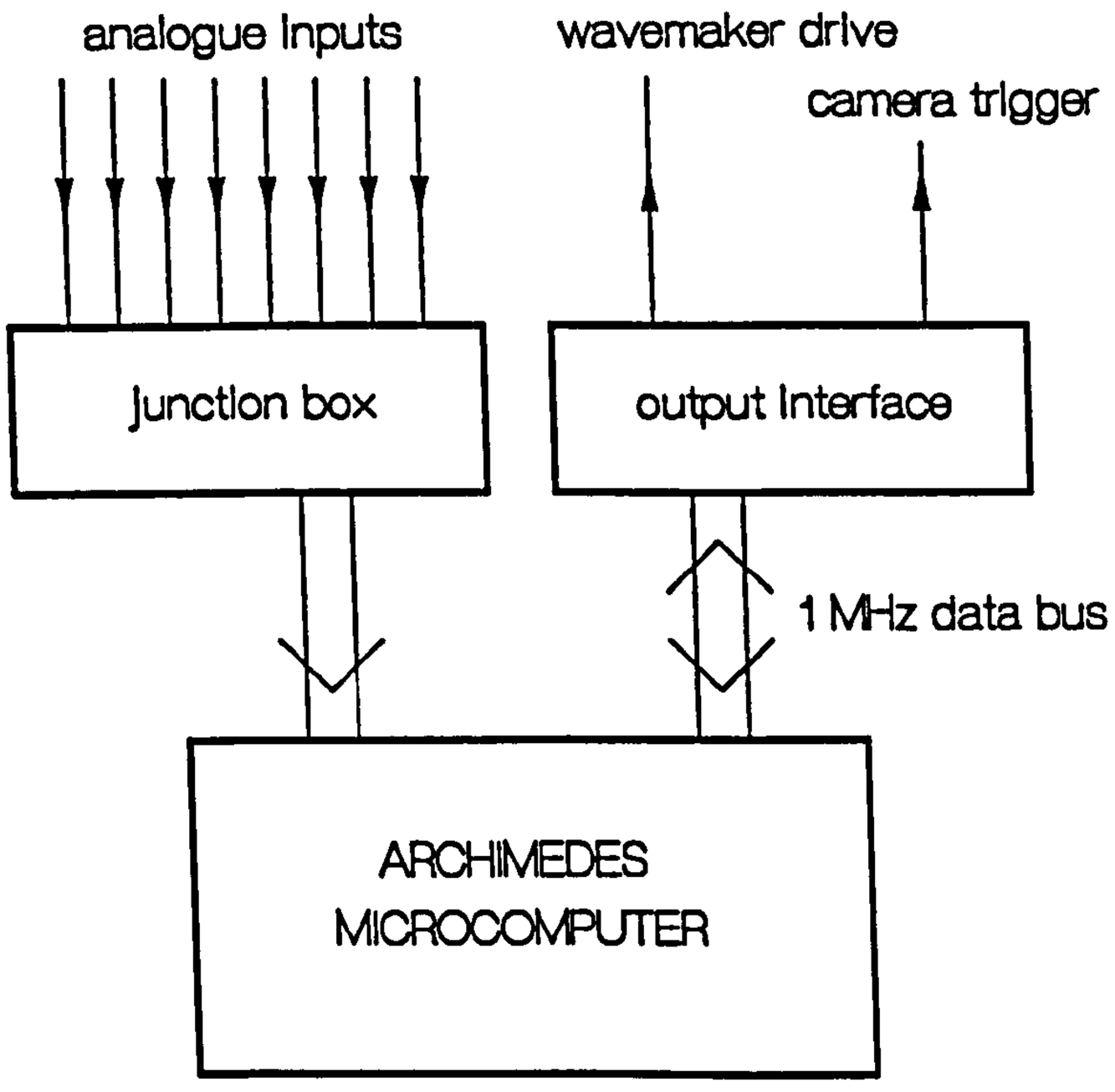

Figure 3.16: Layout of the wave flume sampling system

calculated, if necessary, and after each event the input values are stored. In the intermediate software level input and output devices are regarded as having not specific functions, and the addition of extra devices is possible. This software level is the most flexible, but the programming interface is, in consequence, quite difficult to use. At the top level, the software routines are related directly to the functions of the connected devices, allowing experimental control programs to be written with the minimum of effort.

The experimental control system does not include any real-time control of devices. In other words, in the sequence of input and output events, none of the outputs depend on previous inputs. An individual experimental run, or test, can be regarded as the sequence shown in figure 3.17. Any control loop which exists can only be around the whole of this structure: for instance, the wavemaker drive signal might be set, the test performed, the wave height determined from a recorded wave gauge signal, the wavemaker drive signal modified, and so on. However, the more normal experimental sequence is to loop around a set of tests, each of which has some prespecified parameters, and to recorded any sampled data for

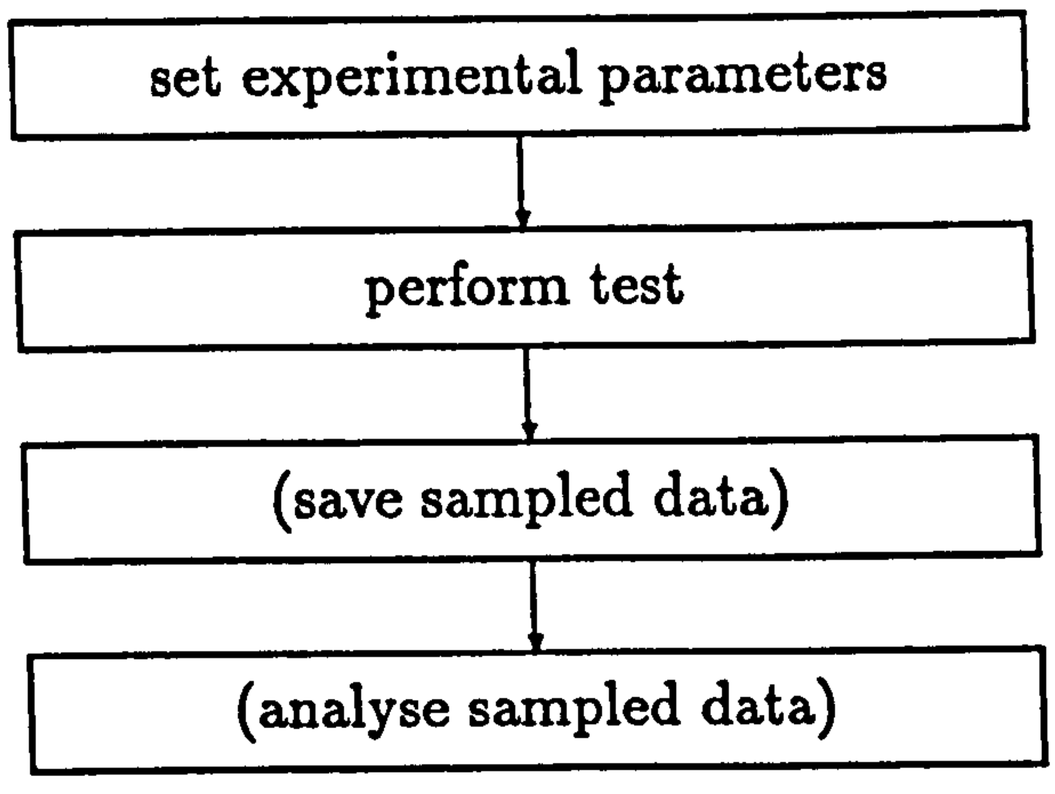

Figure 3.17: An individual automated experimental run, or test

subsequent analysis.

In the present context, the directly settable experimental parameters are the wave spectrum to be generated, the channel numbers to be sampled and the time at which to trigger the camera. Parameters which need to be set manually by the experimenter can also be conceptually included into this list if, at the appropriate time, the software issues instructions to an operator to perform a specific setting task.

The performance of the individual experimental test consists of accomplishing all of the low level input/output operations which result from the parameters which have been set. The test ends when all the measurements have been made, or if other non-directly controllable functions are being performed, after a prescribed time. If signals have been recorded these are generally saved into a formatted samples file for later processing. If analysis of the records is necessary before the next test this is done, and the experimental sequence continues.

Wave Generation Software

The setting of the wave spectrum is more involved than the other experimental parameters. If a wavefield is to be generated that is representative of a continuous spectrum, then the algorithms which generate the desired wave height record

have to be carefully constructed. The conversion from this record to one which is suitable for driving the wavemaker necessitates the use of a transfer function, which is normally experimentally measured.

Wave spectrum generation algorithms were included in the software suite, courtesy of Peter Woodhead. Although the full capabilities of this software were not used fully in the present studies, they are available for future work, and were considered to be worth including at this stage. The software algorithms attempt to represent continuous spectra with a list of linear wave fronts, each with an amplitude, frequency, starting phase and, in general, an angular direction, allowing the same software to be used for 3D tank studies.

The sinusoidal voltage required to drive the wavemaker to produce a wave of given height in the flume depends strongly on the frequency. This is due mainly to the physical characteristics of the wave paddle, and also to the control filters used to drive it. The transfer function between drive voltage and wave amplitude varies both in amplitude and phase with frequency and is plotted in figure 3.18. While the transfer function could be predicted from theory, it is better to measure it in the flume, as all the elements contributing to its value can be found in a straightforward experiment.

The wavemaker transfer function was found by driving the wavemaker with small sinusoidal voltage signals of known amplitude at a series of frequencies. The surface elevation was measured at two positions in the tank, the incident and reflected wave amplitudes extracted, and the transfer function calculated from the incident wave amplitude, shifted back to the wavemaker using linear theory.

Given the inherent non-linearities of steep waves, the transfer function cannot be expected to be able to accurately generate chosen waves in all circumstances. However, in most experiments all that is required from a wavefield being generated in the flume is that it should be close to that desired, and that the actual parameters can be measured. If particular wave parameters are required, this can be achieved by iteration, with the empirical transfer function providing the

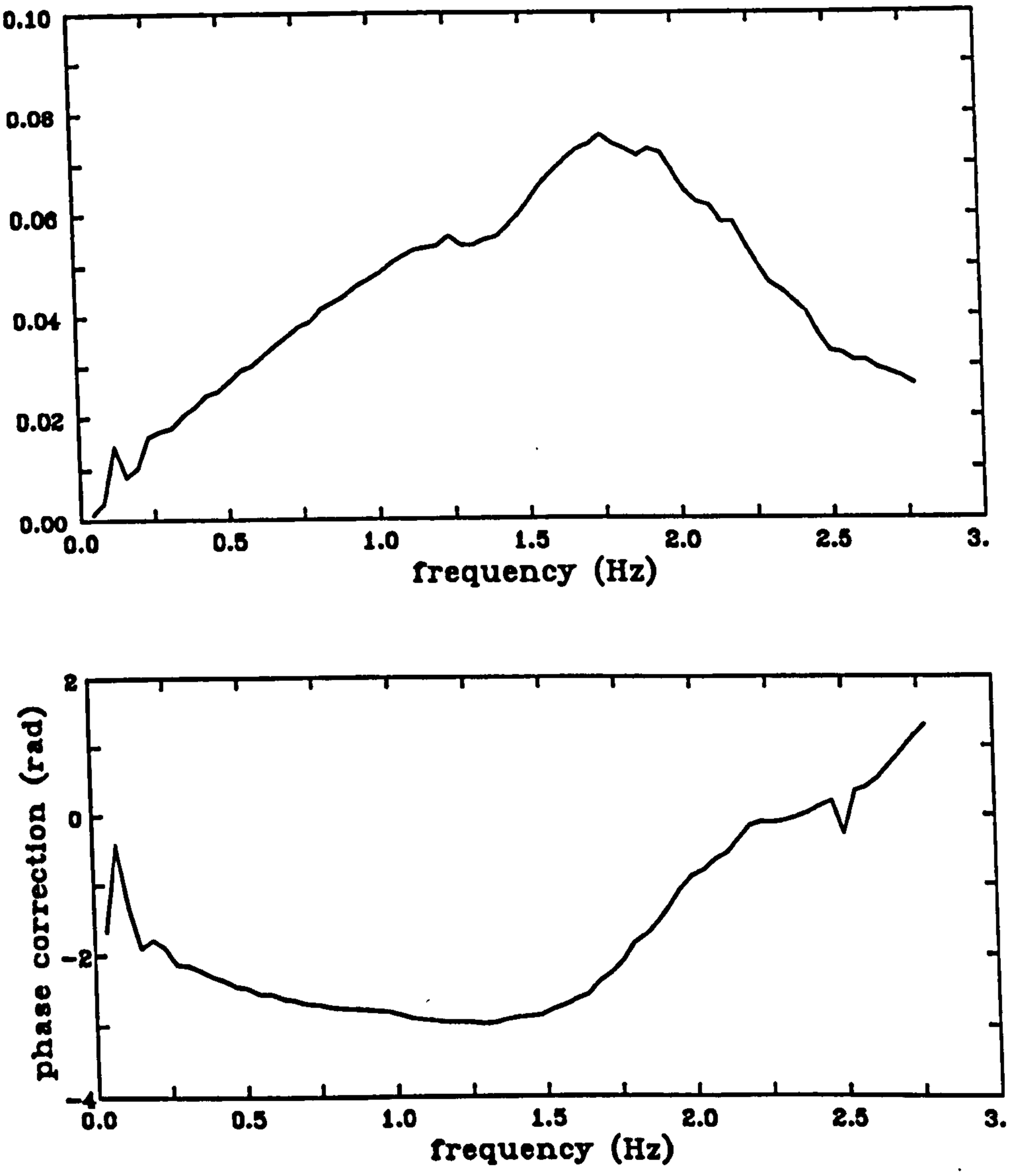

Figure 3.18: The transfer function of the wave maker in the flume

starting values.

Data Analysis Software

Standard software routines are provided to aid the first stages of analysing time-series recorded from the flume. Individual timeseries can be readily extracted from the samples file by specifying the channel number which was sampled. Lin-

ear calibration values which were set at the time of the experiment are used to automatically convert the voltage records into calibrated timeseries. Again, programs can be easily written to loop through the tests which were performed.

The most generally useful means of analysing timeseries is by Fourier transformation. An Fast Fourier Transform (FFT) routine is available for this purpose, which can analyse timeseries containing 2^N points, if N is integral.

3.4 Experimental Procedures

Experimental procedures arise from a number of sources, but primarily by learning from the ways that others operate and from one's own experience. Once standard procedures have been adopted it is sometimes hard to explain why that particular way of operating was chosen. Often practices evolve though habit, and the actual procedure being adopted has limited merit.

In this section the general procedures used in running experiments are described, along with those adopted for the particular experimental techniques used. The acquisition of PIV photographs is the most involved of these, and is dealt with in most depth.

3.4.1 The Running of Experiments

Following on from the design of the experimental control software, experiments are regarded as a set of individual test runs, each of which has something in common. The common element might be the tank configuration, the setting of the current profile, the wave spectrum being generated, and so on. The varying parameters might include the wave height, the triggering time of the camera, etc. Each experiment is assigned an index number, and the individual tests a sub-index. Description and parameters of the experiment are recorded in a lab book.

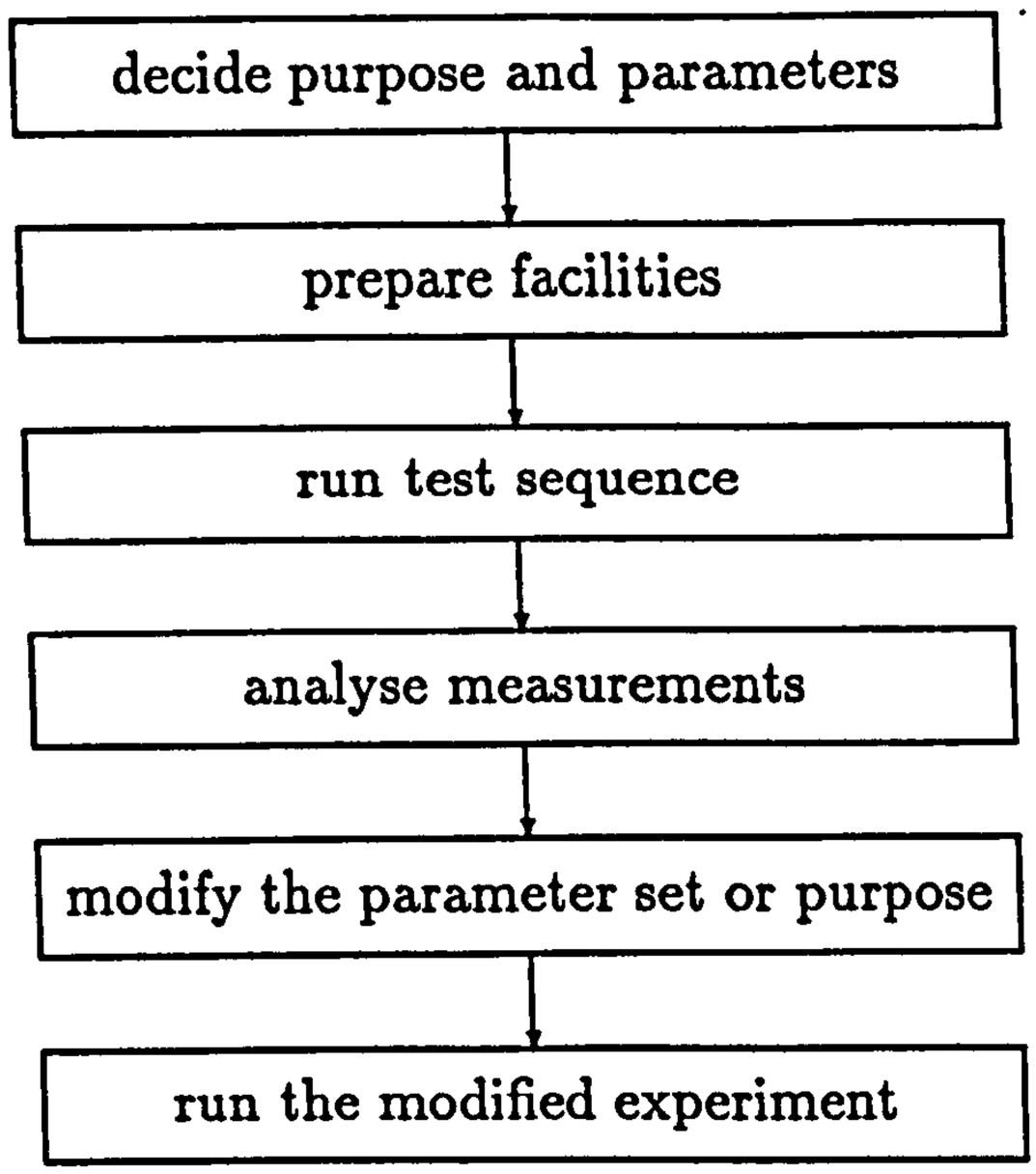

Figure 3.19: Sequence surrounding an individual experiment

The use of an index number to reference the experiment has a big advantage over, for example, a coded reference name. To produce a comprehensive coding scheme requires a future knowledge of the types of experiments which might be performed. As this is not possible, such schemes invariably fall down.

It is not really possible to cleanly sub-divide an experimental project into a set of experiments, each consisting of a sequence of tests over some set of parameters. However, there is some merit in this approach, especially if it makes subsequent analysis of the measurements more straightforward. Figure 3.19 shows the sequence which normally surrounds an individual experiment.

3.4.2 The Use of the Wave Flume

Preparing the Apparatus

There are a number of experimental practices which fall into the category of preparing the experimental facilities, namely the wave flume and associated equip-

ment. The flume itself requires regular cleaning to remove old seeding and the water level needs to be routinely reset because of evaporation.

The wave generator is quite robust, but excessive or rapidly changing drive signals should be avoided. The wave gauges need cleaning periodically, and should be calibrated regular. Calibration was performed before and after all the experiments in the present studies when wave gauges were used, by measuring the output at two known immersions. When using the current, any air must first be expelled from the pipework, by means of a bleed valve. The flow control valves should be set to allow flow in the desired direction, and to minimise transient effects in the flume the pump should be started with the output valve throttled down or the other output valve opened to allow a recirculating path. If the pump has not been used for more than a day, then rust should be removed from the system by pumping the dirty water to beneath the wavemaker followed by draining.

Selecting the Experimental Parameters

In selecting parameters for an experiment, the first consideration is whether the desired test conditions will be achieved. For example, is the wave field steady when a particular measurement is made, if this is to be assumed in the subsequent analysis?

After selecting the wave field to be generated, the next consideration is of the time window available for measurements. The start of this period is normally after the time when the wave field has established in the flume. Ideally, the end should be before reflections come back. If steep waves are being generated, it may be necessary to avoid the time when spurious components arrive from the wavemaker, or when instabilities set up in the waves.

Figure 3.20 shows a typical wave train generated in the flume, with the period suitable for measurements of a steady wave marked. The absorption at the end of the flume has been deliberately degraded to highlight the effect of reflections.

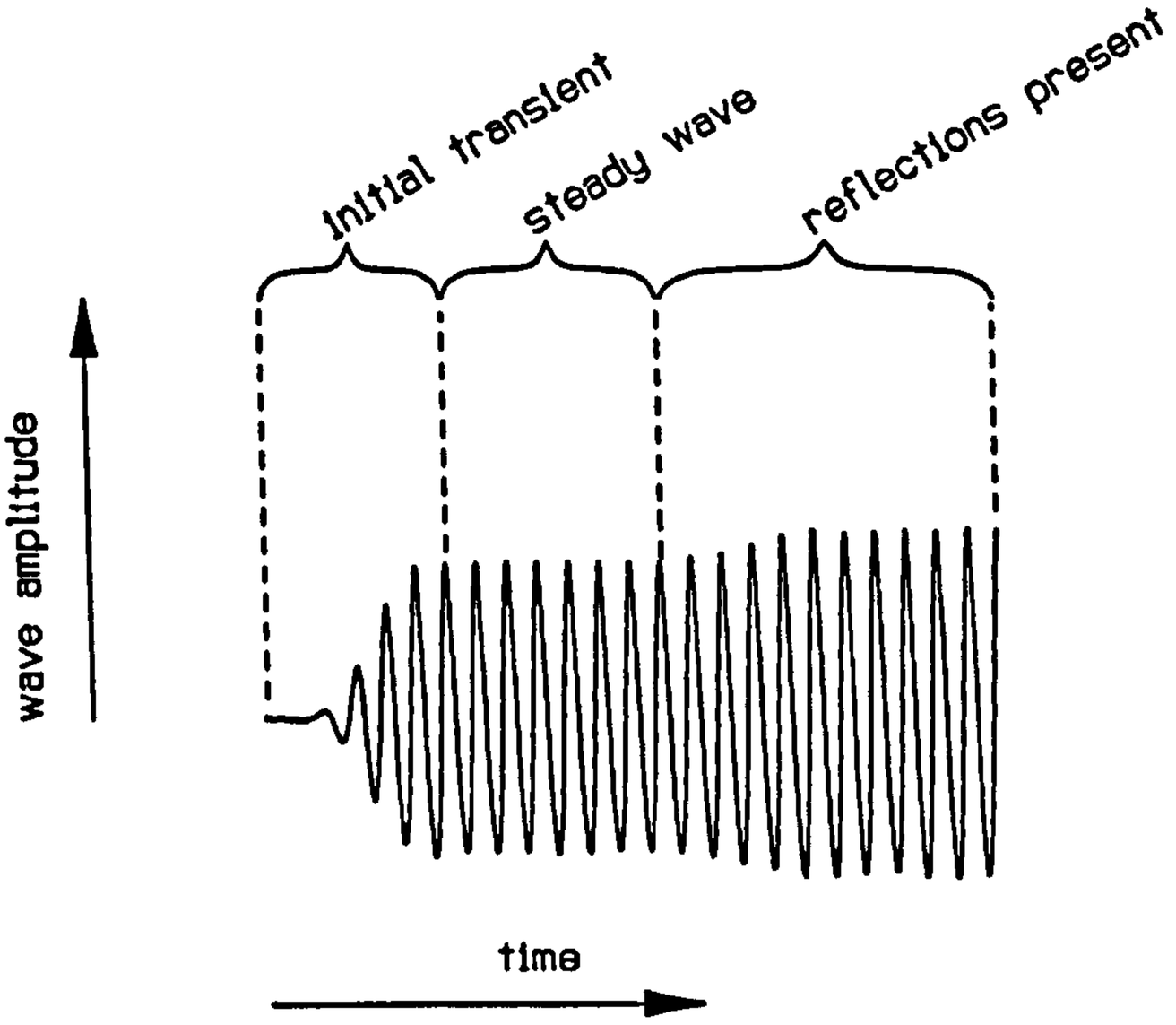

Figure 3.20: Wave gauge signal including steady wave

For instantaneous measurements, such as PIV, measurements would normally be made within the sampling window. When timeseries are being measured, this time period may be too short, and in some circumstances it is better to wait until long-term steadiness is established, and to deal with reflections in the subsequent analysis. Of course, the physics of the flow may have subtly changed by this time, and this should be considered in the analysis.

When timeseries are being measured the approximate start time and duration of sampling are first chosen. The sampling rate is selected so that the highest frequency of interest can be easily resolved, and that there is no aliasing of frequencies present above the Nyquist frequency. Typically 20Hz or 40Hz is suitable. The number of samples in the sequence can then be determined from the required sampling duration, but if Fourier analysis is to be performed with the available FFT it is more convenient to select 2^N samples and to modify the sampling duration if necessary.

Once sampling parameters have been selected it may be advantageous to make some small change to the desired wave parameters. It is *very* convenient if each wave component has integral cycles in the sampling period, if Fourier analysis is

to be performed.

Parameter	Value
Sampling rate	40Hz
Number of samples	2048
=> Sampling period	51.2s
Sampling delay	12s
Wave frequency	n/51.2 Hz

Table 3.3: Typical sampling parameters

3.4.3 Acquisition of PIV Photographs

The experimental arrangement for making PIV measurements under breaking waves is shown in figure 3.21. The magnifying glass shows what a small portion of the developed negative would look like ideally. In this section the best form of such a portion is discussed and experimental practices used to achieve such results suggested.

PIV Acquisition Principles

If PIV photographs are to be acquired which can be analysed with standard techniques, then a number of fundamental requirements have to be fulfilled. For a given set up, the conditions must be such that, on the film, the particle images are in good focus, of a suitable size, in good contrast with the background and of sufficient, but not excessive, number. Each particle must have at least two images. The velocity gradients in the flow must be such that they do not lead to gradients of particle image separation on the film which are too great. Similarly, the time that has elapsed between the first and last exposure must be small compared to

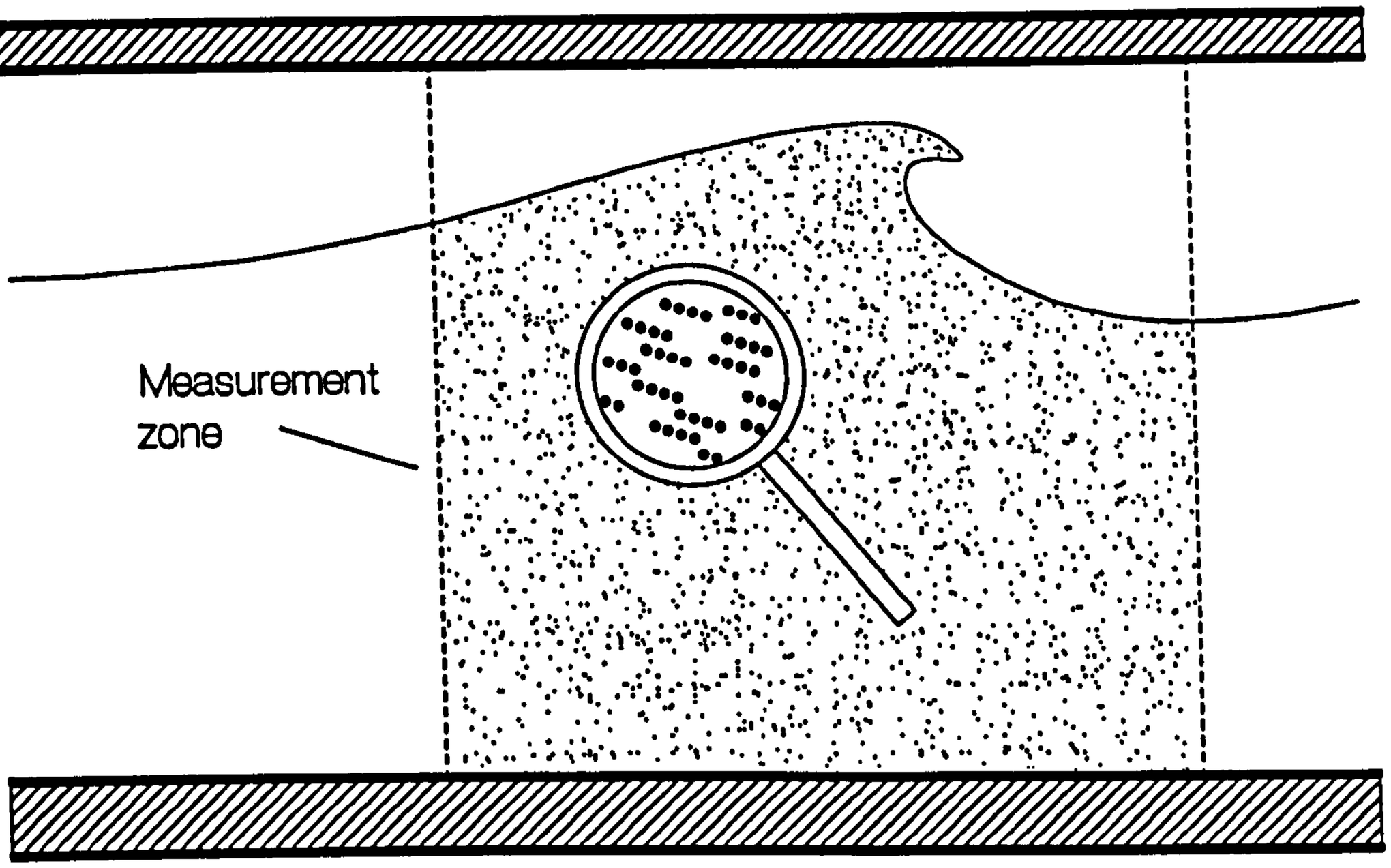

Figure 3.21: PIV measurement under a breaking wave

the time taken for the flow to change significantly.

The setting of the PIV parameters for optimal performance are discussed by Gray [19] and Keane and Adrian [29]. From the experience of these authors and others table 3.4 has been drawn up which gives the PIV settings aimed for in the standard use of this technique at Edinburgh, assuming that the scanning beam illumination method is being used.

PIV Acquisition Practice

The principles for the acquisition of PIV photographs outlined above can be used to indicate areas of concern and to assess success, but are of limited help in isolation when experiments are actually being performed. For instance, the ideal seeding density might be known, but during experiments the seeding is often added

Setting	Range
Number of images of each particle	$3 < N < 6$
Number of different particles	> 10
Displacement gradient	$< 3\%$
Change of displacements over measurement time	$< 3\%$
Particle image size	$<= 20\mu$m
Particle image separations	$30\mu\text{m} < \delta < 200\mu\text{m}$

Table 3.4: Aimed for PIV settings within each interrogation area on the film

according to how much gave good results in a previous run.

A number of practices can be identified which are common to all experiments involving PIV. The order in which they are described is not necessarily exactly the same as might be used when taking a particular set of photographs and often some of the steps can be skipped over, especially if similar experiments have already been performed and the best parameters are known.

One of the first decisions is the choice of viewpoint for the camera. This is of particular importance if some part of the measurement zone might be obscured by something in front of it, for example the wave surface when measurements are being made of a plunging tip, and the final position for the camera might sometimes have to be found by iteration.

The focal length of the lens is selected by balancing the advantages of greater focal length in reducing the effect of out-of-plane motions; and that of seeing more of the measurement plane past obstacles, with the greater difficulty of good focussing and the inevitable reduction in particle exposure.

The physical- to film-plane magnification depends on the focal length of the lens and the distance of the camera from the measurement zone. The considerations here include the extent of the illuminated area which would be imaged and the displacement gradients on the film resulting from velocity gradients in the flow.

The latter may have to be assessed iteratively and the magnification altered accordingly

There are six degrees of freedom which are set when the camera is positioned, comprising three positional coordinates and three angular. Two of the angular degrees of freedom have to be set accurately if the film is to be parallel to the measurement zone, required for good focus. The third angle needs to be set correctly if the measurement zone is not to be rotated relative to the film, which would make for more complicated analysis procedures. Of the three positional coordinates, the two which vary parallel to the measurement zone must be known if registration marks are being used which are not in this plane. The final degree of freedom, the distance the camera is away from the measurement plane, determines the precise value of the magnification. A typical set-up of the camera is illustrated in figure 3.22.

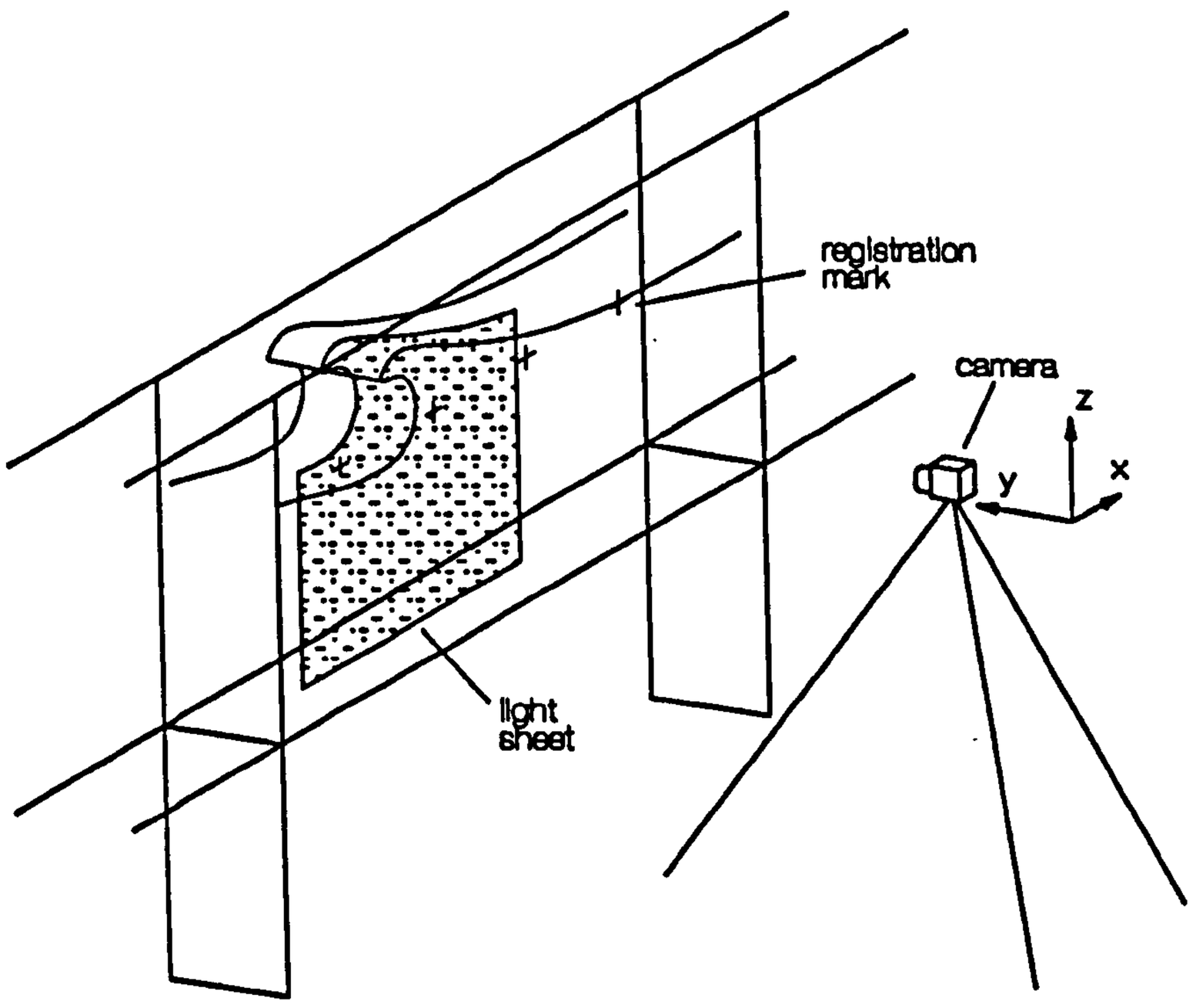

Figure 3.22: Wave flume and camera

For the wave studies described, it was found to be most convenient to set all three positional coordinates of the camera to selected values. An alignment procedure was developed to ensure the correct settings. A small spirit level was used to set

two of the angles, and the camera's own reflection in the glass wall to set the third. The camera's distance from the glass is easily measured and the other two positional coordinates were normally set such that one of the registration marks was exactly in the centre of the field of view.

Suitable use of registration marks is vital if the flow needs to be accurately located relative to some boundary or to a previous measurement of the flow field. Small crosses were placed on the glass wall of the flume, of sufficient size that they were still recorded on the film when out of focus.

Very small amounts of vibrations in the camera can badly affect the quality of the PIV images, because of the the small displacements on the film which are to measured. It is very important that the camera mounting is sufficiently rigid. For the experiments described, the viewing mirror of the camera was raised before each picture and the shutter cocked, considerably reducing vibrations.

Once the camera has been positioned the other photographic parameters needing to be set are: focus, aperture and shutter speed of the camera, laser power and illumination interval.

The illumination interval should be such that the maximum velocity in the flow ends up as the maximum resolvable particle image separation on the film. Normally, an estimate of the maximum velocity can be made. If this value is in doubt, then a test film will be required to check its accuracy, followed by an appropriate modification of the illumination interval. In some circumstances, a modification of the magnification might also be required at this time.

The shutter speed is chosen after the illumination interval in order to set the number of exposures. The change of the flow over the total exposure time should be considered again.

Next, the exposure of the particles onto the film should be optimised. Nearly all of the parameters involved in the acquisition of PIV affect the exposure, but in general most of them can be regarded as fixed at this point, leaving laser power,

film speed and aperture as the main variables, in that order. If, after considering all the combinations of these three values, the exposure is still insufficient, then some of the other parameter values have to be reassessed.

The most important parameters affecting exposure are summarised in table 3.5, along with typical values which lead to adequate exposure and the dependence of the exposure on the particular parameter. Factors such as the magnification are not included, because they are not set directly but in consequence of other parameters. The exposure is dependent on the distance of the camera from the measurement zone and also the magnified size of the images on the film. If that size would be less than the minimum possible given the limits of the lens and film then the dependence with distance is the inverse square, otherwise there is no dependence.

PIV parameter	Typical value	Exposure dependence (parameter exponent)
laser power	15W	1
illumination interval	2ms	1
camera distance	1m	-2 or 0
focal length of lens	80mm	0
aperture (f-number)	f4	-2
film speed (ASA)	100	1
light sheet extent	1m	-1
light sheet thickness	2mm	-1
particle diameter	70μm	3

Table 3.5: PIV parameters affecting exposure

If the ideal exposure cannot be readily achieved by increasing the laser power, then a change in ASA rating, then aperture, should be considered. With higher ASA films, the grain size is larger, but experience suggests that the effects up to 400 ASA are not significant.

As well as considering its implication on exposure, the aperture is set by balancing

the spherical aberration present when the aperture is opened widely with the diffraction effects which happen when it is nearly closed. Typically, the aperture is set one stop down from the maximum opening.

The seeding level is set by considering the theoretical optimum density covered in table 3.4, but primarily by experience from the previous experiment. Uniformity of seeding is very desirable, and given the relatively small volume of the flume this is best achieved by ensuring the whole volume is seeded and well mixed-up. This is normally the case after half an hour of testing in the wave flume, but periodic mixing is normally required. As a result there is a compromise which has to be made between the turbulence level when the photograph is taken and the uniformity of the seeding. In most of the tests in the present studies two minutes was allowed for any residual turbulence to decay.

Once the photographs have been taken they are developed, dried, labelled and stored. If necessary for exposure reasons the negatives are developed for longer than the recommended time. Once dried a first assessment can be made of the quality of the images for PIV analysis. Holding the negatives in front of a low power laser should result in visible fringe patterns.

Of the PIV acquisition parameters, magnification and illumination interval have a particular importance as they affect the calibration of the measurements. The magnification was measured by placing a regular square grid of known grid size into the measurement plane, photographing it, and determining the size on the film. The illumination interval was checked by measuring the scan rate with a photodiode.

As well as the magnification of the measurement zone, that for the reference plane was also measured, in order that the effective positions of registration marks in the measurement zone could be determined. In some of the closer cases its was impossible to focus on the reference plane and the magnification was extrapolated from the values found for other camera positions.

PIV Acquisition Errors and Limitations

The are a number of aspects in the acquisition of PIV photographs which can affect the accuracy of the final velocity measurements, due to inadequacies in the apparatus and the particular settings used. The resulting errors in the PIV measurements can be estimated from the imperfections of the apparatus detailed in section 3.3.4, the particular PIV acquisition parameters covered above and the nature of the flow being measured. The aspects considered here were first discussed by Gray [19] and have been covered further by Quinn [46].

Geometric distortions due to the imperfection of the camera lens and refractive index changes between the camera and the measurement zone can be thought of as introducing a small modification onto the magnification dependent on the position within the negative. Fortunately these tend to cancel in the water wave studies [19]. By ensuring that the region of greatest interest is in the centre of the field of view the consequence of the distortions can be minimised.

A similar type of error is introduced by the deviations of the light sheet from flatness. The consequence of the 3mm variations, mentioned in section 3.3.4, is to give a systematic error of up to 0.3% on the magnification over the field of view when the camera is positioned 1m from the measurement zone. There is also a small random error due to the sheet thickness, 0.2% for the same camera position.

The scan rate of the system is taken to be the illumination interval for the PIV measurements and can be very accurately measured from the response of a photodiode placed in the *scanning-beam* path. However, there is a small systematic error if the illumination interval is determined in this way, as subsequent illuminations of a given particle are at different positions in the measurement zone, and hence different phases of the scan cycle. If the size of the averaging areas for each velocity interrogation in the PIV analysis are small compared to the length of the measurement zone, then these errors are small.

There are two closely connected concerns about how well the seeding follows the

flow; drift and the ability to follow accelerating flows.

Typical errors inherent in the acquisition of PIV photographs are summarised in table 3.6. It should be noticed that the systematic errors could in principle be measured or estimated, and a correction made to the data. However, if these errors are small, in practice they are conveniently ignored.

Factor	Random Error	Systematic Error
Illumination interval	0.2%	
Photographic magnification	0.3%	
Photographic distortion		0.0%-0.3%
Illumination plane flatness		0.0%-0.3%
Illumination plane thickness	0.1%	
Scanning-beam time effect		0.0%-0.2%
Seeding not following flow		0.1%
Combined errors	0.4%	0.1%-0.8%

Table 3.6: Typical errors involved in the acquisition of PIV photographs

3.5 Analysis Techniques

Once the raw experimental measurements have been made, there is often some work to do before usable data is obtained. In this section, the analysis method to extract velocity fields from PIV negatives, the identification of the water surface and spectral analysis methods are covered.

3.5.1 PIV Analysis

The aim in the analysis phase of PIV is to measure as accurately as possible the mean particle displacements from small localised regions or *interrogation areas*

(IAs) on the developed film, and hence determine the local velocity. Figure 3.23 shows the ideal contents of a small portion of a negative. Various methods have been proposed for extracting this information, falling into two general categories. In the first, particles are identified and a scheme, which might be partially ad hoc, is used to match up multiple images of the same particle. In the second, the autocorrelation is made of the IA and, from the resulting peak in this function, the most likely average particle displacement determined. The two approaches are found to be most suitable for low and high seeding densities, respectively.

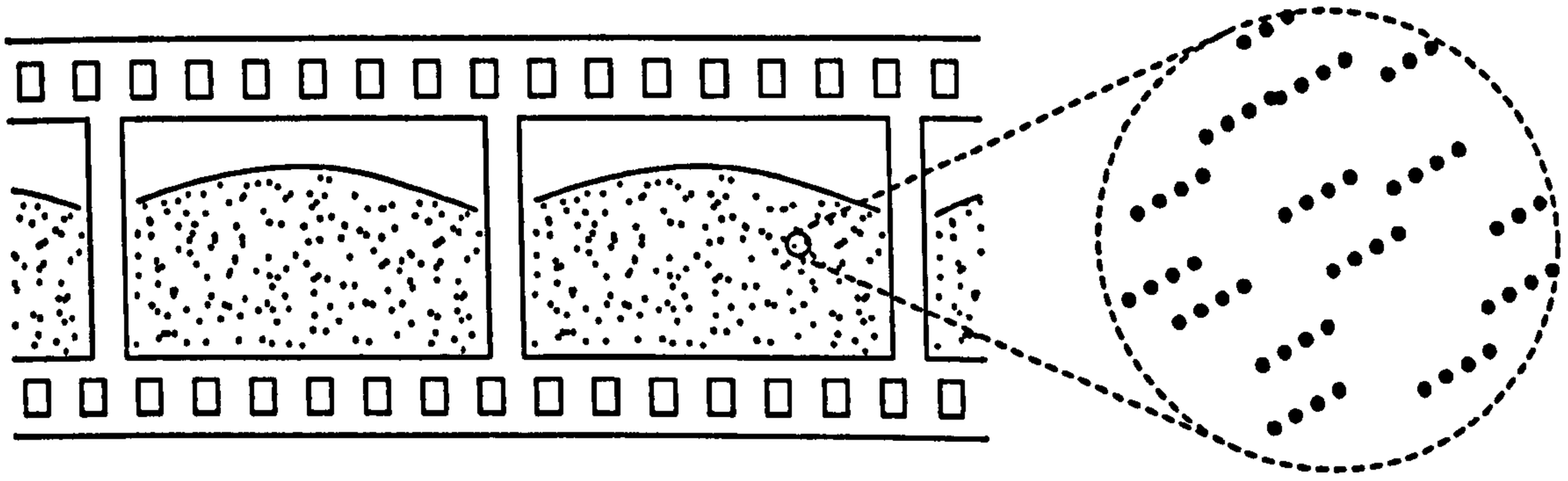

Figure 3.23: An individual interrogation area enlarged from within a particular PIV negative

In the water waves studies, high, homogeneous seeding densities are readily obtained and the autocorrelation approach has been found to be the most appropriate. This method was implemented at Edinburgh by Gray [19] and for the present studies has undergone a software upgrade, programmed by the author, using the same algorithms.

Methods for Calculation the Autocorrelation

For a small area of the film, the requirement is to calculate the autocorrelation

$$A(x,y) = \int\int a(x,y)a(x-x',y-y')dx'dy' \tag{3.13}$$

This can be done with:

$$A(x,y) = FT^{-1}\{[FT\{a(x,y)\}]^2\} \tag{3.14}$$

where $a(x,y)$ is the image intensity of the chosen portion of film, and $A(x,y)$ the autocorrelation function of that area.

If the autocorrelation is accomplished by the Fourier transform method then there is the possibility to do the first, or both, Fourier transforms optically [28].

Implementation of the Young's Fringe Analysis Method

In the Edinburgh PIV analysis system the Fourier method is adopted. The first transform is performed optically and the diffraction pattern collected on a CCD[1] array. Because intensity is detected this pattern is automatically the squared transform. The data then undergoes a computational Fourier transform to yield the autocorrelation.

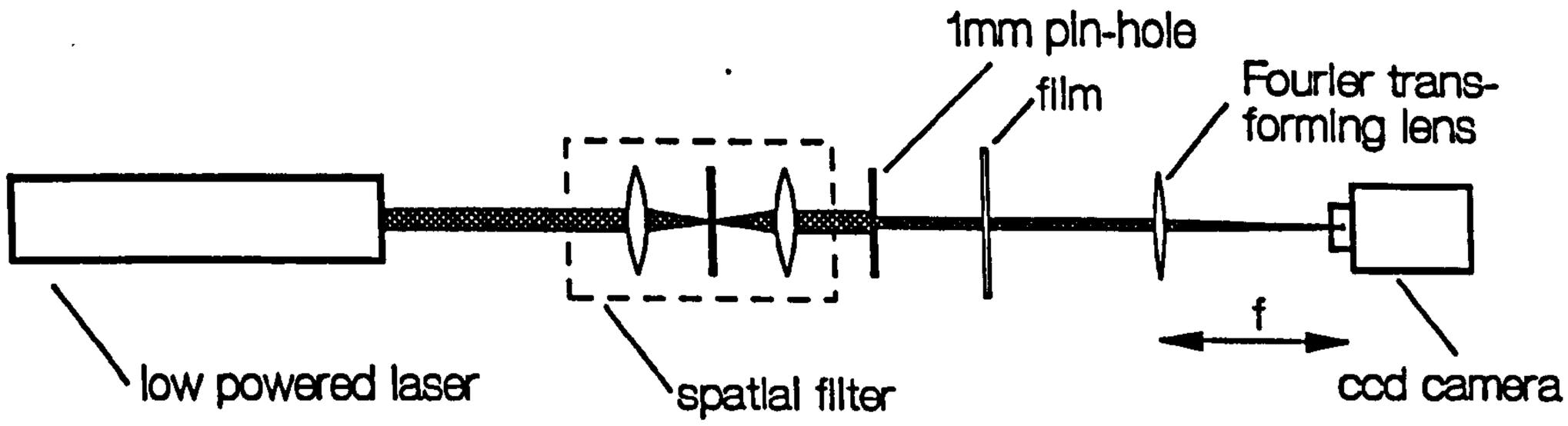

Figure 3.24: Layout of the PIV analysis system

The hardware system used is illustrated in figure 3.24. The optical Fourier transform is achieved by illuminating each 1mm diameter IA on the negative with a

[1]Charge-Coupled Device

coherent, collimated, low-power laser beam. The CCD array is positioned in the Fourier plane of a lens beyond the negative. A two component precision micro-translation stage is used to transport the negative between the fixed optics.

There are a few uncertainties associated with the optical transform. Firstly, the exact diameter of the probing beam is not known and the intensity of the beam will not be uniform. In fact, the beam profile can be regarded as being close to a cropped Gaussian distribution. Secondly, a small spot is placed on the centred of the CCD array to remove the direct beam. This removes information from the transform. Finally, the Fourier transforming lens is limited, due to its finite size and optical properties.

The PIV analysis hardware is interfaced with a microcomputer which can control the movement of the translators and capture the diffraction pattern. The structure of the analysis program used to obtain velocity measurement from a grid of points on a negative is shown in figure 3.25. The software is written is *C* and the routines are available as a programmer's interface. These are currently undergoing a more radical upgrade, so are not detailed.

The averaged diffraction halo corresponds to the diffraction pattern which would be found with a single exposure negative. It is collected by averaging a number of randomly orientated diffraction patterns from the actual negative, and is used to reduce the effect of the self-correlation peak in the autocorrelation plane. The pre-processing simply reduces the digitised image to a 64×64 array of data. The Fourier transformation makes use of a 2D FFT, and computational advantage is taken of the data's initial real state and the resulting symmetries.

The location of the autocorrelation peak involves a search for the maximum value in the data followed by a volume integration to find the centre of mass of the peak. In this way the measured value of the mean particle displacements is found to about one tenth of a grid unit in the autocorrelation plane.

Figure 3.26 shows a typical autocorrelation. The central self-correlation peak has

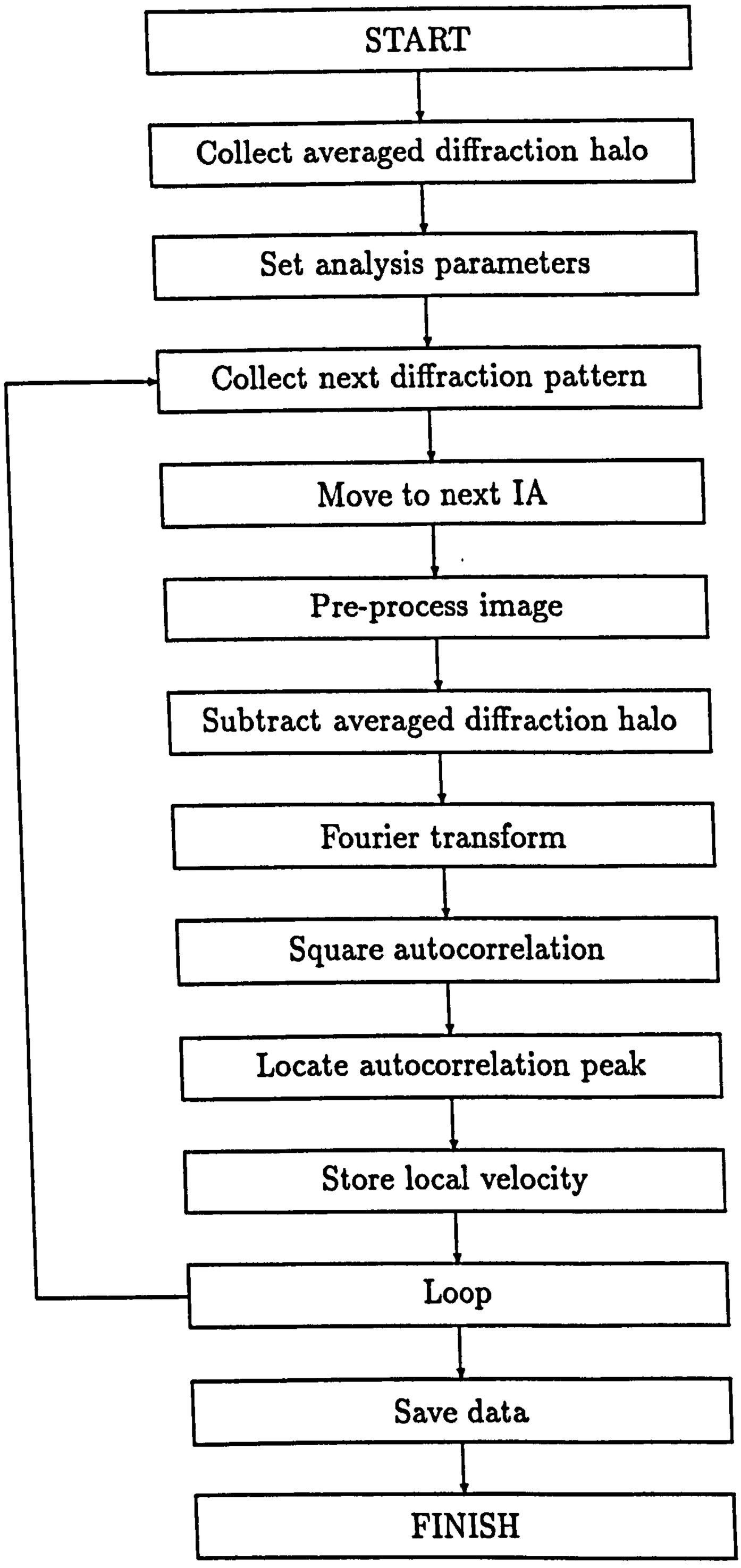

Figure 3.25: Structure of the PIV analysis program

been removed, leaving the two autocorrelation peaks. Above the noise can also be seen two smaller peaks due to the correlation of alternate images in the multiply exposed negative.

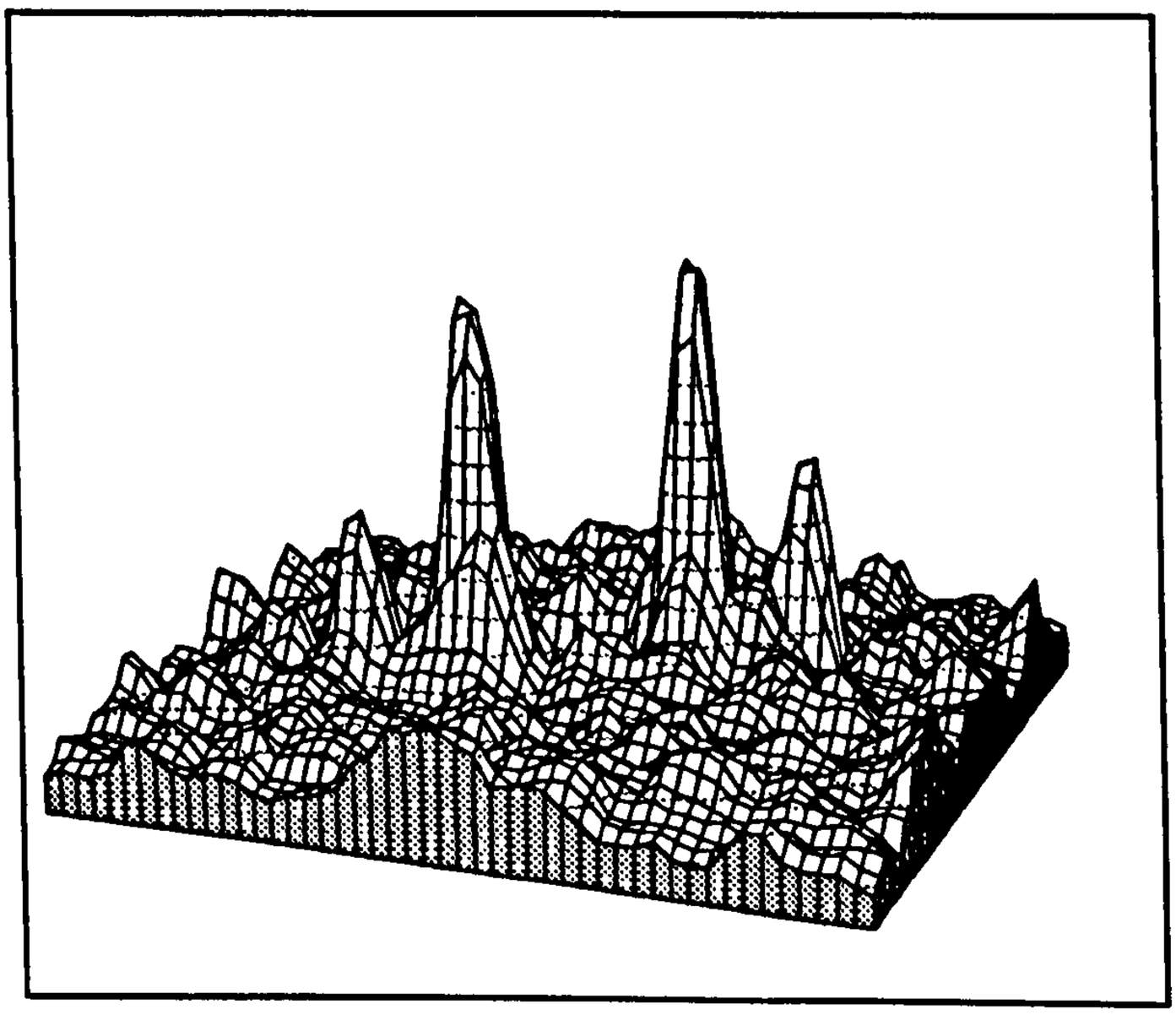

Figure 3.26: A Typical autocorrelation obtained during PIV analysis

PIV Analysis Procedures

Similar procedures were adopted for all PIV photographs analysed in the present studies. The common elements are covered here, and any particular practices adopted are mentioned in the appropriate chapters.

It was considered to be convenient if the grid points of the measured velocity vectors were located at fixed, rational intervals in the measurement zone: for example, every 20mm. This approach has advantages if comparisons are to be made with numerical data on a given grid, or if measurements are repeated with slightly different magnifications. From the selected interval and the photographic magnification the corresponding grid spacing on the film was calculated. The

absolute location of the grid in the measurement zone and on the film were related to each other at analysis time using registration marks present on the negative. The *real-world* coordinates of the registration mark were either known, or known on the glass side wall and readily calculated given the position of the camera, and the magnifications of the measurement zone and the glass. The registration mark was located on the negative by carefully positioning the interrogation beam at this position at the start of the analysis.

An average diffraction halo was collected for each film and used for each frame within the film. Autocorrelation peaks were sought with displacements greater than 30μm or 40μm, depending on the data quality. The processing time for an individual velocity vector is about 7s, so that obtaining the velocity field on a 50×40 grid takes about 4 hours.

PIV Data Validation

Once the array of velocity vectors was extracted from the negative, a number of operations were conducted to weed out bad data and to align velocity vectors if their direction was in doubt. Inevitably, some subjective judgments were made, but, by applying filtering algorithms when possible, these were kept at an acceptable level. It was considered better to lose some good data than to keep spurious values. Ultimately, the success of these filtering operations can be judged from the presented experimental results.

The first filtering operation was to remove all vectors below a specified signal-to-noise ratio. Typically, this level was set such that volume of the signal peak in the autocorrelation plane was 4% of the volume of half the total autocorrelation plane. Normally the area of the signal peak is around 1% of the area of the autocorrelation plane, so this set level is not far from that which would validate data from white noise. Nevertheless, such a value was found to provide a good first-pass at eliminating bad vectors.

If a measured surface was available, all vectors outside the surface were eliminated. If too many apparently good vectors were removed, the relative positions of the surface and the vector field were checked. It is to be expected that some vectors might be 'measured' outside the water surface, as an interrogation area centred close outside the surface might still contain some particle images from within.

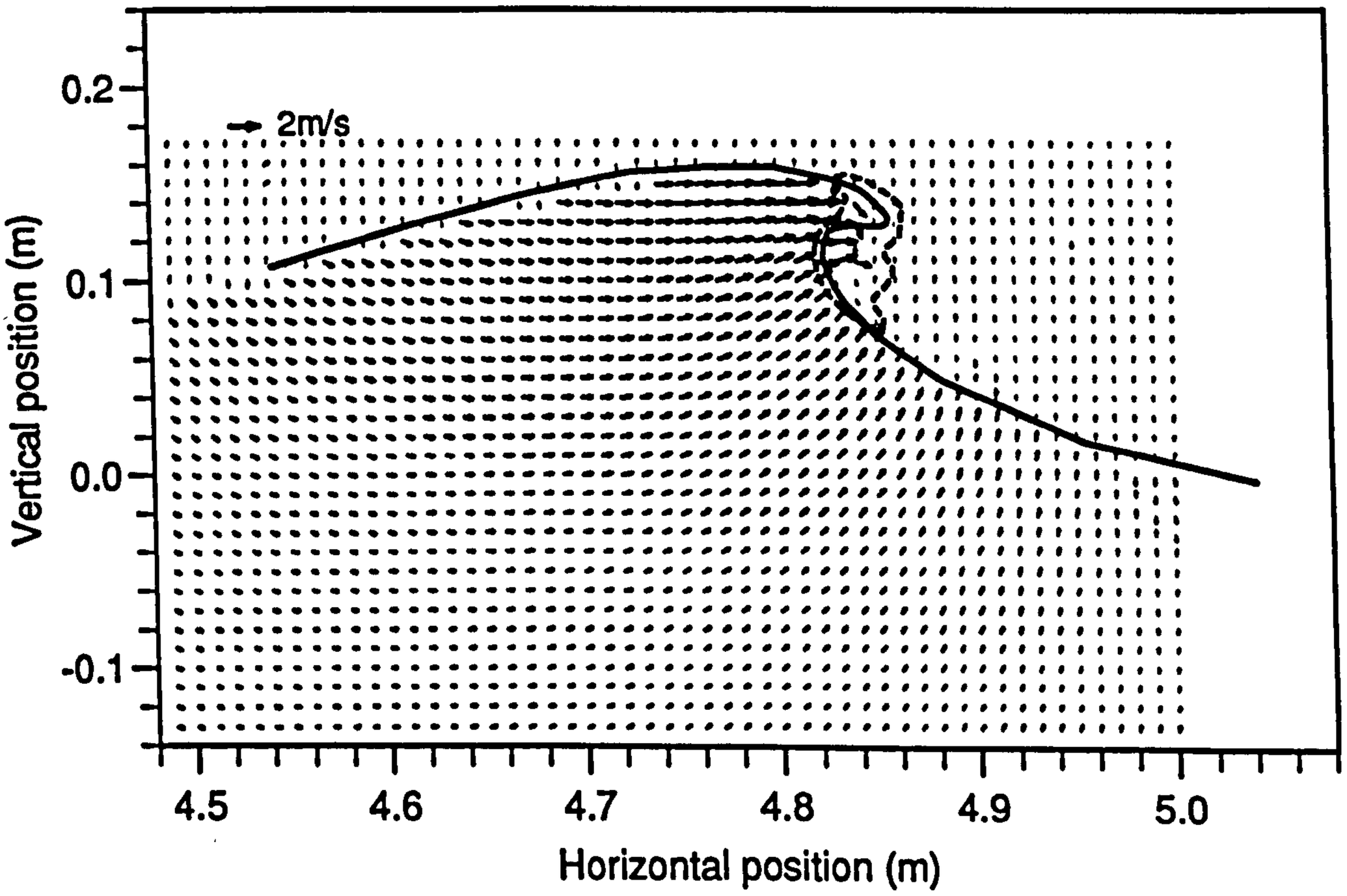

Figure 3.27: PIV data before filtering to remove spurious vectors

In a manual operation, remaining spurious vectors were identified and removed. These vectors were judged by lack of continuity with their neighbours. In principle, this operation could be implemented as an automated procedure.

Alignment of the velocity vectors was affected with some a-priori knowledge of the flow. This is acceptable in wave studies where the wave motion exceeds that due to turbulence.

To illustrate the processes described above, a vector plot of PIV data before validation is shown in figure 3.27, and the remaining velocity vectors after the filtering operations in figure 3.28. In this case, vectors were removed mainly in areas above the water surface and in regions of low velocity, near the bottom. In

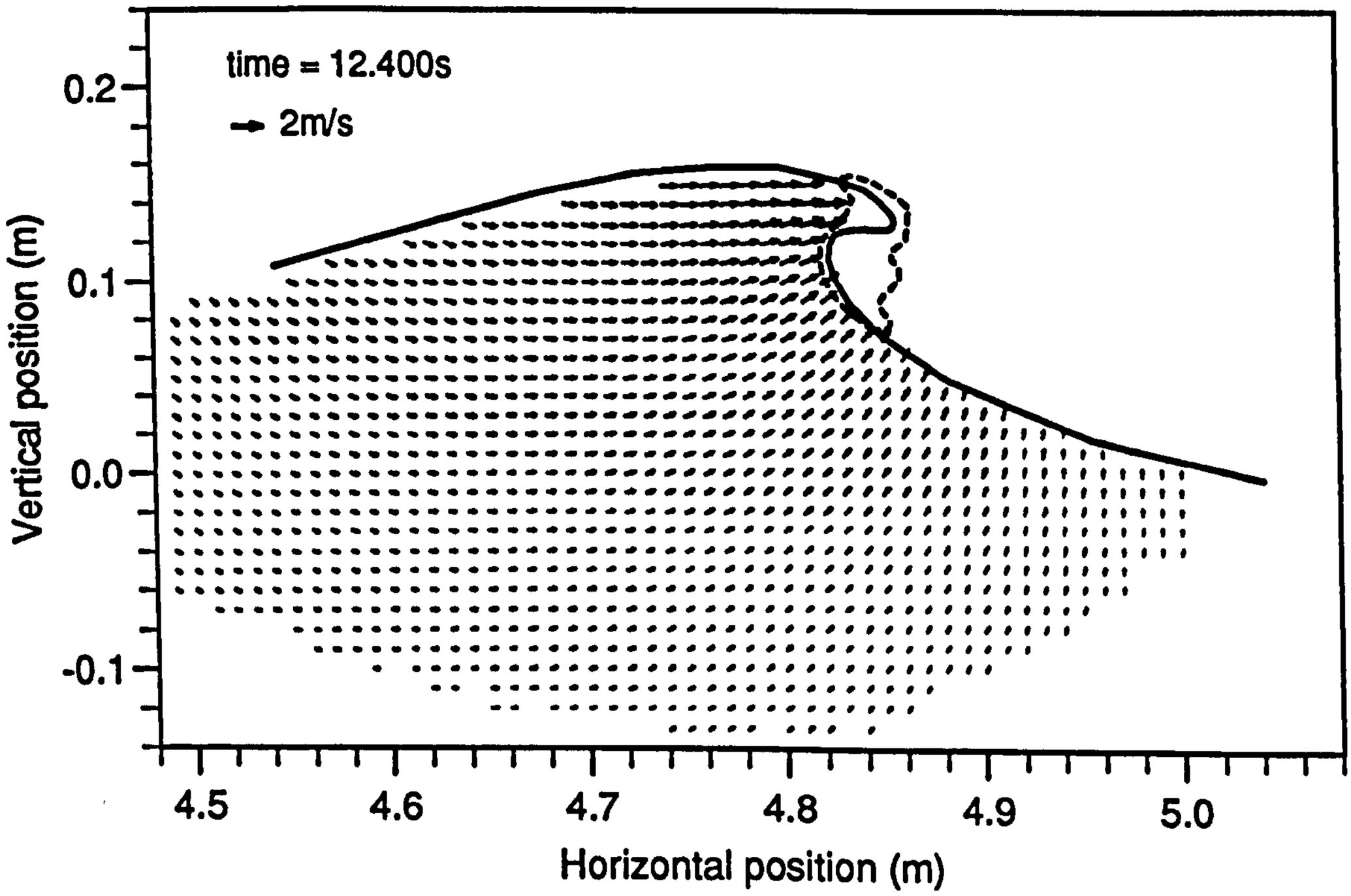

Figure 3.28: PIV data after filtering to remove spurious vectors

addition, a couple of remaining, spurious vectors were identified within the fluid, and one outside the boundary.

PIV Analysis Errors and Limitations

A PIV negative contains information from which the underlying flow can be deduced. The accuracy of this part of the process depends on the optimisation of the PIV acquisition parameters, and, even if these were ideally set, is fundamentally limited. If the seeding density was too low, or the velocity gradients were too great, then high quality measurements cannot be expected. Consideration of the aspects mentioned here led to the suggested settings given previously in table 3.4.

There are two major types of error inherent in the analysis process, random and systematic, each of which varies with the velocity gradients present in the flow. In fact, the dependence is on the displacement gradients present on the film which relates to the velocity gradient by

$$\frac{\partial \delta_x}{\partial x} = \Delta t \frac{\partial u_x}{\partial x} \tag{3.15}$$

For the displacement gradients present in the PIV studies described, the random errors are the the range 0.3% to 0.5% [19]. There is always an uncertainty in the location of the centre of the correlation peak, due to the random sampling of the particles in the interrogation area, and this uncertainty increases as the range of particle displacements increases and the correlation peak broadens.

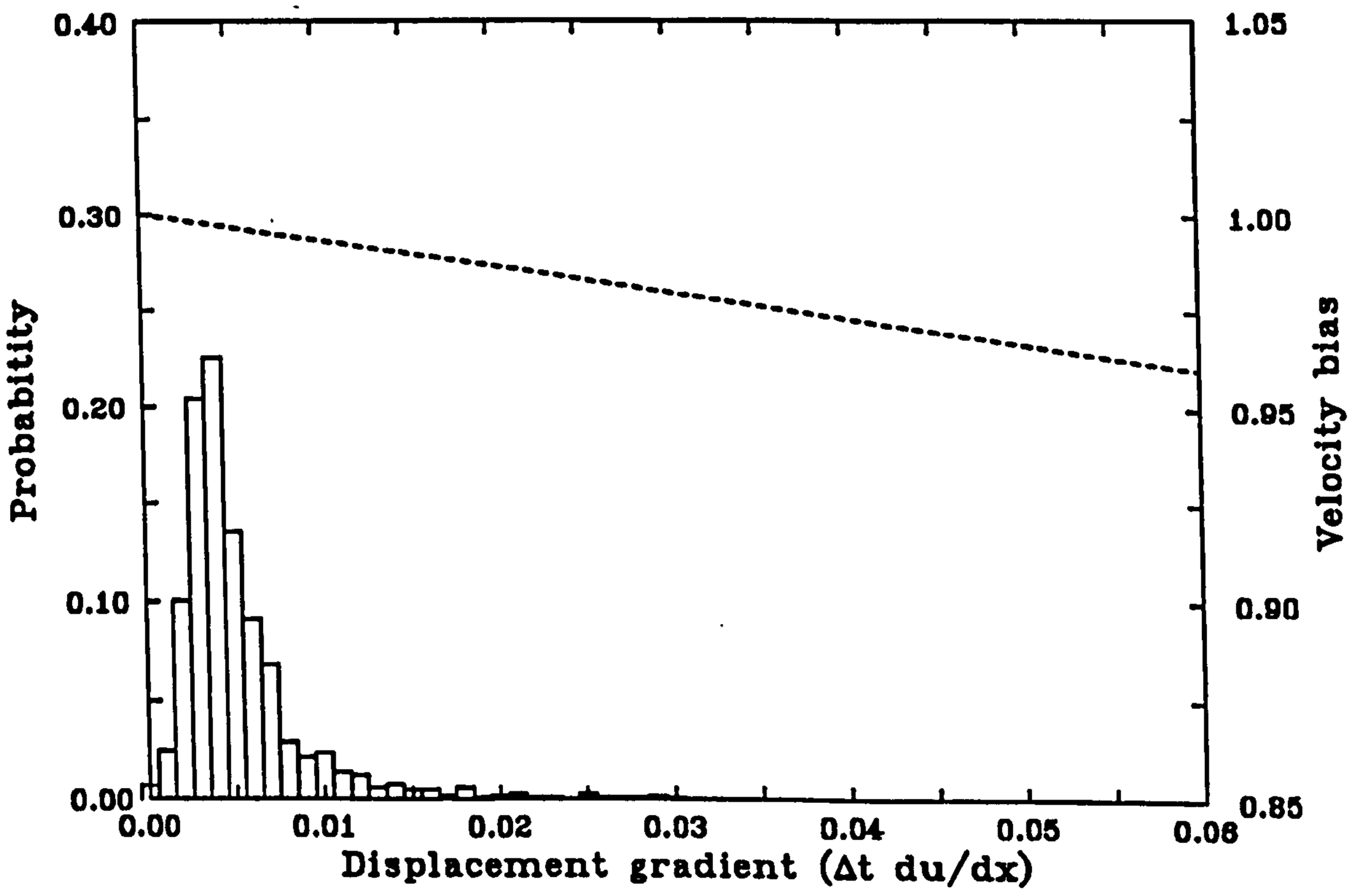

Figure 3.29: Probability of displacement gradients in PIV picture of a breaking wave and corresponding systematic bias of measured velocities

The systematic error associated with the displacement gradient tends to bias the average displacement measurement towards the lower displacements, since the larger the particle image separations the higher the chance of the multiple particle image lying outside the interrogation area. This artificially reduces the seeding density for the larger displacements, and introduces a bias to selecting smaller separations. In algebraic and numerical studies it has been found [29] that there is a systematic bias introduced which varies linearly with displacement gradient.

Figure 3.29 contains the the probability distribution for displacement gradients obtained from the data previously shown in figure 3.28. Also shown is the predicted systematic bias of the measured velocity [29]. The displacement gradient plotted is the magnitude of the inline and perpendicular components, in order to obtain a conservative estimate of the error.

$$\frac{\partial \delta}{\partial x} = \sqrt{\left(\frac{\partial \delta_x}{\partial x}\right)^2 + \left(\frac{\partial \delta_y}{\partial x}\right)^2} \tag{3.16}$$

It can be seen in figure 3.29 that the systematic bias for most of the data is less than 1%. For the highest velocity gradients in this flow, the error could be up to 2%. It should be noted that this dataset contains the highest displacement gradients found in the studies, and that by taking the photographs at higher magnification, thereby reducing the appropriate value of the illumination interval Δt, the errors can be reduced.

The random errors are less serious than the systematic errors, as they manifest themselves clearly when the resulting data is inspected. The systematic bias is potentially more dangerous as trends might be identified in the data which are due to this effect, not to a real physical phenomenum. However, by careful control of the experimental parameters, these errors can be kept small, to within about 1%.

The final source of error in the PIV analysis is in the calibration of the analysis rig. Figure 3.30 shows the calibration curves for each velocity component. These were obtained from artificially generated PIV negatives, made by plotting random patterns of dots, with known separations, followed by photographic reduction. Each point represents the average of 20 measurements of that displacement, and, in this way, the calibration values have been found with an accuracy of about 0.1%. The vertical and horizontal values are different because the pixels on the CCD array are not square.

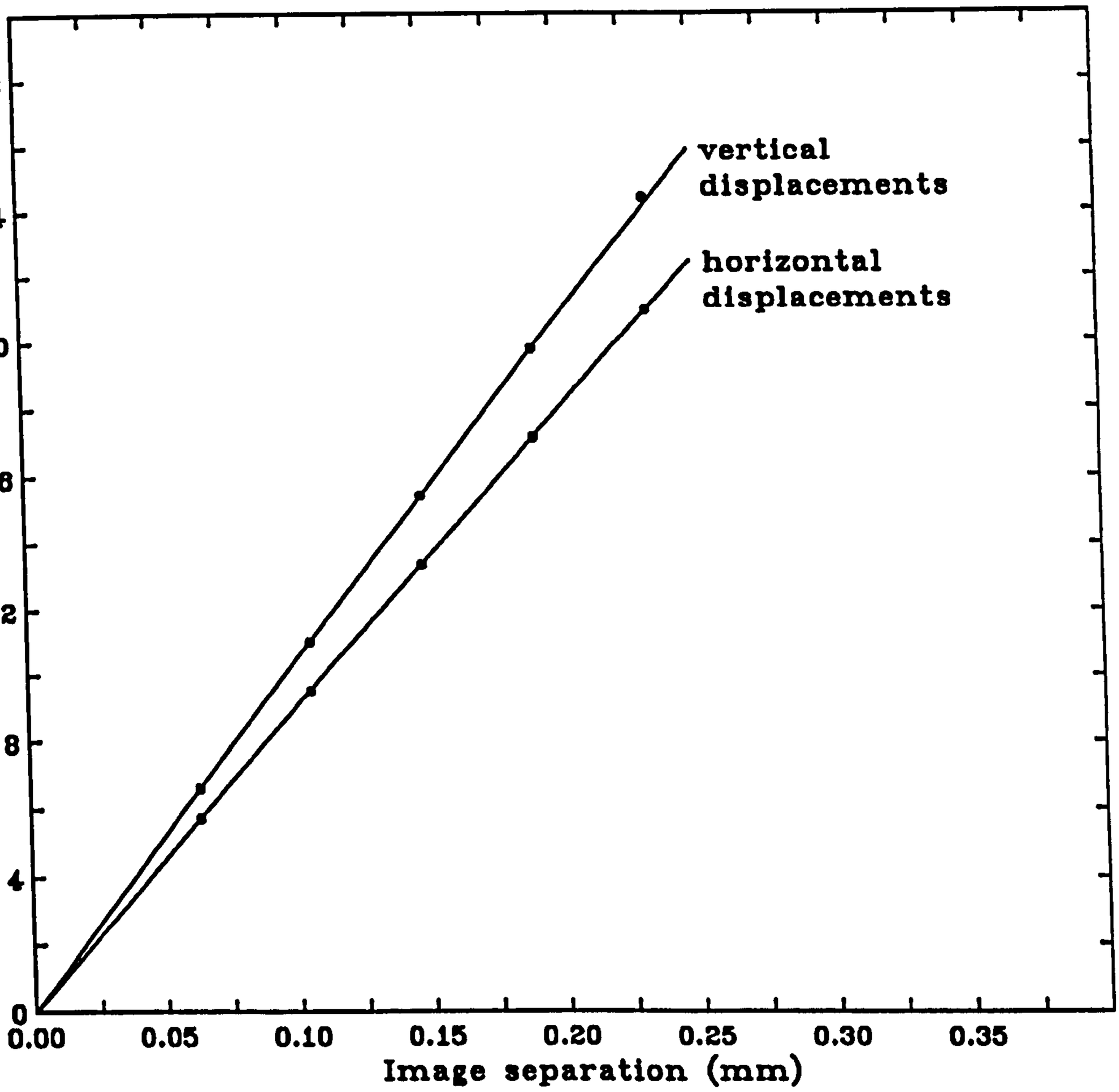

Figure 3.30: Calibration curve for the PIV analysis system

3.5.2 Surface Profile Measurement

The photographic negatives obtain in the PIV process often contain a very clear image of the water surface where the laser sheet passed through. The conditions for this to occur and be readily identified are that the camera view of the surface should be unobscured and that there should be some seeding particles on the surface to scatter the light. The first condition can generally be met by careful

positioning of the camera, and seeding is generally present on the surface, unless the current is being run.

The most successful method found to extract the surface information from the negatives was to enlarge the image with a standard photographic enlarger onto a digitising tablet, and to manually identify points on the surface. Manual processing is necessary given that the quality of the surface image can be quite variable. In some portions, for example where the surface is starting to break, a judgment has to be made as to where the surface actually is, and these areas should be assessed with some caution.

The digitising tablet used is a Numonics 2200/2210 Graphics Digitiser, connected via rs232 to the Archimedes microcomputer. For each negative, a reference point is first located to relate this point on the digitising tablet to known physical coordinates. Next, two known reference points are identified and recorded in order to deduce any rotation between the digitising and physical planes. A sequence of points is now recorded along the water surface and, if appropriate, additional fluid interfaces are recorded. With a knowledge of the enlargement factor and the reference points, the physical coordinates of the surface are determined.

3.5.3 Fourier Analysis of Wave Elevation Time-series

If the wave and sampling parameters have been set as suggested in section 3.4.2, the process of Fourier analysing sampled elevation time-series is simplified as the assumptions of steadiness and periodicity are satisfied.

Figure 3.31 shows the amplitude components obtained from the FFT of a steady wave with integral cycles in the sampling period (figures 5.4, case 4). The fundamental wave component, and first and second harmonic can be easily identified and extracted, and the noise level is low.

For comparison figure 3.32 contains the results of taking an FFT of a wave el-

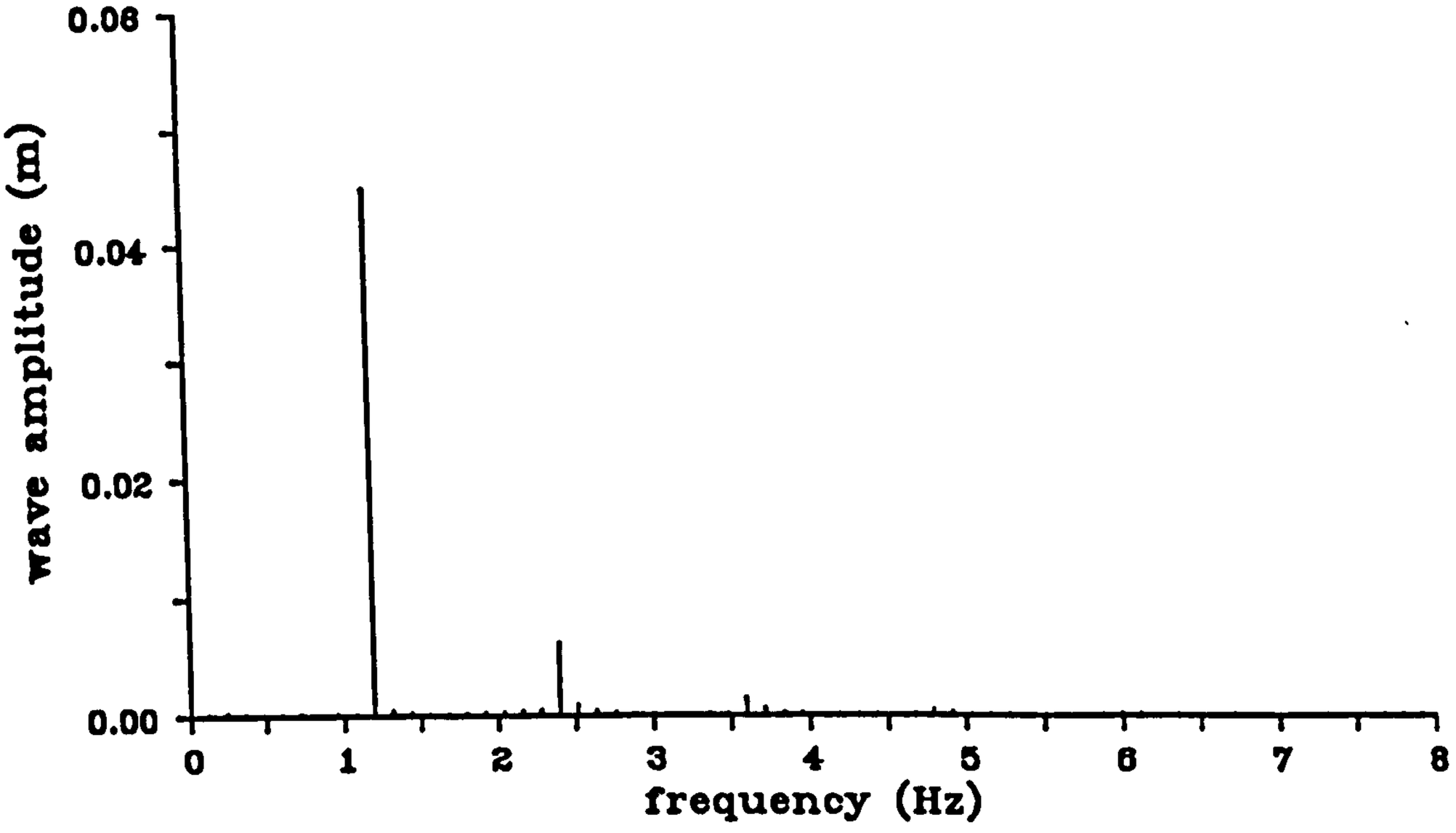

Figure 3.31: FFT of wave amplitude time-series containing integral cycles

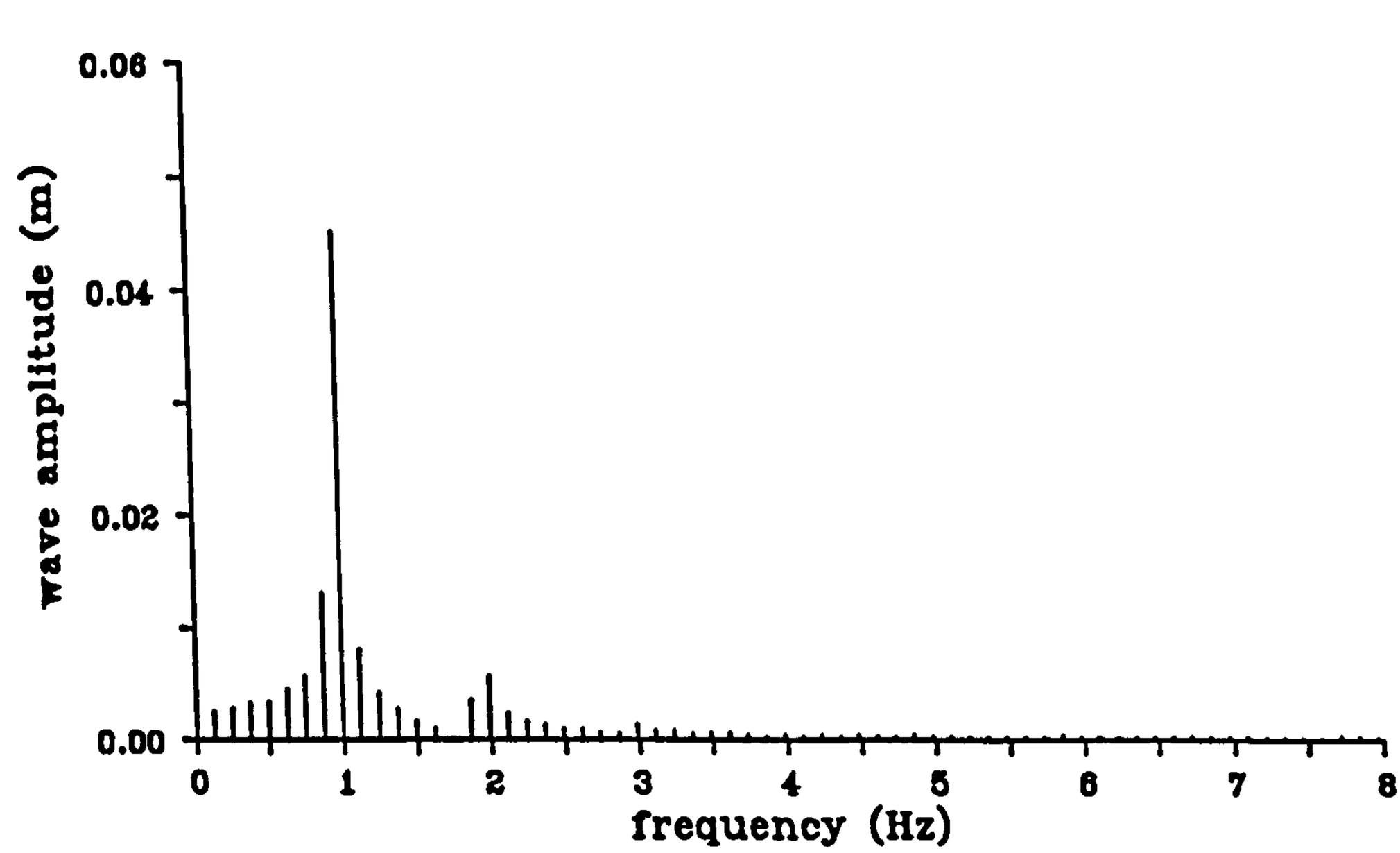

Figure 3.32: FFT of wave amplitude time-series containing non-integral cycles

evation time-series which does not have integral cycles in the sampling period (figure 5.7, case 19). Spillage of the fundamental component into neighbouring frequencies can be seen.

Chapter 4

The Evolution of a Long-Crested Deep-Water Breaking Wave

4.1 Summary

A study to measure the internal kinematics of a breaking wave is described. The selected wave is first generated in a numerical model, then reproduced in the wave flume. Measurements of the internal kinematics are covered and results presented for the different phases of the wave's evolution. When appropriate, the experimental measurements are compared to numerical predictions, and the quality of the match discussed.

4.2 Generation of the Extreme Wave in the Numerical Model

The approach used to generated the breaking wave in the time-stepping numerical model, described in section 2.4.2, was similar to that adopted in the laboratory to produce an extreme wave for demonstration purposes: linear theory was used to force an extreme event, then the parameters of the generation were fine tuned until

a suitable plunging wave resulted. The wave selected was arbitrary, but it was considered more important that similar waves could be generated numerically and experimentally, than that the chosen wave should have any particular parameters, other than being very extreme.

Each attempt at producing a numerical breaker followed the same pattern. First, parameters for a chosen spectrum were selected. Next the surface profile and velocity potential were calculated using equations 2.1 and 2.2 and linear superposition in a similar way to equation 2.8. These quantities were appropriately scaled for the model, and care was taken to ensure that the wavepackets tailed off naturally before the periodic boundaries. The distribution of computational points was also forced to be smooth across the boundary. The numerical wave group was then allowed to propagate until it 'broke' or passed the place where breaking was expected. Depending on the result from the run, the spectral parameters were altered until a plunging breaker was produced which just avoided breaking at the penultimate crest. The main parameter to be modified was the overall size of the spectrum.

In order to limit the number of parameters the spectral shape was selected such that the components had amplitudes given by

$$A_n = (a_0 + a_1\omega_n)\exp\left(-\left|\frac{\omega - \Omega_1}{\Omega_0}\right|^s\right) \tag{4.17}$$

where

$$\omega_n = \frac{2\pi n}{102.4} \tag{4.18}$$

The phases α_n were chosen so that, if linear theory applied, the components would have some common phase Φ at $x = 0, t = 0$.

The spectral form given in equation 4.17 was selected as covering the 'flat top' spectral shape often used in the generation of freak waves [15, 22], while allowing

the spectrum to tail off smoothly at the extremes. Initial parameters were chosen with a knowledge of the dimensions and capabilities of the wave flume (see sections 3.3.1 and 3.3.2).

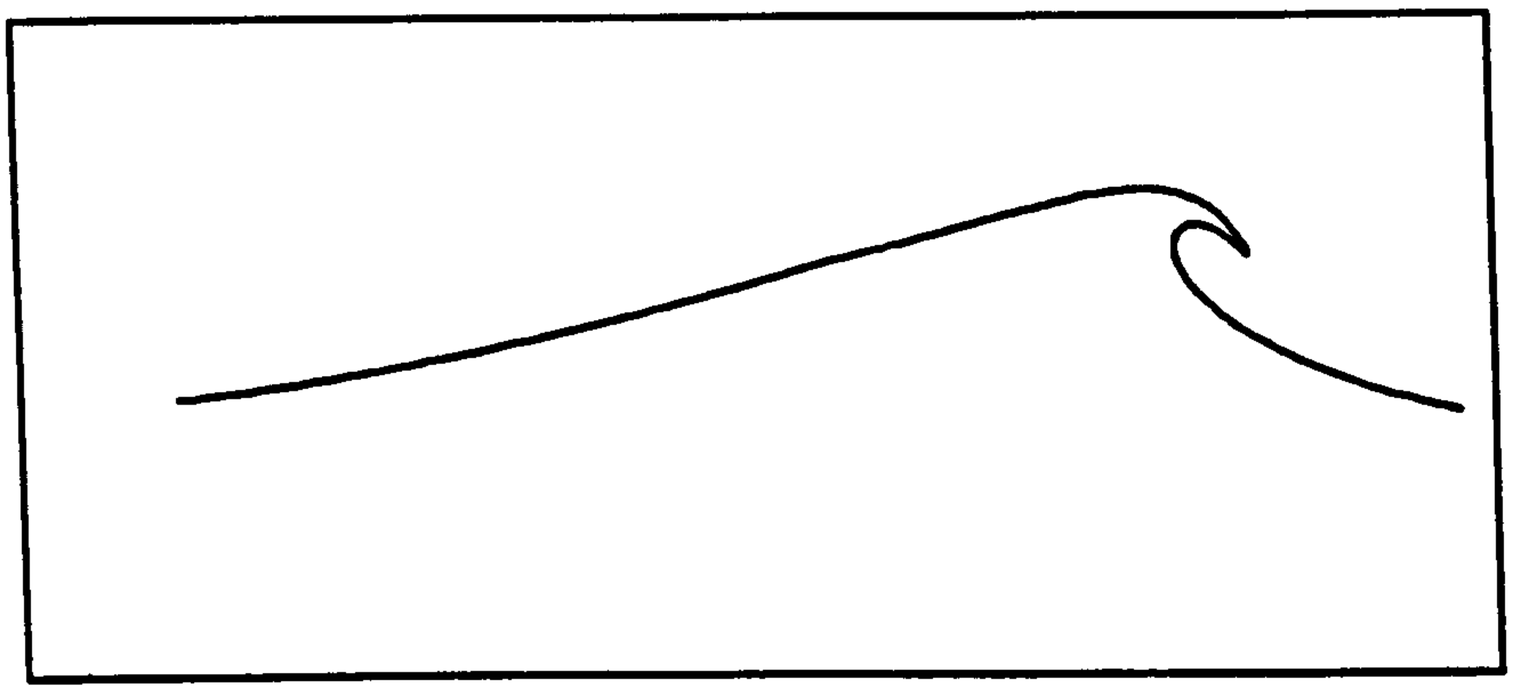

Figure 4.1: Final surface profile as the numerical wave approaches breaking

With 200 computational points it was possible to try another iteration every few hours, and after a couple of dozen iterations a suitable breaker was arrived upon. The chosen wave was then rerun with twice the number of computational points. The profile of the wave as it nears breaking, used to judge its suitability, is plotted in figure 4.1, after rescaling to flume units.

Parameter	Value
a_0	0.75498 mm
a_1	1.4161 mm s rad^{-1}
Ω_0	2.93230 rad s^{-1}
Ω_1	4.53174 rad s^{-1}
s	16

Table 4.1: Parameters selected for the spectrum used to calculated the starting conditions for the numerical model

The spectral shape which yielded this final profile is plotted in figure 4.2 and the spectral parameters noted in table 4.1. The spectrum shown is somewhat different from those naturally occurring in the oceans, where normally the wave component

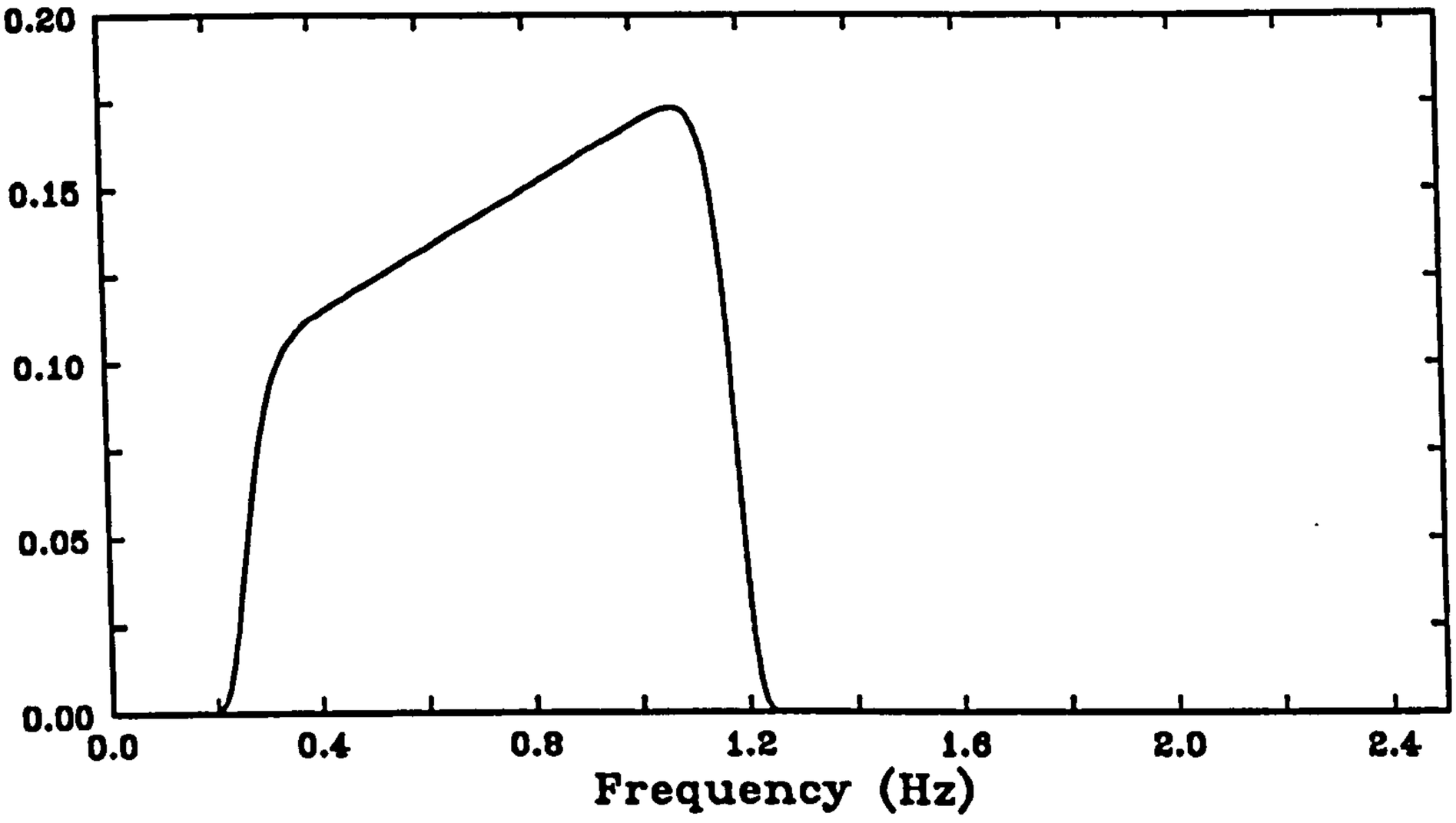

Figure 4.2: Wave amplitude spectrum found to produce a suitable numerical breaker

amplitude tails off with frequency above the central value. However, this was the spectrum which generated the most extreme wave, and was therefore the one used. When the wave packet reaches the wave flume, its spectral form has modified to one which is more acceptable, as can be seen by looking forward to figure 4.7. For the purpose of non-dimensionalising the results the mean frequency of the spectrum has been calculated as $f_m = 0.818$Hz, with corresponding wavelength $\lambda_m = 2.26$m.

The starting conditions for the numerical model calculated from this spectrum are plotted, at tank scale, in figure 4.3 along with the distribution function used to obtain the coordinates of the computational points. The distribution function peaks near the place where breaking is expected, in order that there are enough points where the surface curvature is the highest and the greatest accuracy is required. Note that the horizontal extent of the starting conditions is about five times longer than the wave flume.

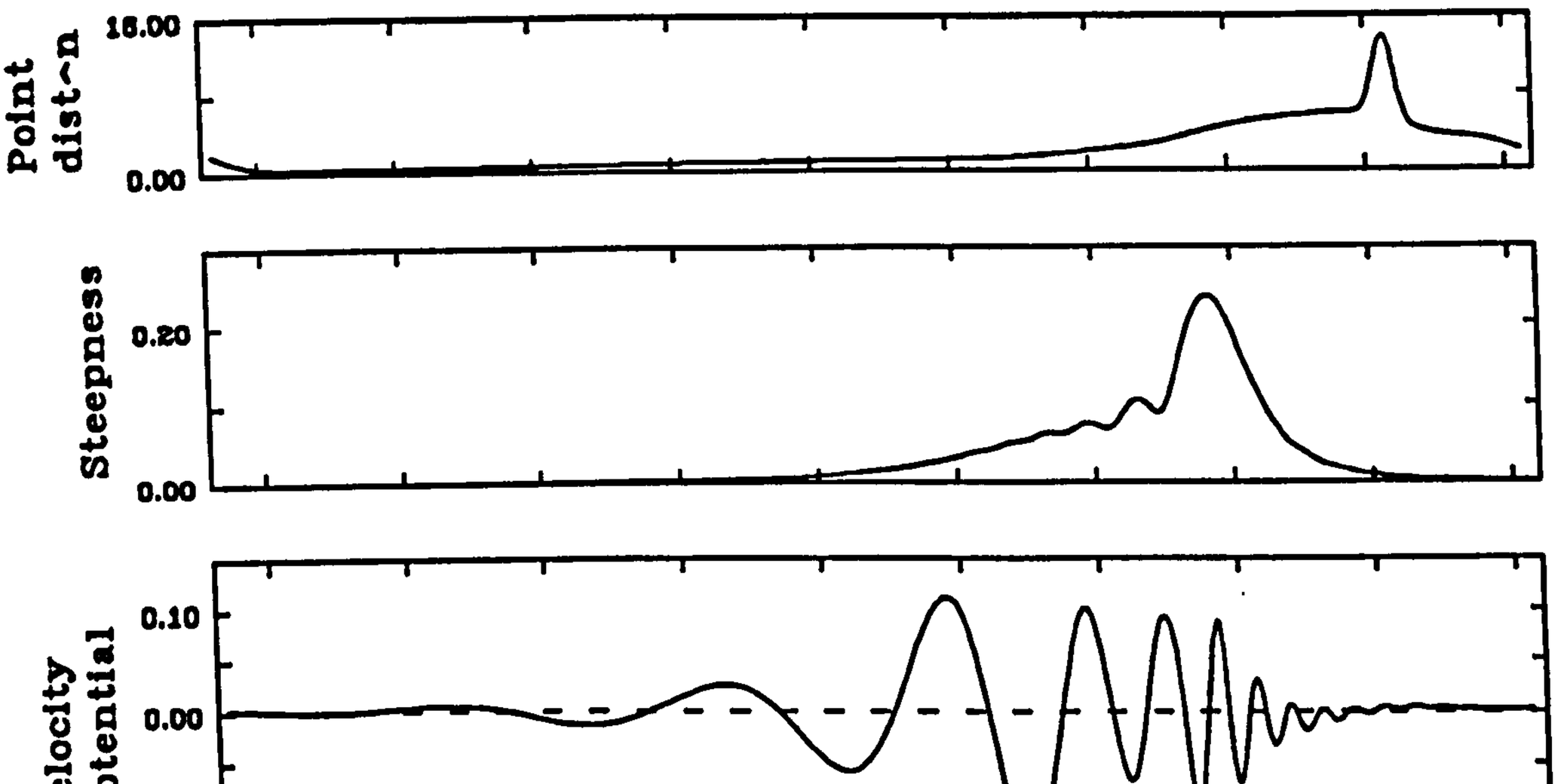

Figure 4.3: Starting profile and velocity potential calculated by linear theory 7.3 seconds before expected linear focus

4.3 Replication of Numerical Wave in the Wave Flume

4.3.1 Strategy for Matching the Waves

From the data produced by the numerical model it is possible to extract any physical information about the wave packet as it propagates from the starting conditions until the program halts at the breaking point. While it would be possible to calculate a wave time-series to be produced at the wavemaker, this is not practical as the travelling wave at this position is distorted by the transient effects of the wave paddle [27]. A better strategy is to obtain a wave height time-series from the model and to attempt to reproduce this in the flume far enough in front of the wavemaker to avoid transient effects.

A position for the wavegauge in the numerical wave tank was selected to be at $x_m = -1.6$m, which is about 2m before the final breaking position. By interpolating between the records at the neighbouring computational points a wave height time-series was extracted from the numerical data. The equivalent position in the physical wave flume was selected to be at $x = 2.2$m, from considerations of the part of the flume where PIV measurements of the breaking kinematics would be easiest to make. The sensitivity of the generated wave to these somewhat arbitrarily selected values are considered later.

The criterion for success in the replication is that the wave height time-series should match reasonably well at the selected wave gauge position. Any scheme which achieves this end is acceptable, even if the method is ad hoc. The approach adopted was to form the amplitude and phase spectrum of the numerical time-series and to attempt to reproduce this in the tank. Because the waves are markedly non-linear at the selected position, the linear wavemaker transfer function detailed in section 3.3.6 cannot be expected to produce the require record directly, and an iterative scheme was attempted.

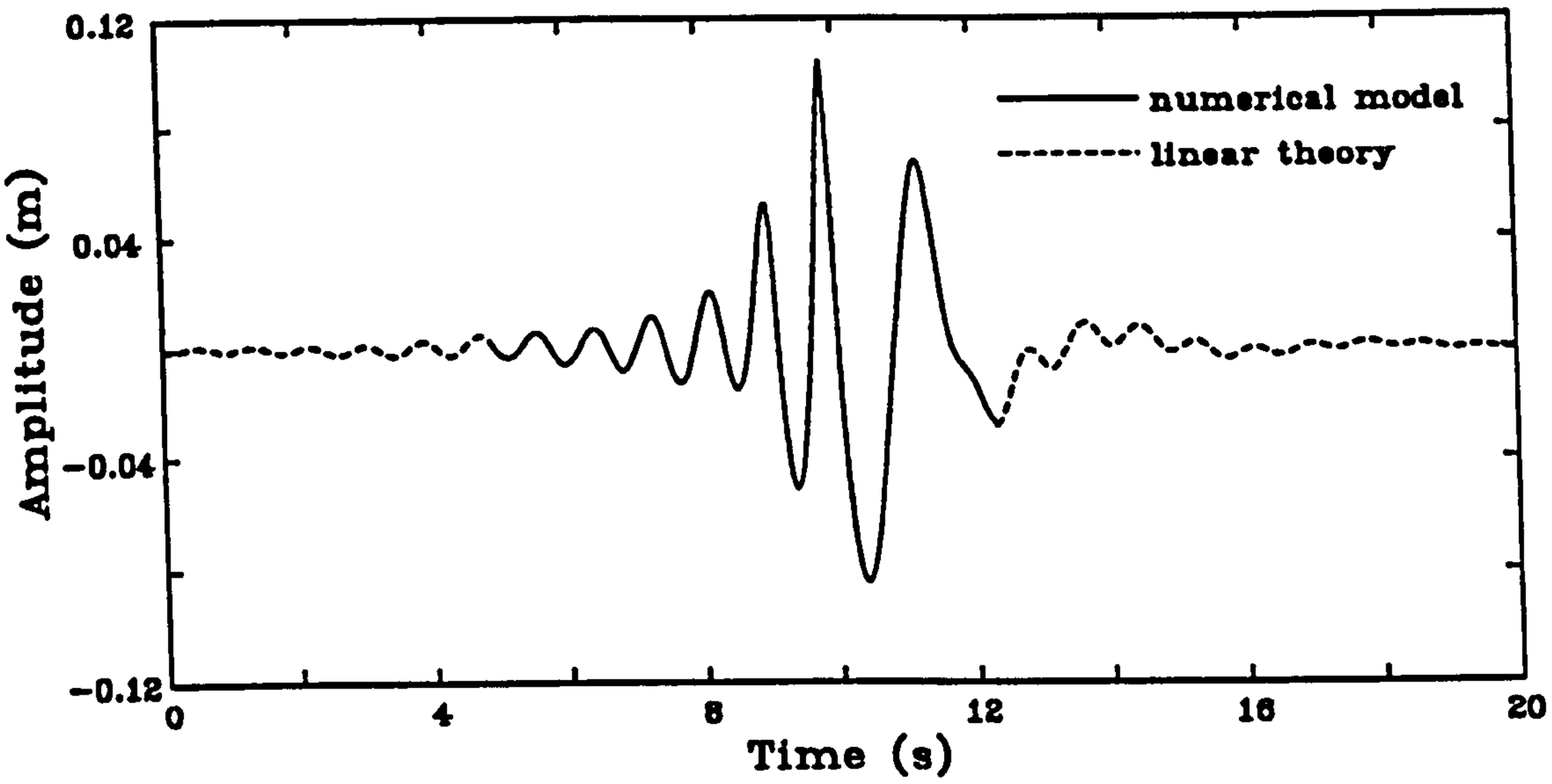

Figure 4.4: Composite wave amplitude timeseries from the numerical model and linear theory

In forming the spectrum of the numerical time-series a difficulty is encountered: only part of the time-series exists, from the chosen start until wave breaking. The time-series was extended outside this range by calculation with linear theory from the starting spectrum. The composite time-series obtained in this way is shown in figure 4.4. The linear focus was arranged to be at 12.071 seconds.

4.3.2 Experimental Replication of Numerical Wave in the Wave Flume

Figure 4.5 shows the configuration of the wave flume for the experimental replication of the numerical wave, including the position of the wave gauge. Also shown are the actual wave profiles obtained in the experiments and the physical and numerical coordinate systems.

The parameters involved in attempting to reproduce the required wave spectrum are the frequency limits of the wavemaker drive spectrum, f_1 and f_2, and the position of the wave gauge. In addition there is the details of the iterative scheme

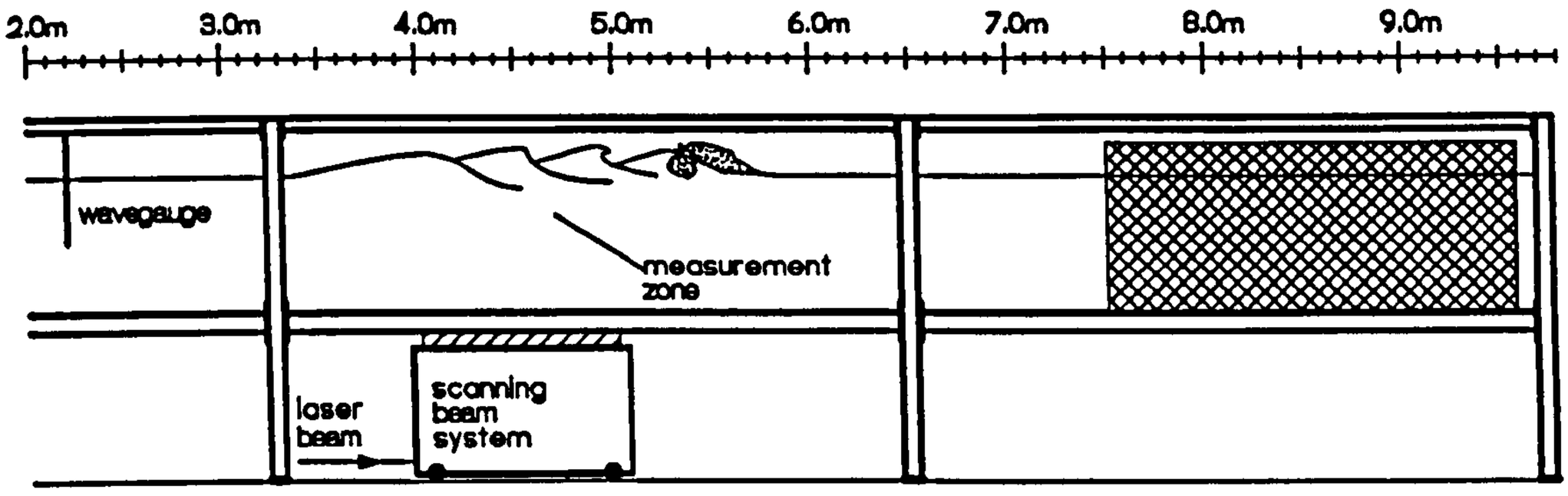

Figure 4.5: Configuration of the wave flume from the measurement of breaking waves

and the number of iterations involved. A sensitivity analysis was conducted on these quantities.

The initial wavemaker drive spectrum was calculated from the linear transfer function and tried in the flume. The wavegauge was sampled as the wavegroup passed. The later portion of the wave record, after the breaking, contains reflections and spurious high frequencies from the wavemaker's final large motion which are difficult to disentangle in a non-linear wavefield. Therefore, the experimental wave record was patched with the linearly expected time-series used to extend the numerical record. In this way, the same operations were performed on both the numerical and experimental wave time-series before transformation. The required and obtained spectra were then compared. If the match was judged inadequate, then each component in the drive spectrum was modified in both amplitude and phase by multiplication by the complex quantity $R(\omega)$ given by

$$R(\omega) = \sqrt{\frac{A(\omega)_{required}}{A(\omega)_{obtained}}} \tag{4.19}$$

This modifier has the effect of stepping halfway to that required in both amplitude and phase and was used because the simple ratio was found to overshoot.

Iterations were continued until the obtained spectrum was judged to match that required sufficiently closely. In the iterations the lower frequencies were found

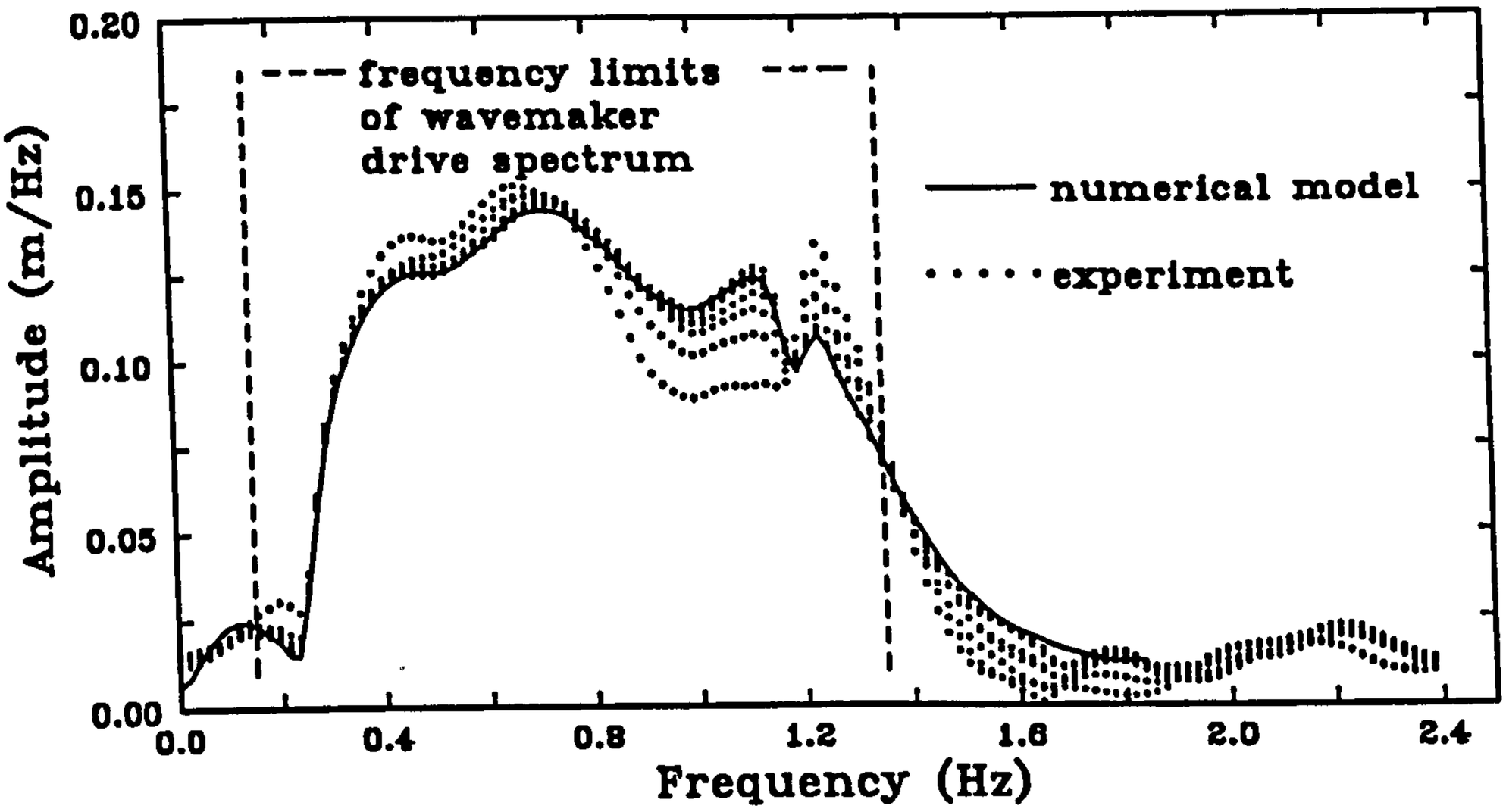

Figure 4.6: Experimental iterations towards the required wave amplitude spectrum

to converge first, which is expected because the higher frequencies are partially composed of their harmonics. This can be seen in figure 4.6 which shows the convergence of the experimental wave spectrum to that required over six iterations.

Contained in figure 4.7 are the amplitude and phase of the experimental wave spectrum finally achieved compared to the required spectrum. The spectra can be seen to have been forced to be very similar within the frequency range for which waves were generated

The actual wave amplitude time-series is plotted in figure 4.8 and is compared to the time-series extracted from the numerical model. The match is generally good in the main part of the wave group. However, there is a tendency for the largest crests to be not well replicated. It should be noted that the portion after breaking is not relevant as it has no influence on the breaking event.

The repeatability of the generated wave spectrum is shown in figure 4.9. The short vertical lines show the standard deviation of each Fourier coefficient about their mean values. These statistics were calculated from 72 runs of the wave field in the main experimental sequence to measure the internal kinematics. It

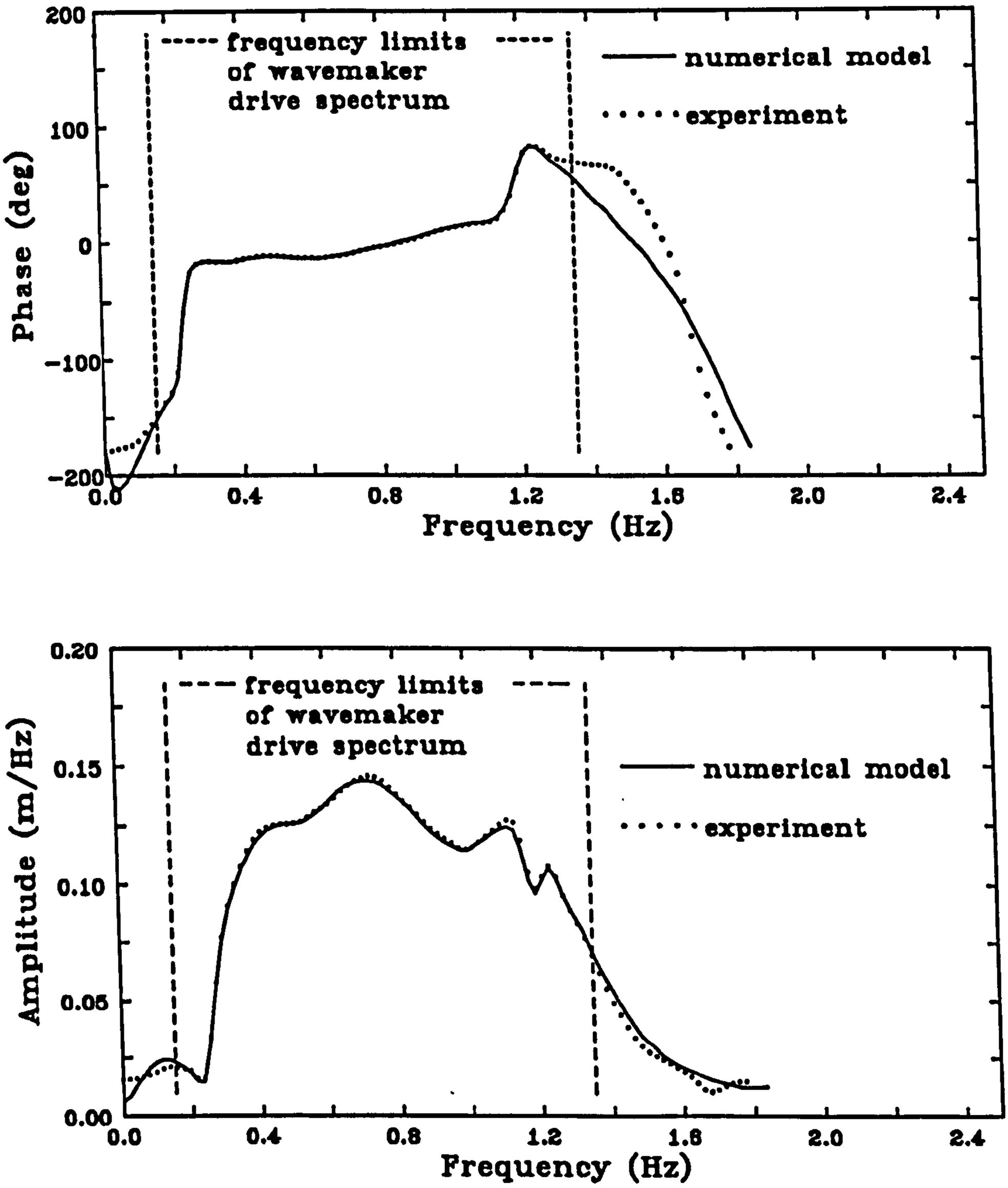

Figure 4.7: Experimental wave spectrum found by iteration compared to the required spectrum

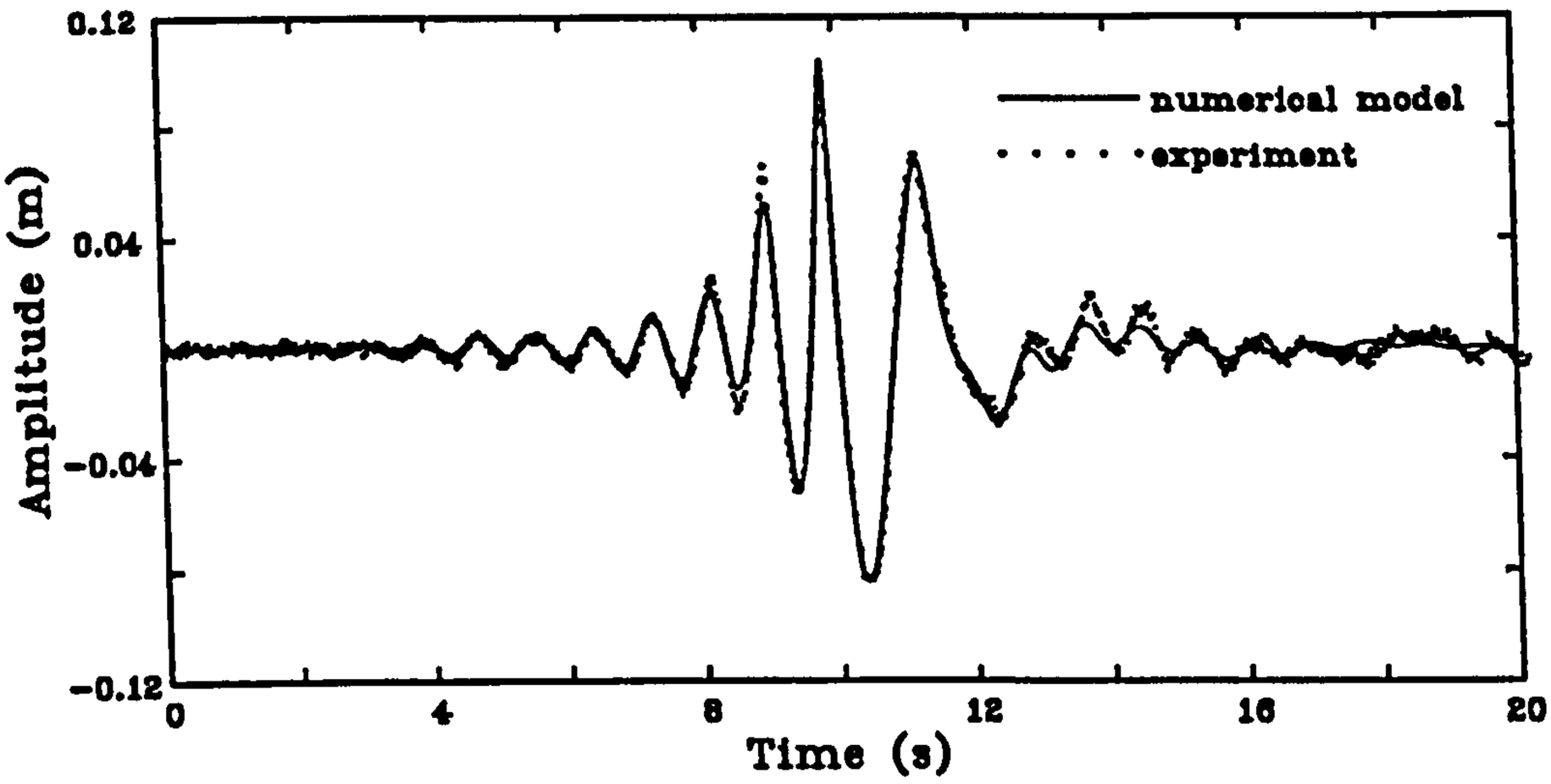

Figure 4.8: Experimental wave amplitude timeseries compared to the timeseries extracted from the numerical model

should be noted that the values previously plotted in figure 4.7 lie outside the repeatability scatter in some places. For instance, at the highest part of the amplitude plot the experimental points lie above the numerical curve in this figure, whereas in figure 4.9 they lie below. This is an indication of the repeatability of the wavemaker between the sets of tests which were separated by a few days.

The repeatability of the wave spectrum is excellent. However, it can be expected that the exact form of the breaking wave will be very sensitive to small changes in the starting conditions of its evolution.

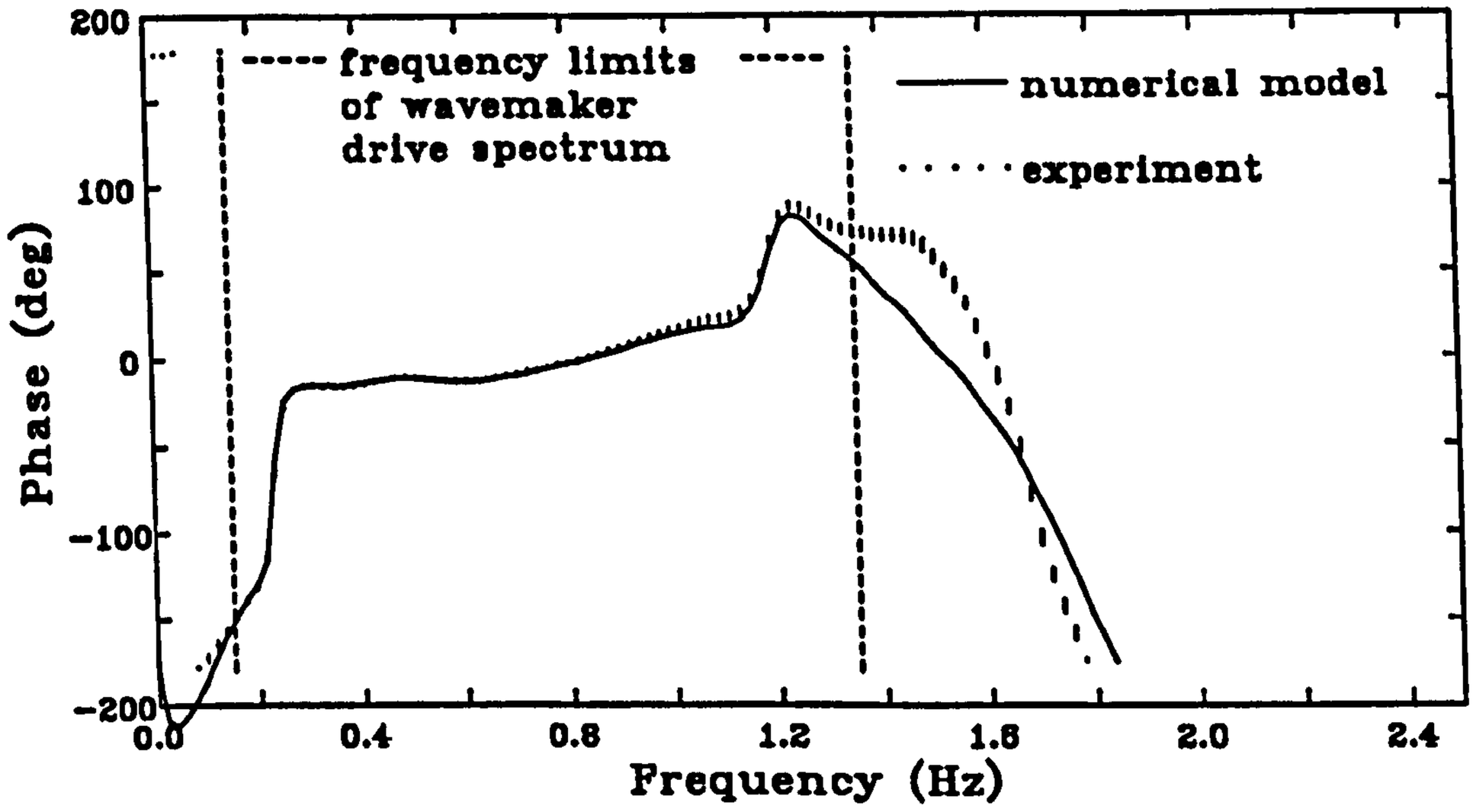

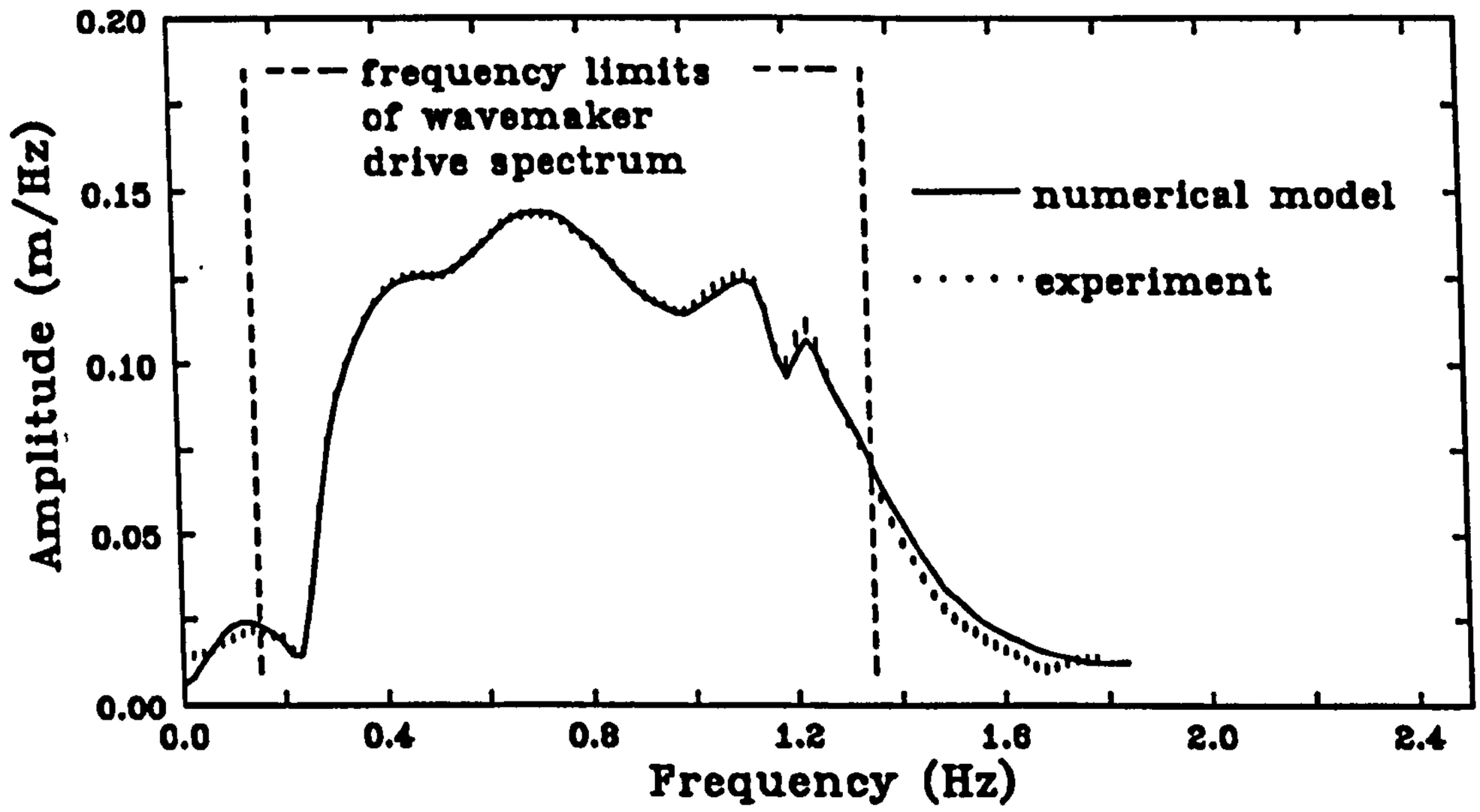

Figure 4.9: Repeatability of the experimentally measured wave spectrum

4.3.3 Sensitivity of Breaker Form to Replication Parameters

The form of the breaking wave produced by the described means depends, to some extent, on the parameters involved in the replication. It is important to understand the sensitivity of the form to these parameters in order they are not confused with judgments on the differences between the numerical and experimental waves at breaking.

There are many parameters to consider when assessing the sensitivity of the breakers form. Firstly, there is the position chosen for the measurement of the wave height time-series in the numerical model, relative to the expected breaking position. Next, there are the parameters involved in the experimental reproduction: the frequency limits of the wavemaker drive spectrum, f_1 and f_2, and the position of the wave gauge in the flume, relative to the wavemaker. Finally there are other aspects of the experiments to consider, such as the accuracy of the wavegauge's calibration and the number of iterations used in the replication.

In the sensitivity analysis the effect on the breaking wave's form, near breaking, was measured for small changes in the noted parameters compared to the central set of the parameters actually selected for the main experiments. In the graphs which follow, the measured profiles are plotted along with the profile obtained for the central set. The surface profiles were measured from photographs of the surface at the near glass wall, illuminated by flash. The calibration of this data is only approximate, and the graphs should only be judged for the relative effect of changing the parameters.

A common tendency was observed during the attempted replication process. If the upper end of the frequency range, f_2, was set too high, then invariably the wave train would break at the crest which forms just before the main breaking. This was considered undesirable as it seemed to have a strong influence on the breaking of the main crest, and combinations of parameters which caused this

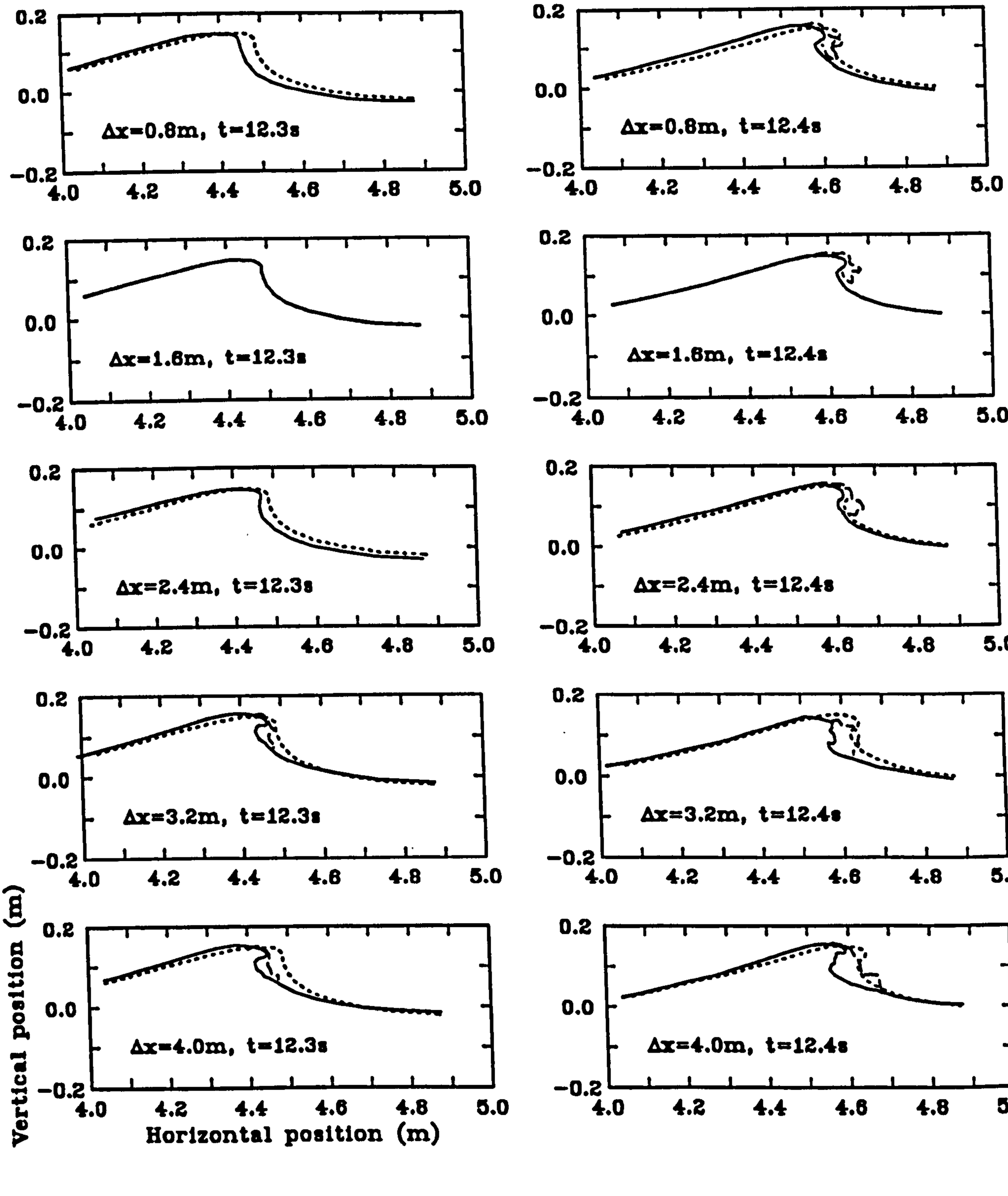

Figure 4.10: Sensitivity of the breaking wave form to the position of the wavegauge relative to the breaking. — surface profile, – – extent of splash, - - - profile for central parameters

effect were avoided.

The sensitivity of the breaking wave form to the distance, Δx, between the wavegauge and the expected breaking position is shown in a series of graphs in figure 4.10. Each row contains two graphs with measurement times 12.3s and 12.4s respectively, with the same Δx. The central case is plotted in the second row down, and it can be seen from the rows above and below that the effect of modest changes in Δx is not great. There is a tendency for the wave to be further advanced in its breaking as Δx is increased. However, in order to avoid breaking of the penultimate crest, the upper frequency limit of the wave generating spectrum had to be lowered. This, together with practical difficulties associated with the limited length of the flume, mitigated against the selection of larger values of Δx.

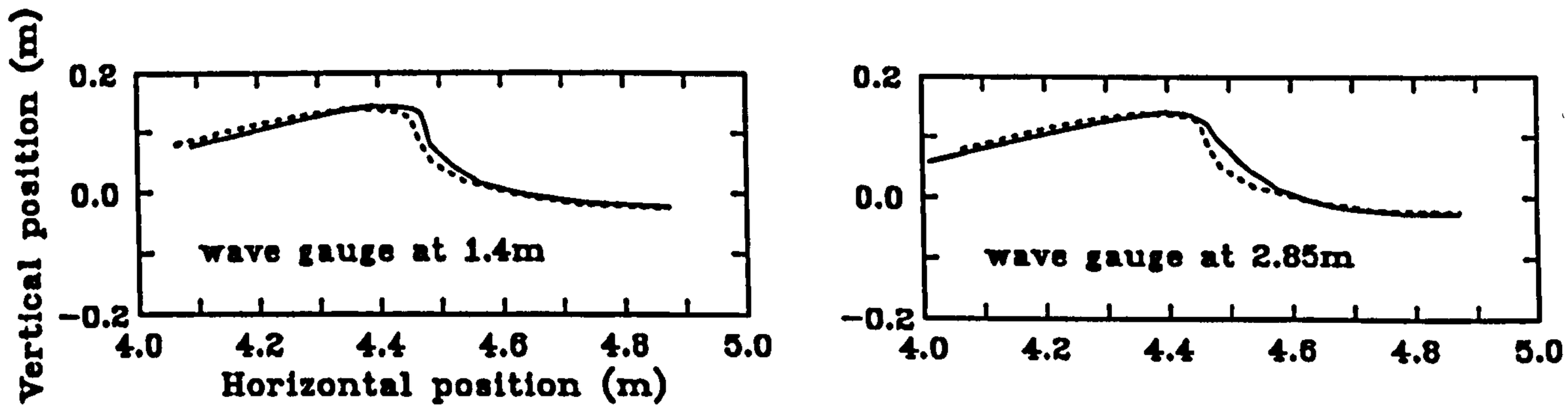

Figure 4.11: Sensitivity of the breaking wave form to position of the wavegauge relative to the wavemaker. — surface profile, – – extent of splash, - - - profile for central parameters

The sensitivity of the breaking wave form to position of the wavegauge relative to the wavemaker is shown in figure 4.11. The form is quite insensitive to this parameter, and the actual choice of its value is safely chosen from other tank considerations. The measurement time in these, and subsequent graphs, was 12.3s.

In figure 4.12 the sensitivity of the breaking wave form to the top frequency limit of the wavemaker spectrum is shown. The form is quite sensitive to this limit, and the value selected was the highest possible to avoid early breaking of the wave.

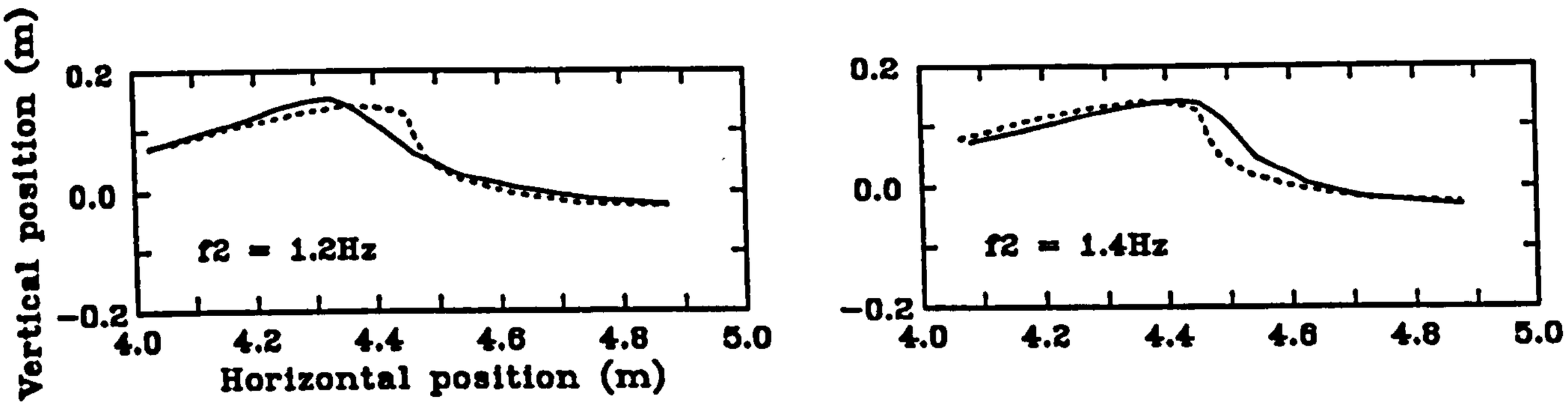

Figure 4.12: Sensitivity of the breaking wave form to the top frequency limit of the wavemaker spectrum. — surface profile, – – extent of splash, - - - profile for central parameters

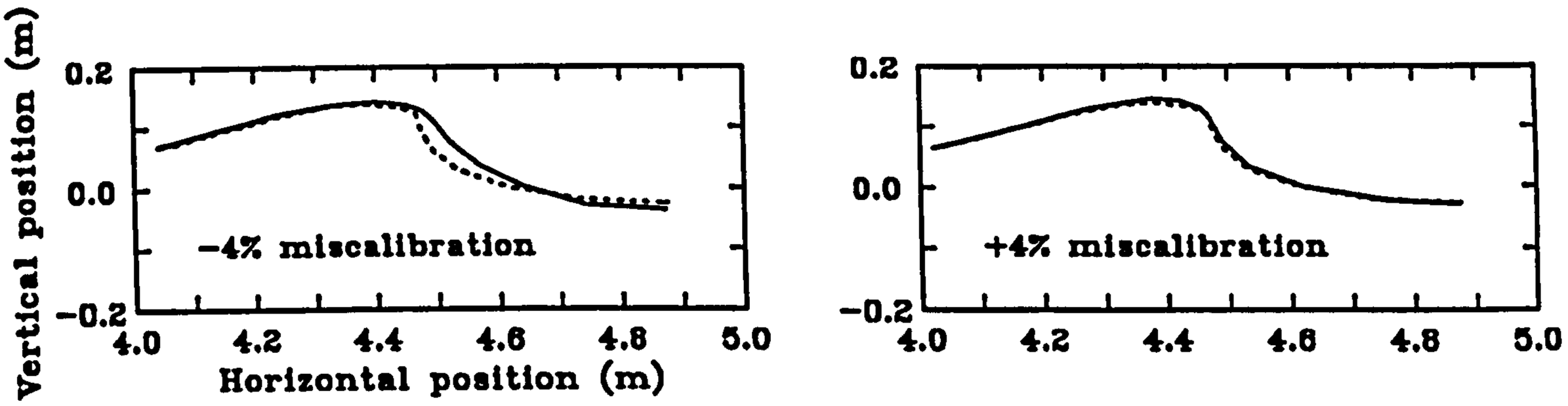

Figure 4.13: Sensitivity of the breaking wave form to the calibration value of the wavegauge. — surface profile, – – extent of splash, - - - profile for central parameters

The process of reproducing the wave in the flume is very dependent on measurements made with the wave gauge. Therefore, the sensitivity of the breaking wave form to the calibration value of this instrument was measured, and is shown in figure 4.13. 4% variations in the calibration value were considered, and the change on the breaker's form was found to be surprisingly small.

The sensitivity of the breaking wave form to the number of iterations involved in its replication is shown in figure 4.14. The form after every iteration is quite close to that finally obtained, and even the starting case (iteration 0) is surprisingly similar.

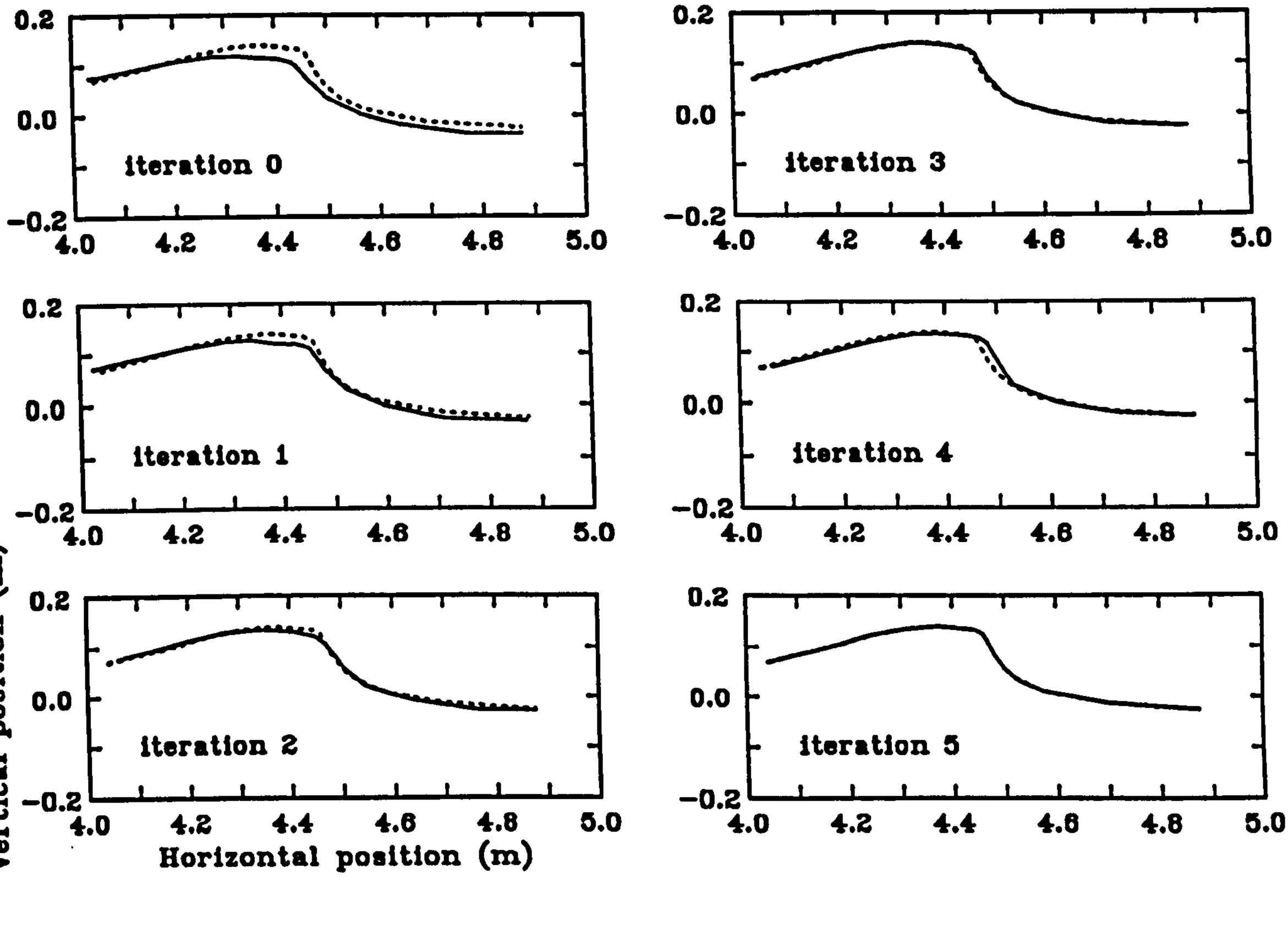

Figure 4.14: Sensitivity of the breaking wave form to the number of iterations in its replication. — surface profile, – – extent of splash, - - - profile for central parameters

In summary, of all the parameters considered, the effect of changing the top frequency limit of the generating spectrum seemed to have the biggest effect on the breaking wave's form, although, of course, it is not possible to equate relative changes of the different parameters. It may be that, given the instability of the penultimate wave crest, it is not possible to exactly replicate the numerical wave, and that the only way to proceed towards the goal of a *perfect* match would be to consider a different numerical wave.

4.4 Experimental Measurements

In a series of experiments, the wavefield obtained in section 4.3.2 was regenerated in the flume and PIV measurements made of the internal kinematics at various stages of the wave's evolution.

4.4.1 Experimental Preparations

The main parameter in the recording of the breaking sequence is the time at which to make each measurement. The breaking event is over within about a second, so a set of times was selected, separated by 1/40s, from 12.000s to 13.000s. The times for later measurements were chosen to be at gradually increasing intervals until several seconds after the breaking. The set of measuring times evolved over a few runs of the entire experiment, and a few extra times were also included in order to be able to assess the short and medium term repeatability of the process.

The wave flume was configured in the same way as for the original replication of the wave, illustrated previously in figure 4.5, except that the wave gauges were not always present.

PIV Acquisition Parameters

Given the set of measurement times, the best set of parameters for the PIV photography were arrived upon in the manner generally described in section 3.4.2. The procedures particular to this study and the specific parameters used are covered below.

For main portion of the tests a long focal length lens was used on the Hasselblad, and the camera was mounted on a trolley which runs on a parallel water tank. The convenience of this mounting was that it allowed very easy movement of

the camera to each of the twenty one different mounting positions used in the sequence. Different vertical positions were accommodated by a slide present on the trolley. In subsequent tests, where greater detail of the waves was desired, the camera was mounted on a tripod, and a shorter lens with closer focus was used.

The best horizontal and vertical positions for the camera were found iteratively for each time of measurement. The first set of positions was chosen with a knowledge of the progression of the numerical wave combined with observation of the wave in the flume. Measurements at these positions then enabled modifications to be made, if needed. Similarly the illumination interval was arrived upon by initially estimating the maximum velocity present at each stage from the data available numerically combined with estimates after the breaking. Again a test film revealed the change needed.

The rest of the PIV parameters were selected in the standard way, and all the parameters used in the main portion of these experiments are summarised in table 4.2.

After good PIV records had been obtained for the tests whose parameters are summarised in table 4.2, some of the test conditions were revisited with a higher magnification in order to obtain more detail of the flows. With a knowledge of the parameters which had given good results in the main set, the PIV parameters were reset accordingly. The magnifications selected and the stages of the breaking wave's evolution which they covered are summarised in table 4.3. In experiment (e) the camera was moving in order to obtain a shifting velocity.

4.4.2 PIV Acquisition Experiments

Structure of the Automated Experiment

In the experimental program, a sequence of tests was to be performed consisting of reruns of the breaking wave each with a given trigger time, camera position,

PIV parameter	Setting
Camera	Hasselblad 500 *EL/M*
Lens	150mm
Magnification	18.05:1
Horizontal position	4.10m - 5.90m
Vertical position	0.00m - 0.14m
Trigger time	12.000s - 19.000s
Illumination interval	7.860ms - 1.785ms
Shutter time	1/30s - 1/125s
Aperture	$f4$
Laser power	10W - 12W
Film speed	$400ASA$

Table 4.2: PIV acquisition parameters used in the primary breaking wave experiment (a)

Experiment	Film numbers	Coverage description	Coverage times (s)	Magnification (measurement zone)	Magnification (reference plane)
(a)	94 - 99	Full evolution	12.000-19.000	18.05	16.98
(b)	100 - 103	Breaking	12.300-12.950	9.754	7.86
(c)	104 - 105	Plunging	12.300-12.450	6.144	4.20
(d)	106	Post-breaking	13.400-18.000	9.426	8.457
(e)	107 - 108	Post-breaking	13.200-40.000	18.05	16.98

Table 4.3: Magnifications used for the different stages of the breaking wave's evolution

illumination interval and shutter speed. The trigger time was set by the controlling computer, taking account of the inherent delay and half the shutter speed, and the other parameters set from the computer via instructions to the experimenter. Between each run of the wave, first the seeding near the surface was disturbed by

a high frequency wave programmed into the sequence, then a settling time of 120s was allowed to pass. Provision was made for the sequence to be interrupted, in case some manual intervention was required.

Automated Experiment Run

Before each experimental run started, the wave flume was heavily seeded and extra seeding was added as necessary during halts in the automated sequence. Each experiment took up to several hours to perform, and the laser required regular attention to maintain the required power level. A couple of failures of the camera to wind on correctly meant that the collected records were not exactly the set intended.

4.5 Analysis of the Photographs

The photographic records of the flow collected in the described experiments each contain a great amount of information. Along with the multiple particle images required to discover the internal kinematics with the PIV technique, the water surface is generally readily detected where it intersects the laser sheet. Spray and bubbles tend to be overexposed, but, nevertheless, some qualitative information can be extracted in these regions.

A typical photograph of the breaking wave at a particular phase of its evolution is reproduced in plate 1. Particle images can be clearly seen, and the surface is well defined in most regions.

4.5.1 Determining the Surface Profiles

From each photograph the surface profiles were measured using the procedure described in section 3.5.2. In the areas where the surface was well defined, the central exposure of the surface was traced. Where the surface was found to be indistinct, perhaps due to early breaking at the near wall, an estimate of the obscured surface was made, so long as this portion was quite small. When the wave breaking was well established, the boundary between the clear and aerated water was traced, along with the boundary between the spray and the air.

Inevitably there is some bias in the surface measurements due to the subjective nature of the judgments made of the boundaries between indistinct fluid regions. In addition, because the measurement zone, defined by the plane of the illuminating light sheet, is a further away than the glass wall, the true fluid boundaries in the measurement plane are obscured by events in the foreground in some places. These effects were minimised by careful choice of viewing angle of the camera, and by the use of a long focal length lens, flattening the perspective. However, all the boundaries with aerated water should be regarded as approximate.

4.5.2 Extracting the Internal Kinematics

The internal kinematics were extracted from each photograph using the standard procedures described in section 3.5.1. It was considered particularly important that the resulting vector field should be correctly positioned relative to the measured surfaces, and the absolute coordinates of the tank. This was achieved by ensuring accurate location of the registration marks, present on the glass wall, before each photographic analysis. If the camera's field of view was centred on one of these marks, then the coordinates of the mark in the measurement plane are the same. Otherwise, the position in the measurement plane is calculated with a knowledge of the camera's coordinates, the registration marks' coordinates, and the magnifications of the measurement and reference planes.

Each extracted velocity field was filtered to eliminated invalid and spurious velocity vectors. This process consisted primarily of eliminating vectors with a poor signal-to-noise ratio, along with those outside the fluid boundaries. A small number of spurious vectors remained which were identified due to their inconsistency with their neighbours, and removed manually.

4.6 Experimental Results

In this section the experimental results are presented in a raw form, that is, with no further processing other than the analysis of the photographs already described. The results are shown by each of four presentation methods, in turn. First the surface profiles are plotted to give an overview of the breaking wave's evolution, to establish the comparison with the numerical model and to provide a context for later results. Next, a few photographs of different phases of the wave are reproduced to reveal qualitatively the internal flows, especially for the post-breaking phase, where the quantitative results were poor. The velocity fields obtained with PIV are then plotted in vector form. Finally, a number of methods of graphing the velocity components of the data are illustrated.

For each presentation method, results are first presented for the main experimental sequence (a) (this is the case for all figures unless otherwise stated). Further data is then shown from the subsequent experiments with increased magnification. Where appropriate, the experimental results are compared to the numerical predictions. Repeatability of the wave properties is assessed.

4.6.1 Measured Surface Profiles

The surface profiles obtained from the photographs are shown in figures 4.15 to 4.18, for the main experimental sequence (a). The figures cover one second of the wave's evolution, at 1/40s intervals, and the time of the measurements is noted

in each plot. The frame around the graphs is moving at $1.57 ms^{-1}$, determined empirically, in order that the wave crest should be near the centre of each plot.

In each of the graphs, the solid lines represent the interface between water which is not aerated and the air, or water which contains air. The dashed lines roughly indicates the boundary between area of spray and the air. The smooth progression of these surface profiles is a good indication of the repeatability of the measurements, given that each corresponds to a separate run of the wave.

The sequence of surface profiles shown in figures 4.15 to 4.18 are similar in form to those reported elsewhere, for example by Tallent [63] in a study of depth-induced breaking. In contrast to that work, the present study concentrated on measuring the internal kinematics rather than trying to trace the motions of the plunging tip and spray after impact.

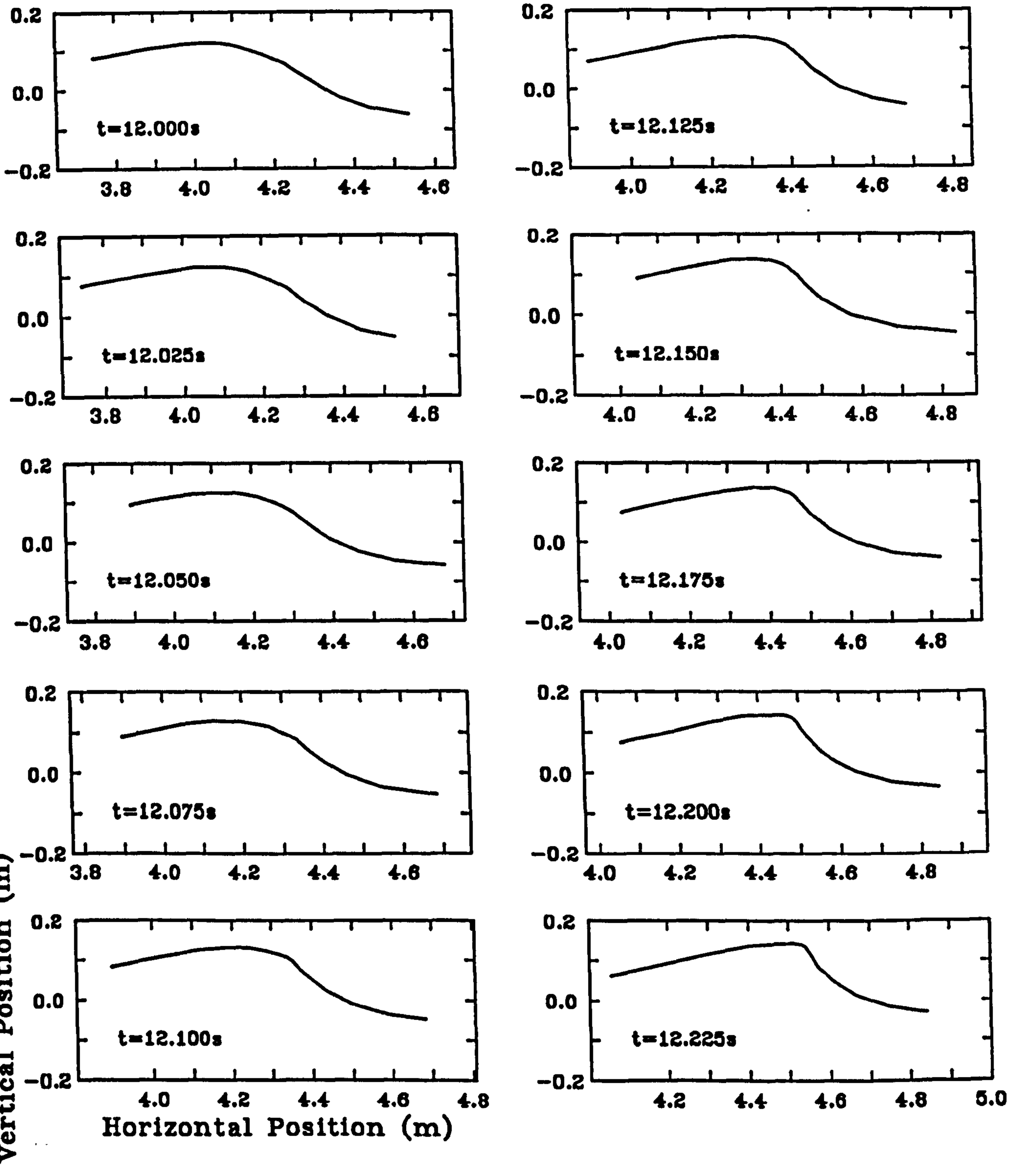

Figure 4.15: Breaking wave surface profiles, $t = 12.000$s to 12.225s

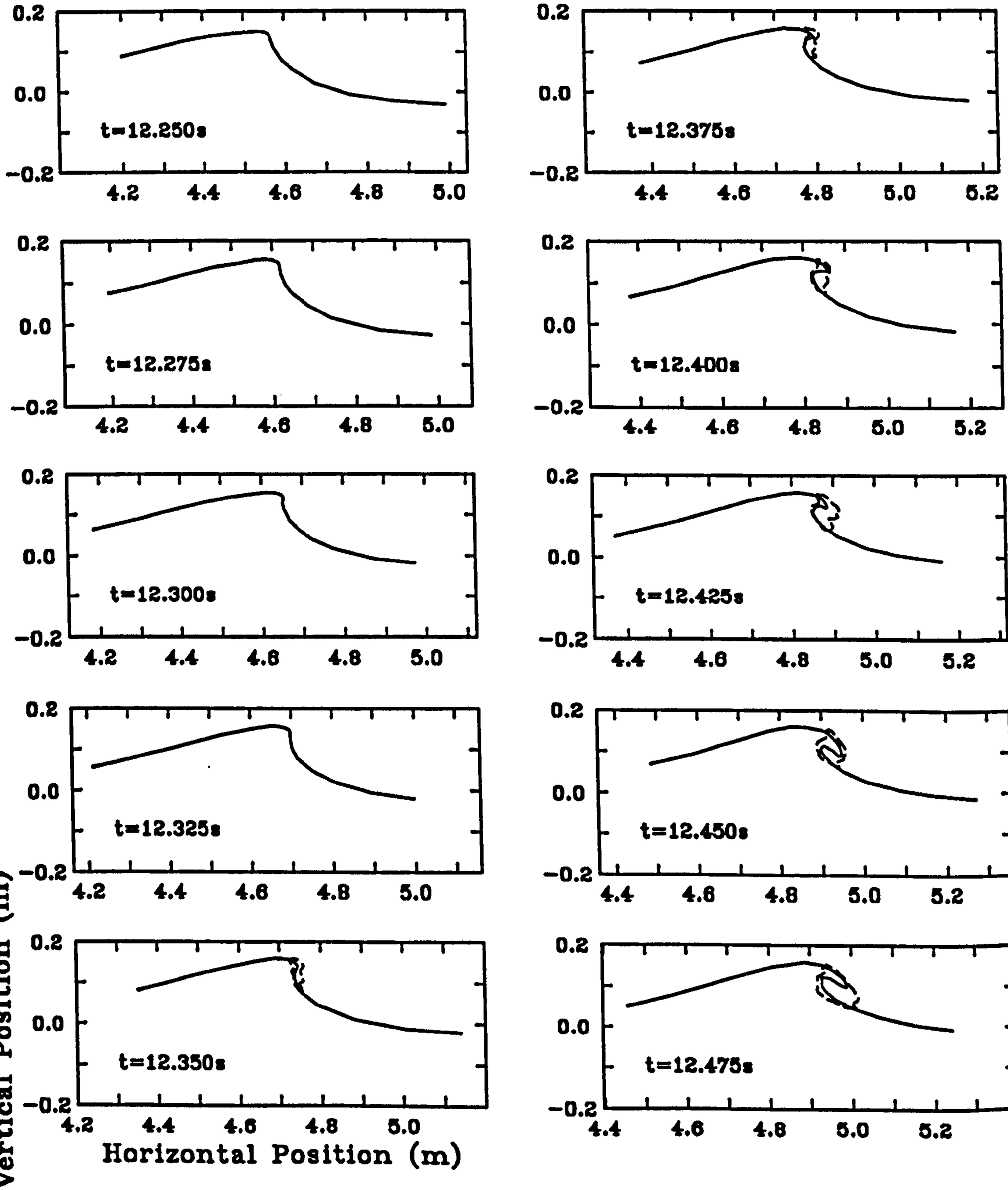

Figure 4.16: Breaking wave surface profiles, $t = 12.250$s to 12.475s

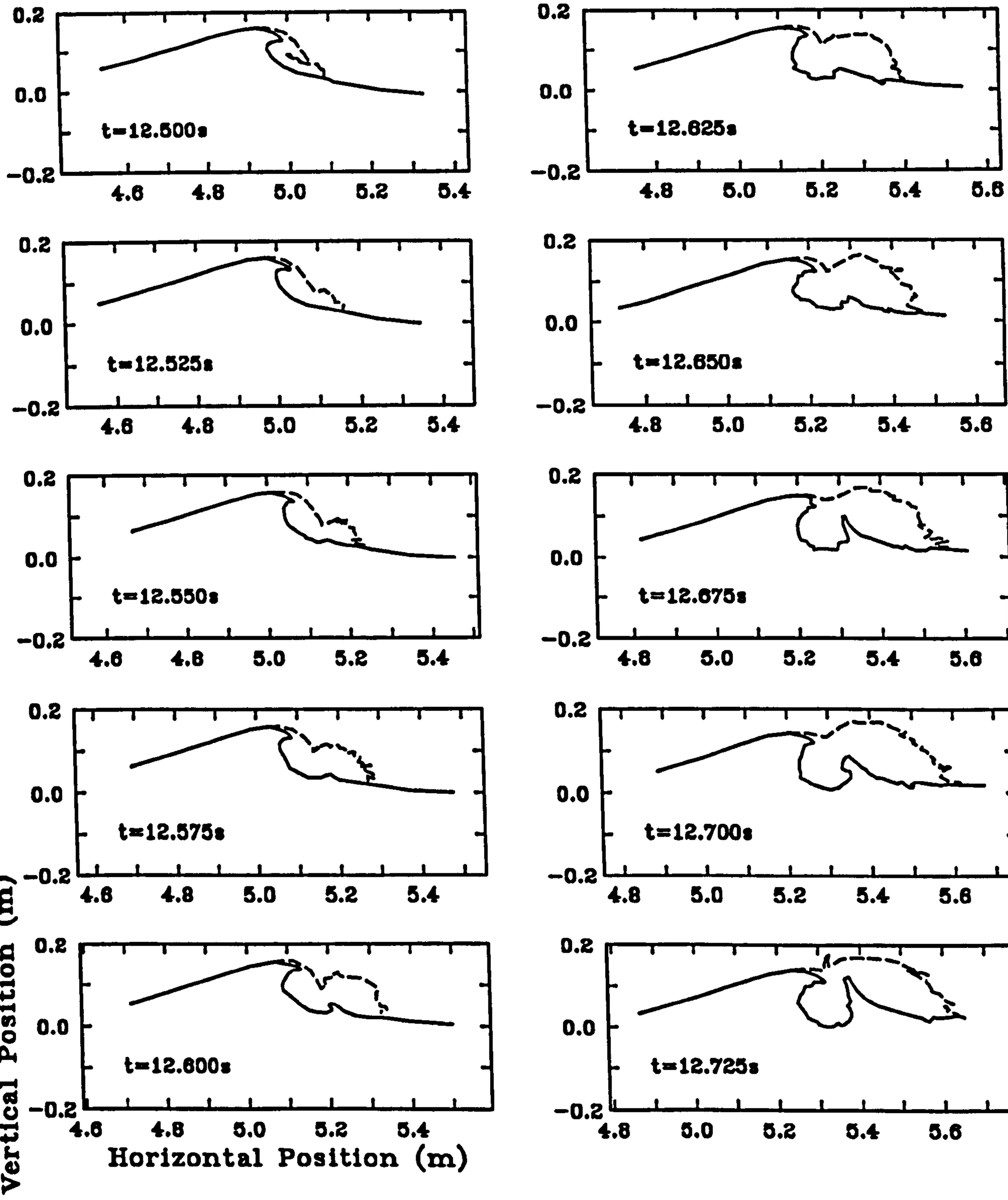

Figure 4.17: Breaking wave surface profiles, $t = 12.500$s to 12.725s

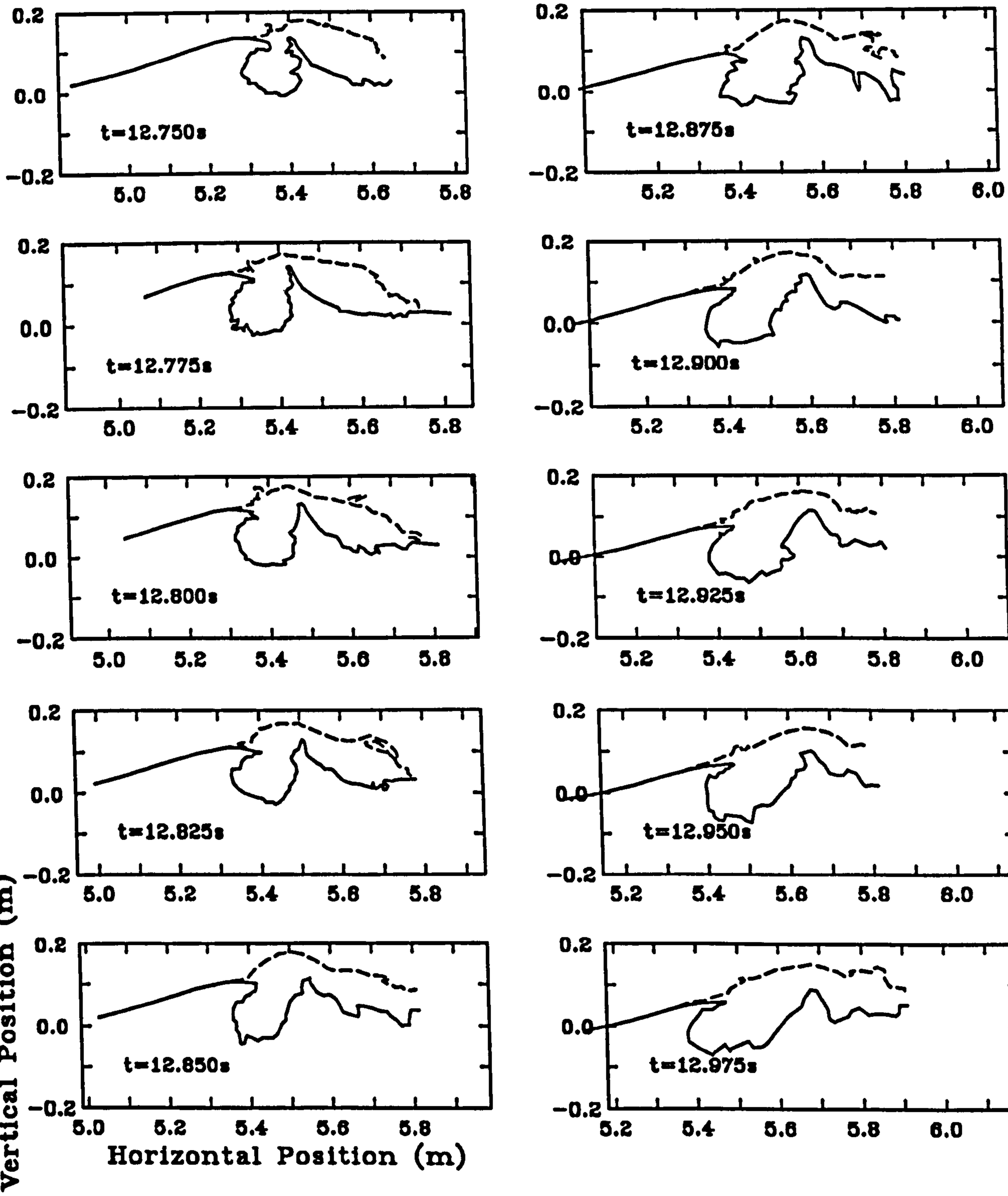

Figure 4.18: Breaking wave surface profiles, $t = 12.750$s to 12.975s

Comparison of Experimental and Numerical Surface Profiles

In order to show the progression of the wave to breaking, a sequence of the surface profiles from figures 4.15 and 4.16 are plotted in figure 4.19. Given the small increase between the times for each measurement, the assumed repeatability of the wave's generation can be seen to be very good, with the largest discrepancy from the sequence being equivalent to a time error of 1/80s or a spatial shift of about 20mm.

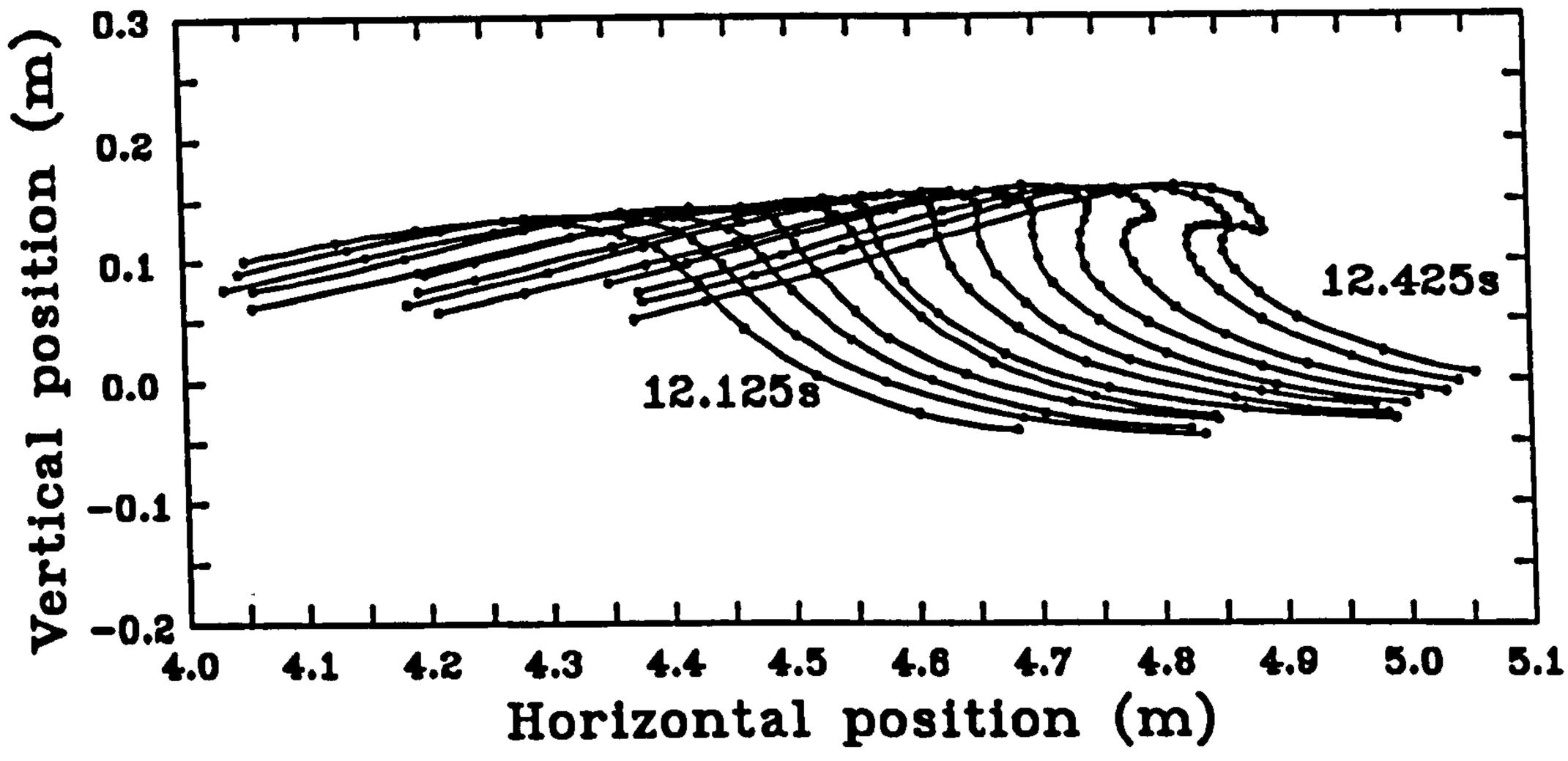

Figure 4.19: Surface profiles as the experimental wave approaches breaking

For comparison, figure 4.20 contains surface profiles from the numerical model for the final thirteen phases before breaking. It should be noted, however, in comparing figures 4.19 and 4.20 that the times of the phases in the numerical sequence are each .125s earlier than those in the experimental sequence with the same form. In addition the range of the horizontal axis has been shifted by .22m.

Figure 4.21 contains the experimental and numerical surface profiles in the same graph, without any shift of the numerical results. It can be seen that while the overall position of each phase is in close agreement with the prediction, the form of each phase is not.

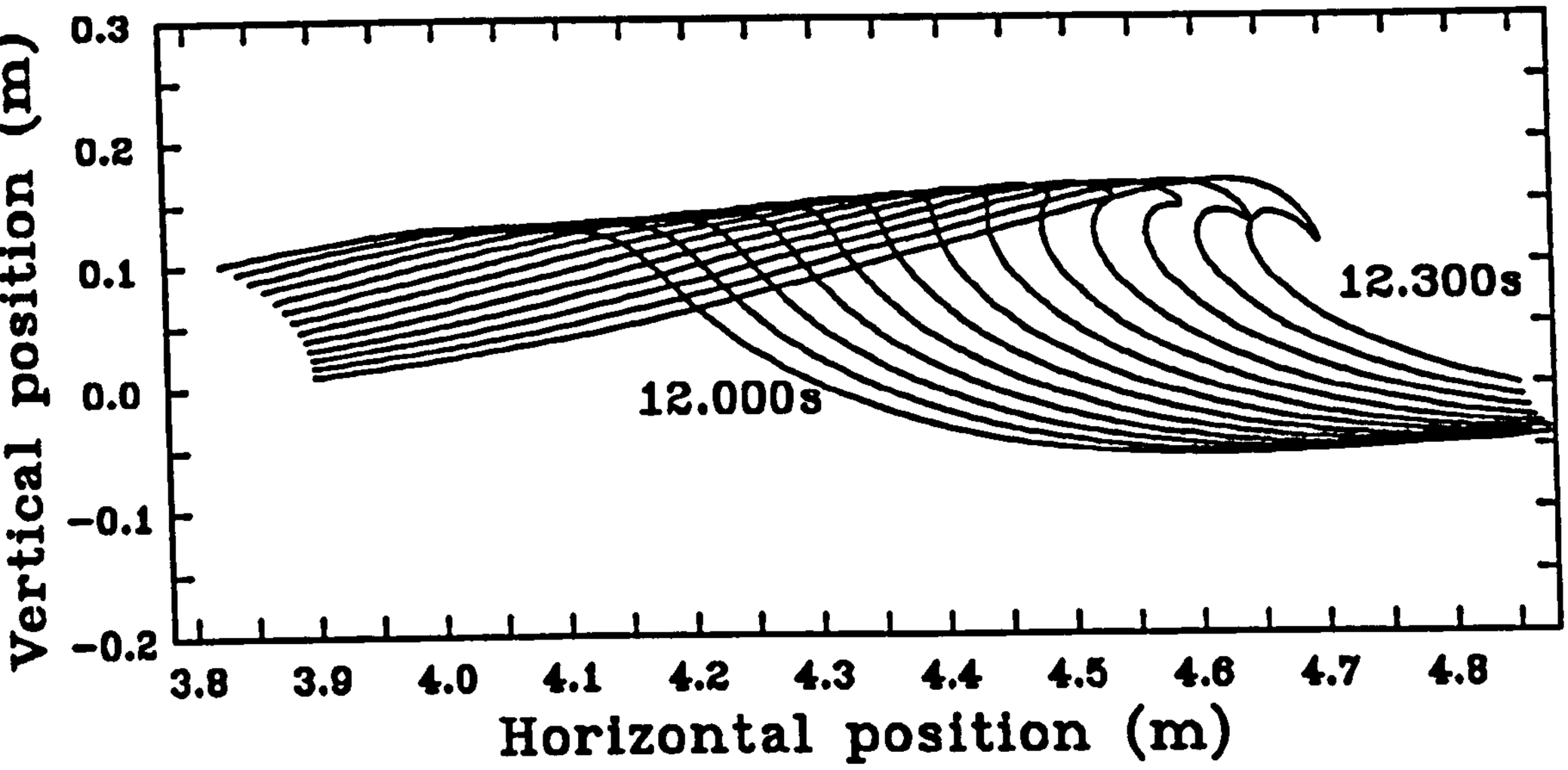

Figure 4.20: Surface profiles as the numerical wave approaches breaking

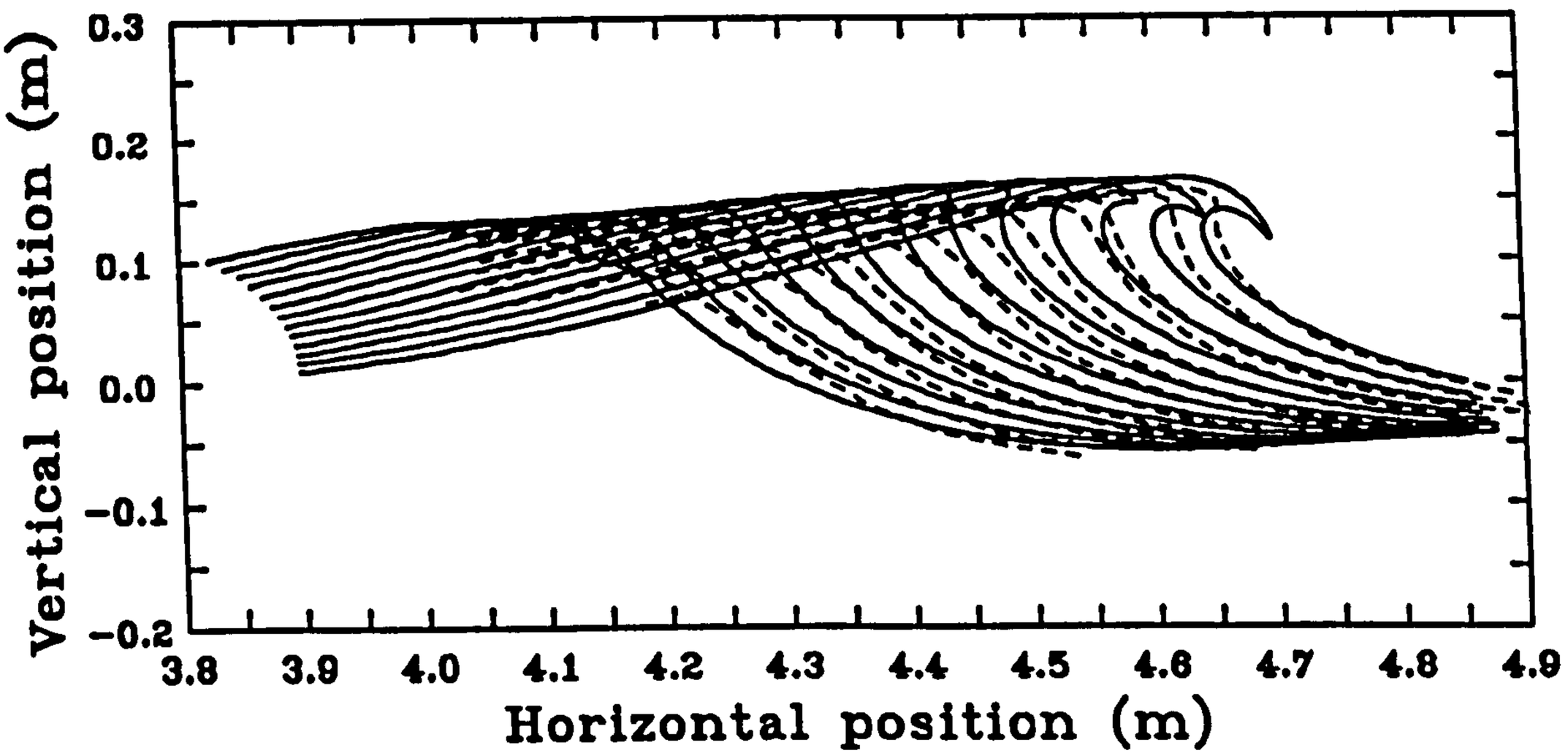

Figure 4.21: Comparison of experimental and numerical surface profiles. - - - experimental measurements. — numerical predictions

While it would be preferable to compare the internal kinematics between the experimental results with predictions at the same time and place, the difference in form of such paired phases makes this ideal approach pointless. The results from the sensitivity analysis of the breaking wave's form to the parameters used in its reproduction, described in section 4.3.3, indicate that there is some fundamental

reason why the match of the surface profiles cannot be improved.

It was decided, for the purpose of the later comparison of the internal kinematics, that the numerical sequence should be considered as being shift forward in time by .125s and forward in space by .22m. The shifted numerical surface profiles are plotted along with their corresponding experimental profiles in figure 4.22. While the method used for replicating the numerical wave in the tank failed to produce an exact match of the profiles near breaking, it did produce a short sequence of waves which had very similar form numerically and experimentally.

Reasons were sought which might explain the shift between the numerical and experimental sequences. For instance, the mean current might have been different in the numerical model from that in the flume, but calculations from the numerical data indicated that the differences were negligible compared to the wave speed. It was thought possible that differences in the long wavelength components might account for some of the discrepancy, but reference back to figure 4.7 reveals that these components were very similar in magnitude.

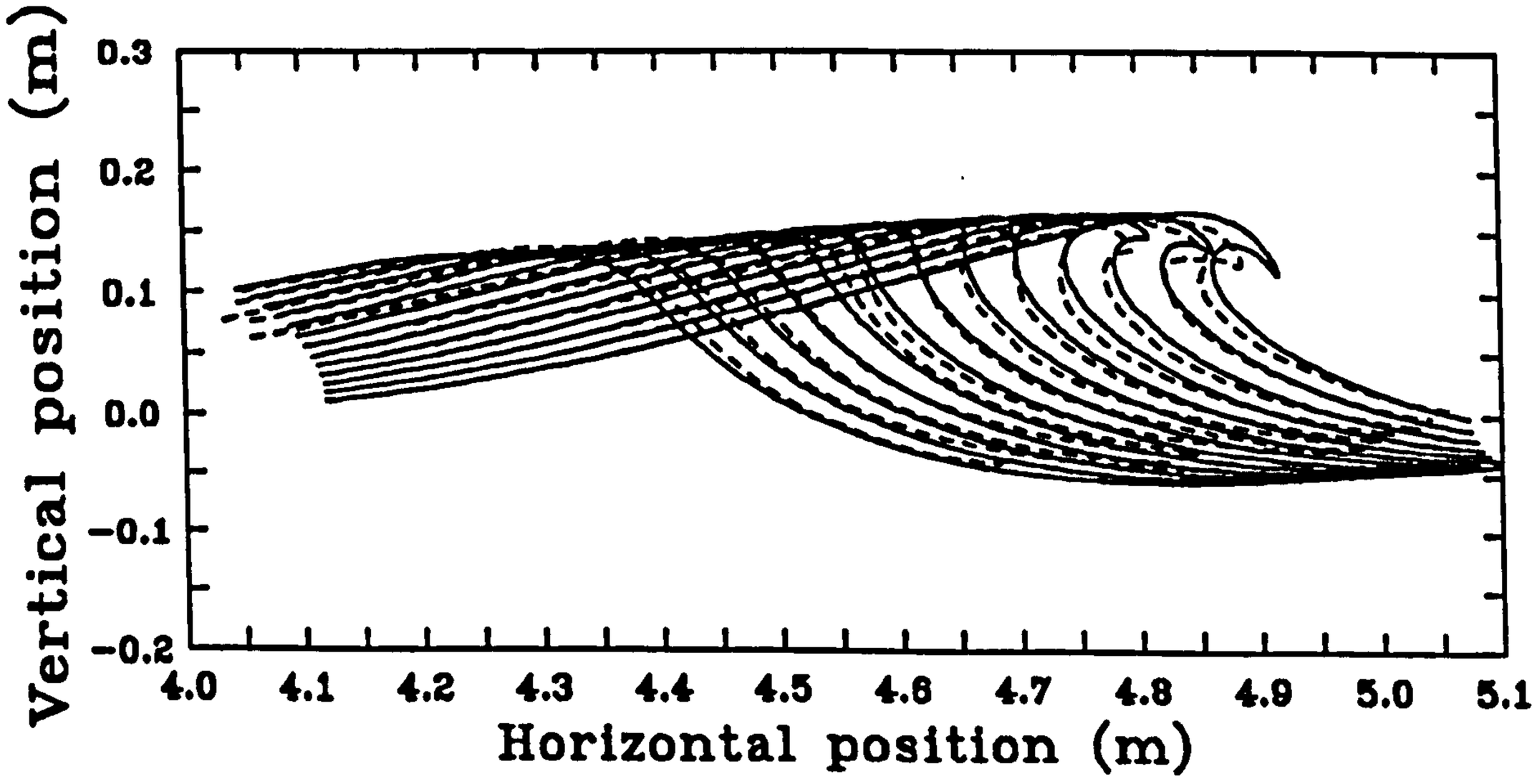

Figure 4.22: Comparison of experimental and shifted numerical surface profiles. - - - experimental measurements. — shifted numerical predictions

Surface Profile Repeatability

In order to assess the repeatability of the wave packet, figure 4.23 contains graphs of the surface profiles at various triggering times, along with repeated measurements. The solid lines and long dashes show the fluid regions of the first measurement, and the short dashes all the boundaries of the second measurement. In most of the cases, the second measurement was taken a short period after the first, except that marked *long-term* which was repeated after a few hours. In all cases the repeatability is excellent.

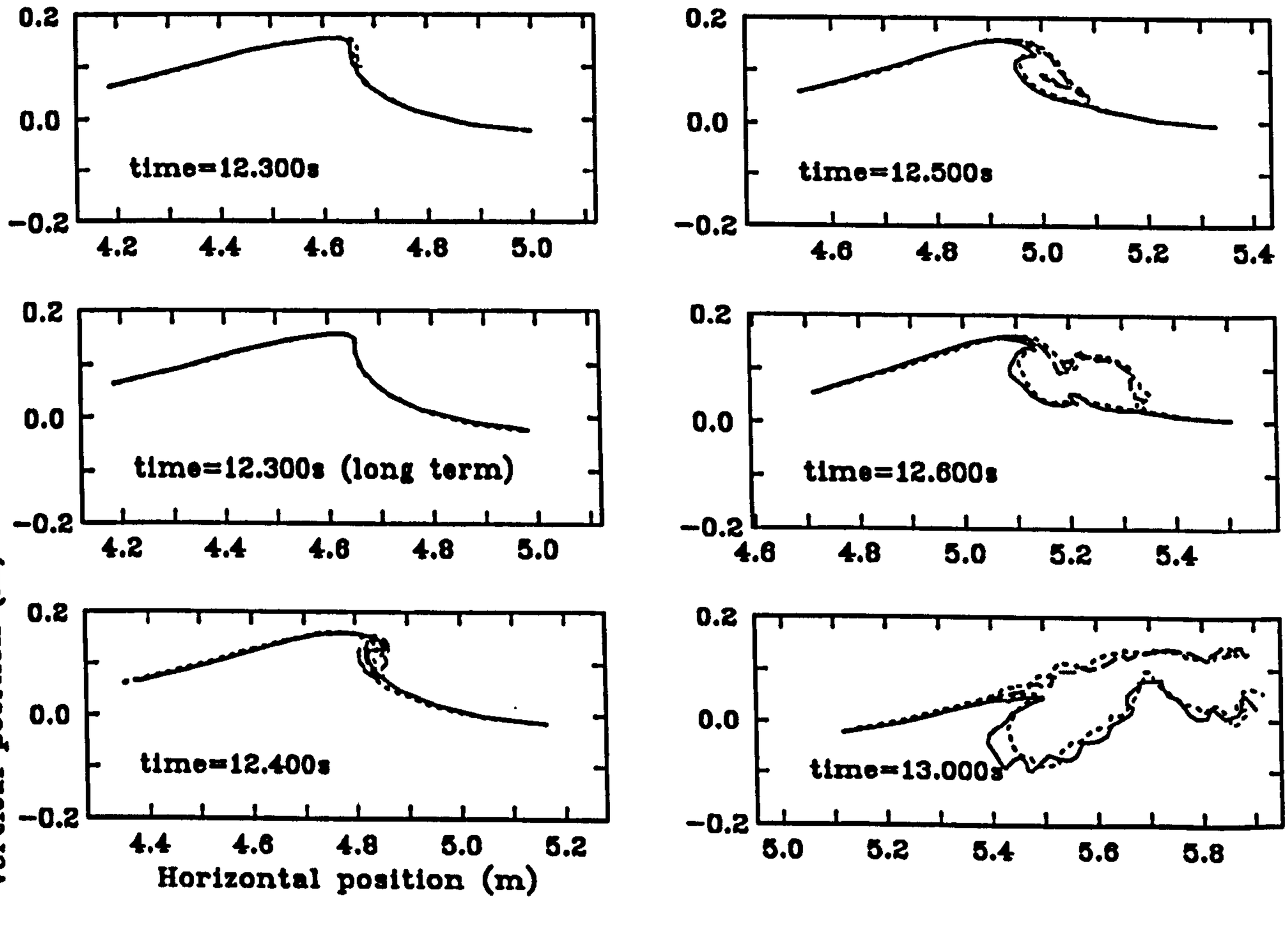

Figure 4.23: Repeatability of the surface profiles

4.6.2 Photographic Recordings of the Flow

The PIV photographs contain more information than the two quantities which are readily extractable, ie. the surface profiles and the internal kinematics. In particular, other features of the flow, such as spray and aeration, can be seen. Moreover, a good qualitative feel for the fluid motion can be gleaned, and photographs have been selected which are representative of the different phases of the wave's evolution.

The following pages contain prints of five phases of the breaking wave's evolution. The measurement times for each photograph are summarised in table 4.4. The first picture, plate 1, shows the wave when it is vertically fronted, with the water surface being readily identified.

In the plate 2, the best close-up of the plunging tip is reproduced. This picture was obtained in experiment (c) at $t = 12.400$s. Multiple particle images, about five in each row, trace out the direction and magnitude of the flow, and can be clearly seen even into the tip.

The wave during breaking, at $t = 12.7$s, is shown in plate 3. Here, the camera was carefully positioned to allow a clear view into the area where the water is being forced up by the re-entry of the jet, and good quality particle images have been recorded. The photograph also shows the spray resulting from the breaking. In fact, multiple images of some of the water droplets are visible, and velocities could be deduced: for example, the rightmost line of dots implies a velocity of about 3ms^{-1}. With a suitable exposure reduction, it might be possible to make some measurements of the motion in this region.

The next photograph, plate 4, shows the aeration present shortly after the wave has broken, at $t = 13.7$s. Some confusion is apparent in the water around the bubbles, and it was not possible to obtain velocities with the standard PIV process in this portion of the negative.

Finally, plate 5 show the fluid flow a little later, at $t = 14.5$s. The vortex produced in the breaking is clearly seen, along with a good deal of turbulence lower in the flow. While these features are qualitatively readily identified, complete velocity fields could not be extracted from the photographs. Image-shifting [2], where an offset is added to all velocities when the photographs are taken, is needed to resolve the near-zero velocities.

Plate	Description	Time (s)
1	Vertically fronted wave	12.30
2	Pluniging tip	12.40
3	Breaking wave	12.70
4	Aeration after breaking	13.70
5	Vorticity after breaking	14.50

Table 4.4: Summary of the photographs reproduced in the following pages

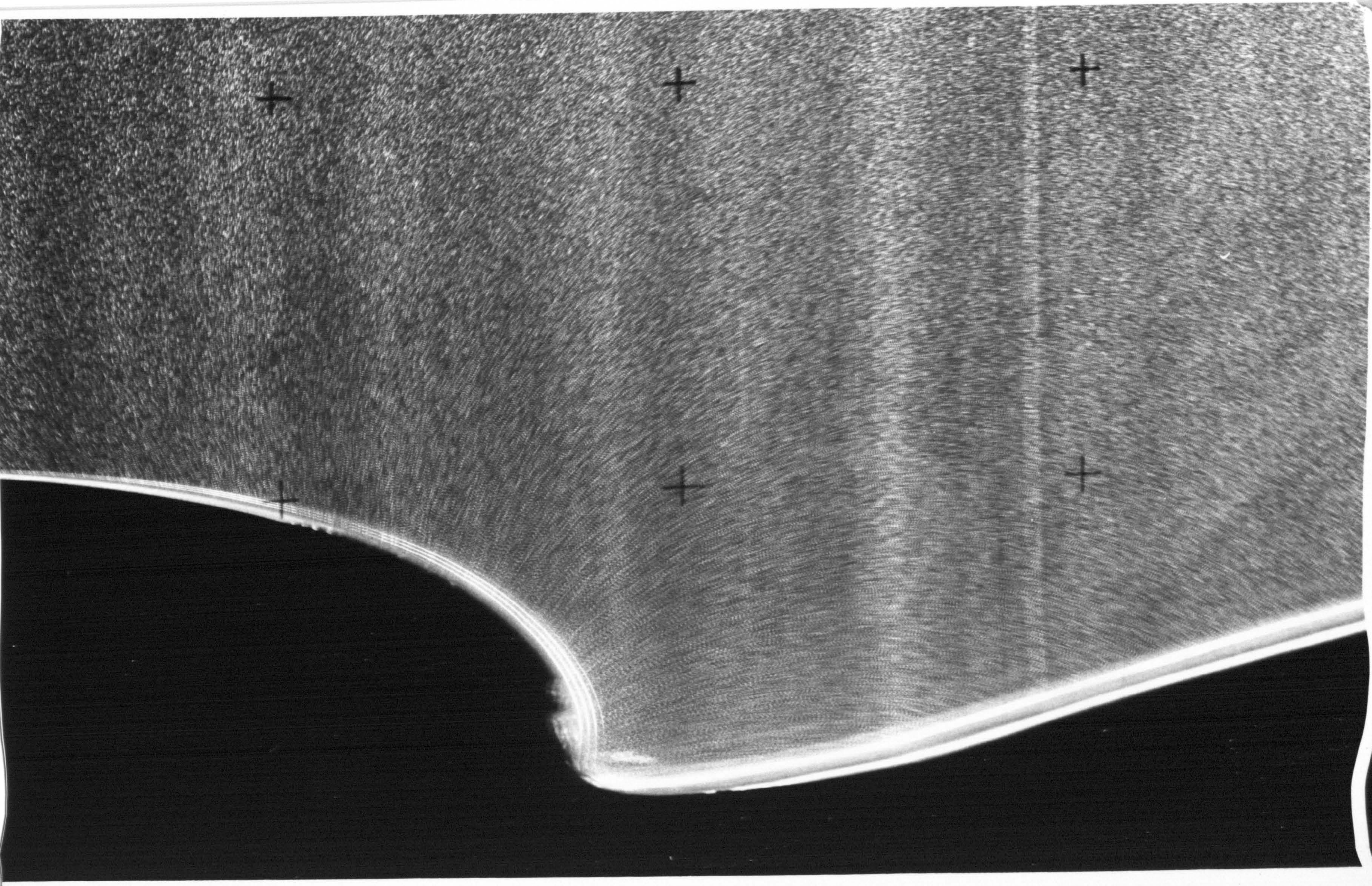

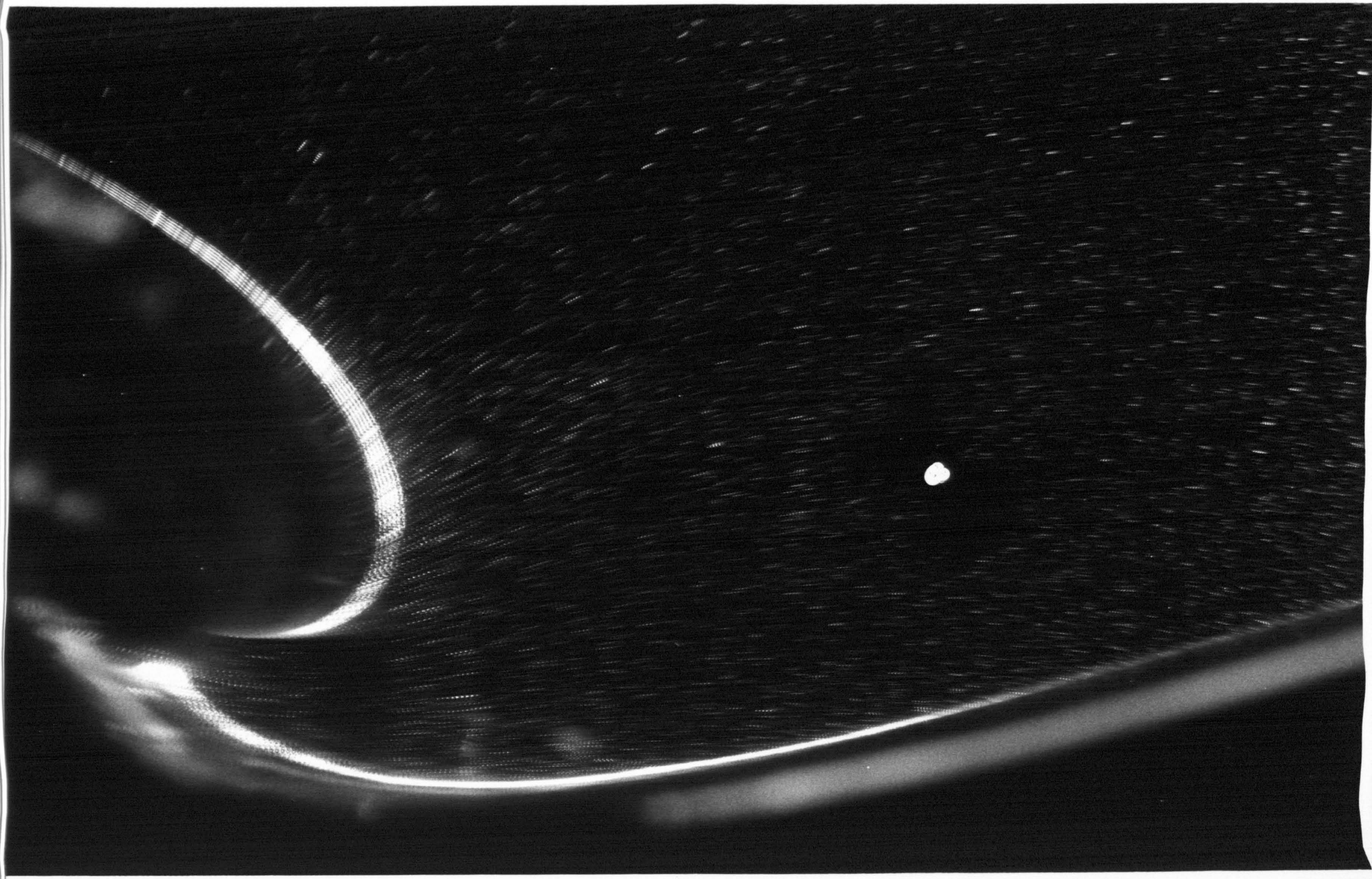

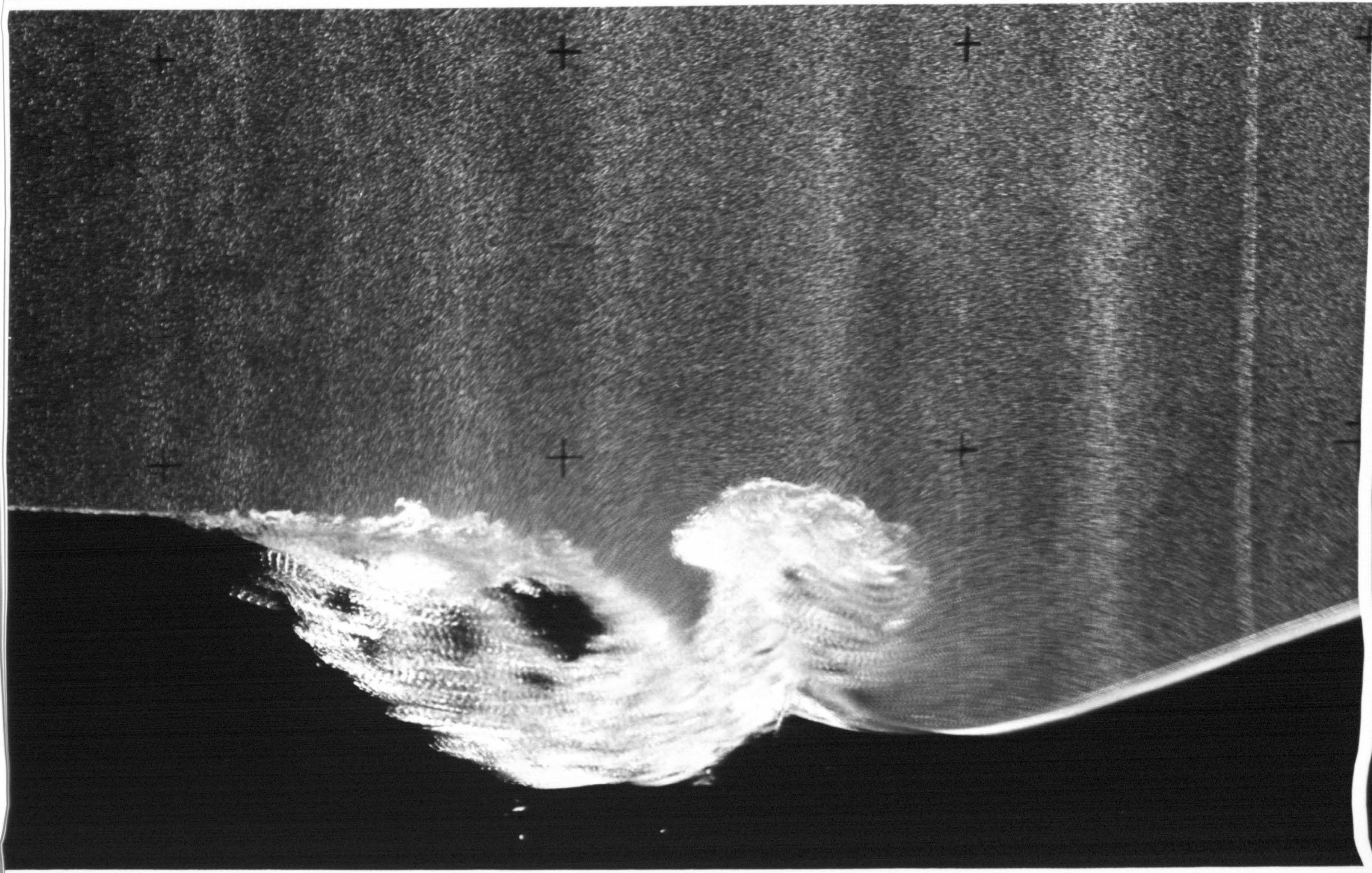

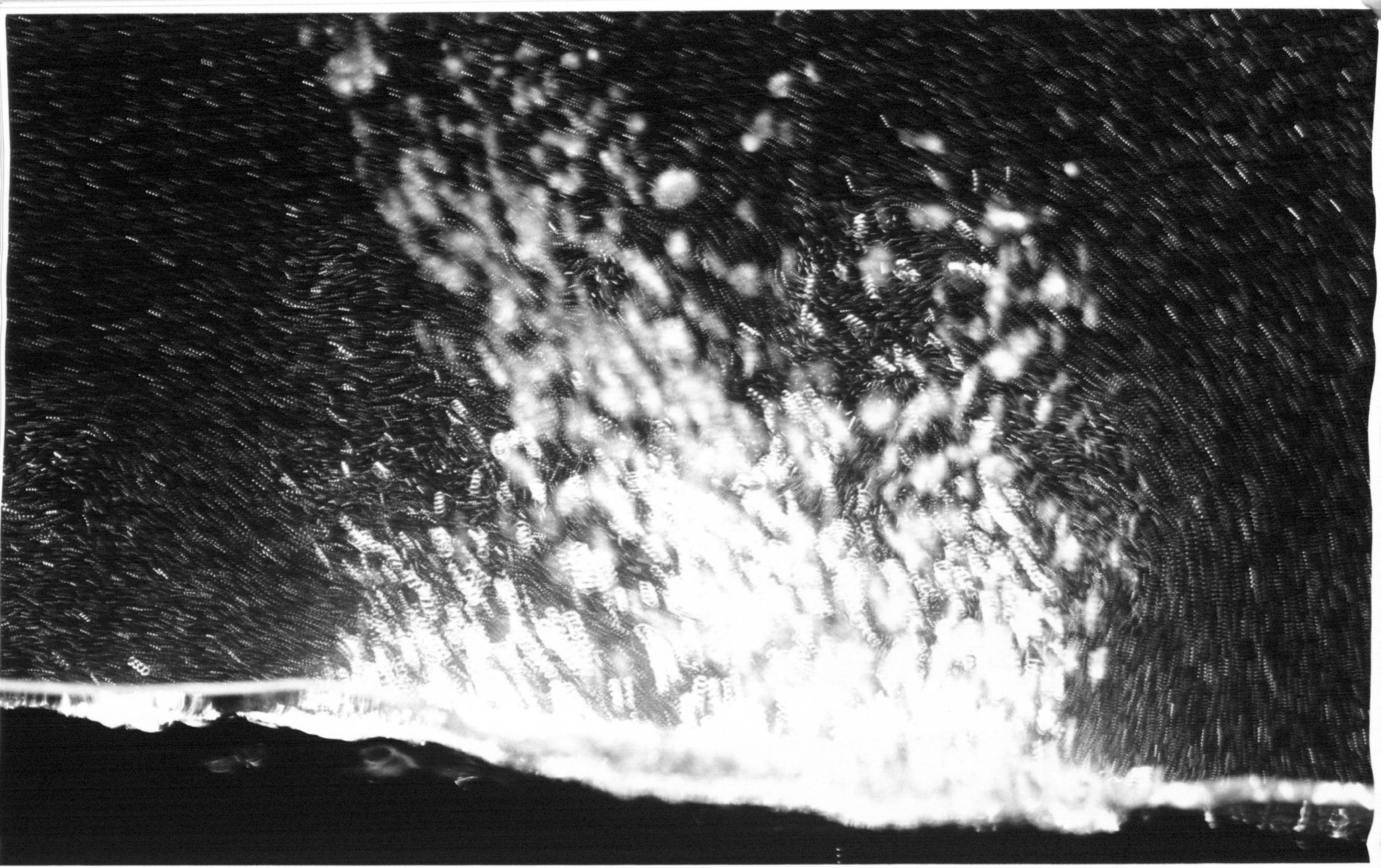

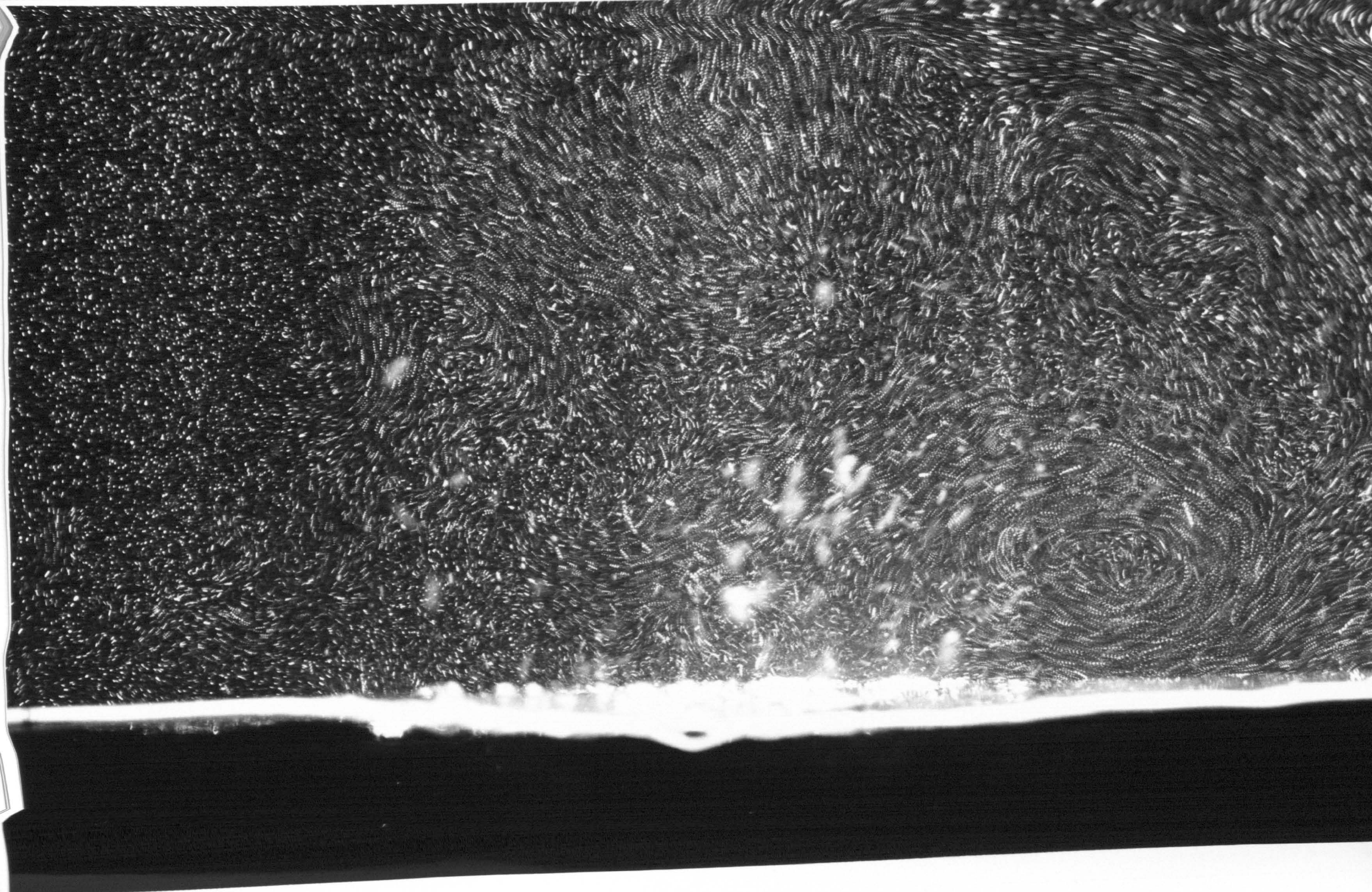

4.6.3 Internal Kinematics Obtained with PIV

Internal Kinematics from the Main Experimental Sequence

The internal flow fields obtained with PIV in experiment (a) are shown in figures 4.24 to 4.43 as a sequence of vector plots, covering about 1 second of the wave's evolution. The measurement time of each plot is separated by 1/20th second, and the surround frame for each has been moved on with a velocity of $1.57 ms^{-1}$.

It is intended that the figures should be viewed as a sequence, noting particularly the smooth progression until the wave is vertically fronted, the formation of the plunging spout in the region of highest horizontal velocity, and the velocity vectors in the area of water which is thrown up by the re-entering jet.

In the individual figures, it can be seen that measurement of velocity has been possible in almost all regions were the water is not aerated, even in the fluid forced up by the re-entering jet (figures 4.36 onwards). As before, the solid lines mark the interfaces of such regions and the dashed lines the extent of the spray.

In the places where odd vectors are missing, the reasons are straightforward. In figure 4.31, vectors were not obtained near the bottom of the area shown, because of their relatively low velocity compared with the crest. In figure 4.39 the missing vectors around $x = 5.5m$ are due to air entrainment.

Measurements have not been obtained right into the spout in figure 4.32 mainly due to the blocking of the view by breaking at the wall of the flume, combined with the low light level which can be expected in the spout if the beam has to travel through the water surface. Near fluid boundaries more missing vectors are likely due to scattered light from the interface resulting in lower contrast of the particle images.

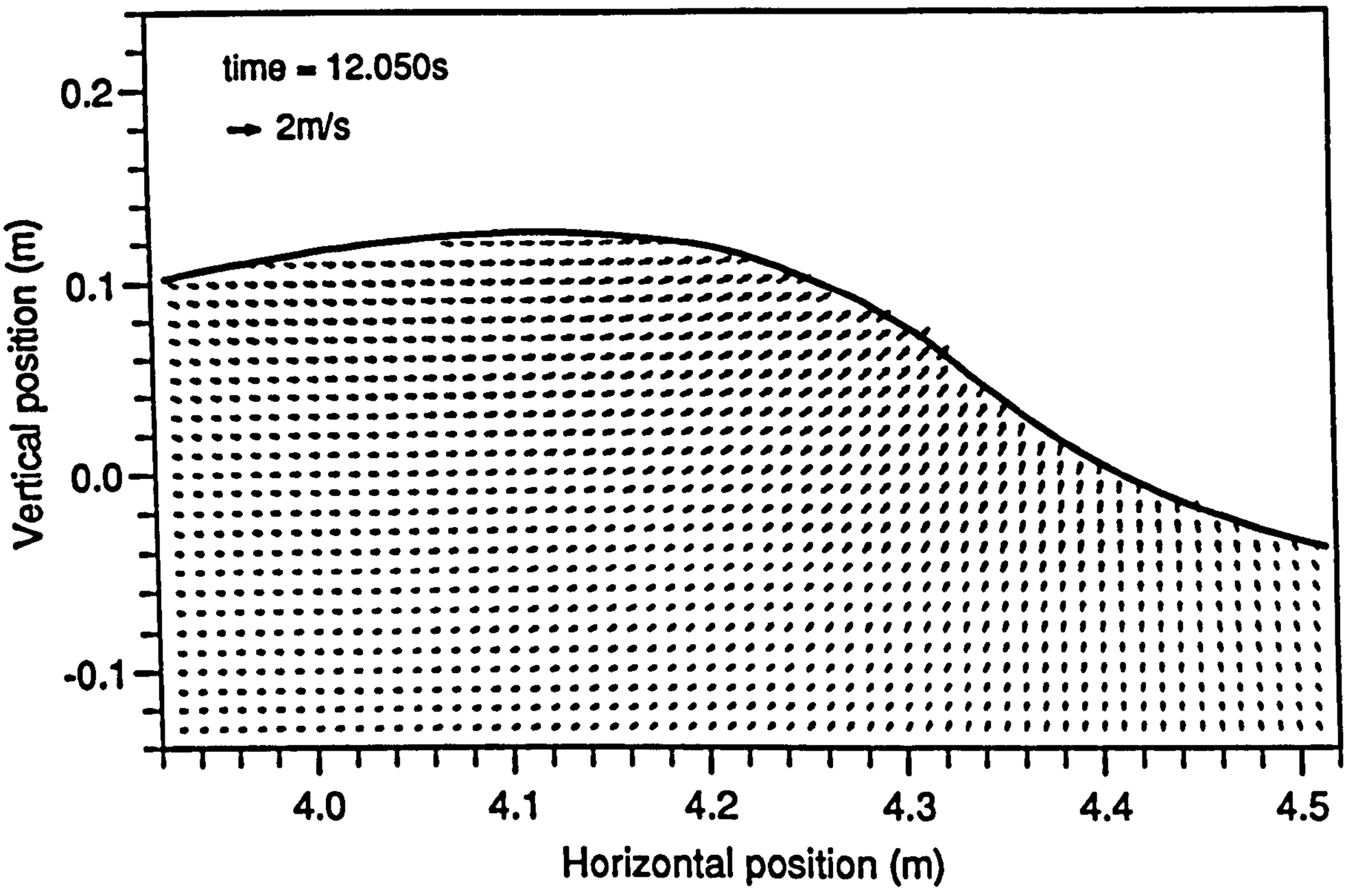

Figure 4.24: Experimentally measured velocity field, $t = 12.050$s

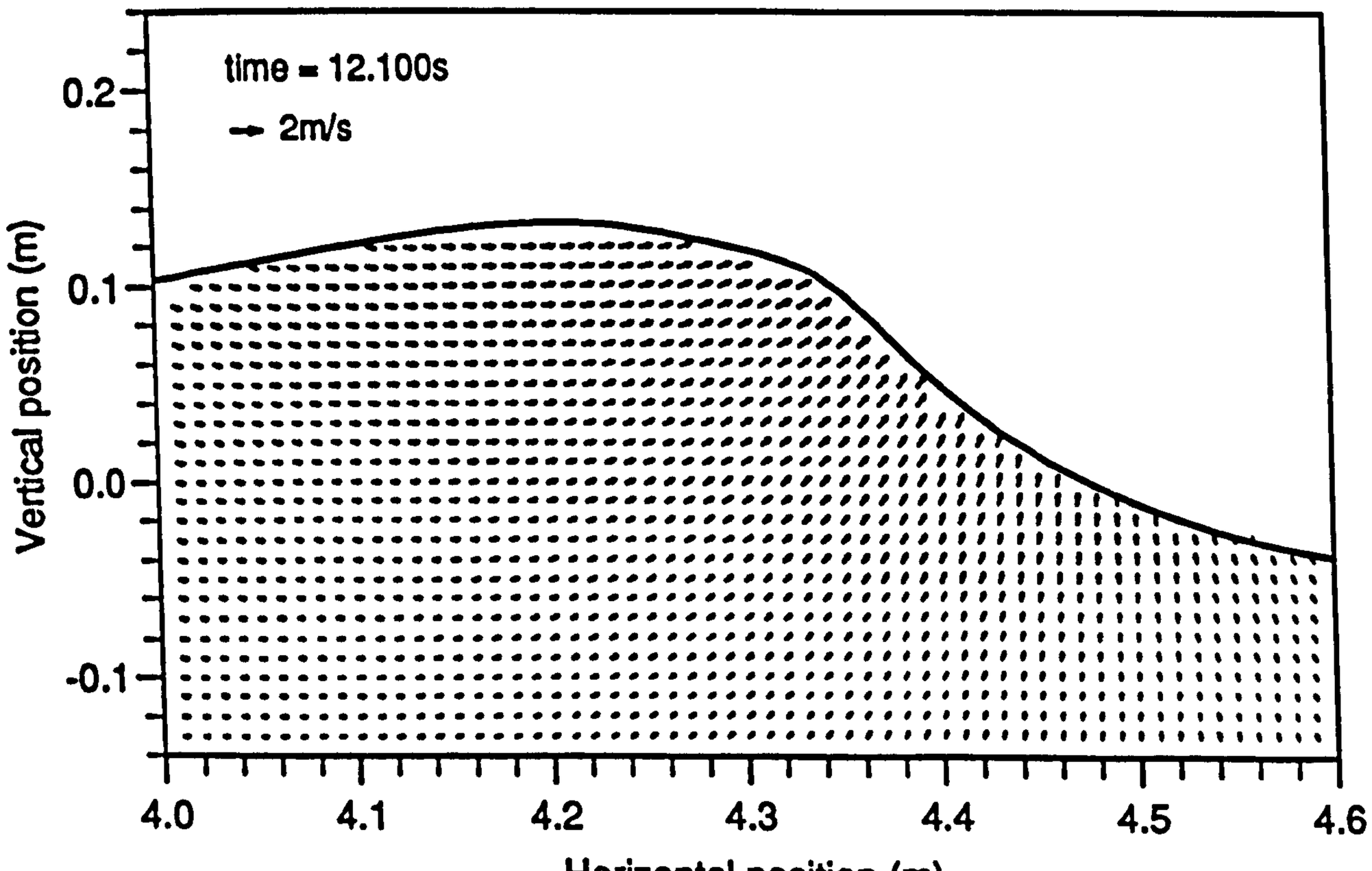

Figure 4.25: Experimentally measured velocity field, $t = 12.100$s

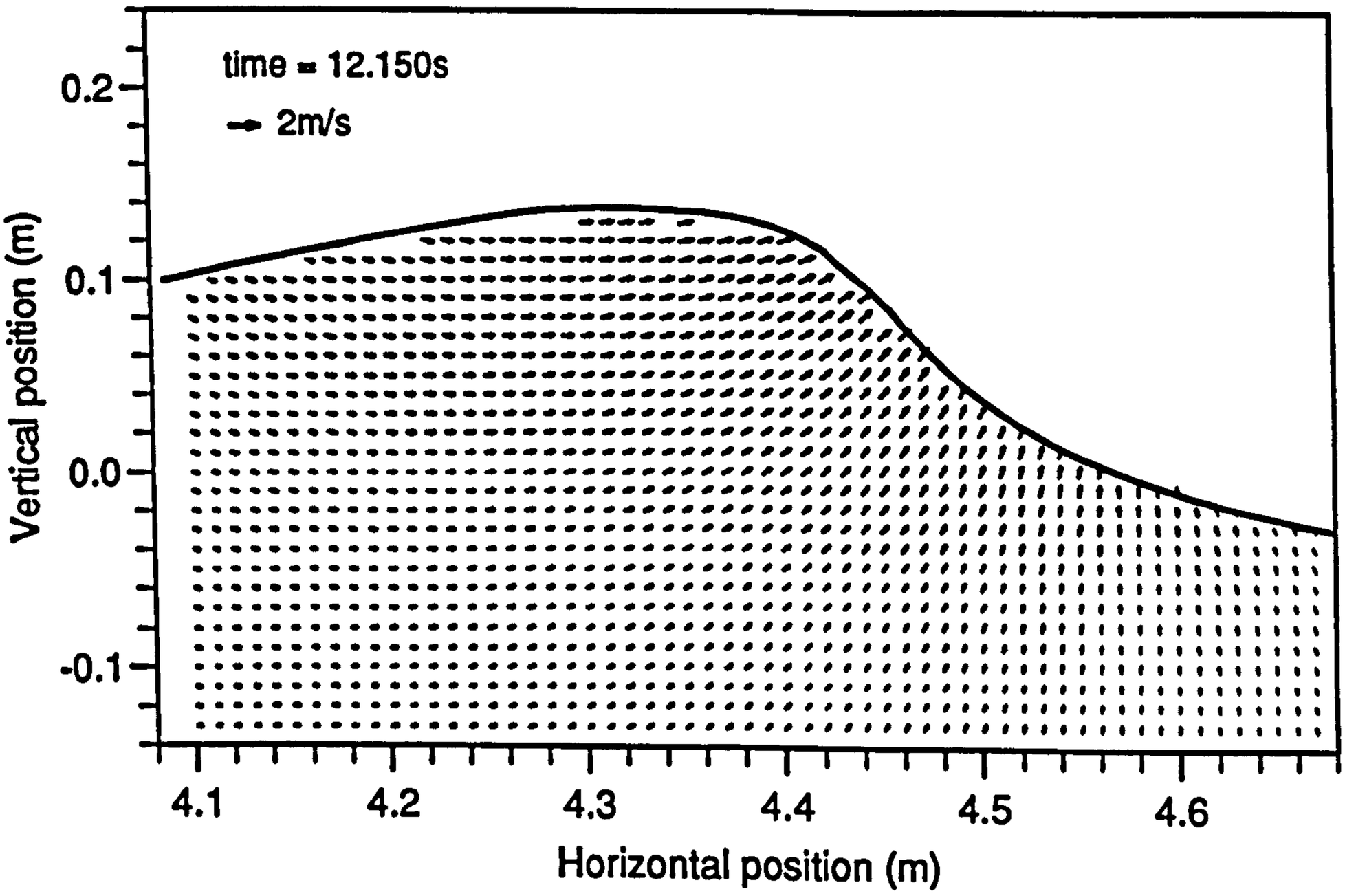

Figure 4.26: Experimentally measured velocity field, $t = 12.150$s

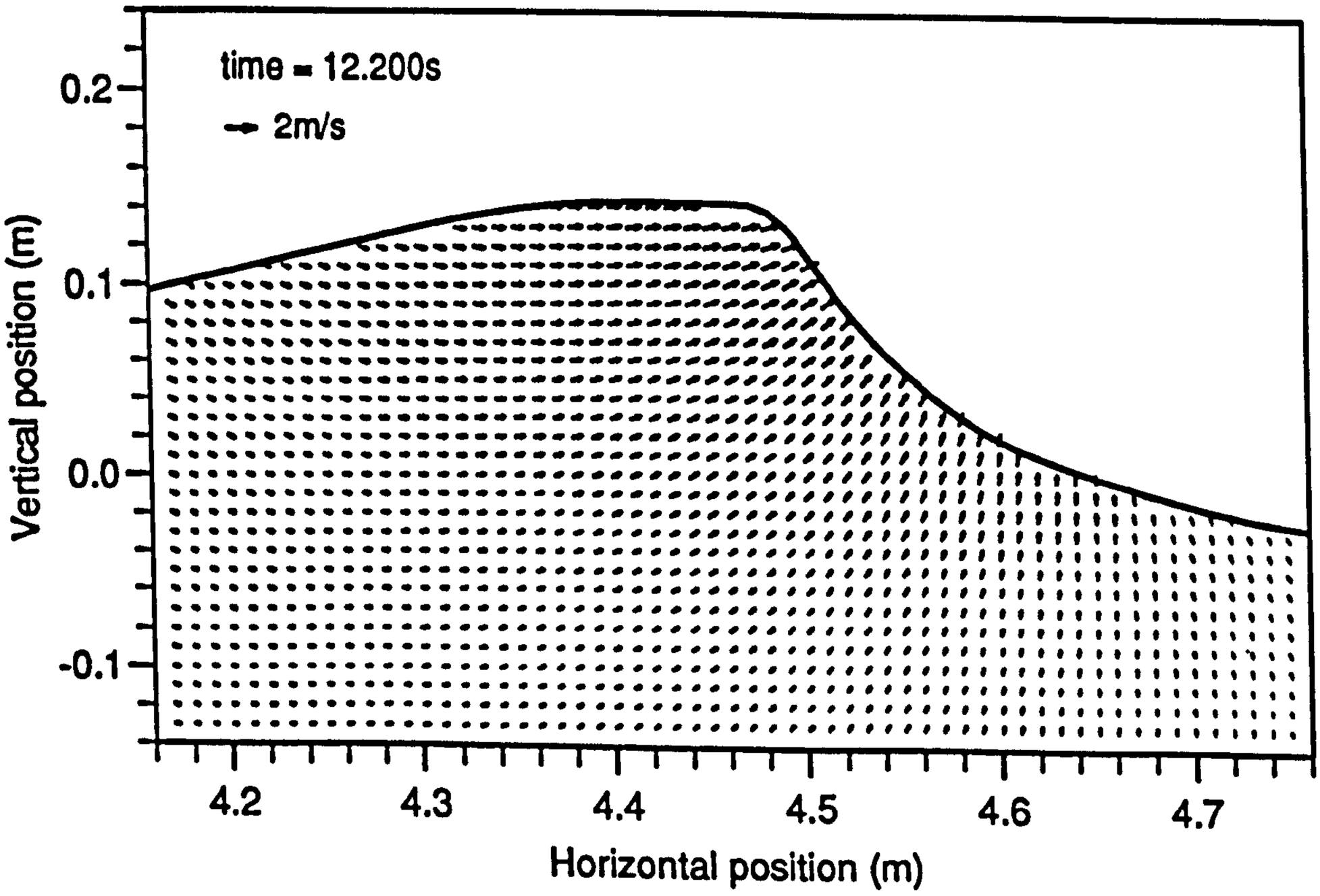

Figure 4.27: Experimentally measured velocity field, $t = 12.200$s

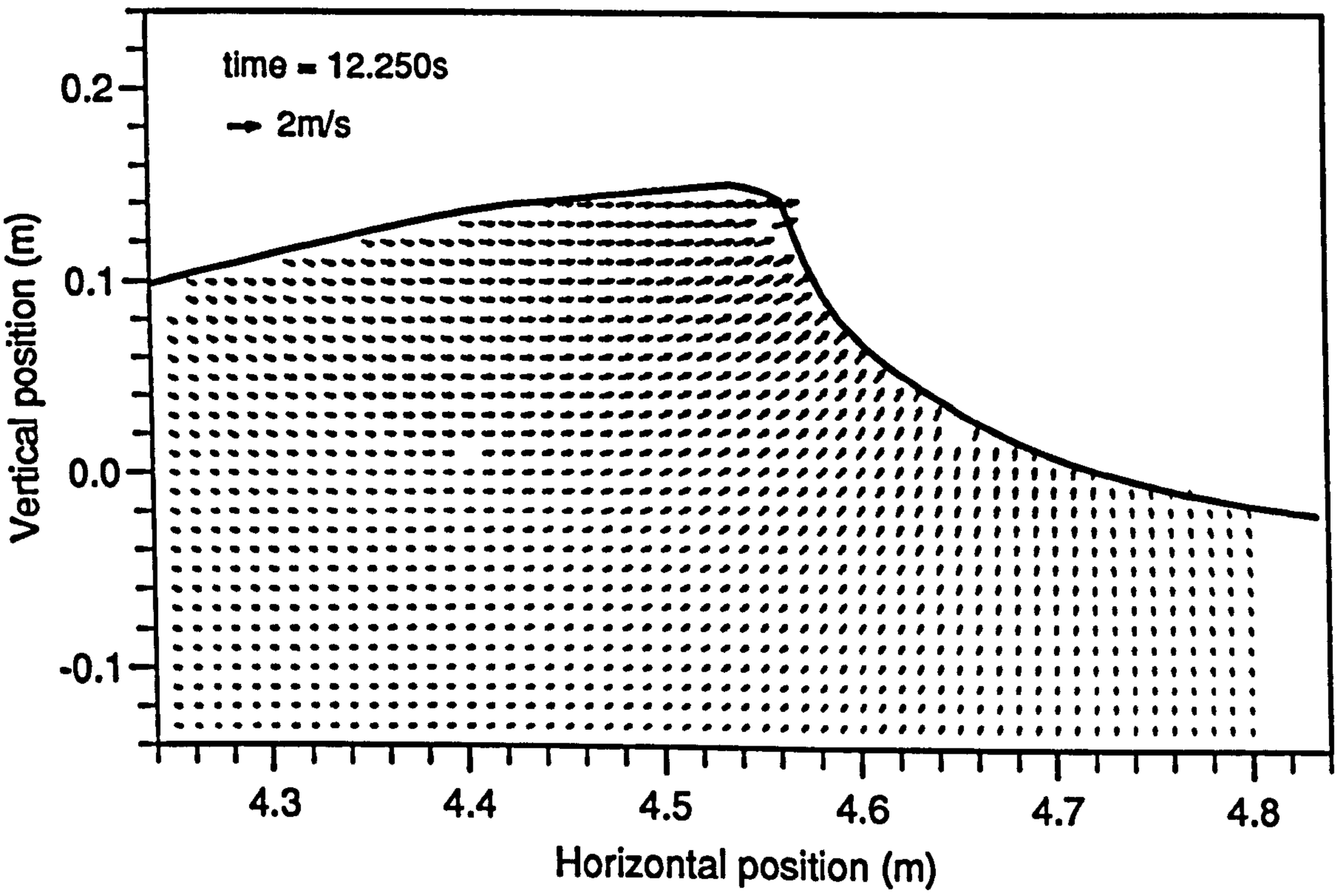

Figure 4.28: Experimentally measured velocity field, $t = 12.250$s

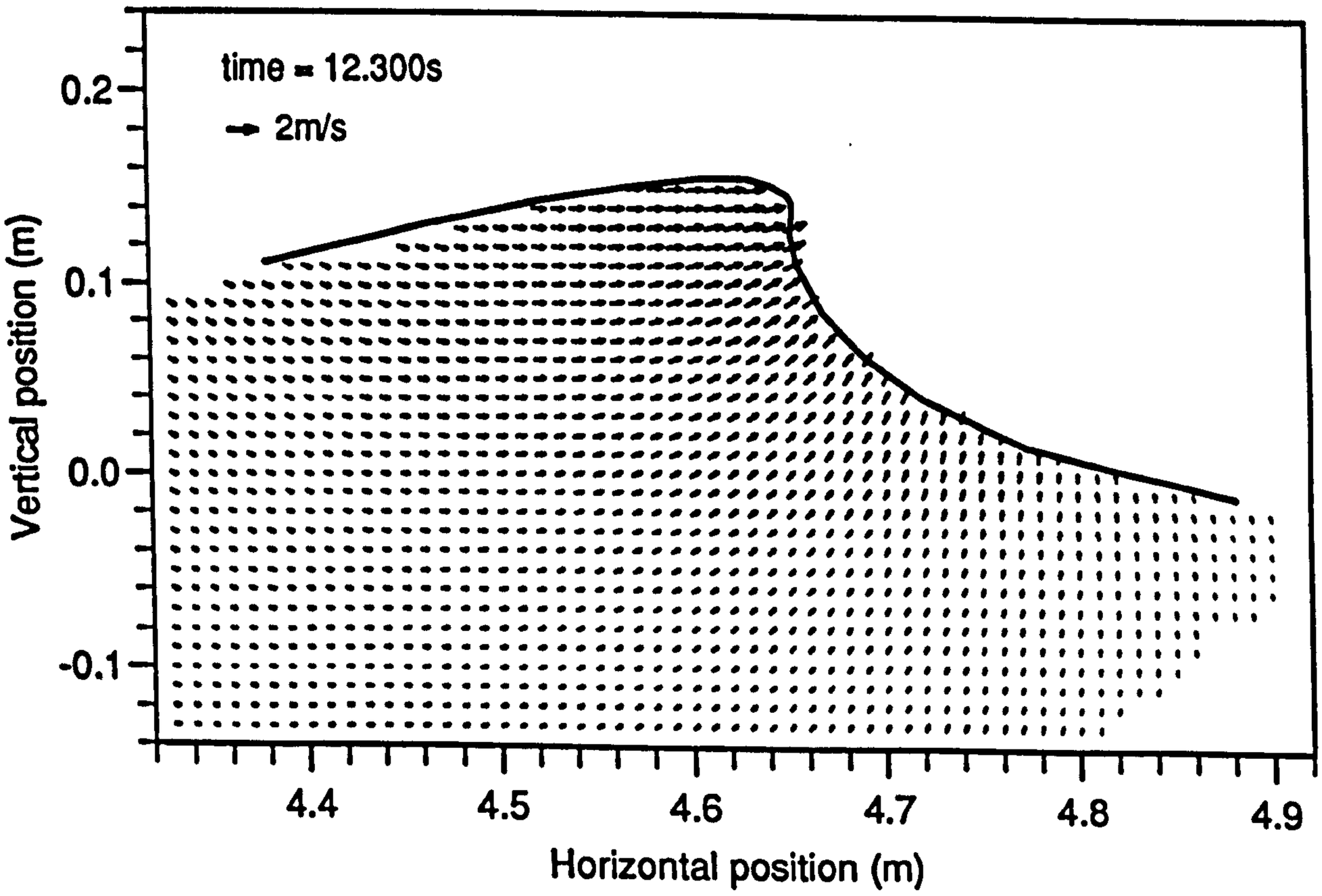

Figure 4.29: Experimentally measured velocity field, $t = 12.300$s

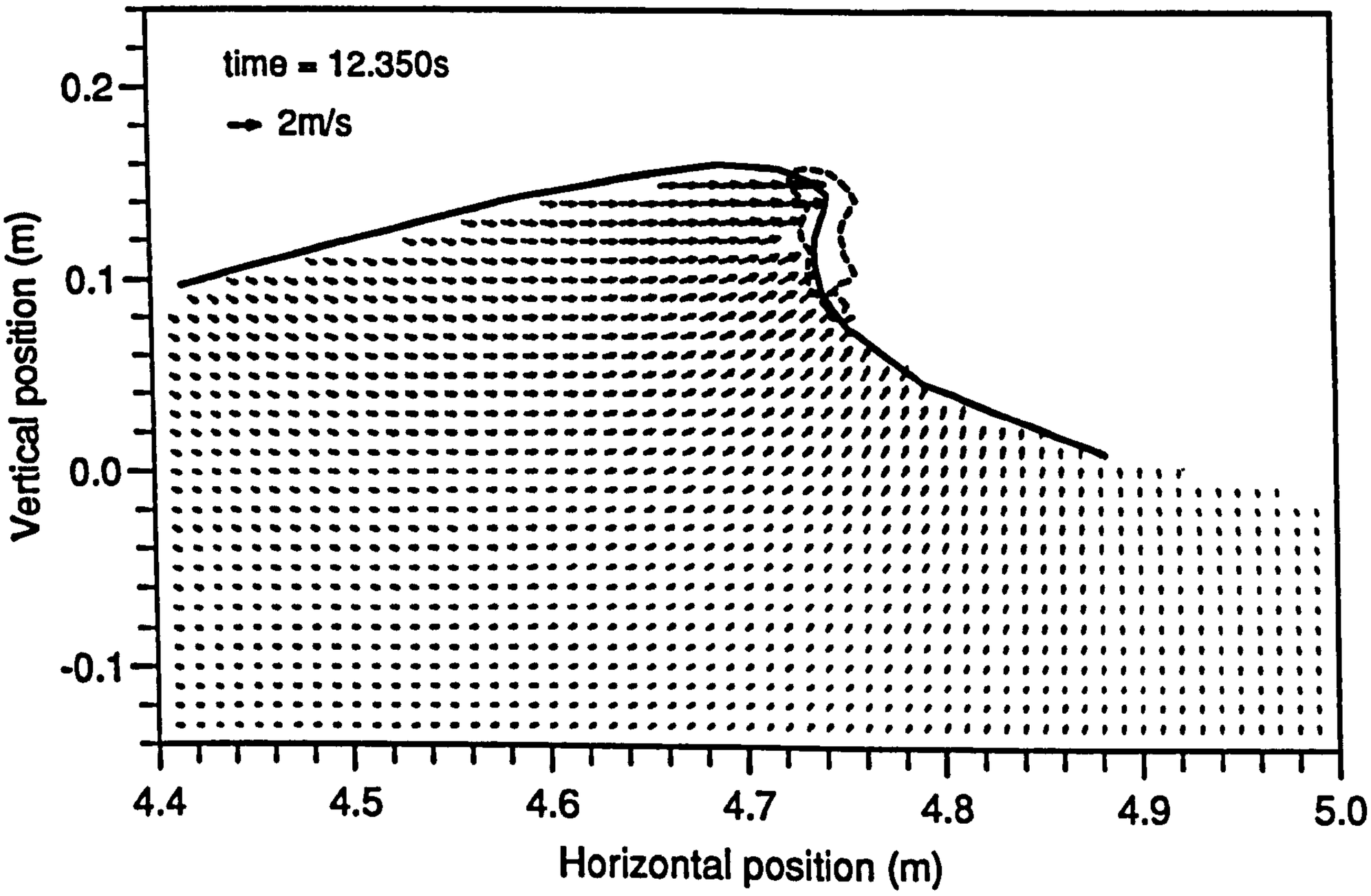

Figure 4.30: Experimentally measured velocity field, $t = 12.350$s

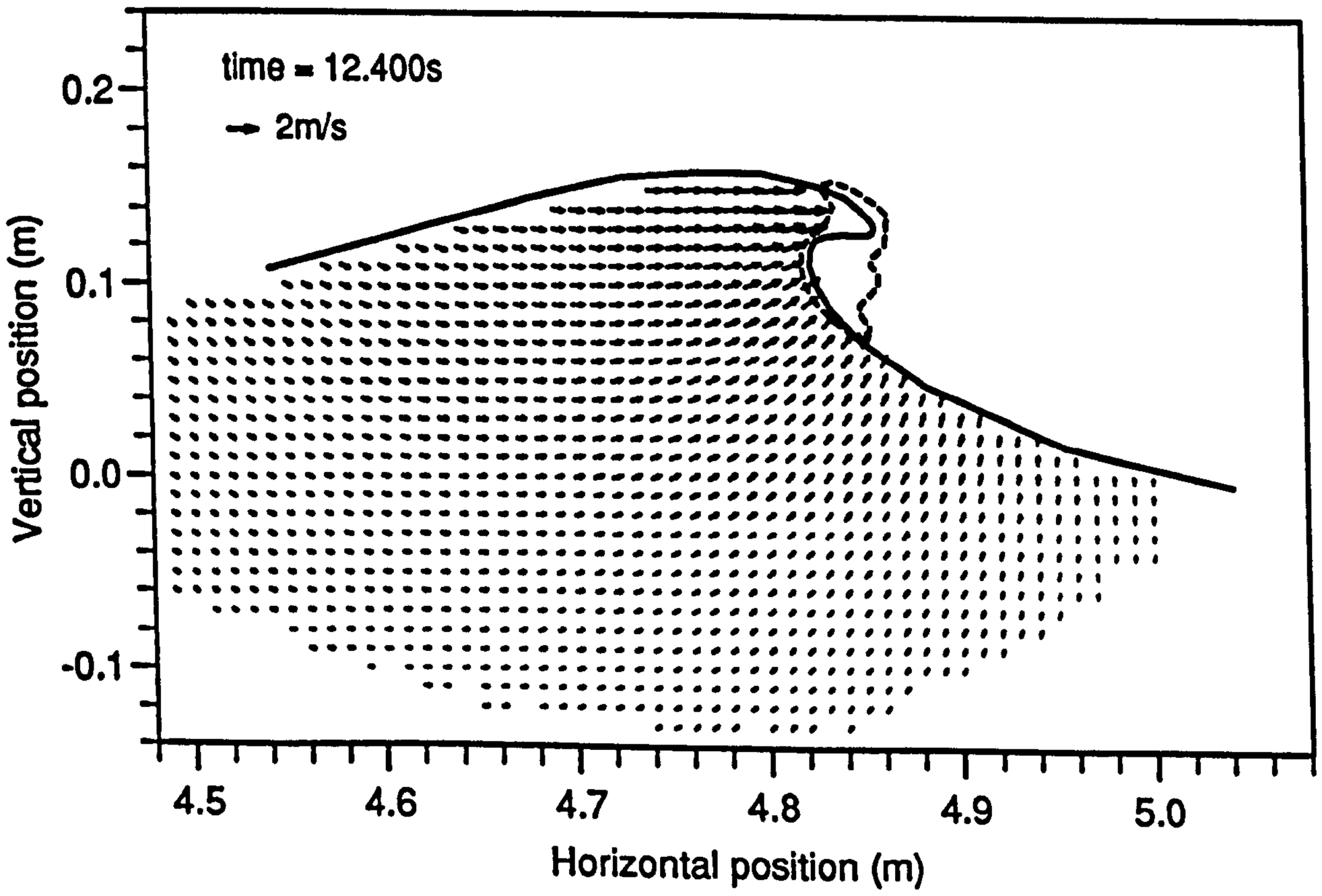

Figure 4.31: Experimentally measured velocity field, $t = 12.400$s

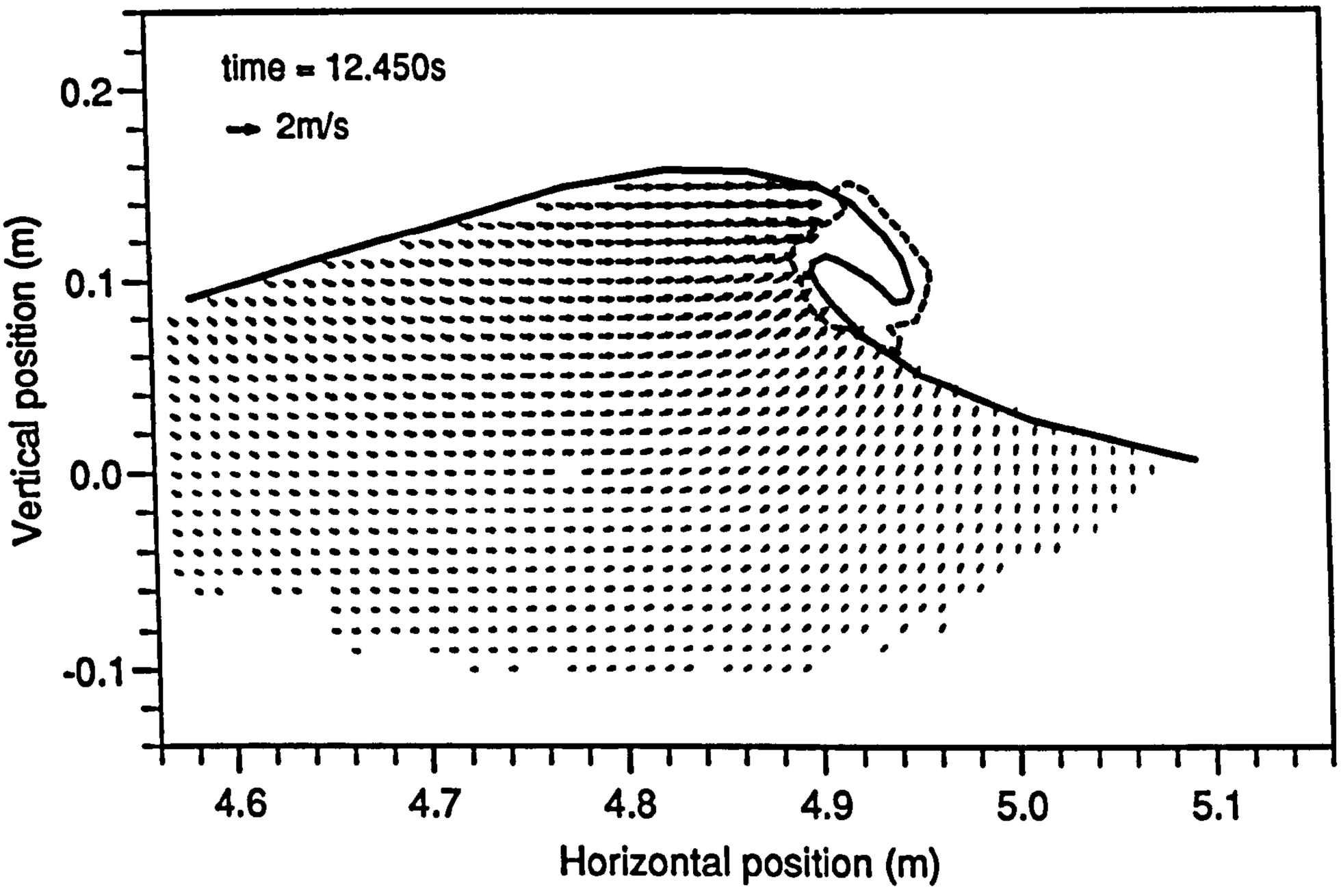

Figure 4.32: Experimentally measured velocity field, $t = 12.450$s

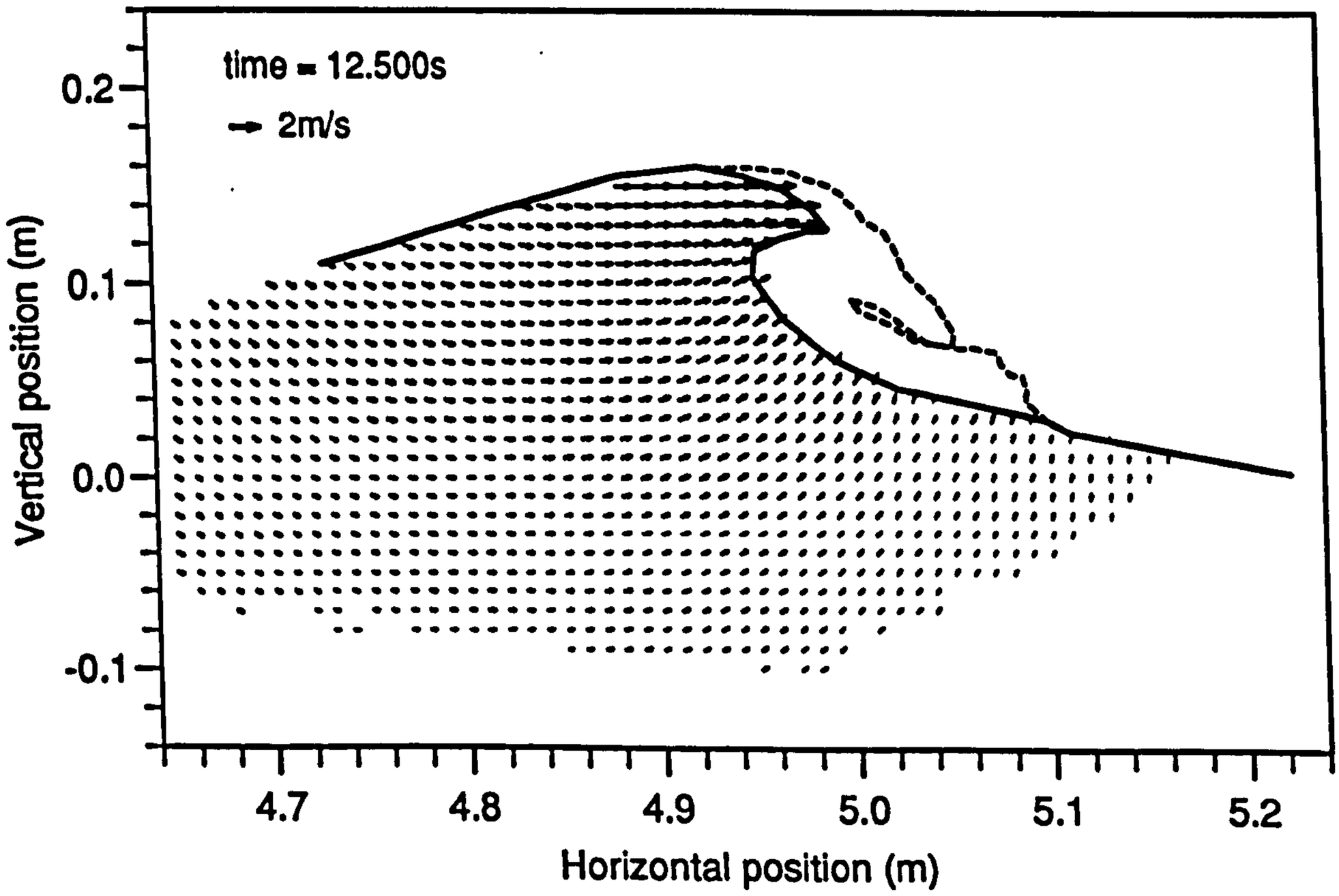

Figure 4.33: Experimentally measured velocity field, $t = 12.500$s

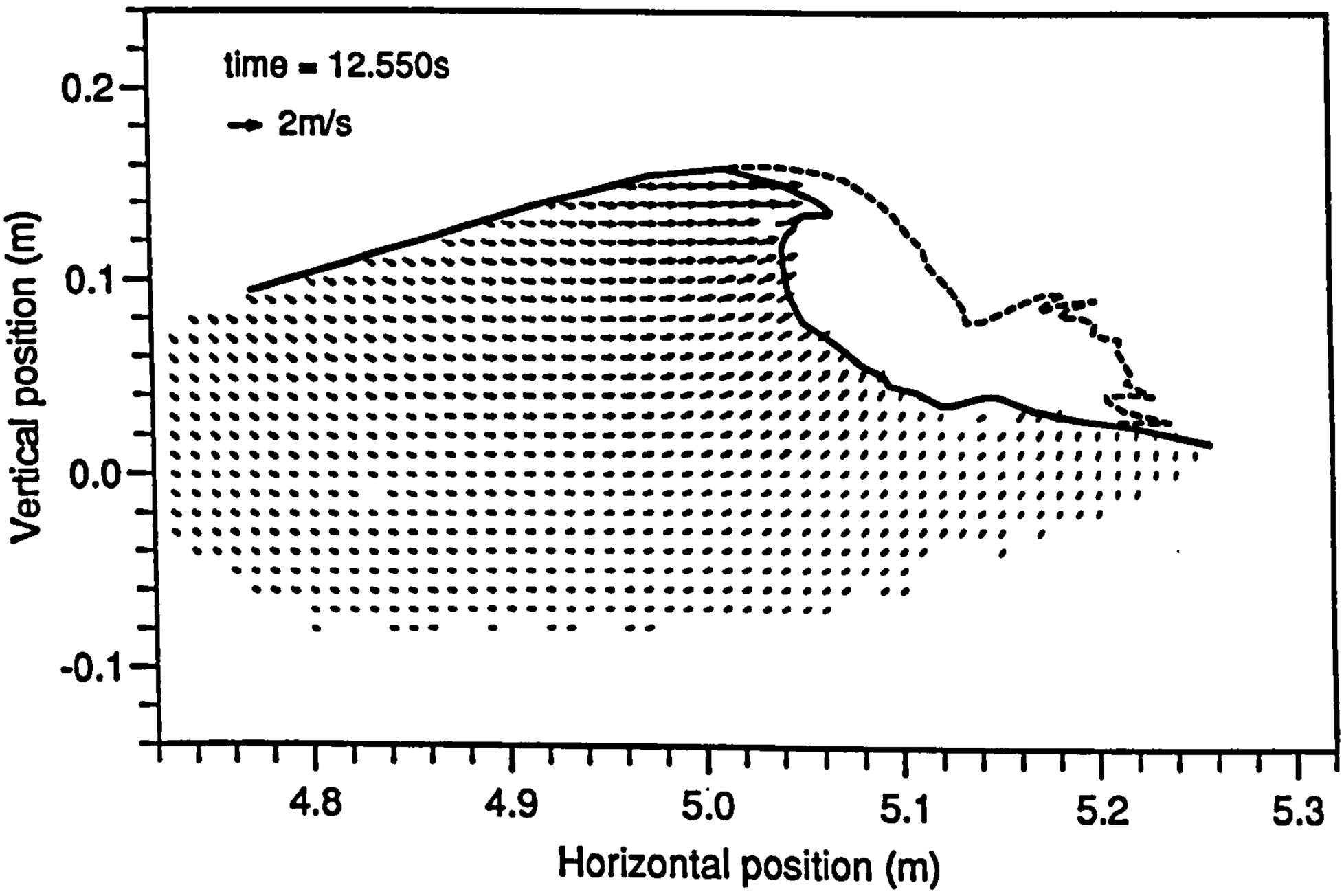

Figure 4.34: Experimentally measured velocity field, $t = 12.550$s

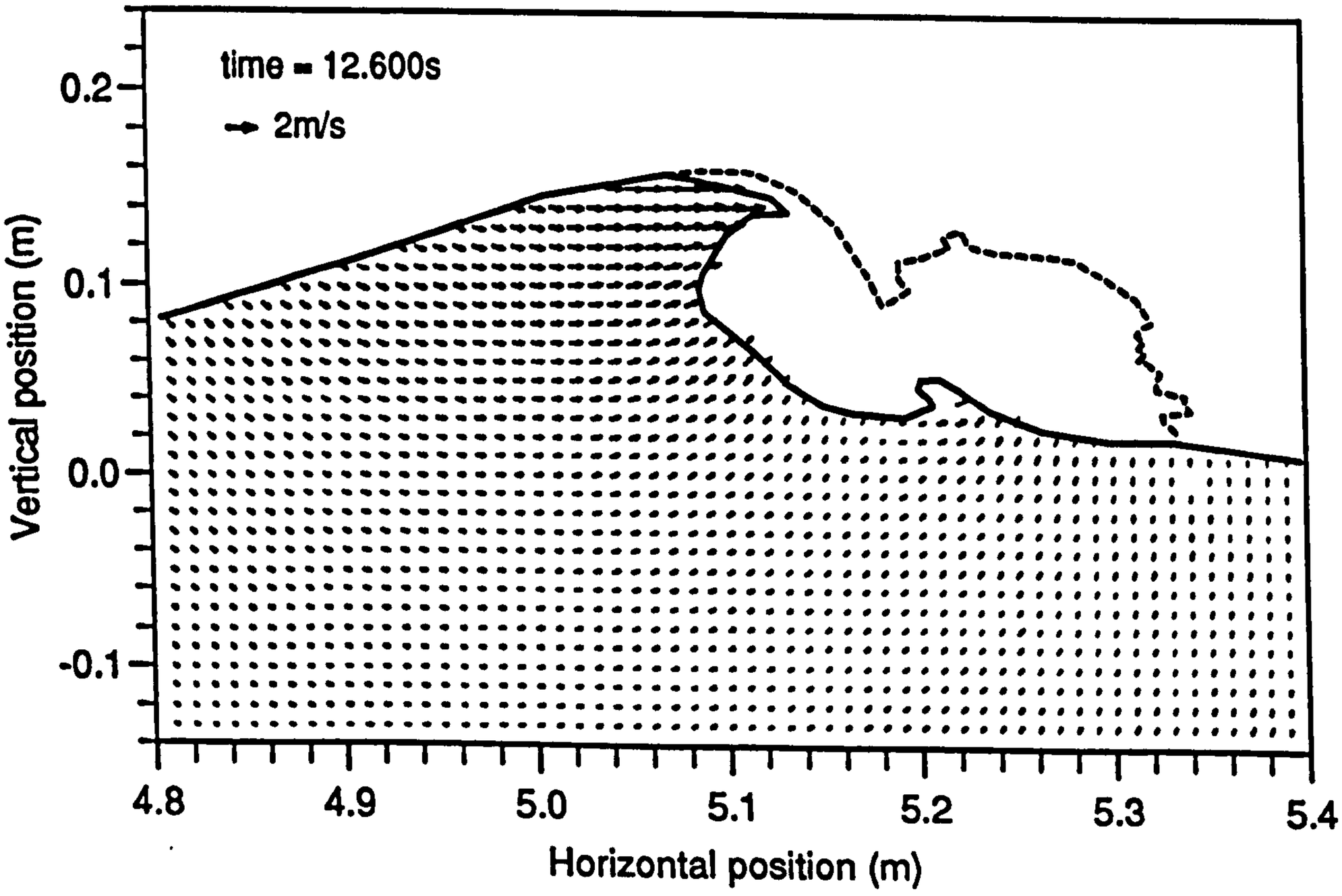

Figure 4.35: Experimentally measured velocity field, $t = 12.600$s

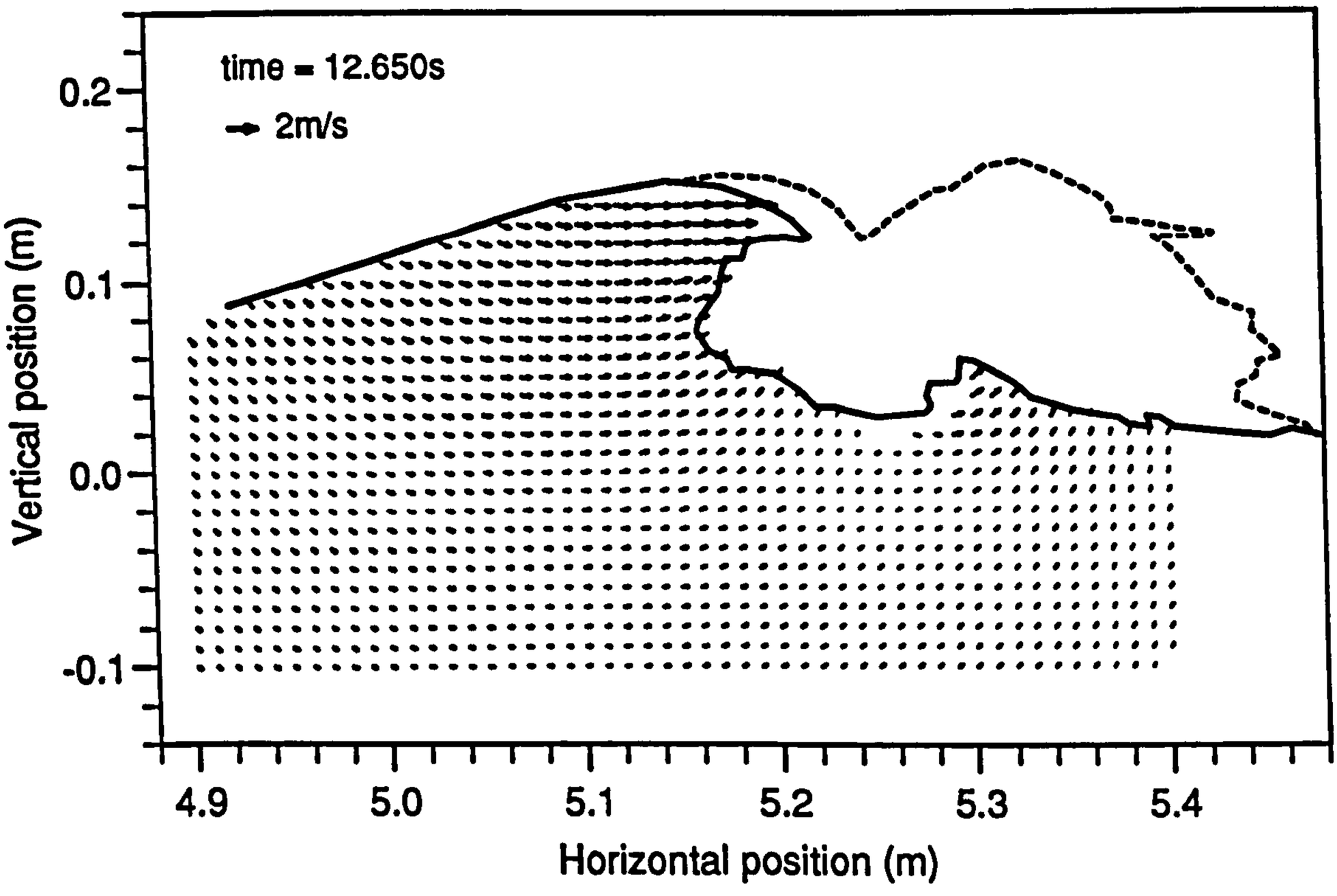

Figure 4.36: Experimentally measured velocity field, $t = 12.650$s

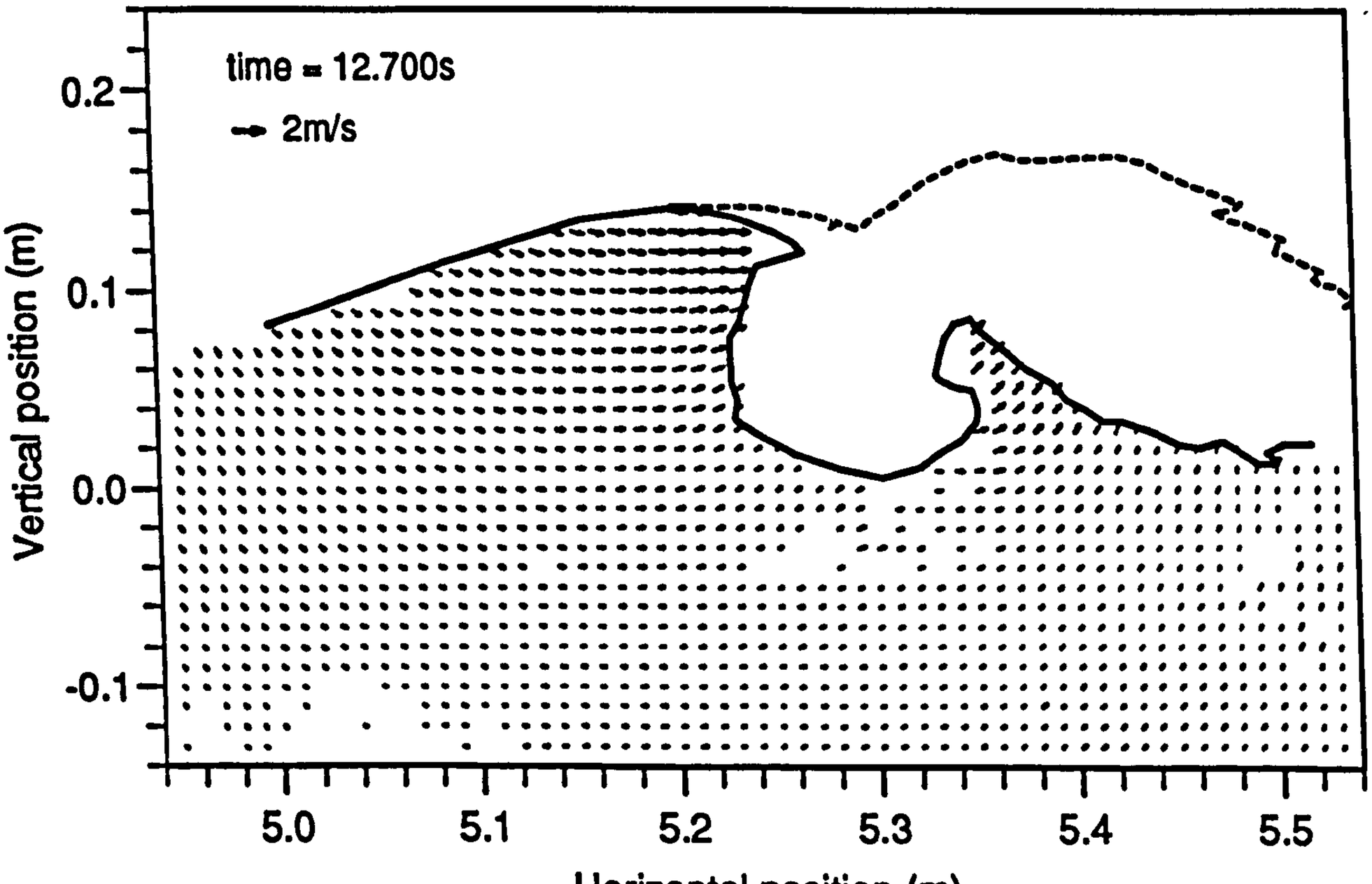

Figure 4.37: Experimentally measured velocity field, $t = 12.700$s

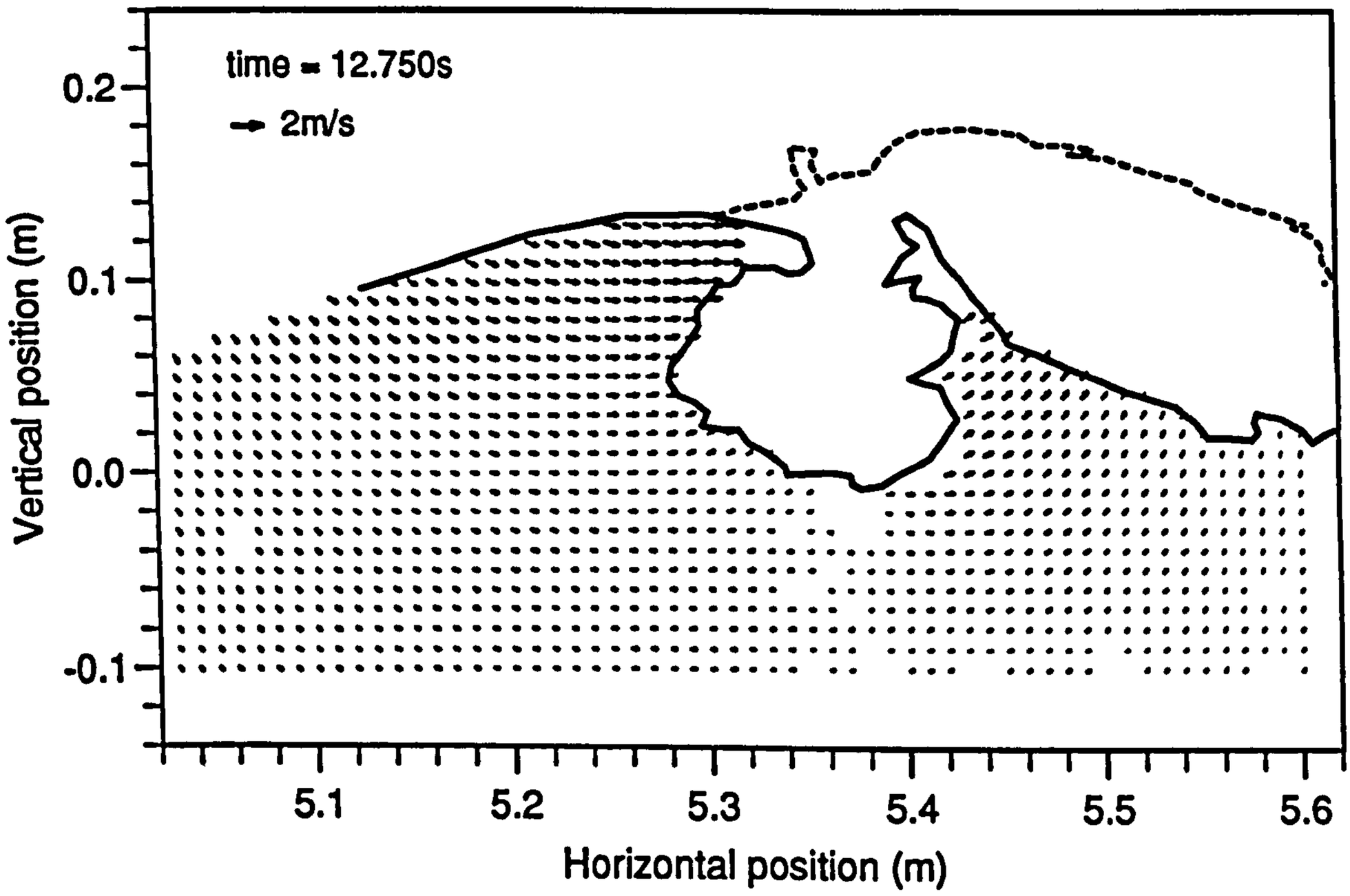

Figure 4.38: Experimentally measured velocity field, $t = 12.750$s

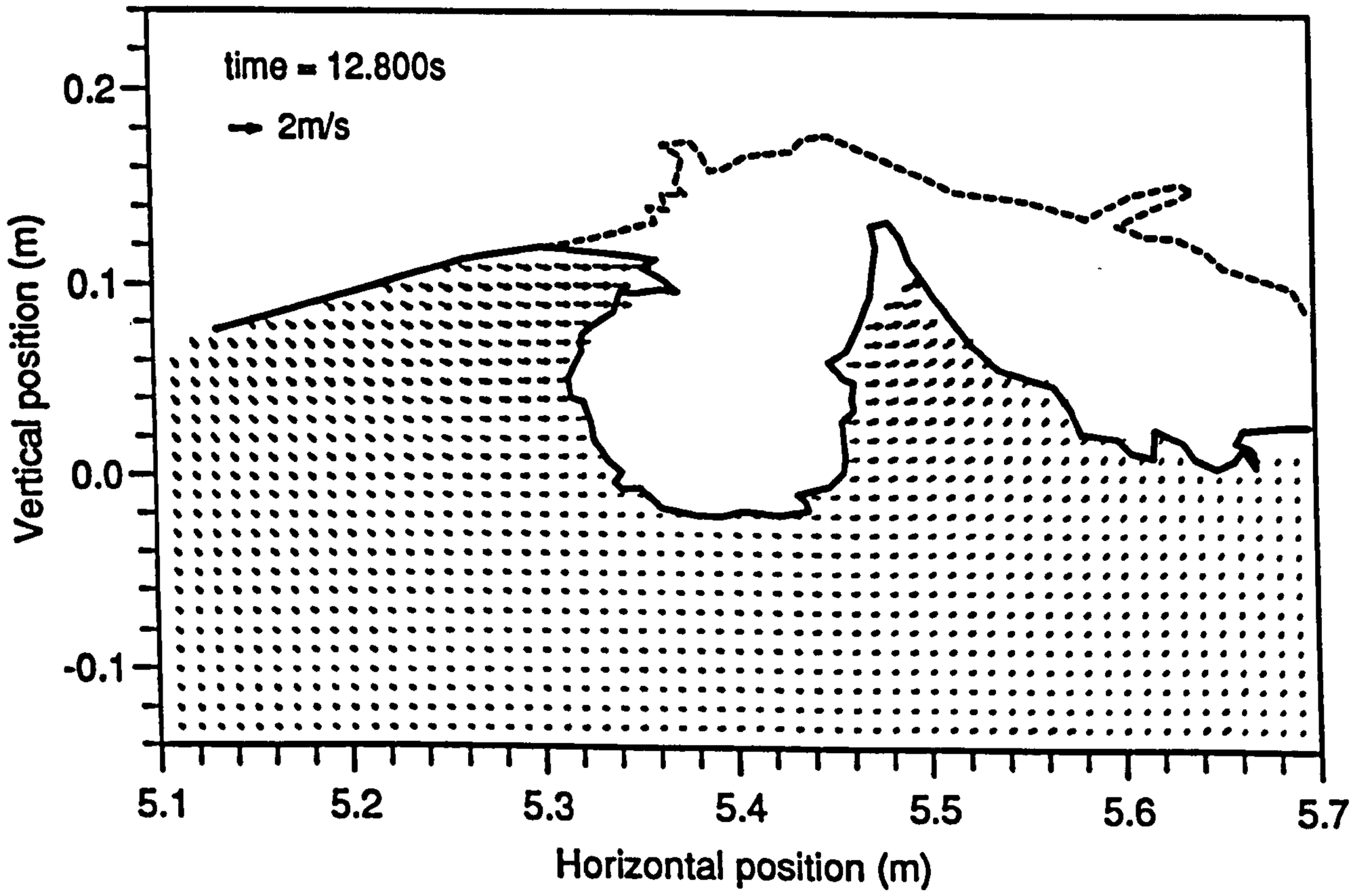

Figure 4.39: Experimentally measured velocity field, $t = 12.800$s

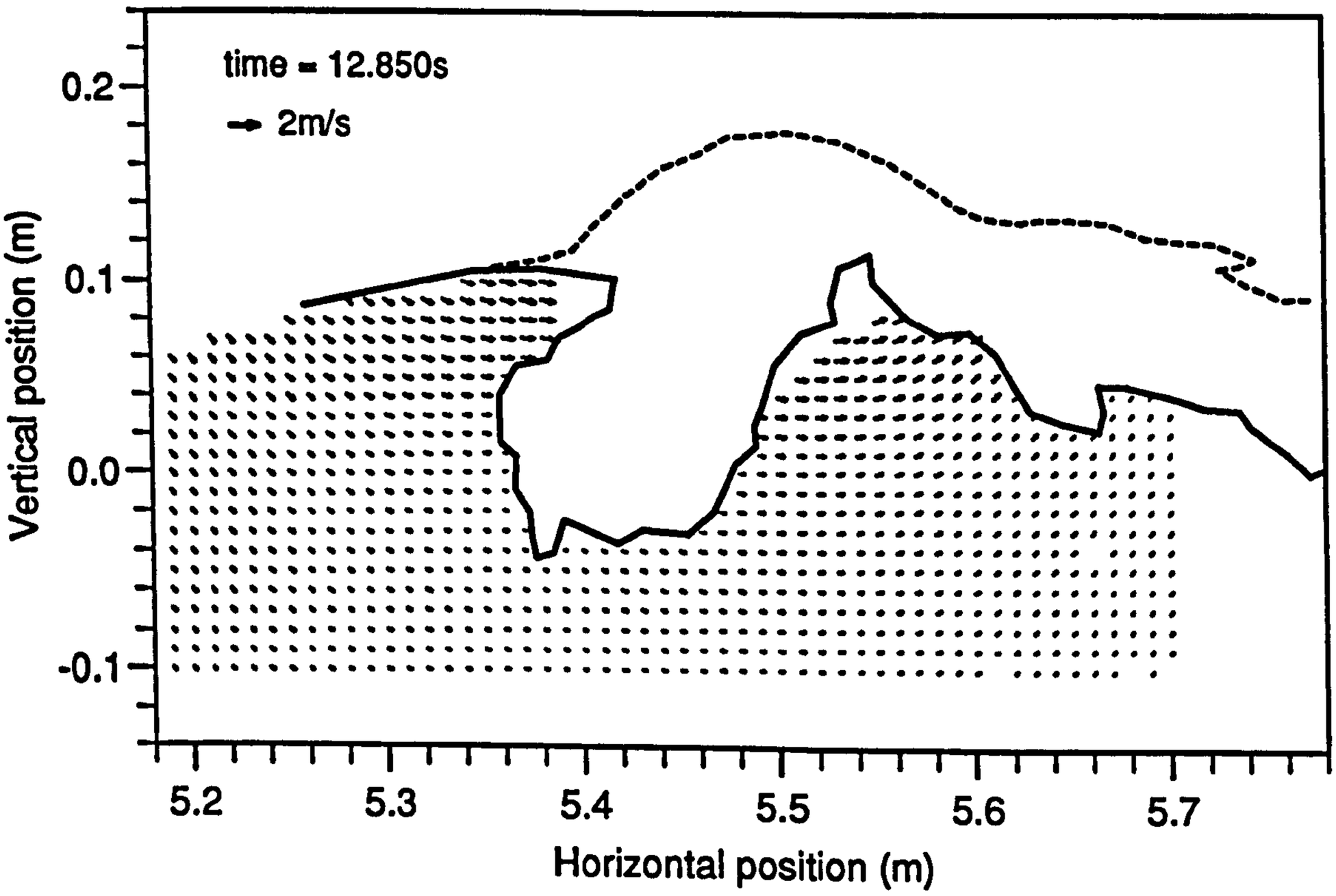

Figure 4.40: Experimentally measured velocity field, $t = 12.850$s

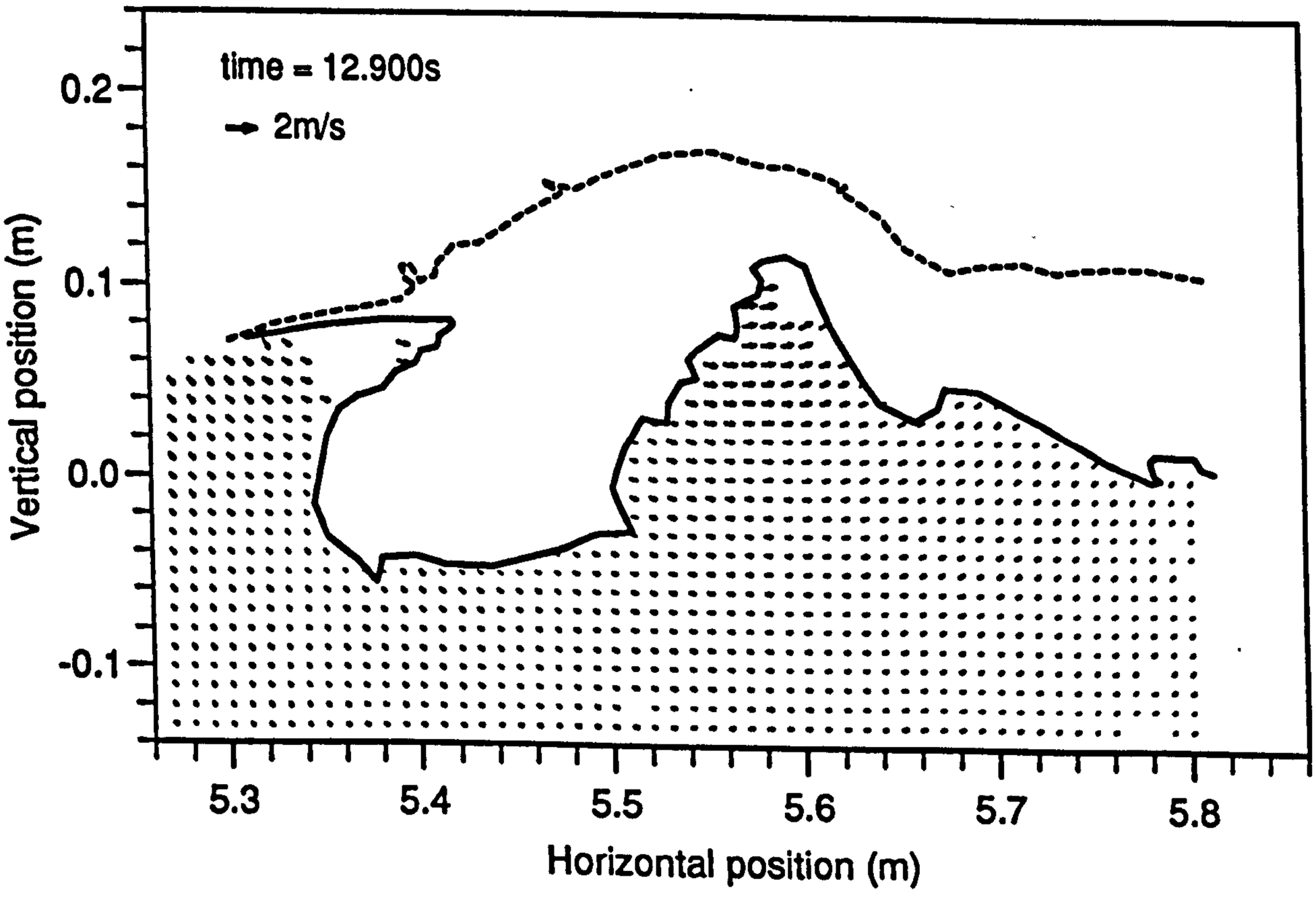

Figure 4.41: Experimentally measured velocity field, $t = 12.900$s

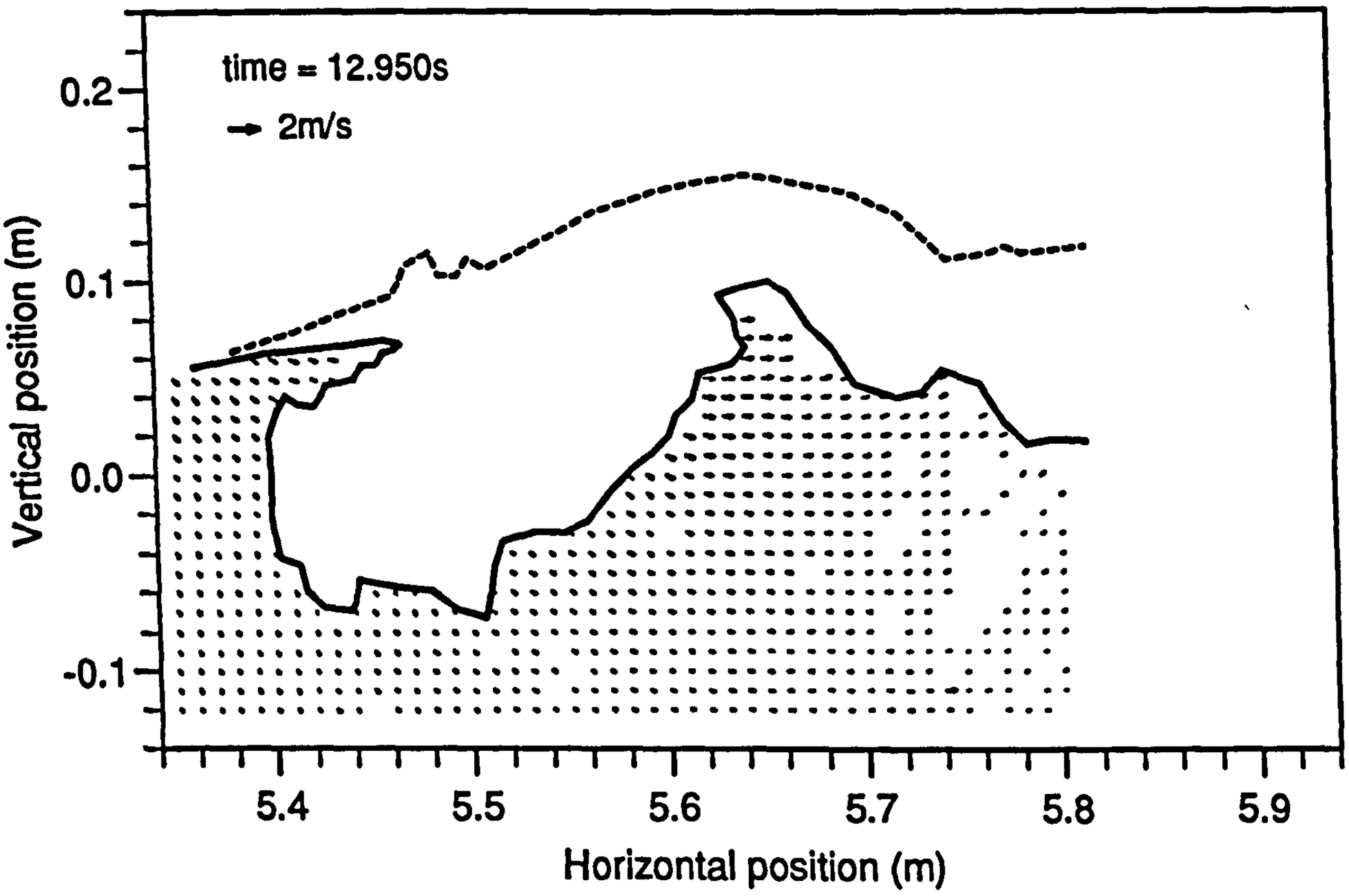

Figure 4.42: Experimentally measured velocity field, $t = 12.950$s

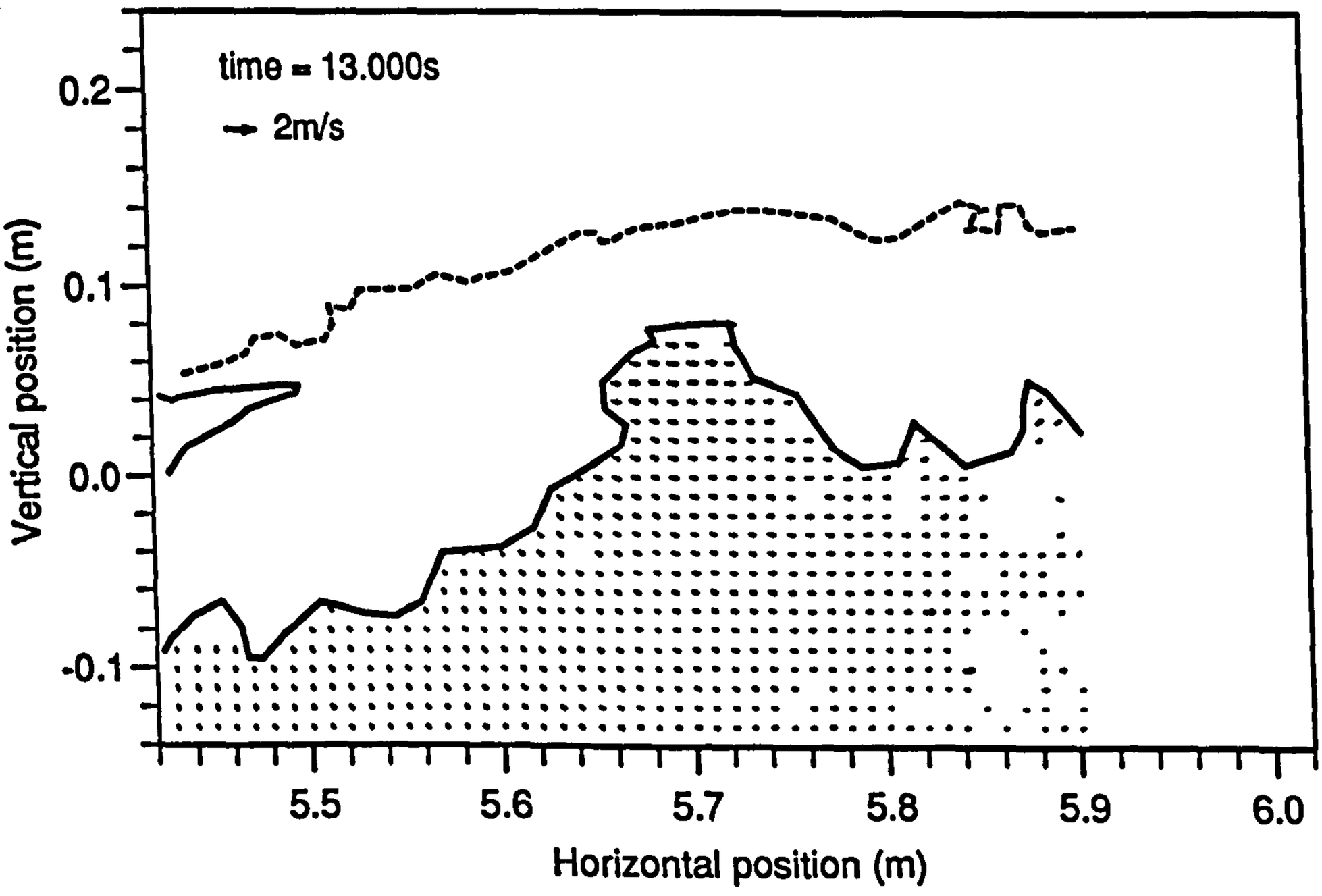

Figure 4.43: Experimentally measured velocity field, $t = 13.000$s

Comparison of Experimental and Numerical Internal Kinematics

For comparison with the experimental data, numerical vector plots up to breaking are plotted in figures 4.44 to 4.49. The numerical data was generated using the Bristol model, and is plotted at 1/20 second intervals, as the experimental measurements, up to the point close to where computations ceased.

In section 4.6.1 it was decided that the experimental and numerical data should be compared assuming a time shift $\Delta t = .125$s, and a spatial shift $\Delta x = .22$m. Assuming these shifts then figure 4.44 should be compared with figure 4.26, figure 4.45 with figure 4.27, etc.

In comparing the experimental and numerical velocity data, it can be seen that the major features of the flow are the same: the velocities are much greater near the crest and almost horizontal in this region; elsewhere the directions of the velocity vectors are very similar. Qualitatively the match between experimental data and numerical data is very good, but given the small size of the vectors in the plots, this is not a very sensitive method of comparison.

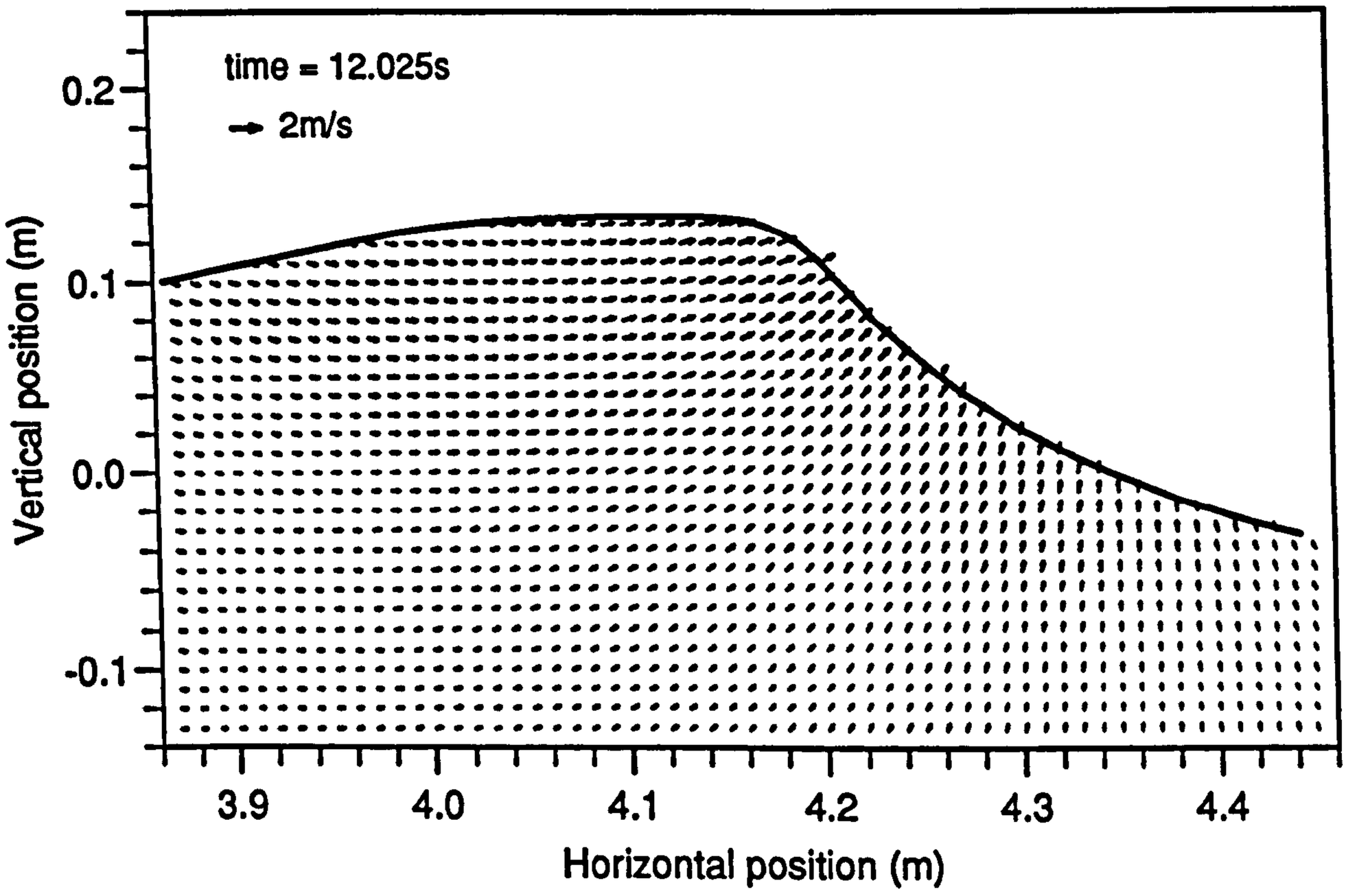

Figure 4.44: Numerically generated velocity field, $t = 12.025$s (compare 12.150s)

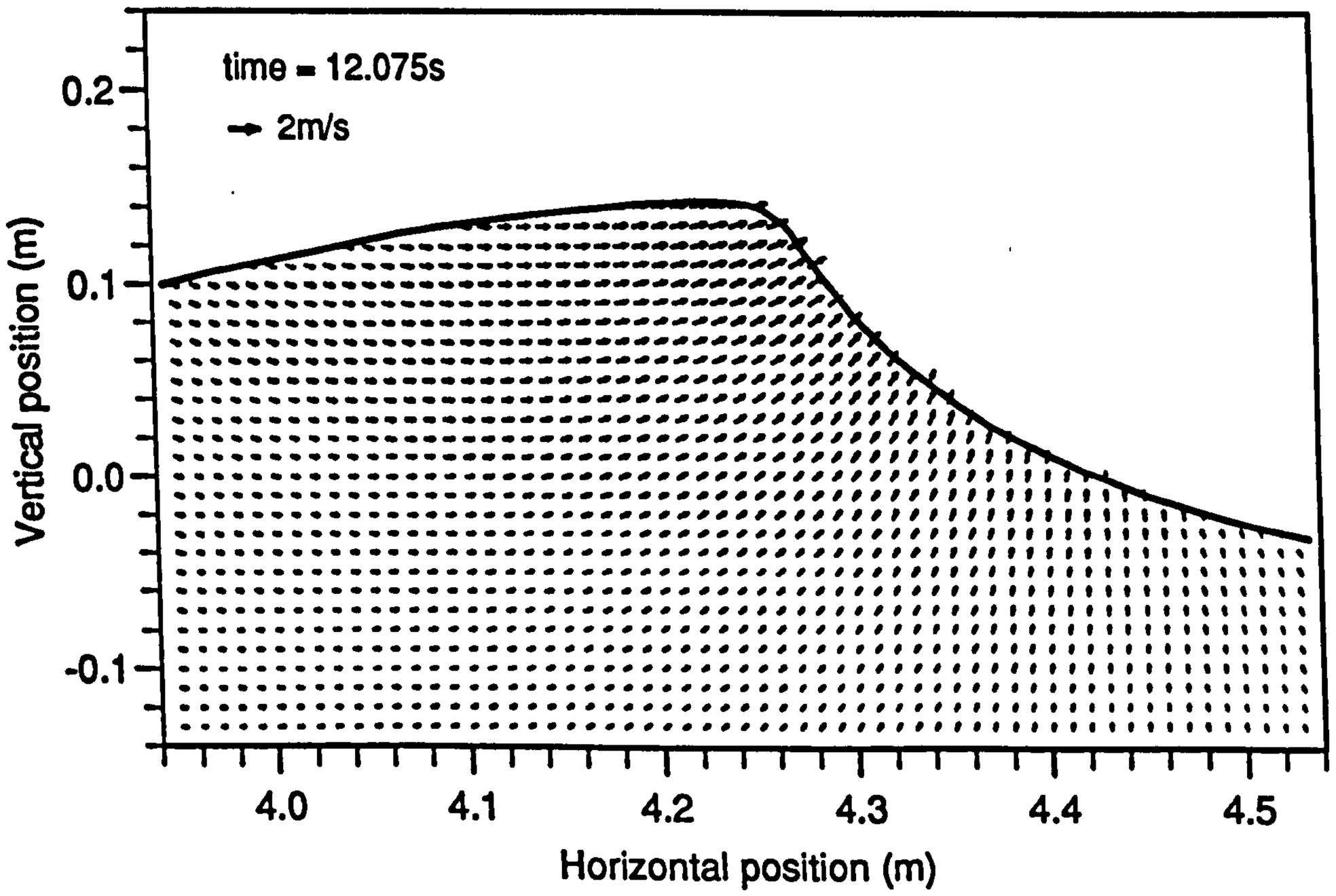

Figure 4.45: Numerically generated velocity field, $t = 12.075$s (compare 12.200s)

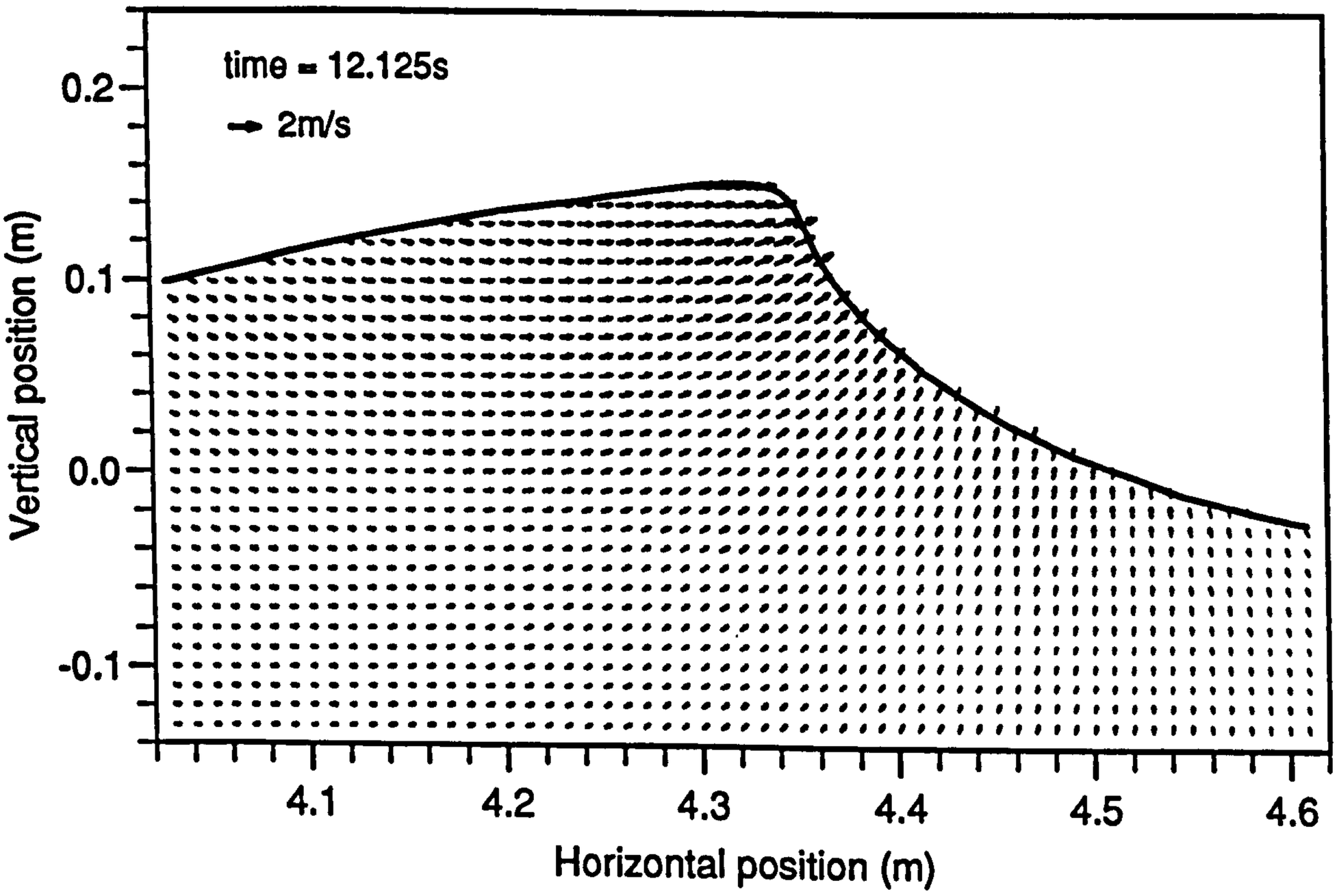

Figure 4.46: Numerically generated velocity field, $t = 12.125$s (compare 12.250s)

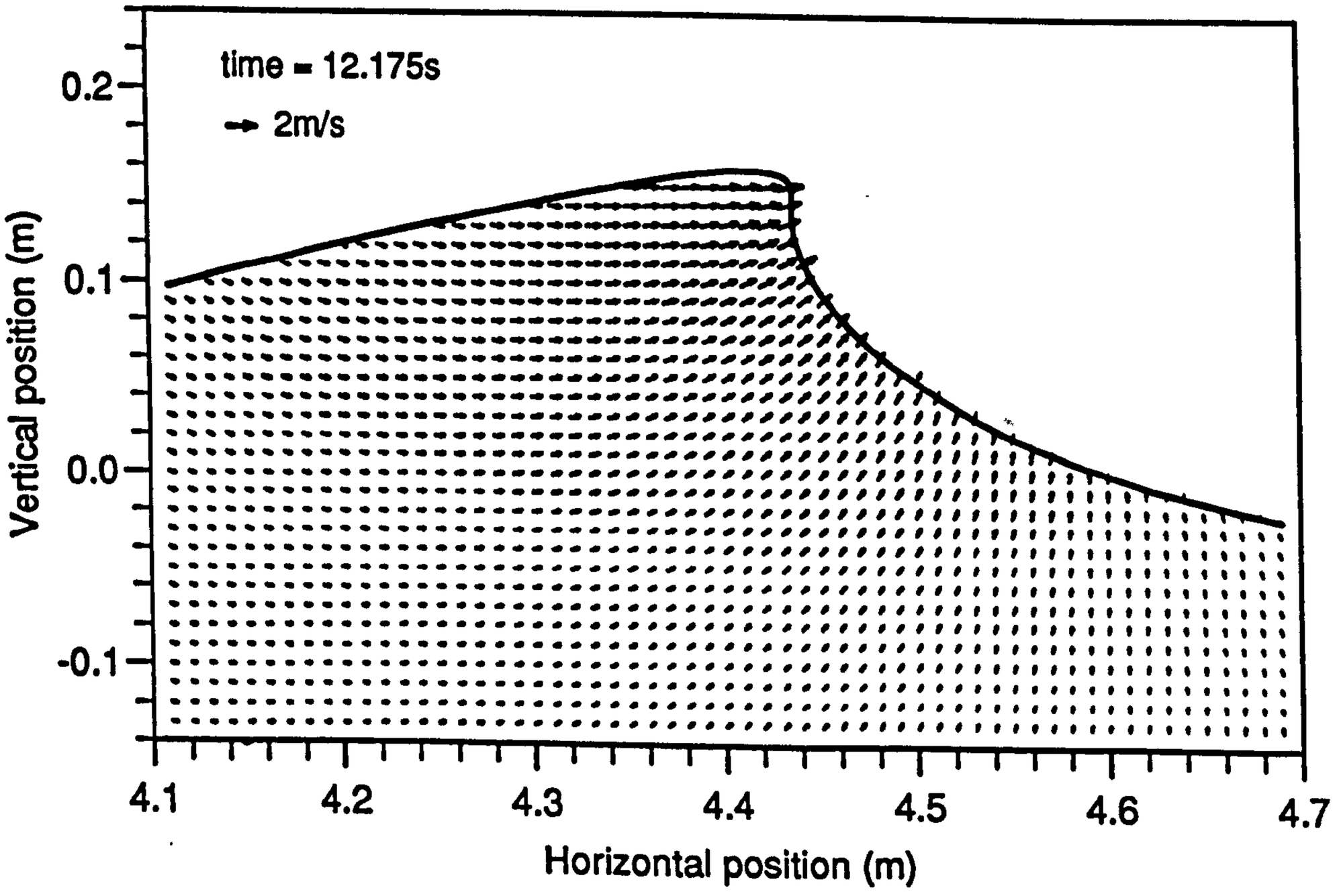

Figure 4.47: Numerically generated velocity field, $t = 12.175$s (compare 12.300s)

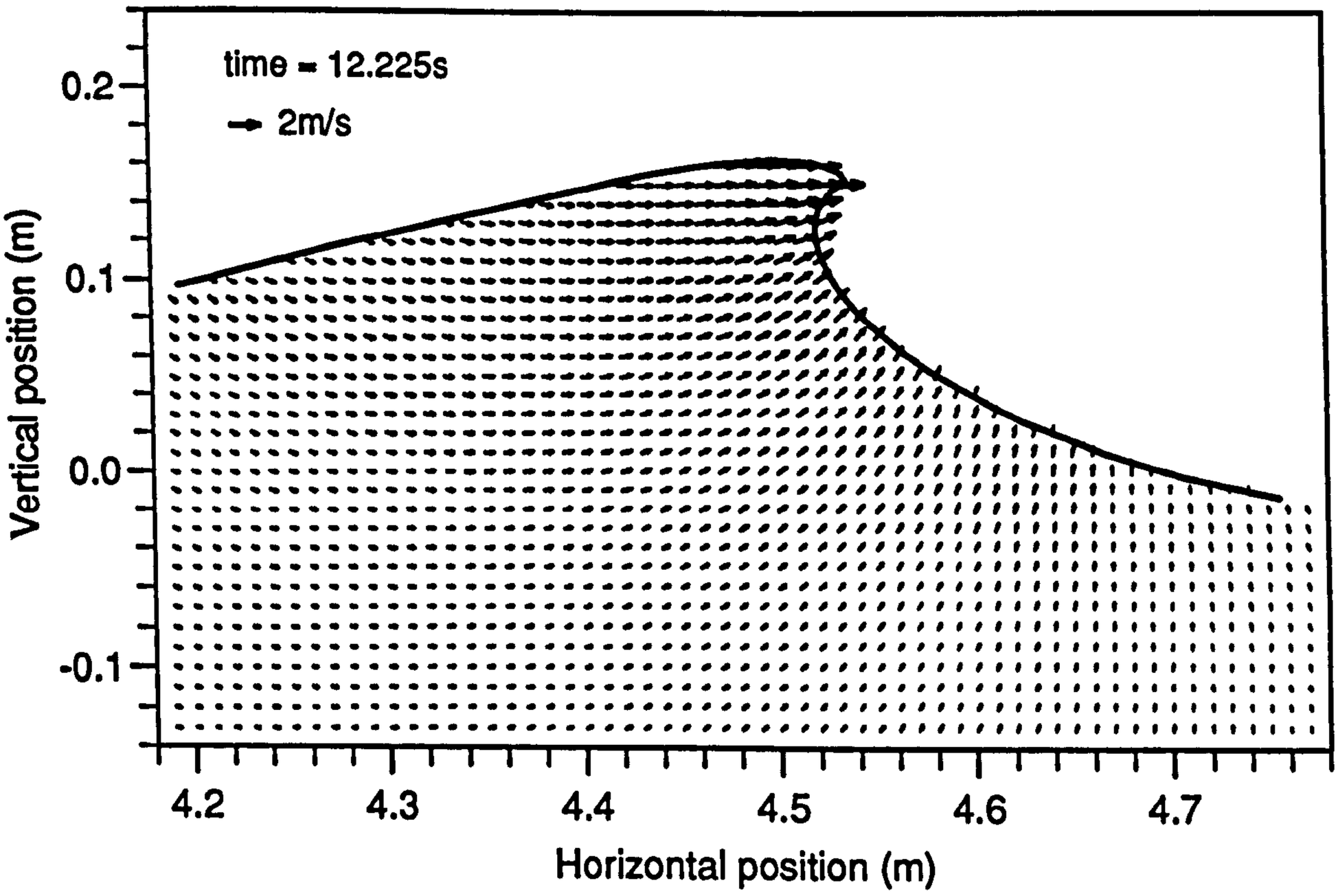

Figure 4.48: Numerically generated velocity field, $t = 12.225$s (compare 12.350s)

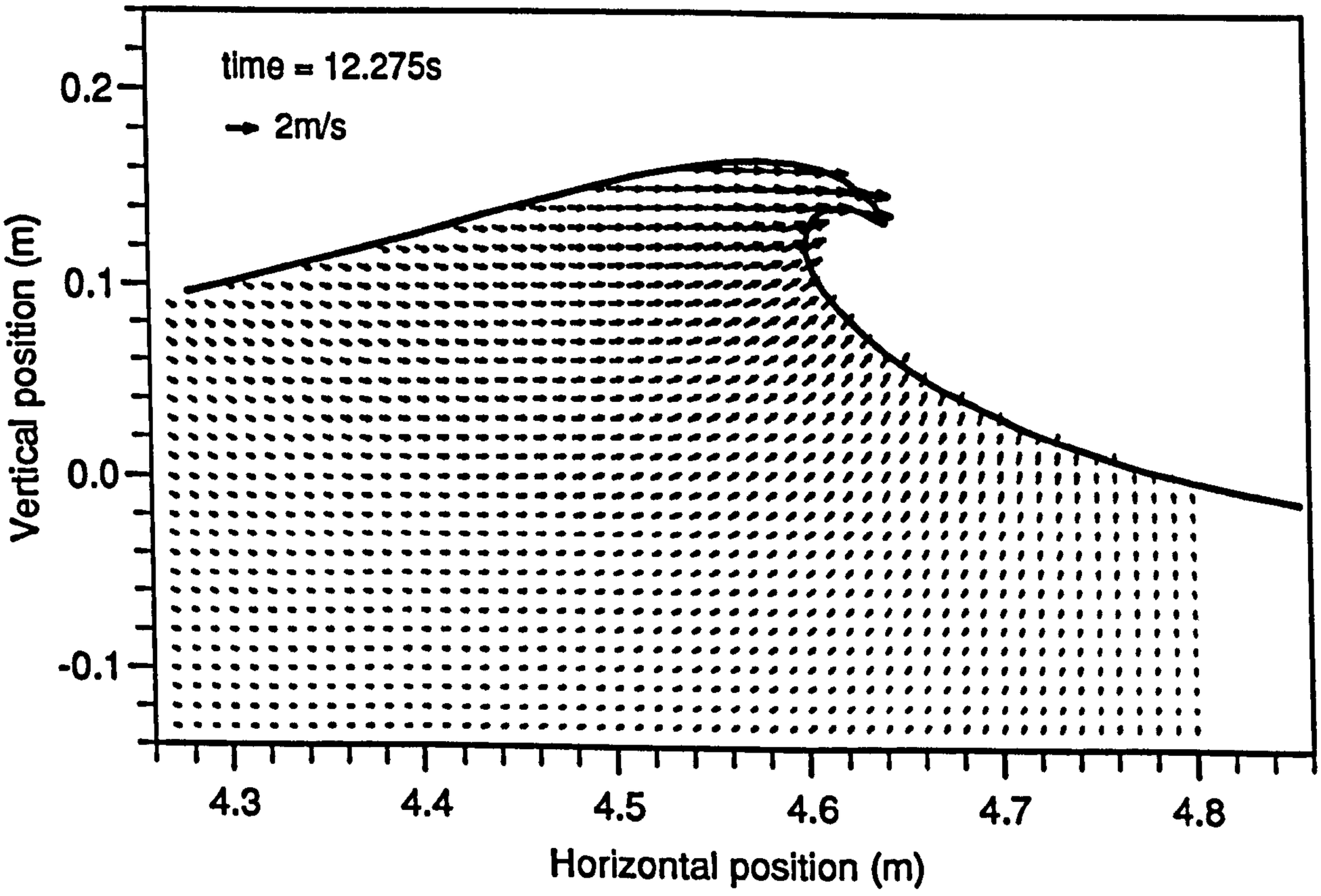

Figure 4.49: Numerically generated velocity field, $t = 12.275$s (compare 12.400s)

Difference between Experimental and Numerical Kinematics

In order to magnify the differences between the experimental measured and numerically generated velocity fields, the two sets of data were subtracted in two cases.

Figure 4.50 contains the numerical data previously plotted in figure 4.47 subtracted from the experimental data shown in figure 4.29. Each dataset corresponds to the phase when the wave is vertically fronted. As before, the numerical data has been shifted sideways by .22m so that the surface profiles almost match.

The vectors in the plot are drawn 10 times bigger than in the previous figures, in order to enhance the differences. It can be seen that the differences in the crest region are very small, whereas there is a non-negligible systematic difference in

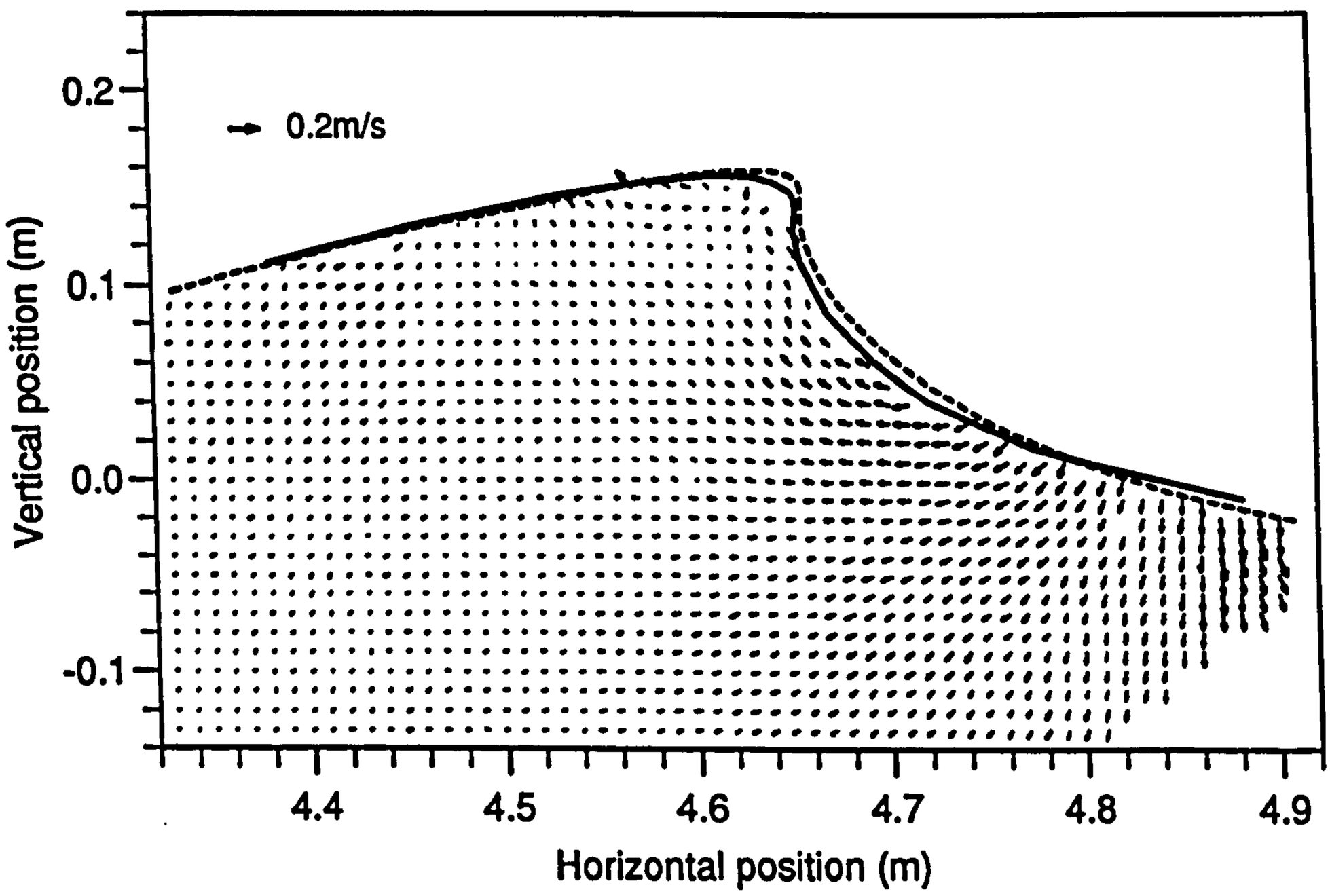

Figure 4.50: Difference between experimentally measured velocity field, t = 12.300s, and numerical data, t = 12.175s. — experimental surface, - - - numerical surface

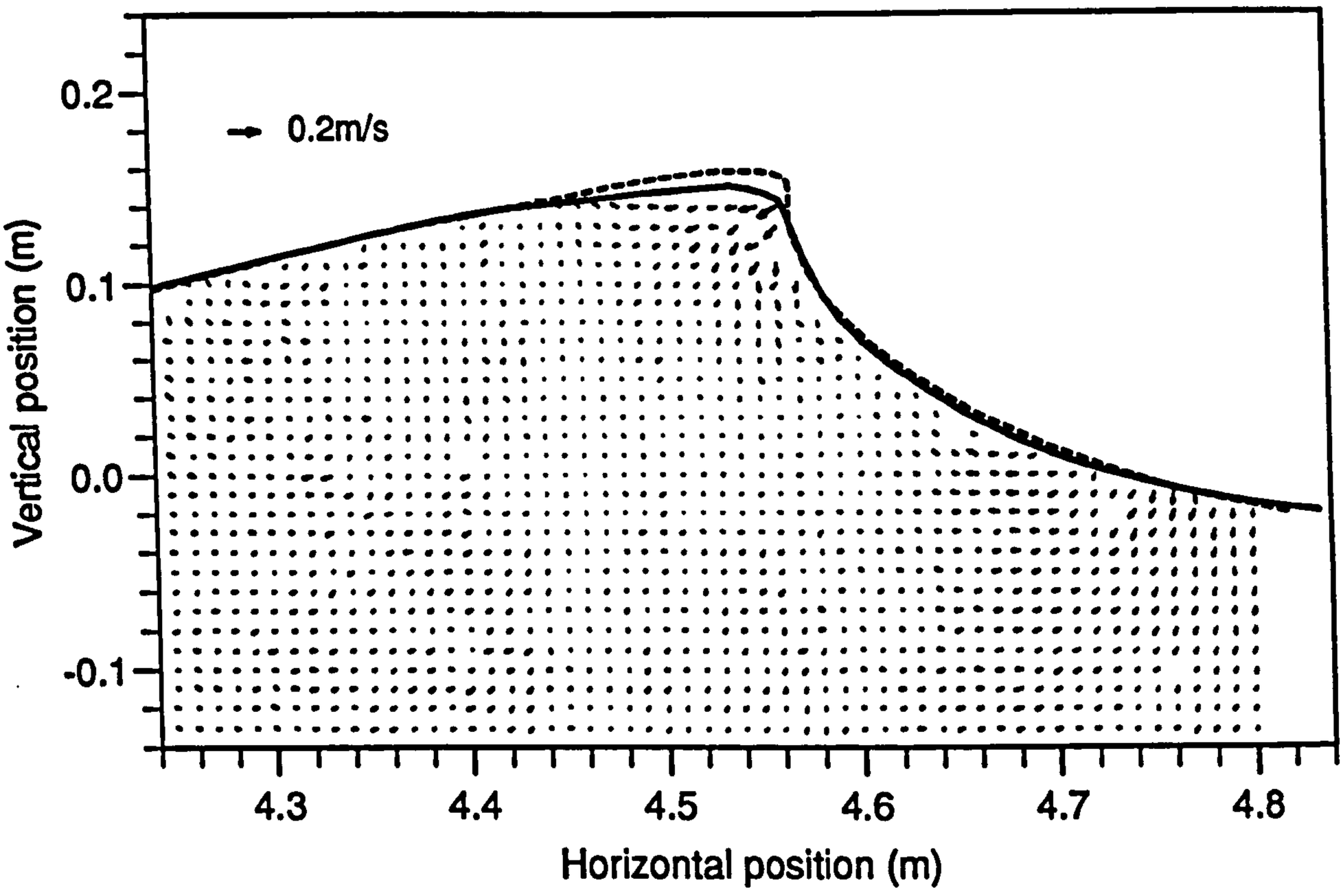

Figure 4.51: Difference between experimentally measured velocity field, $t = 12.250$s, and numerical data, $t = 12.175$s. — experimental surface, - - - numerical surface

the area below and in front of the crest. Given that the surface profiles are not very well matched above this region, this is not too surprising.

The maximum, numerically determined velocity of this phase of the wave is 1.82ms^{-1}. Various statistics were derived from the difference data, which can be used to quantify the match. The mean of the magnitude of the subtracted velocities is $.041\text{ms}^{-1}$ and the standard deviation $.023\text{ms}^{-1}$, which, compared to the maximum velocity, are 2.3% and 1.3% respectively. The mean of v_x corresponds to 1.7% and of v_z to 0.8%.

The overall quality of this match is taken to be 2.3%. In the region below and in front of the crest the figure derived in the same way would be about 4%, and in the crest about 1%. The overall value can be reduced by shifting the numerical data by .21m instead of .22m

To gauge the sensitivity of this comparison process, the same numerical data was subtracted from experimental data for a slightly earlier phase, that plotted in figure 4.28. Figure 4.51 shows the data obtained in this way, with the numerical data shifted sideways by .13m. While the match of the surface and internal velocities in the crest regions is less good, the overall agreement is better, possibly because the surface match is better when judged over the whole wave. From the statistics the overall match quality is 1.4%

It is clear that by careful selection and shifting of the data, the quality of the match can be brought into the range 1% to 2%. However, this approach could be slightly misleading, and it is perhaps better to say that the match is good to within about $2\frac{1}{2}\%$, as obtained from figure 4.50.

Internal Kinematics of the Plunging Phase

In experiment (c), close-up photographs were taken of the plunging tip. The internal kinematics obtained from plate 1 are shown in figure 4.52 in the form of a vector plot. Velocity vectors are present in the crest, even into the plunging tip, where the illuminating beam must have passed through two water surfaces.

In order to gauge repeatability, figure 4.53 contains a vector plot of a repeat of the same experimental conditions and triggering time. The two plots compare as favourably as can be assessed from this type of representation of the data, and the different locations of the missing vectors is the only noticeable feature. It should be noted that the large patch of missing vectors in the middle of each figure is due to a registration mark on the glass obscuring the view.

In figure 4.54, a numerically generated velocity field is plotted for the phase matching that shown in the experimental plots, figures 4.52 and 4.53. The similarity is striking, and if not for the missing vectors, it would be hard to tell the difference, with this means of graphical rendering, between experimental measurements and numerical predictions.

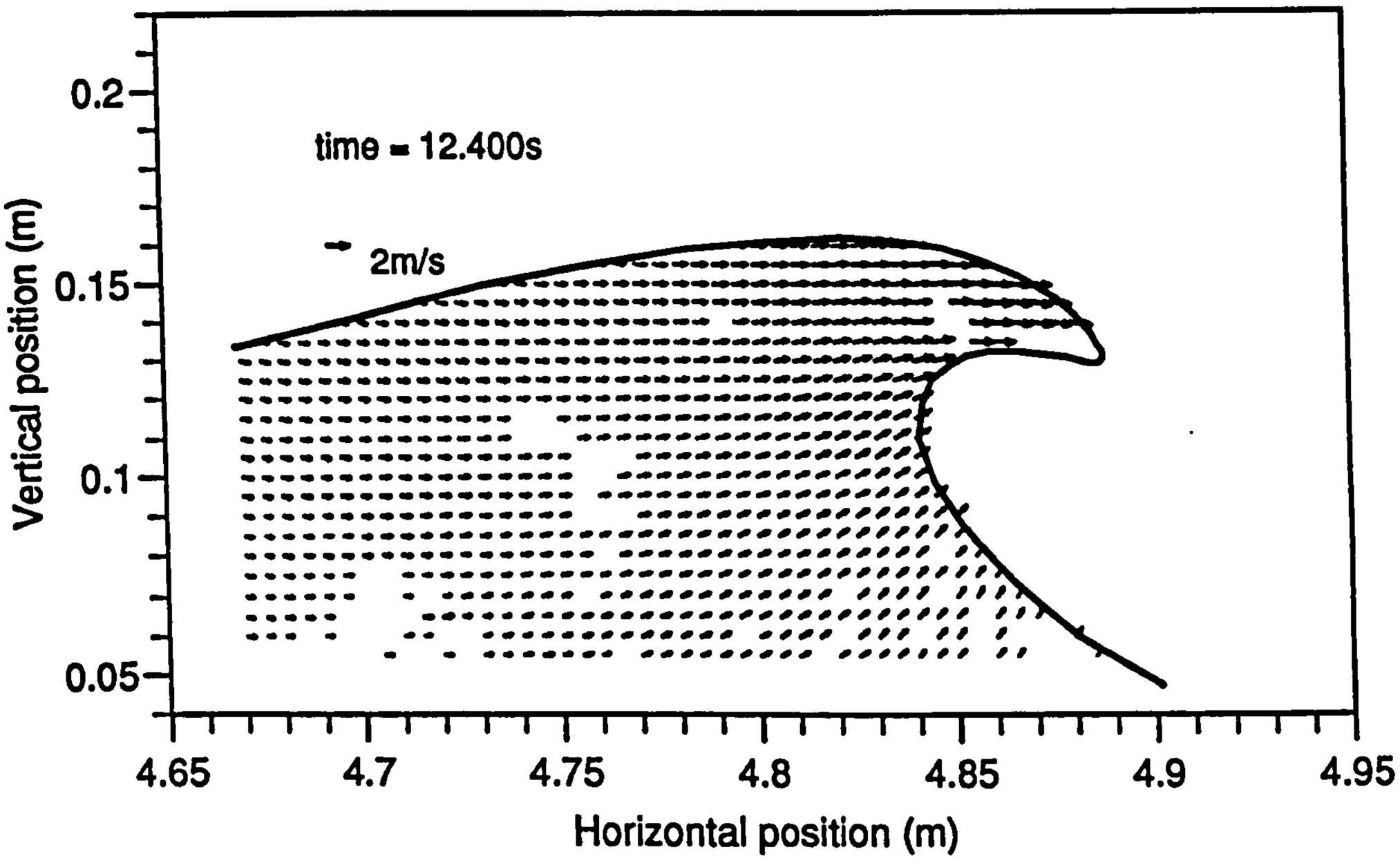

Figure 4.52: Experimentally measured velocity field, plunging phase, $t = 12.4$s

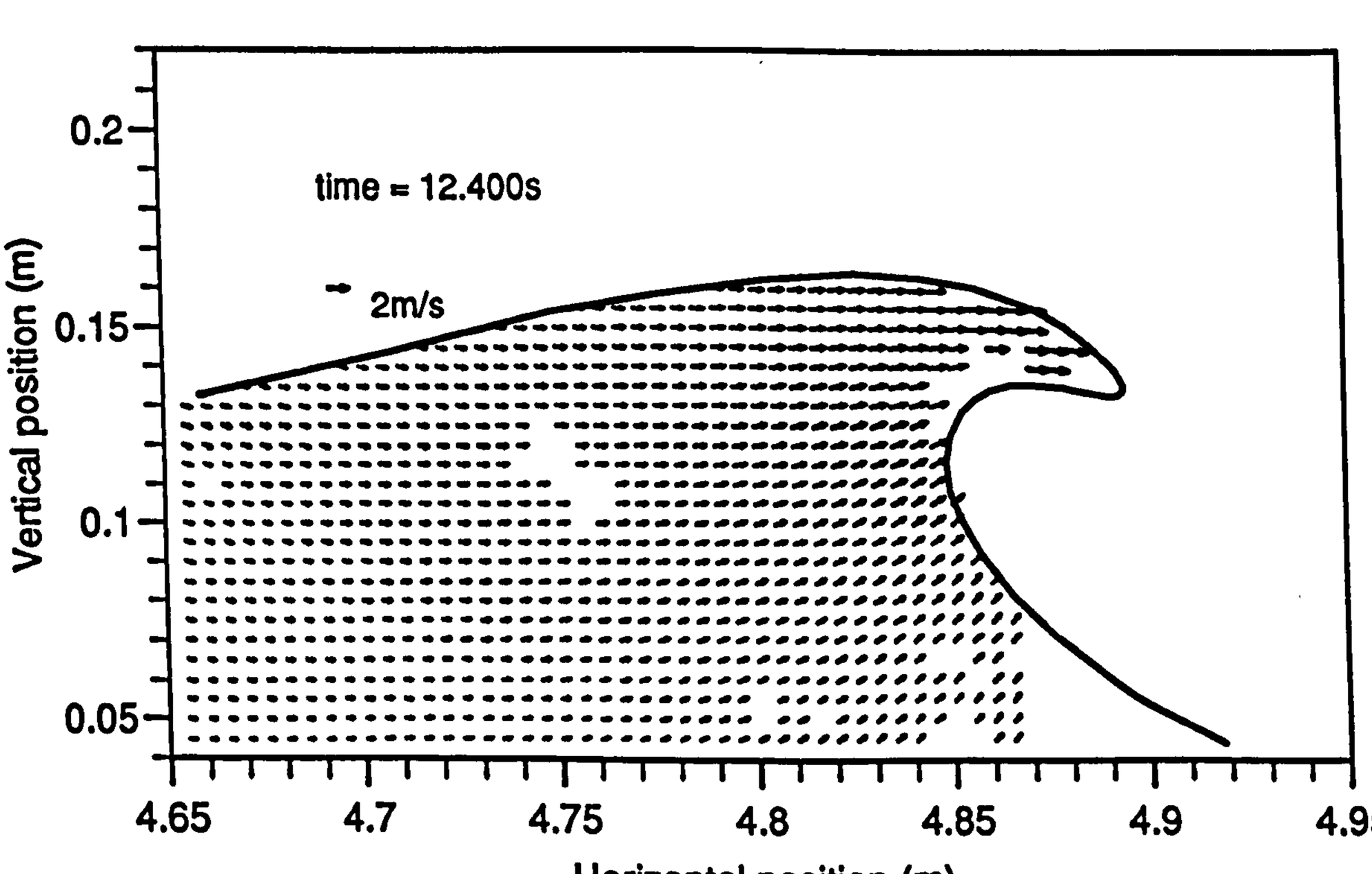

Figure 4.53: Experimentally measured velocity field, plunging (repeat), $t = 12.4$s

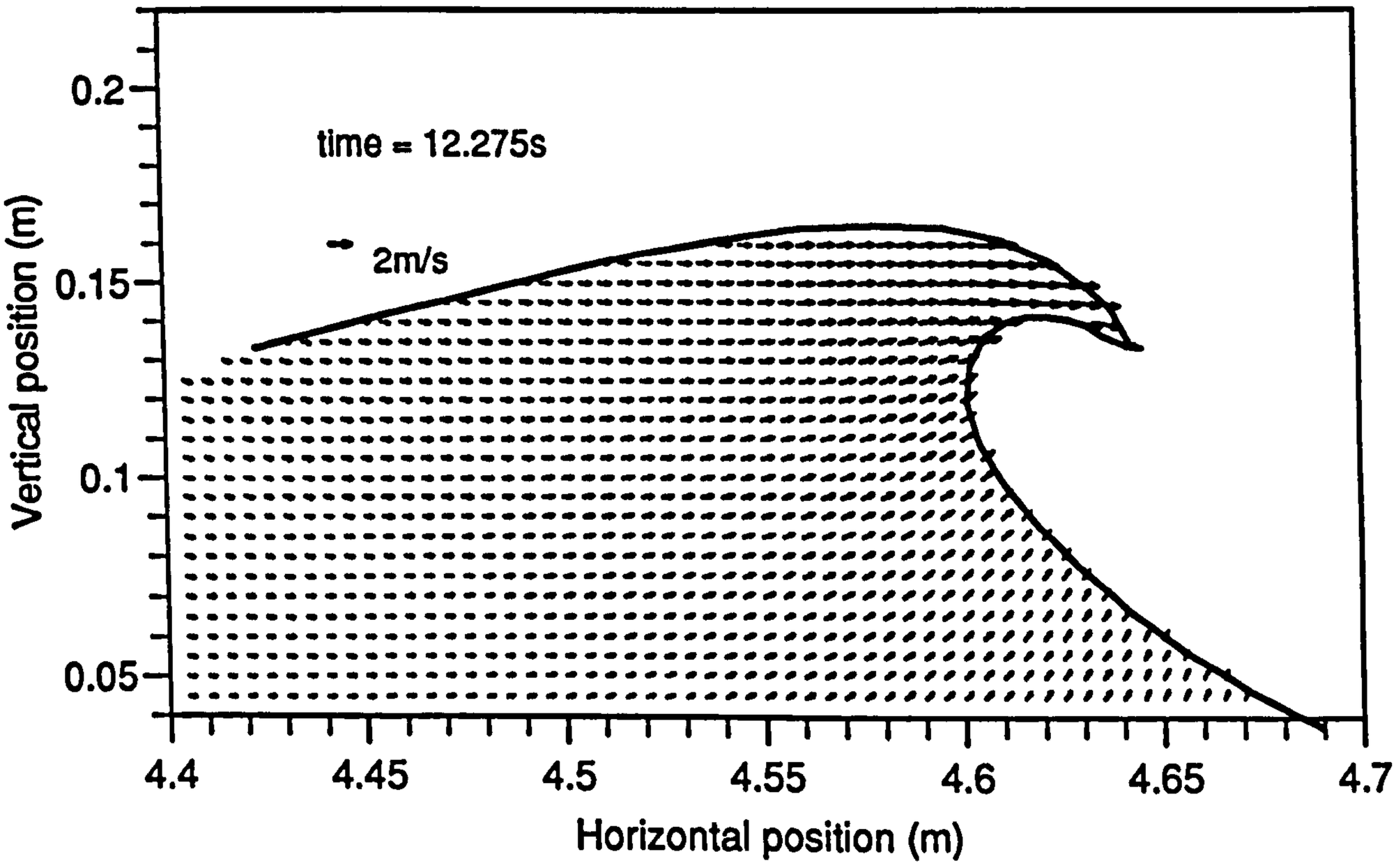

Figure 4.54: Numerically generated velocity field, $t = 12.275$s (compare 12.4s)

To highlight the differences between the experimentally measured and numerically generated vector fields, the data was subtracted. Figure 4.55 contains the difference between 4.52 and figures 4.54. This time the numerical data has been shifted sideway by .24m and *upwards* by .005m. The velocity vectors are plotted 10 times bigger than in the plots of the raw data.

The overall quality of the match is very high, with many areas containing only very small vectors. However, in the region where the water surface is vertically-fronted there are some significant discrepancies, which is to be expected in this area of high acceleration if the relative positioning of the vector fields is not quite right.

From the maximum numerical velocity (2.3ms^{-1}) and the mean of the magnitudes of the subtracted velocities ($.039\text{ms}^{-1}$), the quality of the match can be estimated to be 1.7%. The standard deviation of the velocity magnitudes corresponds to 1.2%, the mean of the v_x components to .2% and the mean of the v_z components

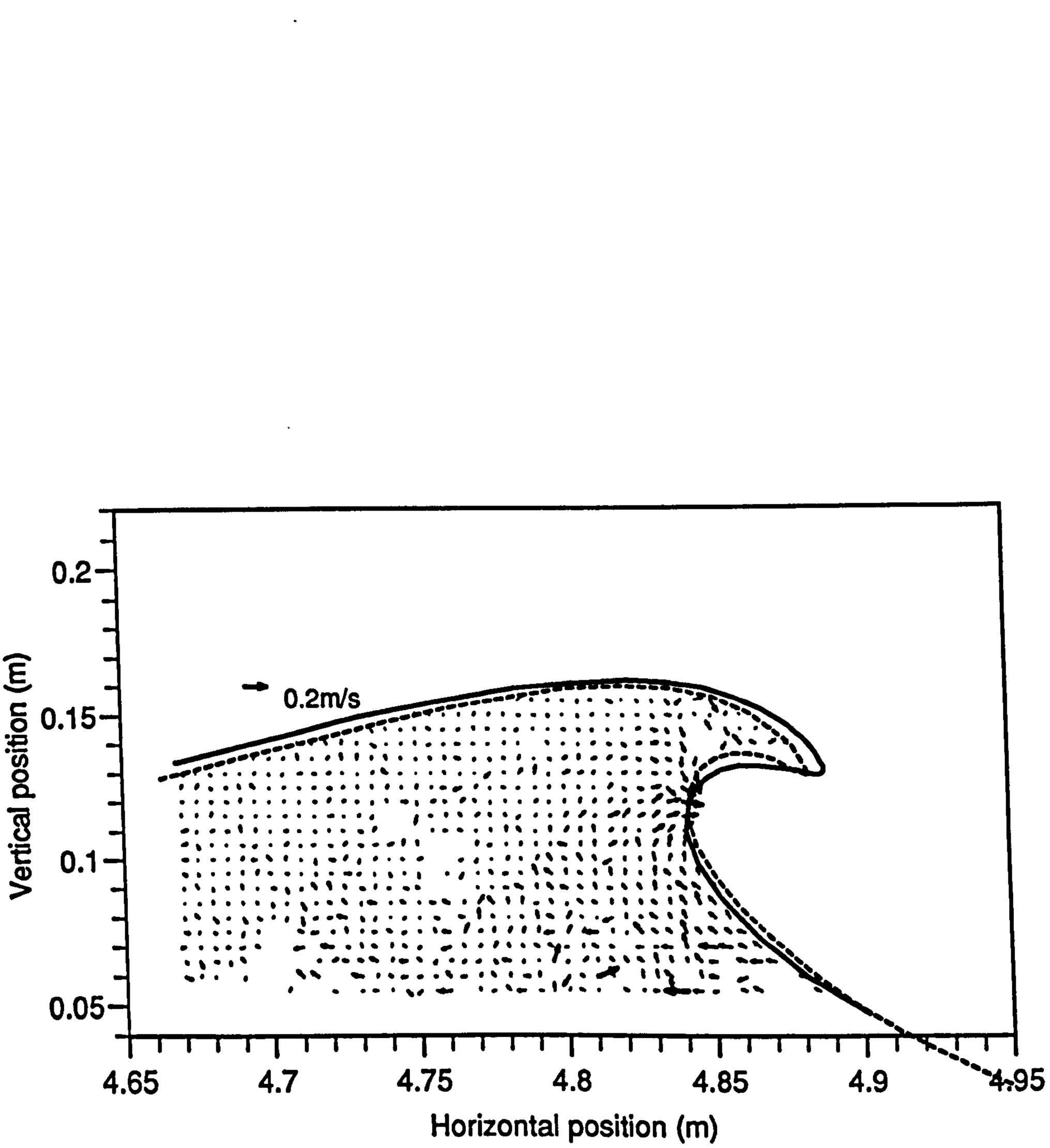

Figure 4.55: Difference between experimentally measured velocity field, $t = 12.400$s, and numerical data, $t = 12.275$s. — experimental surface, - - - numerical surface

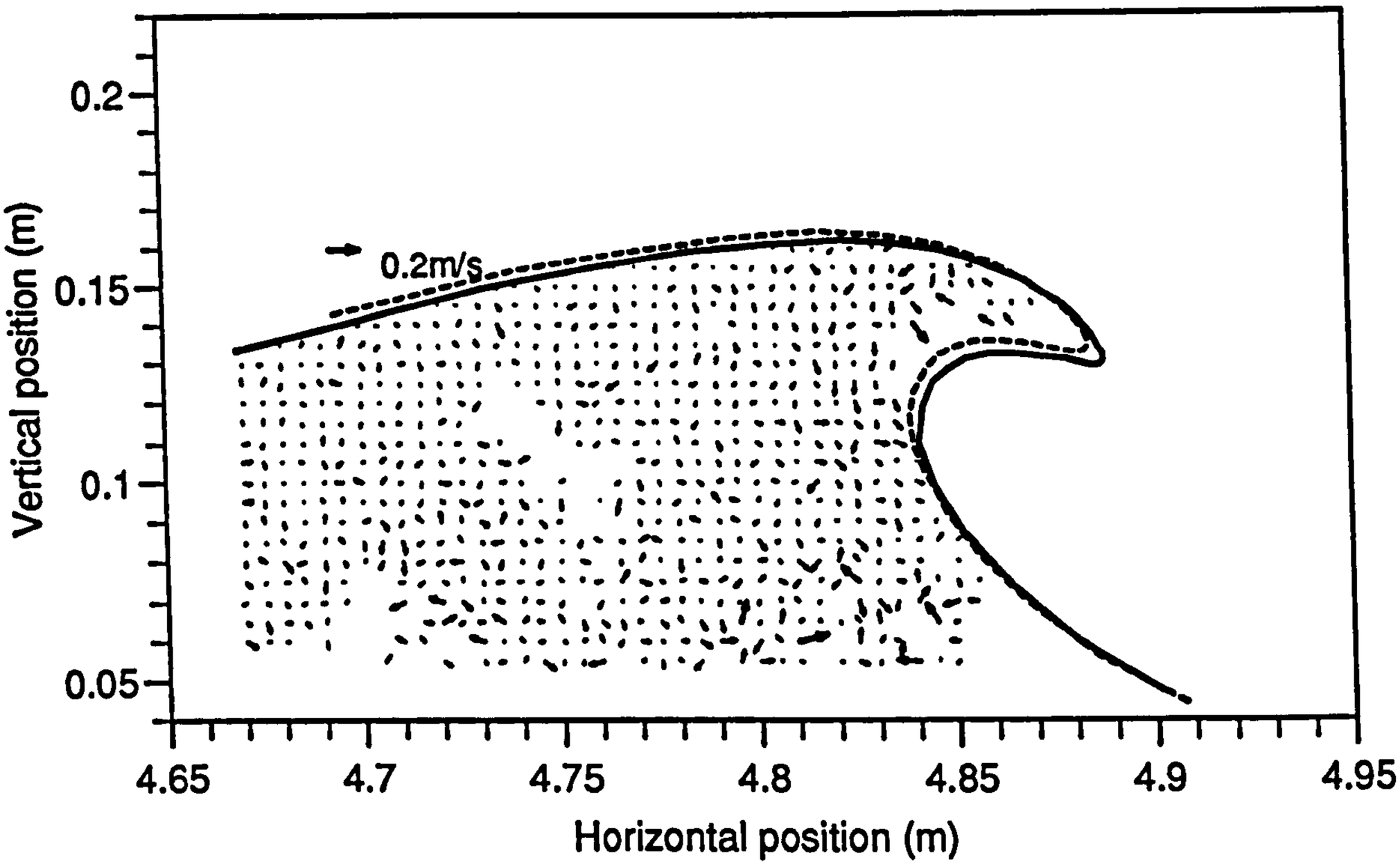

Figure 4.56: Difference between two experimentally measured velocity fields, $t = 12.400$s. — experimental surface, - - - surface of the repeated wave

to .5%. There is no apparent systematic trend in the data and it is not clear which is the most appropriate statistic for judging the match. Depending on which statistic is chosen, the quality of the match can be found to be anywhere in the range 0.5% to 2.0%.

In order to gauge repeatability and experimental noise, the two experimental vector fields for this phase of the wave were subtracted and the result plotted in figure 4.56. One of the flow fields was shifted by .02m before the subtraction so that the surface profiles would match. The match appears slightly better than that between experiment and prediction, with no systematic trends near the front face of the wave. Applying the same calculations to the statistics, the mean value of the velocity magnitudes was found to be 1.1% of the maximum velocity, the mean of v_x to be 0.8% and the mean of v_z to be 0.4%.

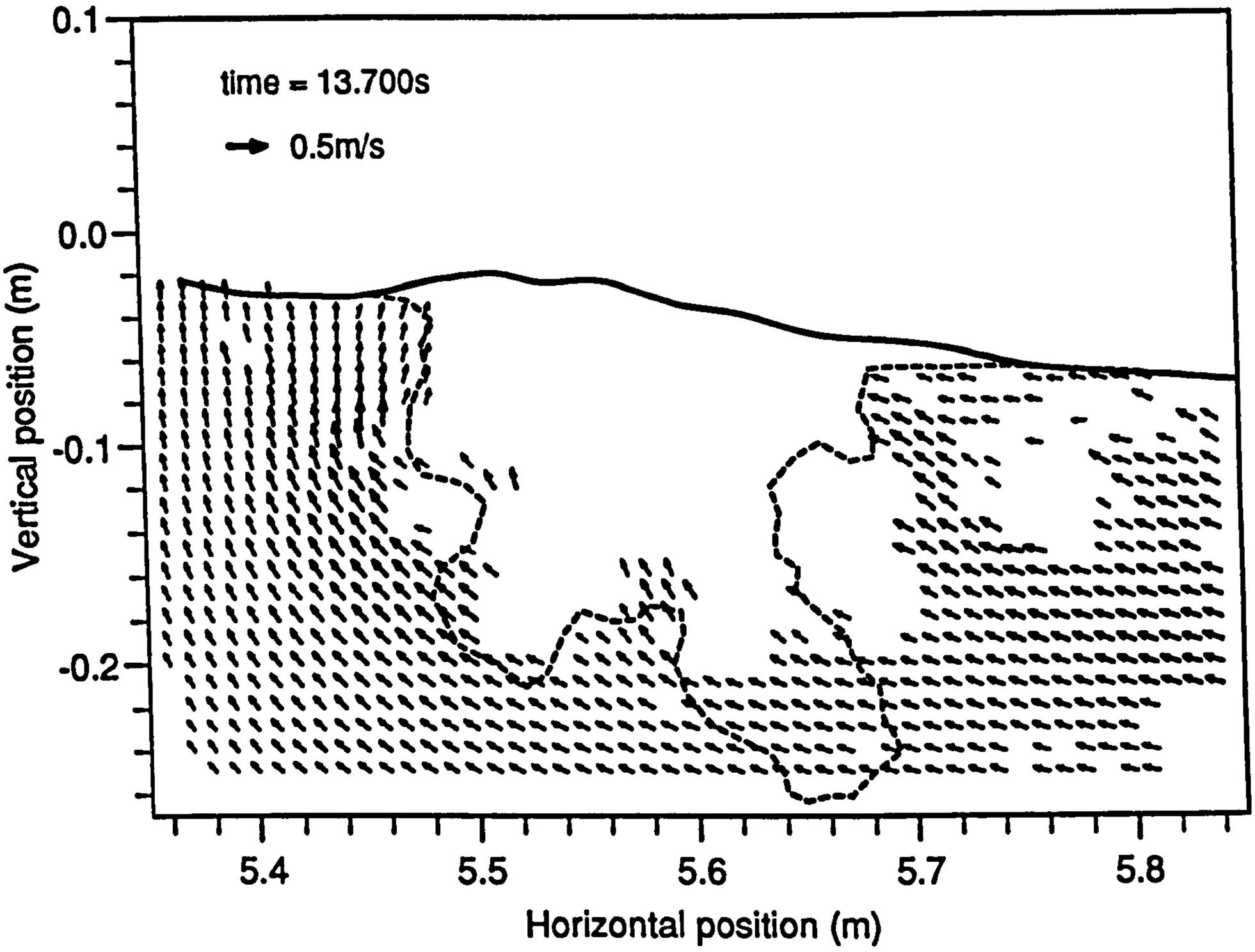

Figure 4.57: Experimentally measured velocity field, shortly after breaking, $t = 13.7$s

Internal Kinematics of the Post-breaking Phase

The quality of the results after breaking was not as high: this was to be expected as the flow was very turbulent and there was a considerable amount of air entrainment. Nevertheless, some measurements of velocity were extracted, such as those illustrated in figure 4.57. These kinematics were obtained from plate 3, and as expected, no vectors were achieved in the region of high aeration. In the graph, a small area of high shear can be seen near the top left extent of the aerated region.

4.7 Different Ways of Presenting at the Experimental Data

The velocity vector plots of the internal kinematics illustrated in figures 4.24 onwards provide the most natural way of presenting the raw experimental data. However, they are somewhat limited as the size of each vector is small and fine detail of the flow field is not resolved. In addition, the visual effect of the data is somewhat dependent on the density of the grid.

4.7.1 Iso-velocity Graphs

A useful, general way of presenting flow field data is by means of contour plots of the velocity components. Contour plots are preferred to 3-D representation of the data as quantitative assessments are more readily made, and, more importantly, both components can be seen on the same graph. The resulting graphs are independent of the velocity vector density, so that data on different spatial grids can be more easily compared.

In the iso-velocity plots that follow, the contour interval is $0.1 ms^{-1}$, with the contours at $0.5 ms^{-1}$ intervals labelled and drawn dashed. The contours of constant horizontal velocity component appear like arcs centred near the top of the crest, with their maximum value normally at the top. Contours of constant vertical velocity component cross at right angles, and generally increase in the same direction as the wave propagation, from left to right. The $v_z = 0$ contour can be identified in most cases as the dashed line that meets the surface near the crest. There is no interpolation or extrapolation of data in any of the graphs.

Figures 4.58 to 4.77 contain the same data as was plotted in figures 4.24 to 4.43, this time as iso-velocity contour plots of the horizontal and vertical components. The most striking feature of these graphs is the smoothness of the contours which indicates a lack of turbulence in the flow and of random errors in the PIV process.

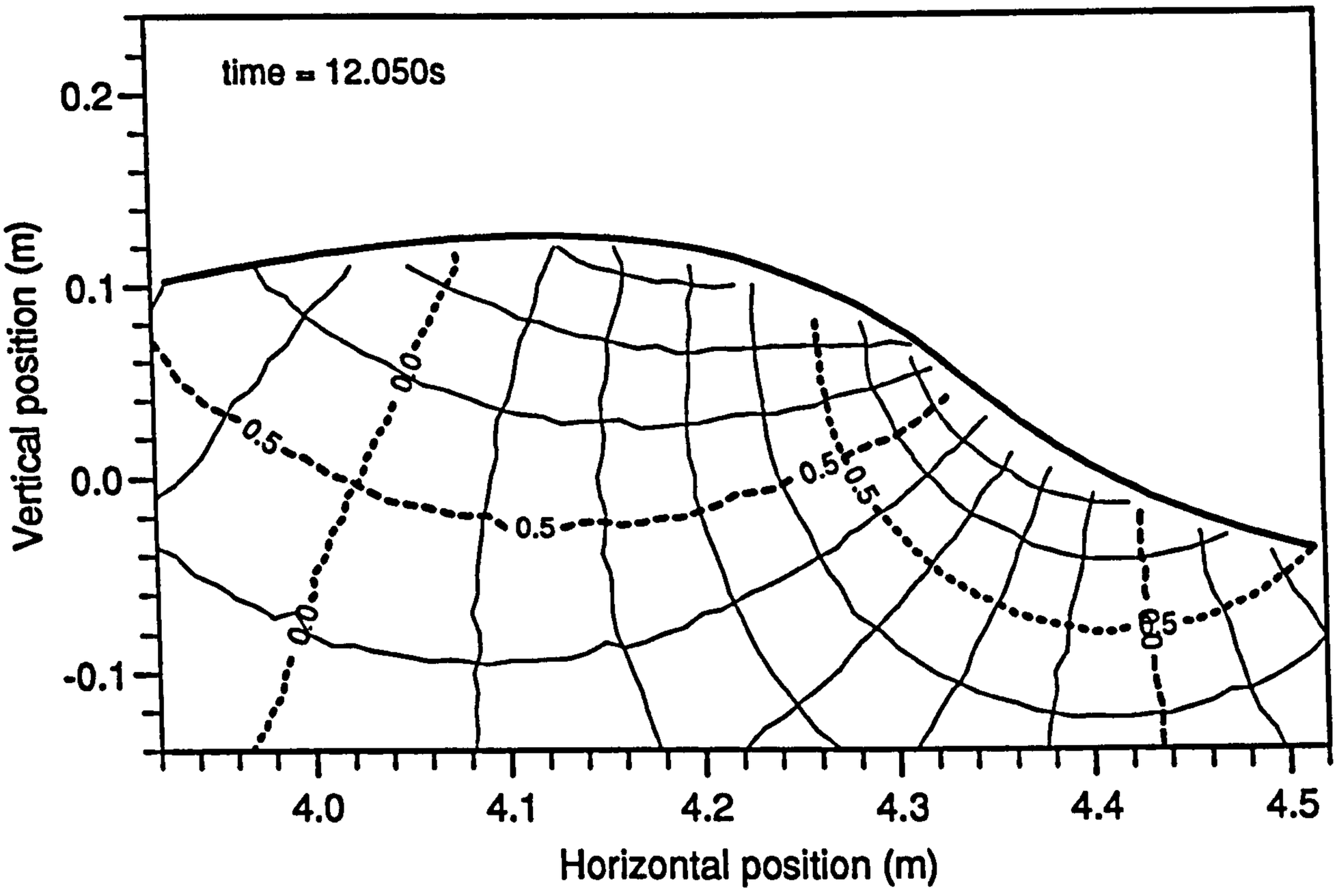

Figure 4.58: Experimentally derived isovelocity contours, $t = 12.050$s

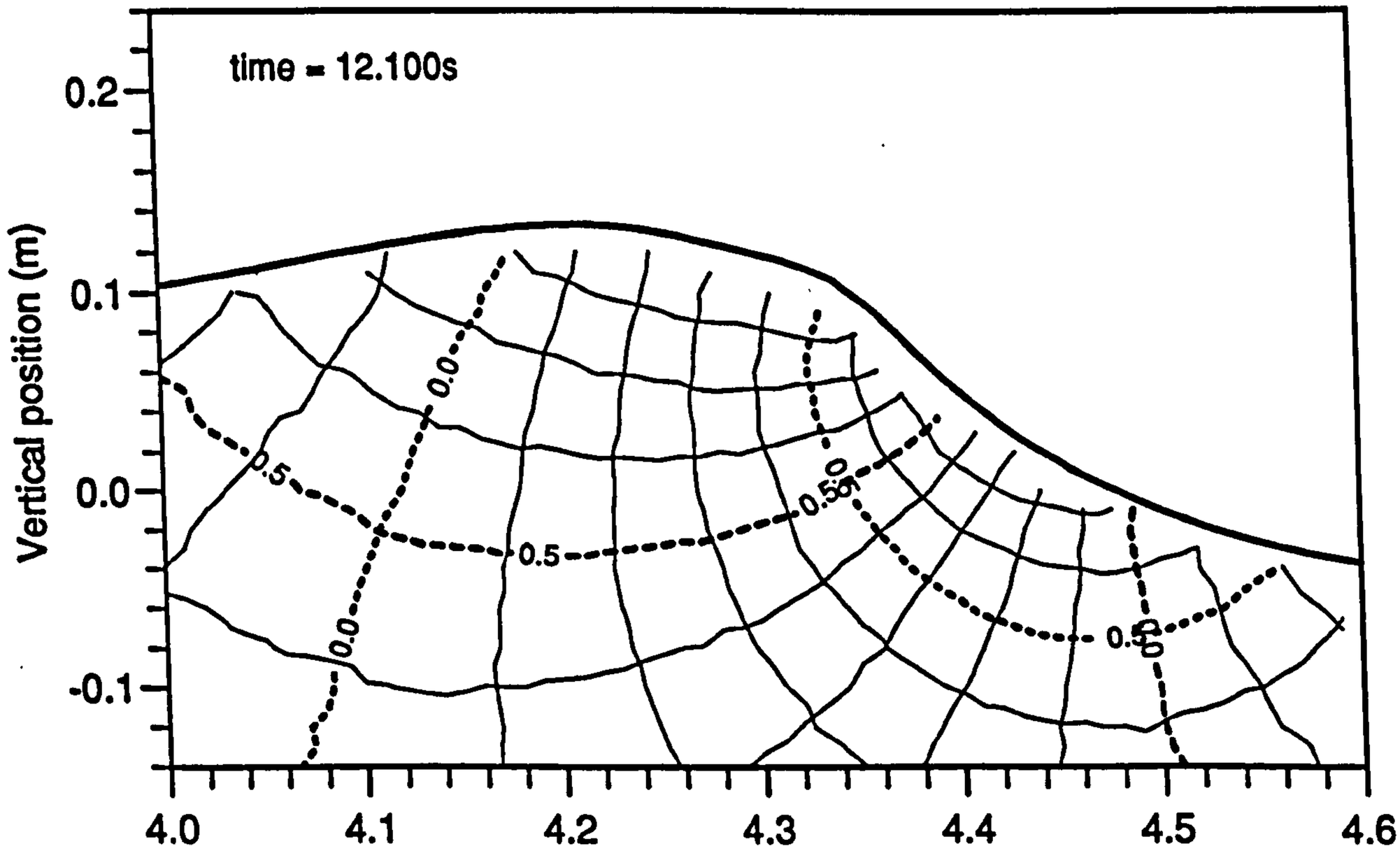

Figure 4.59: Experimentally derived isovelocity contours, $t = 12.100$s

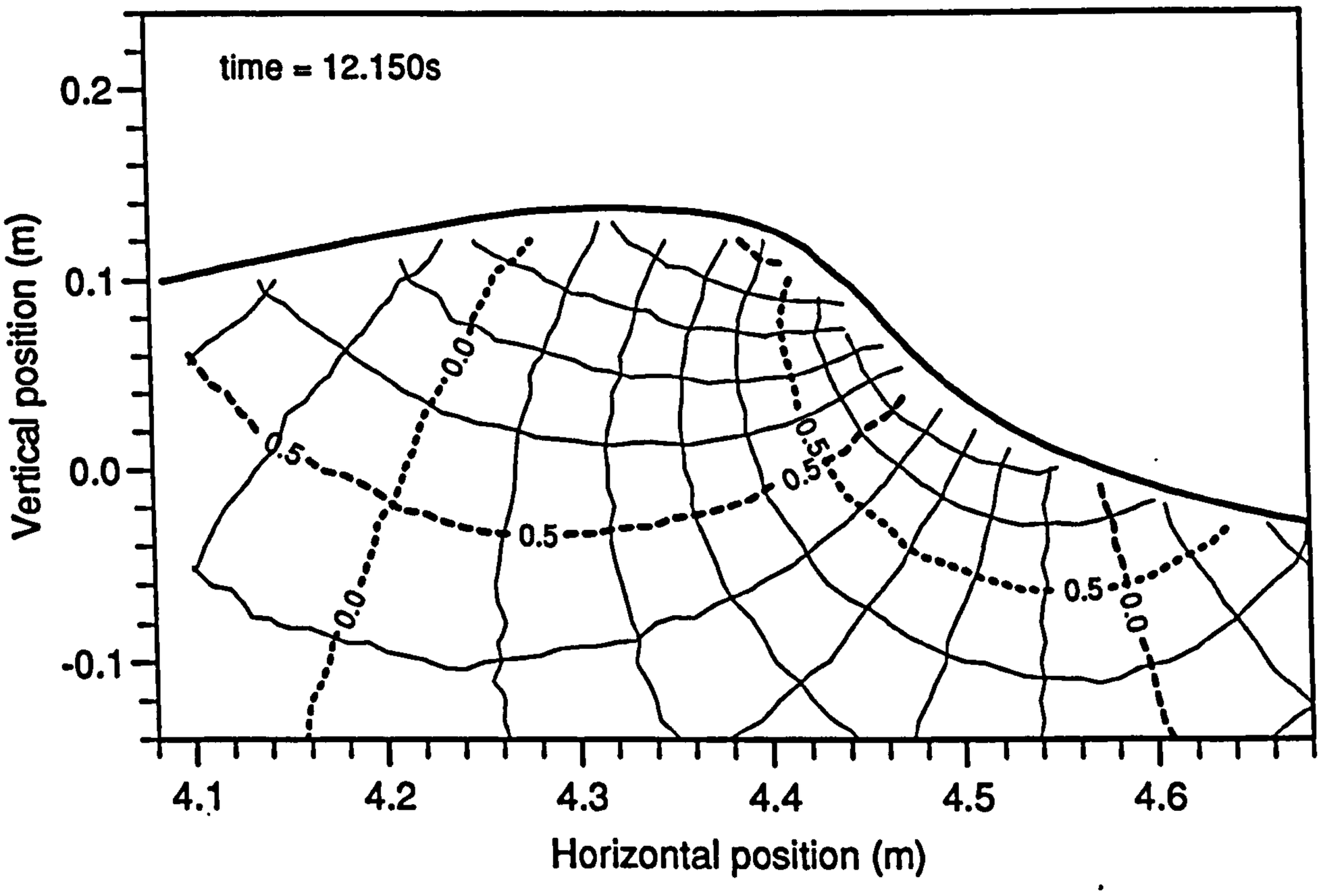

Figure 4.60: Experimentally derived isovelocity contours, $t = 12.150$s

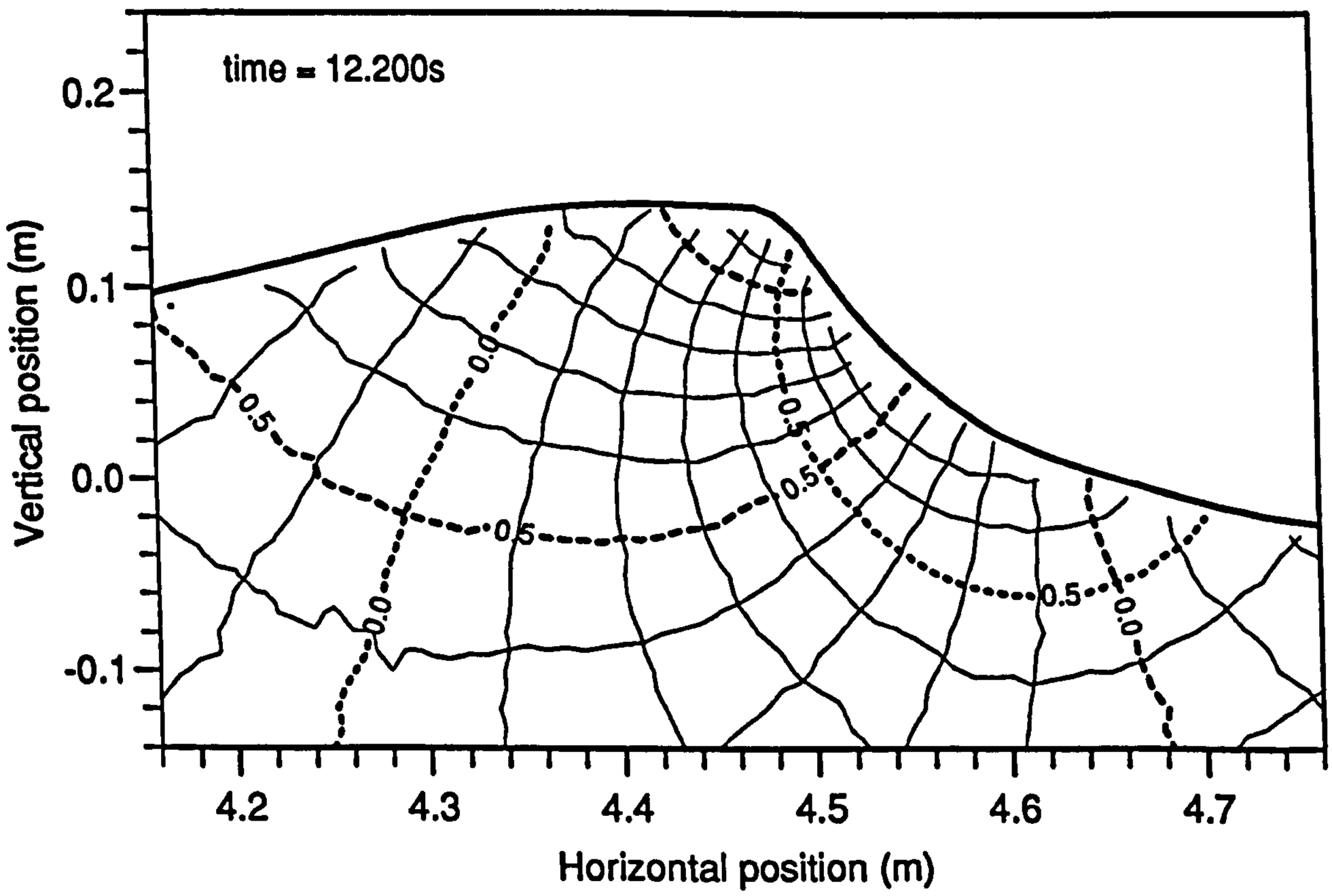

Figure 4.61: Experimentally derived isovelocity contours, $t = 12.200$s

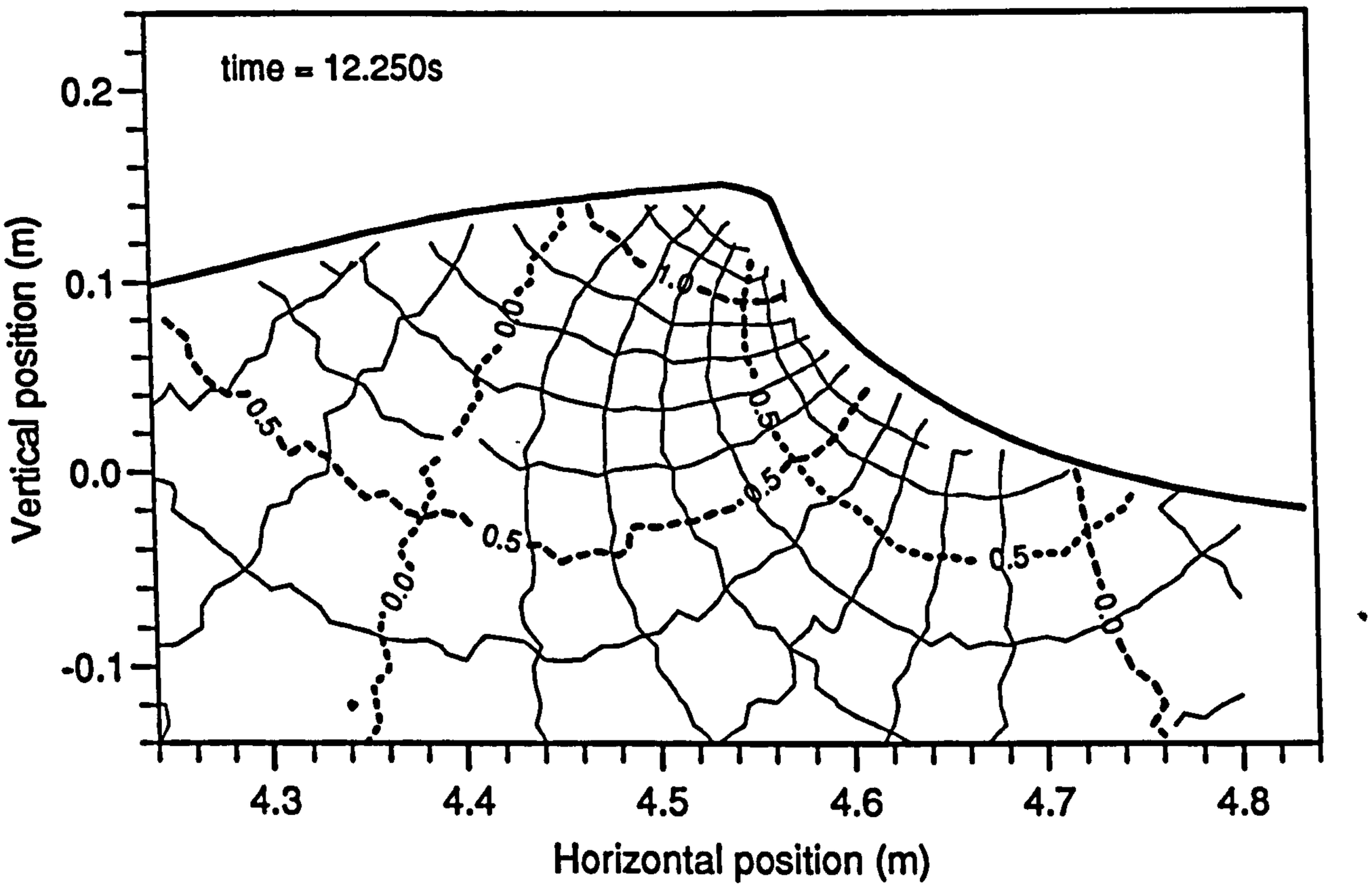

Figure 4.62: Experimentally derived isovelocity contours, $t = 12.250$s

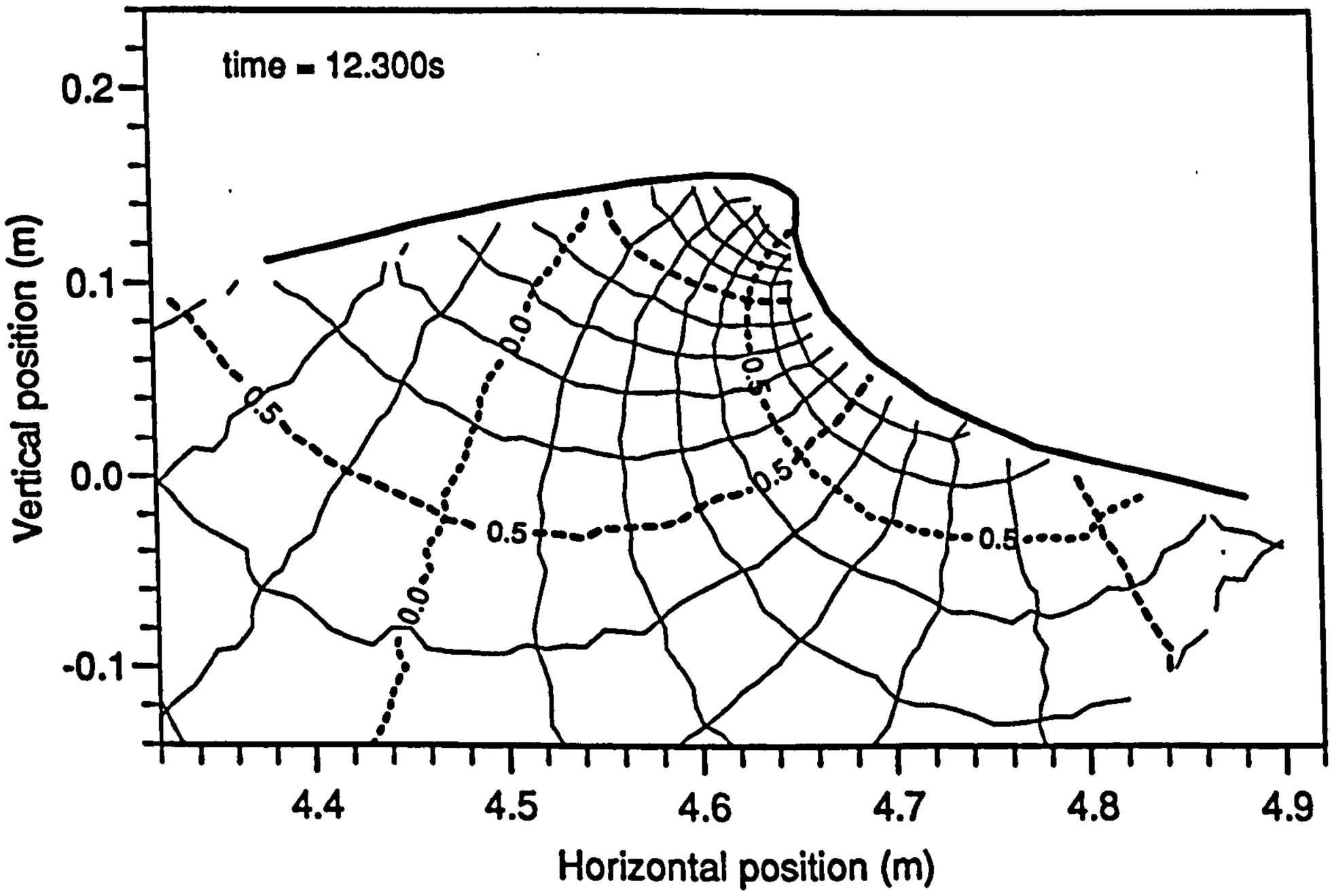

Figure 4.63: Experimentally derived isovelocity contours, $t = 12.300$s

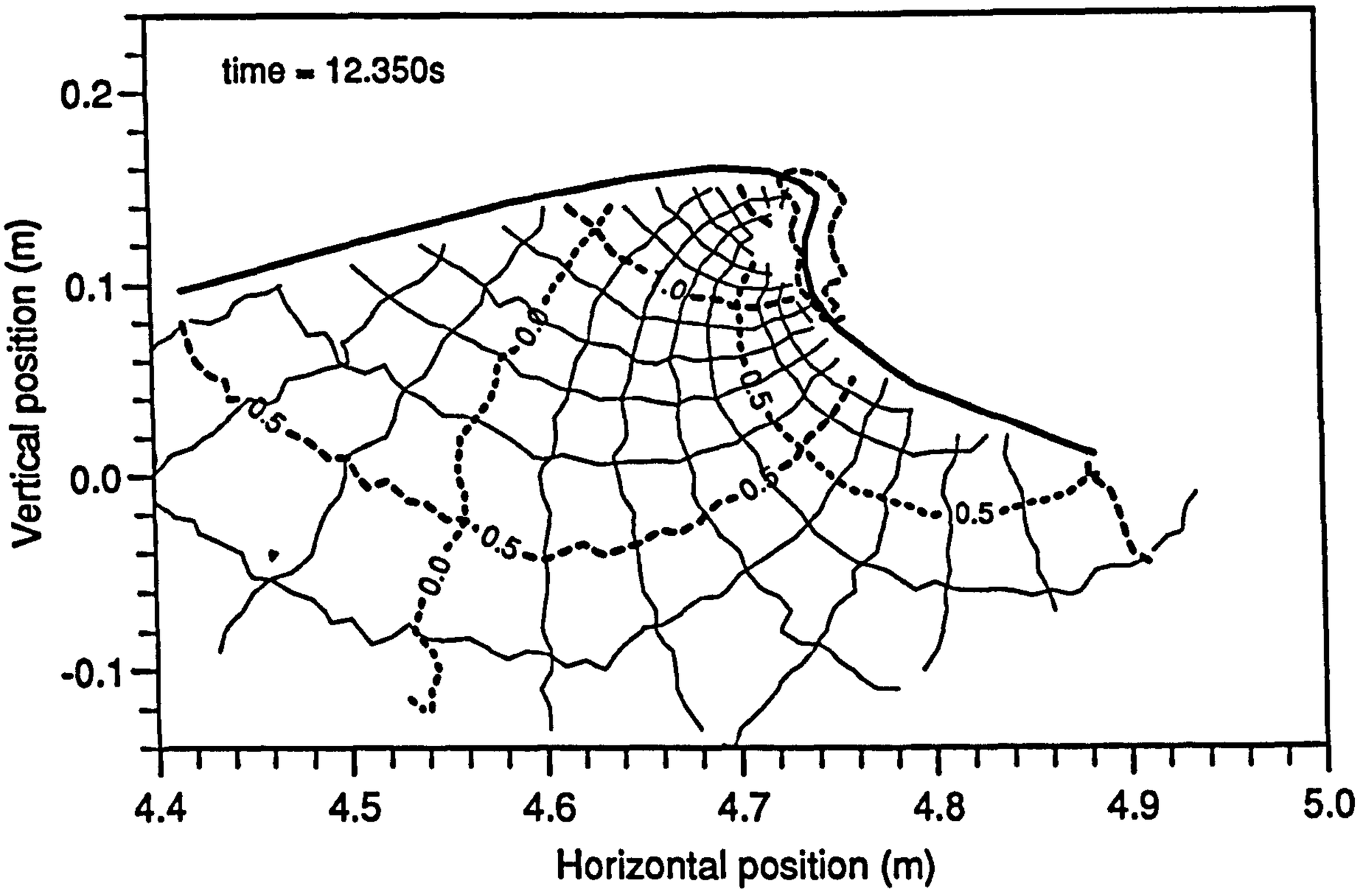

Figure 4.64: Experimentally derived isovelocity contours, $t = 12.350$s

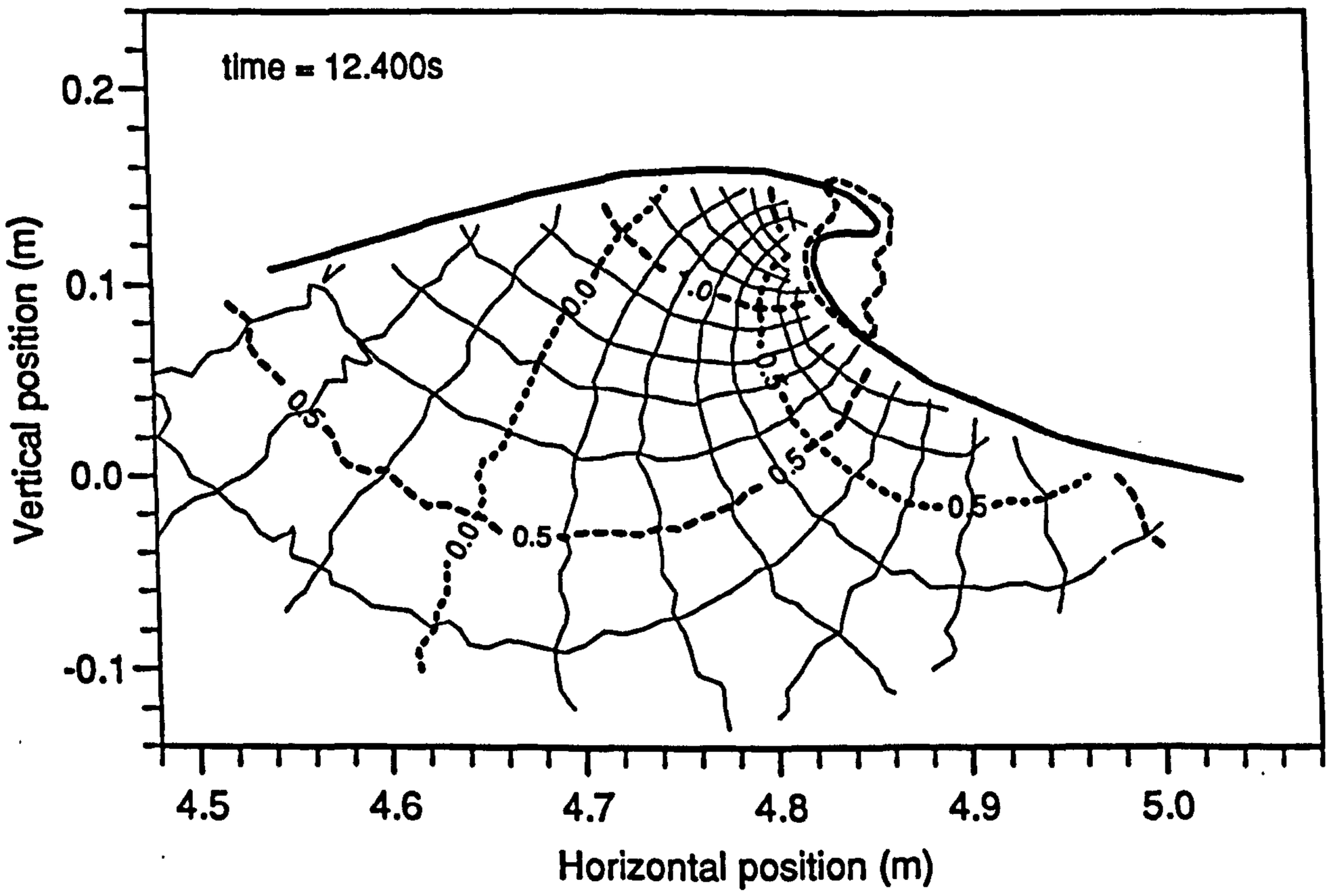

Figure 4.65: Experimentally derived isovelocity contours, $t = 12.400$s

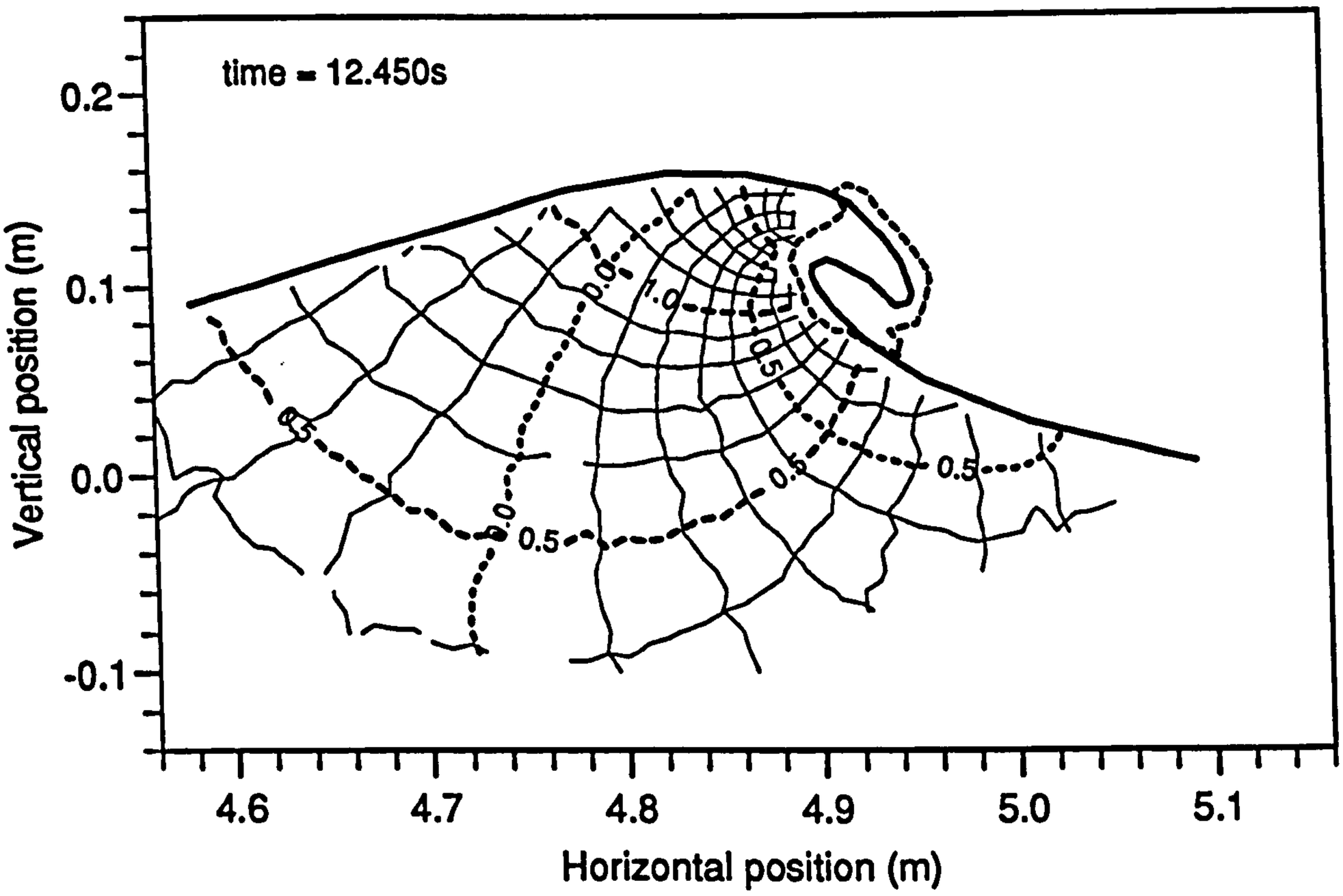

Figure 4.66: Experimentally derived isovelocity contours, $t = 12.450$s

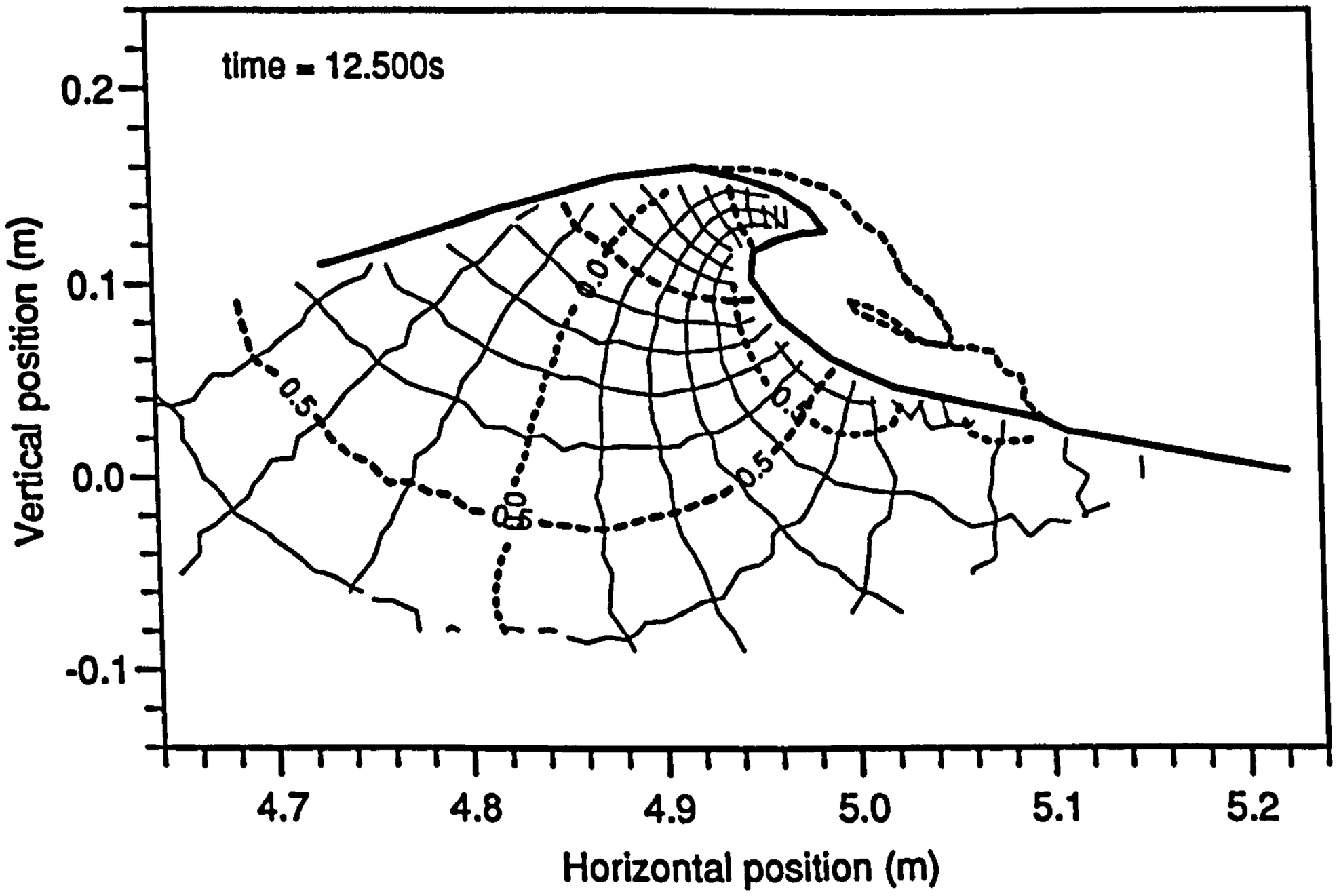

Figure 4.67: Experimentally derived isovelocity contours, $t = 12.500$s

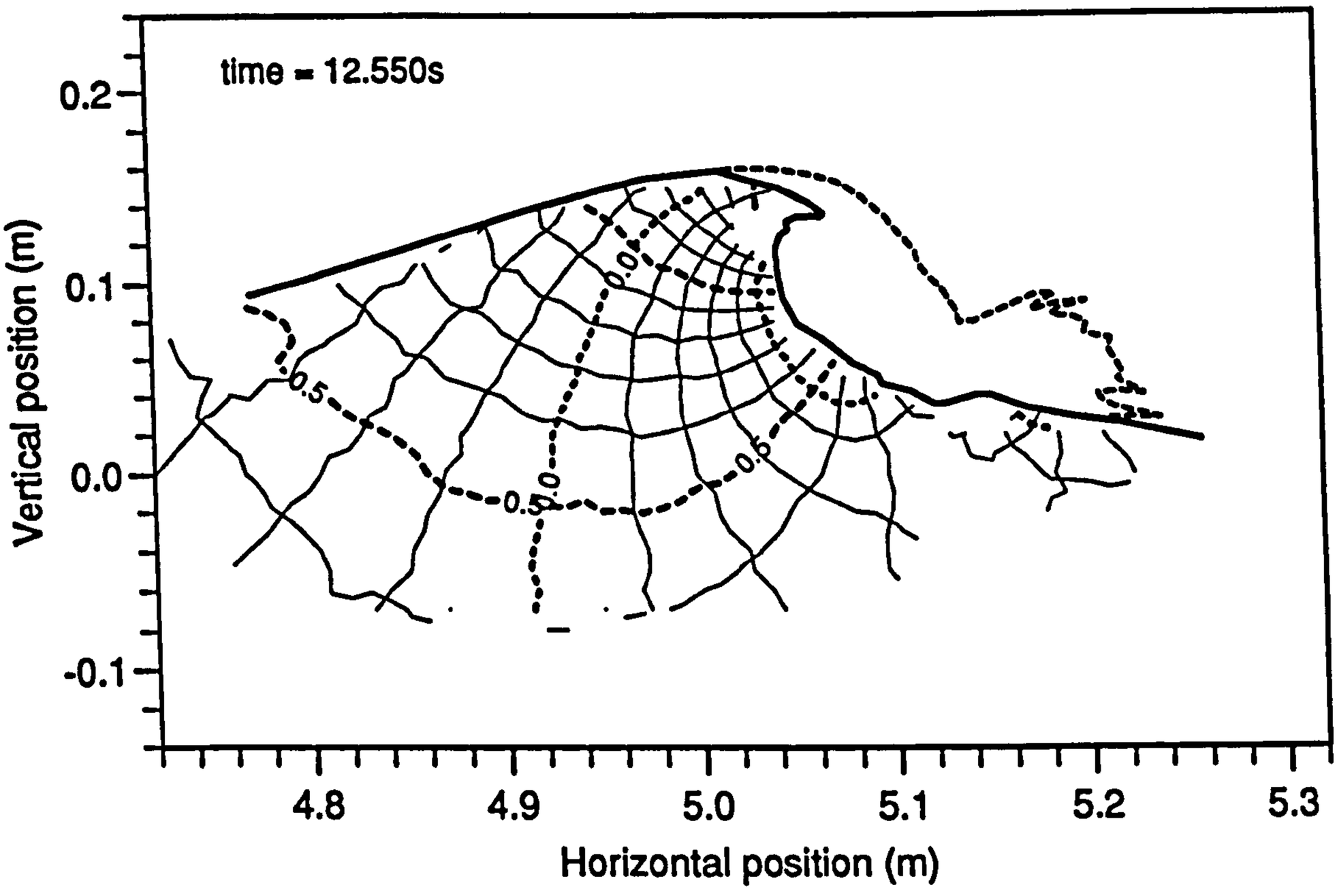

Figure 4.68: Experimentally derived isovelocity contours, $t = 12.550$s

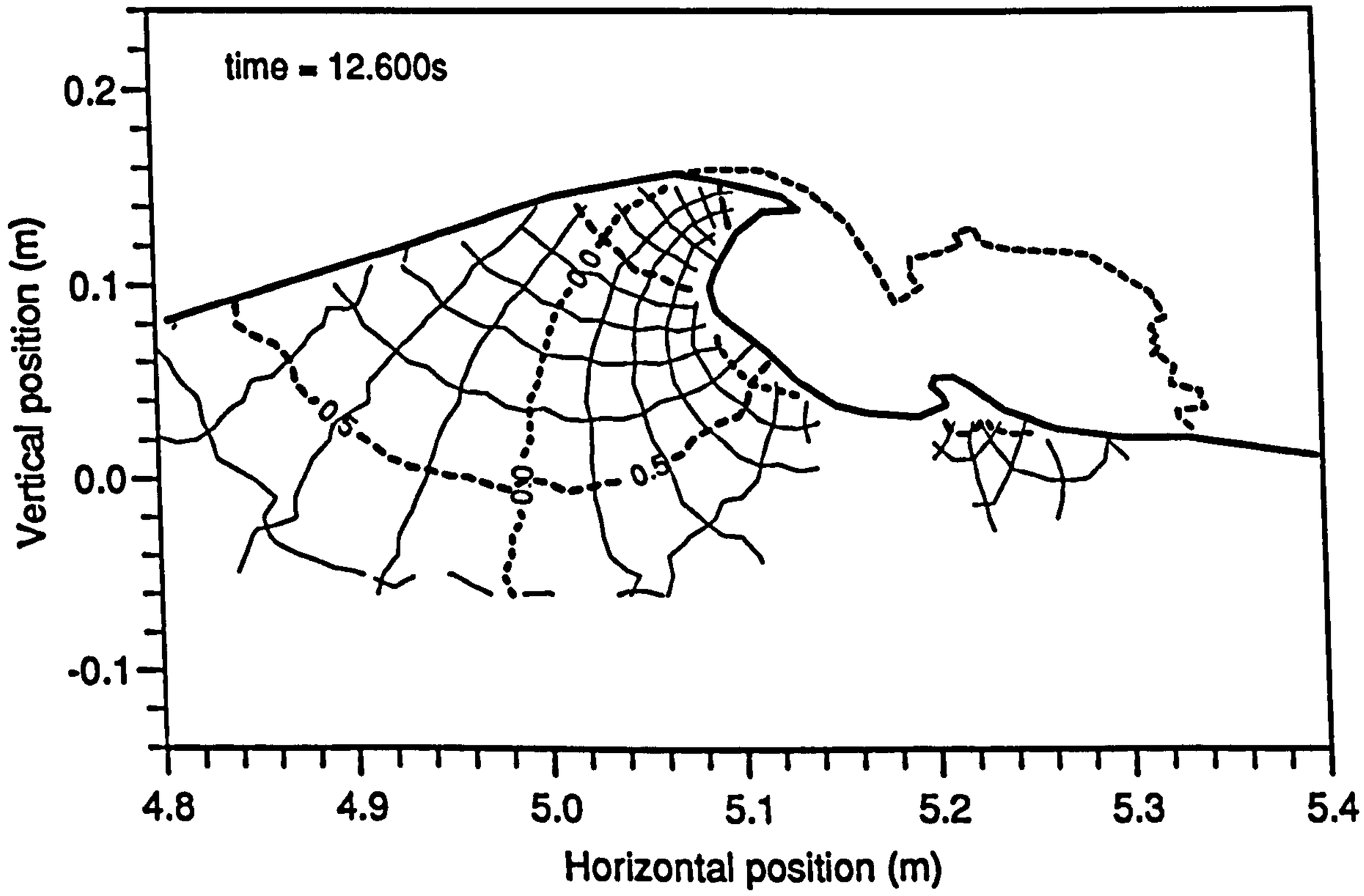

Figure 4.69: Experimentally derived isovelocity contours, $t = 12.600$s

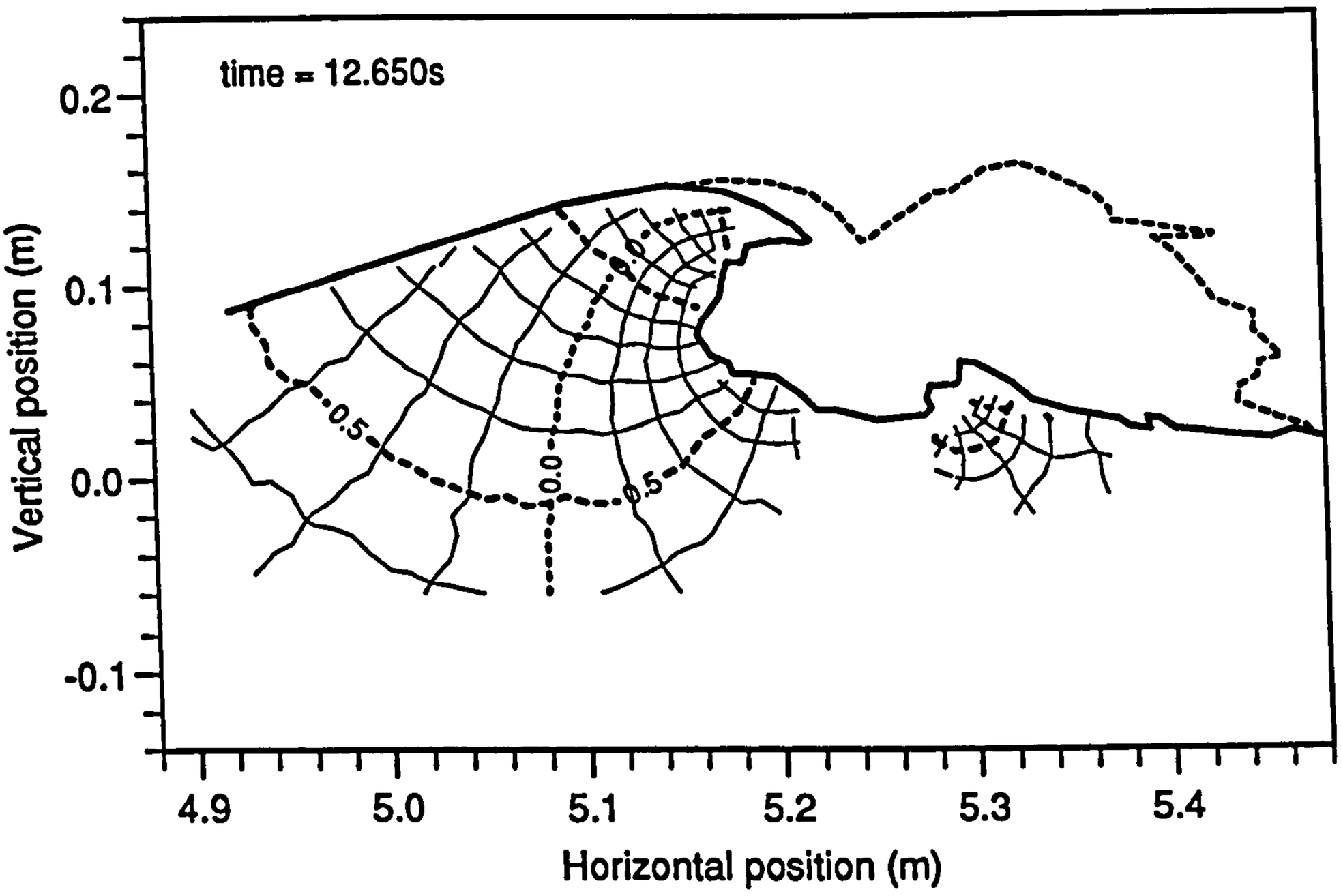

Figure 4.70: Experimentally derived isovelocity contours, $t = 12.650$s

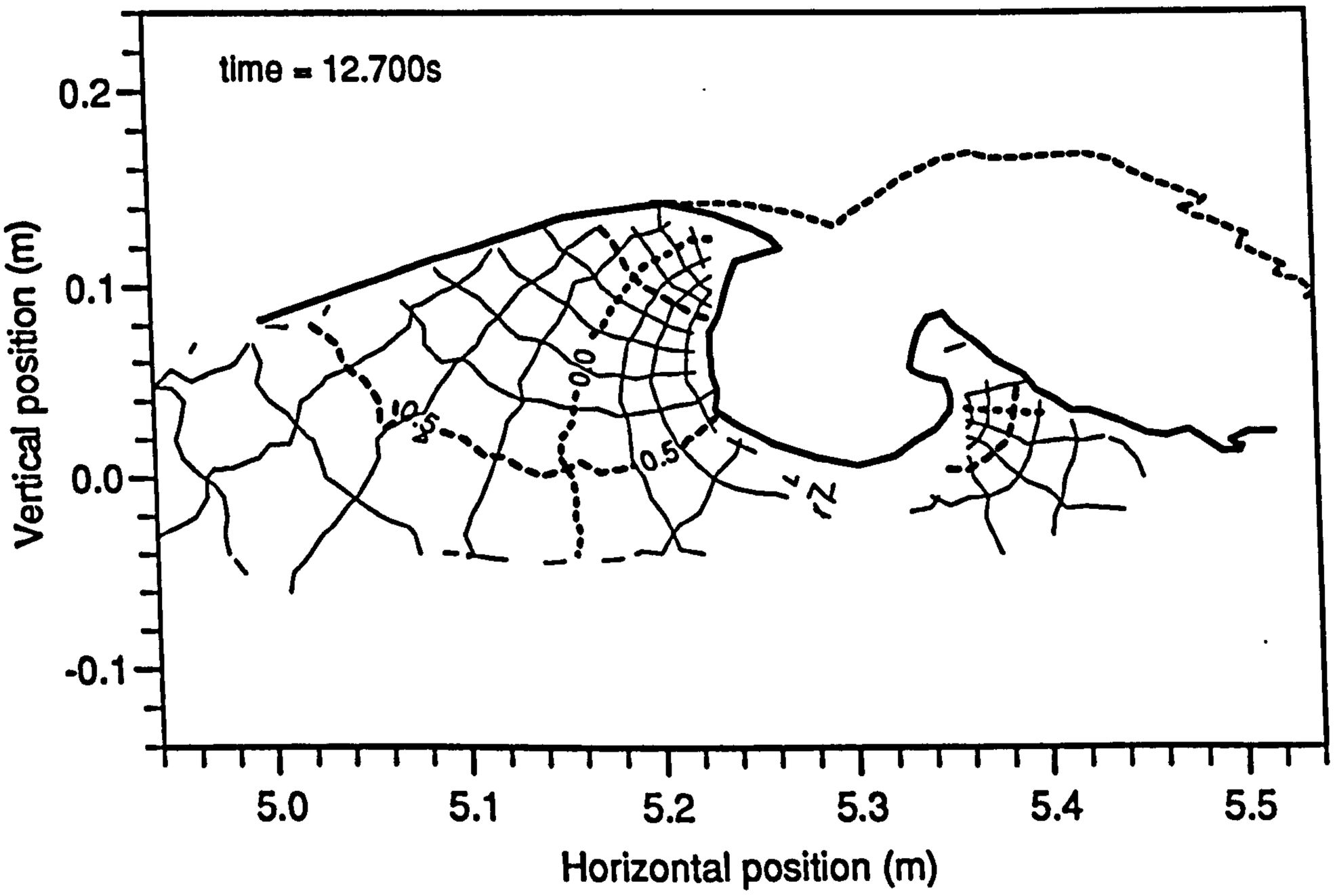

Figure 4.71: Experimentally derived isovelocity contours, $t = 12.700$s

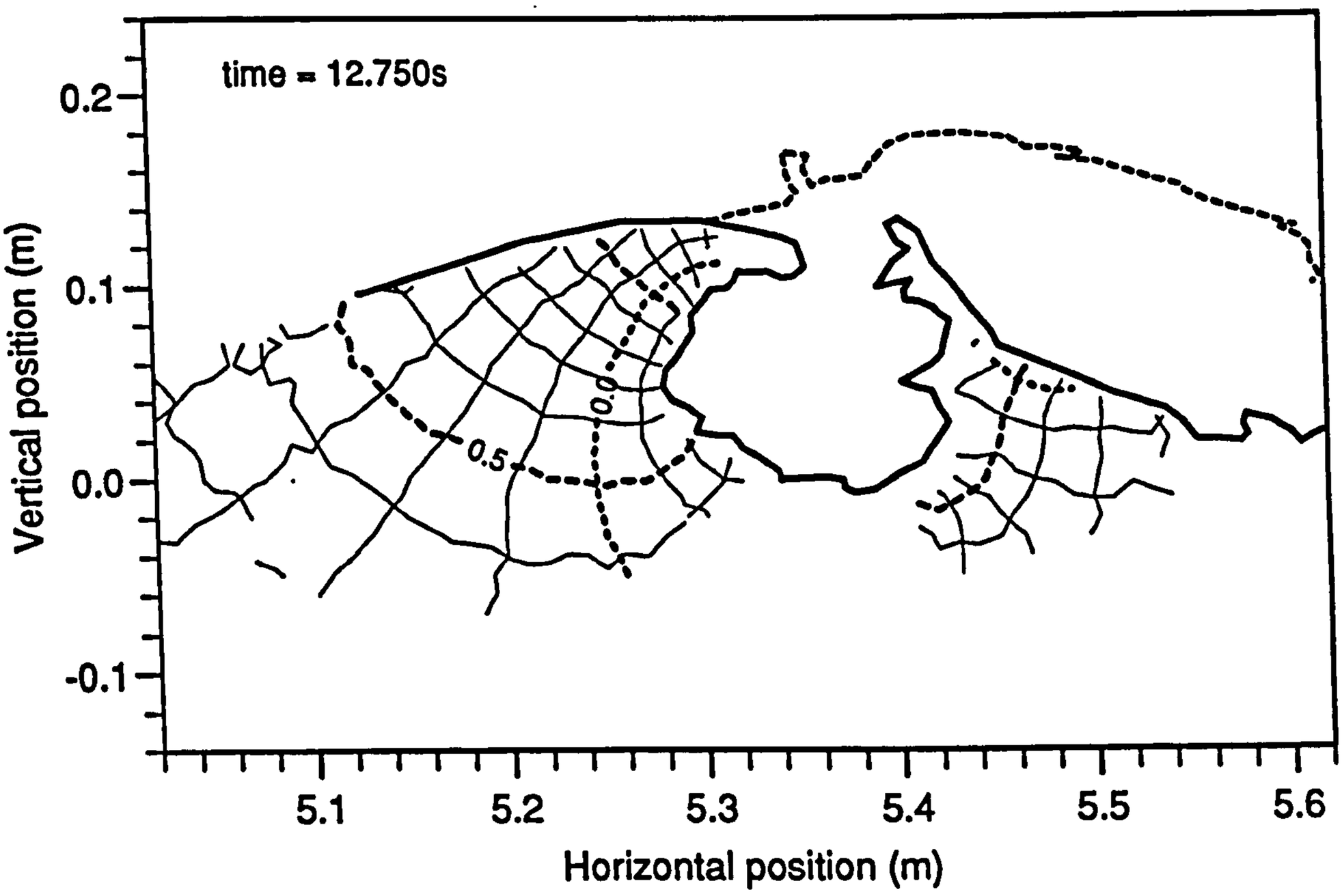

Figure 4.72: Experimentally derived isovelocity contours, $t = 12.750$s

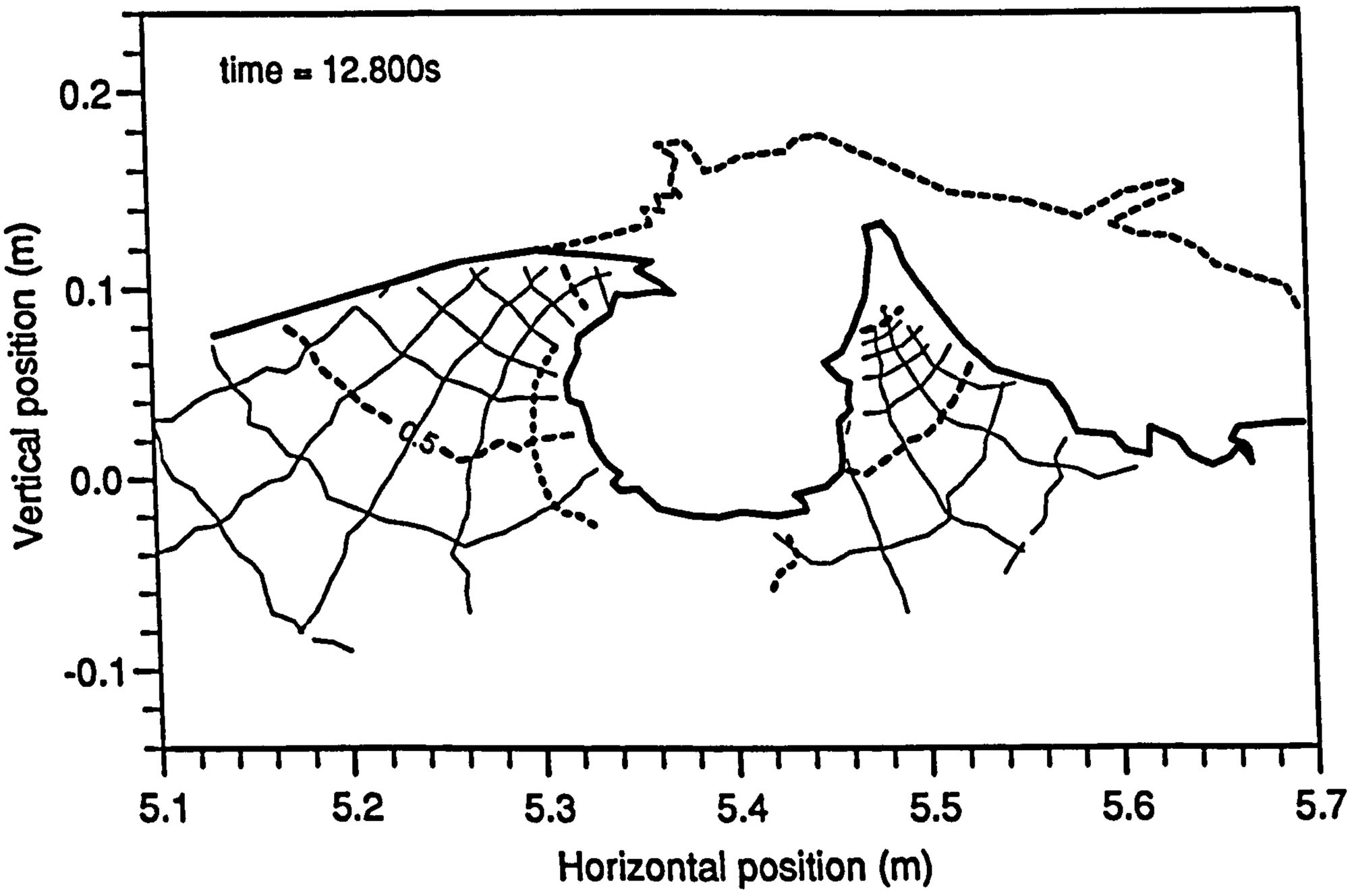

Figure 4.73: Experimentally derived isovelocity contours, $t = 12.800$s

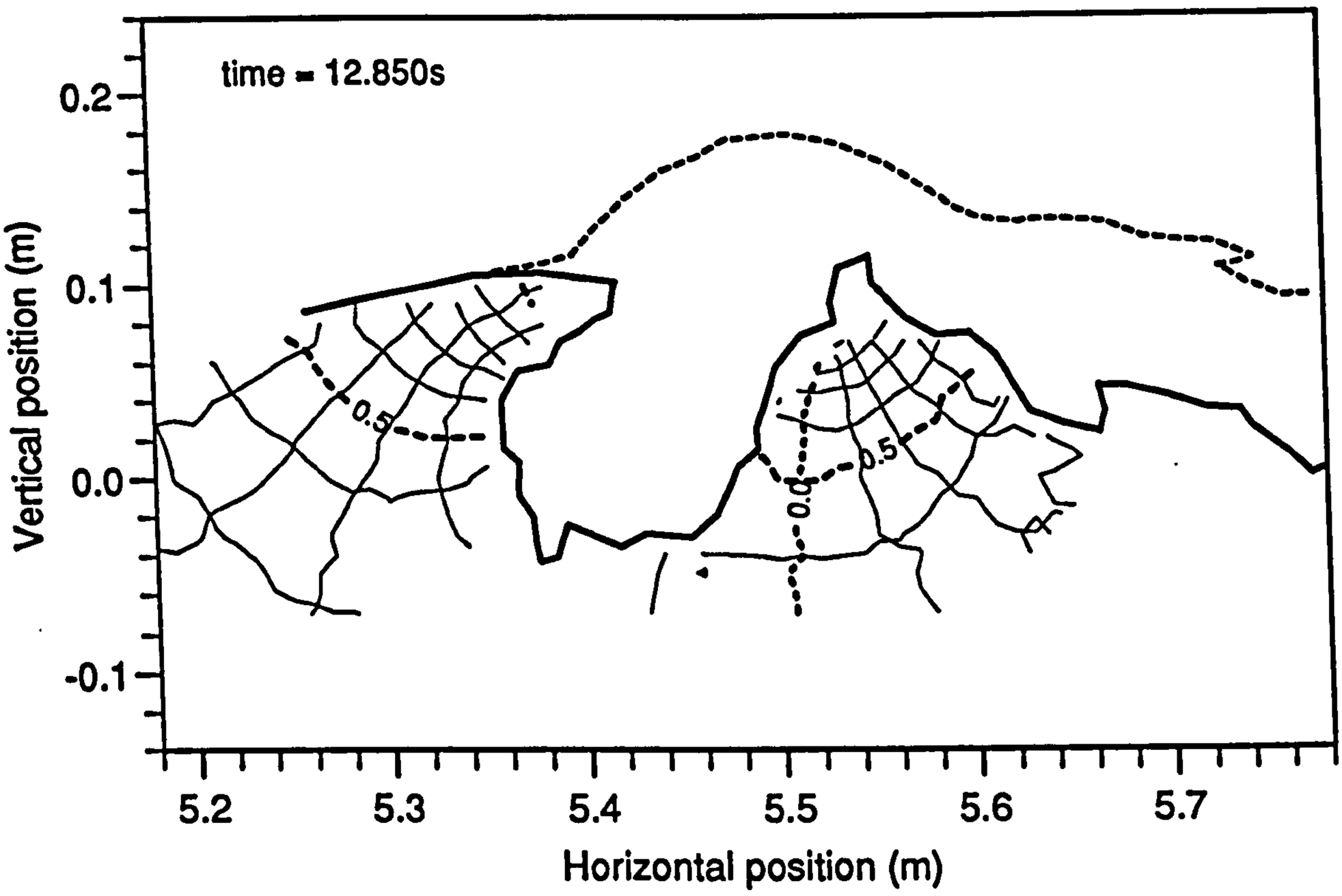

Figure 4.74: Experimentally derived isovelocity contours, $t = 12.850$s

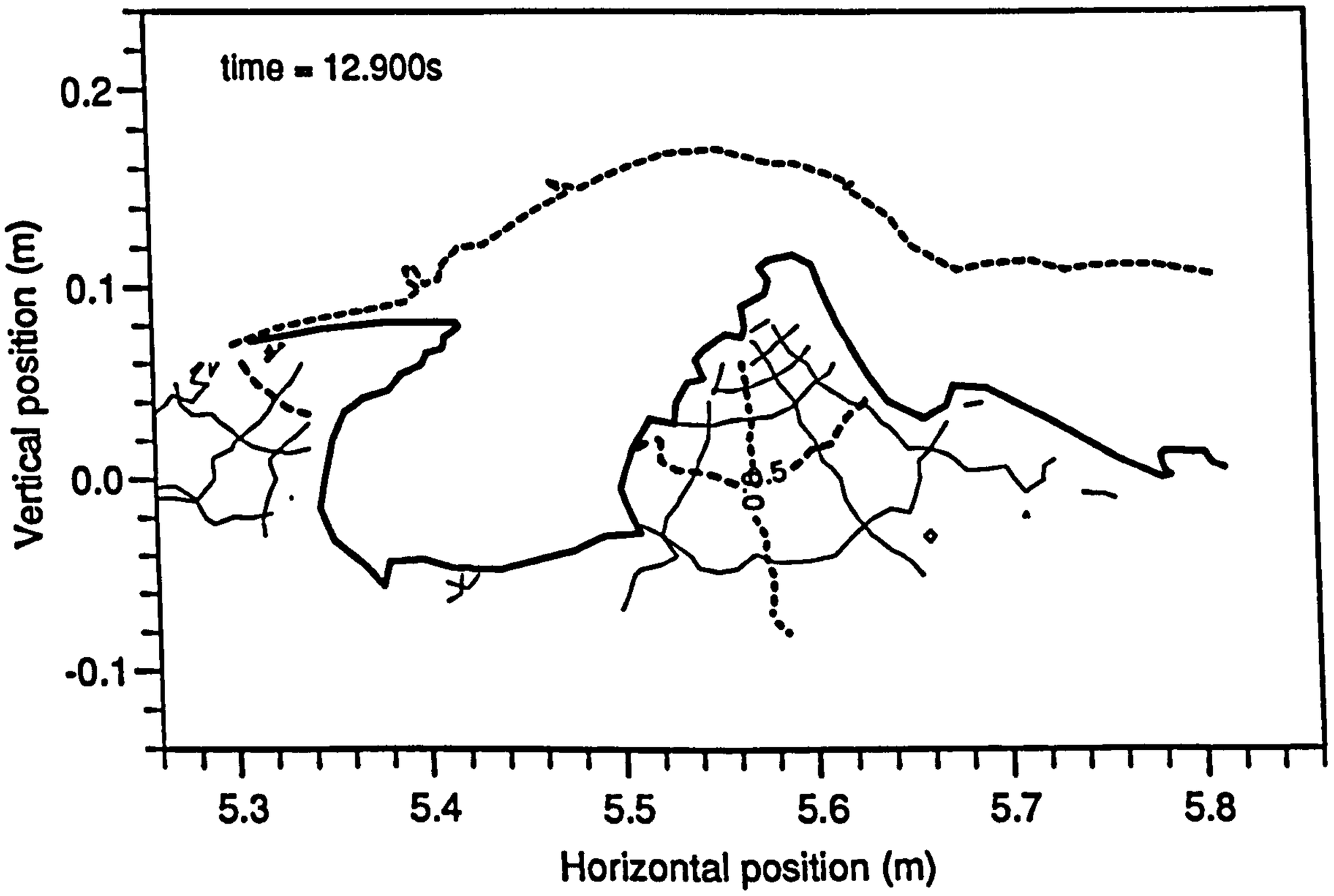

Figure 4.75: Experimentally derived isovelocity contours, $t = 12.900$s

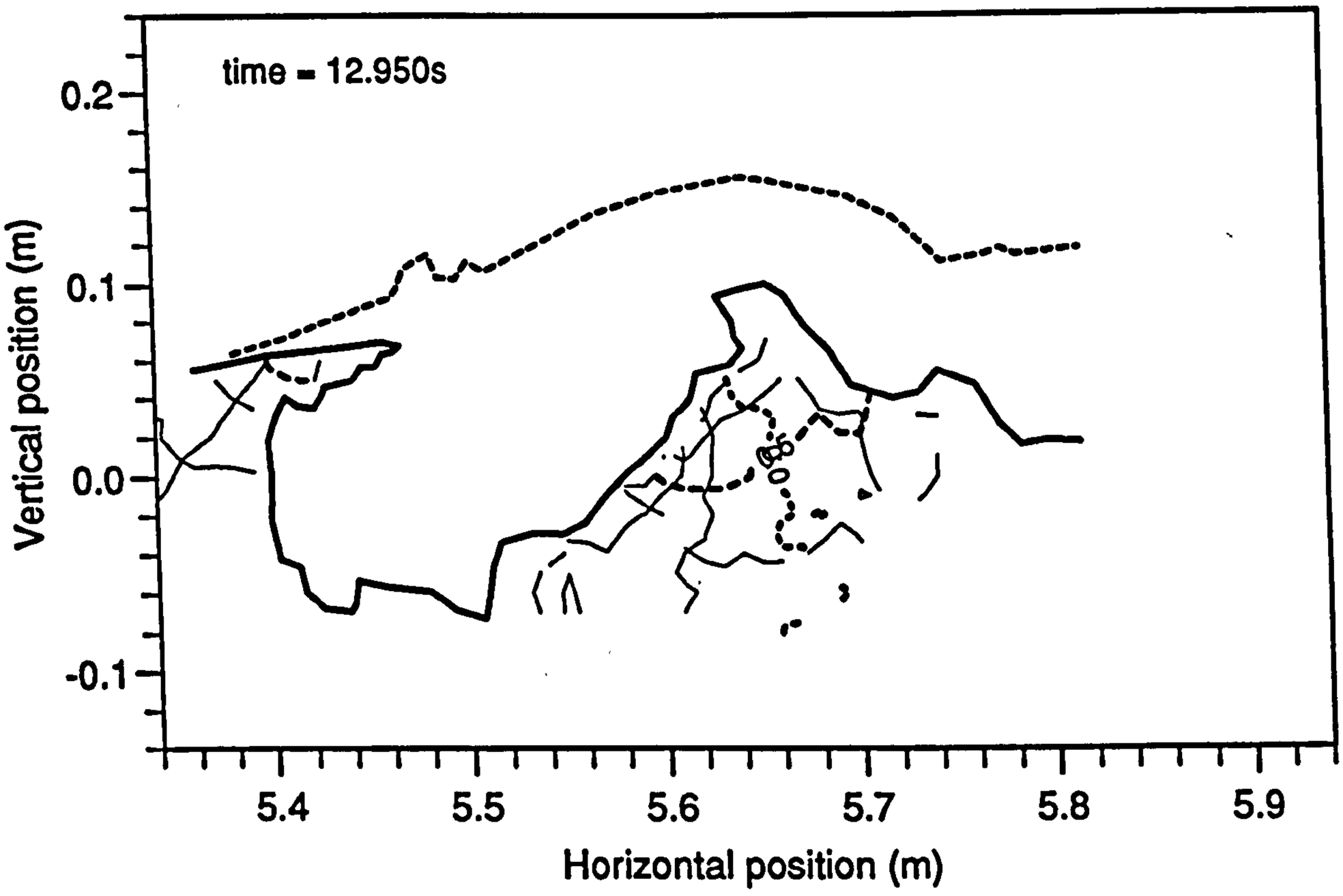

Figure 4.76: Experimentally derived isovelocity contours, $t = 12.950$s

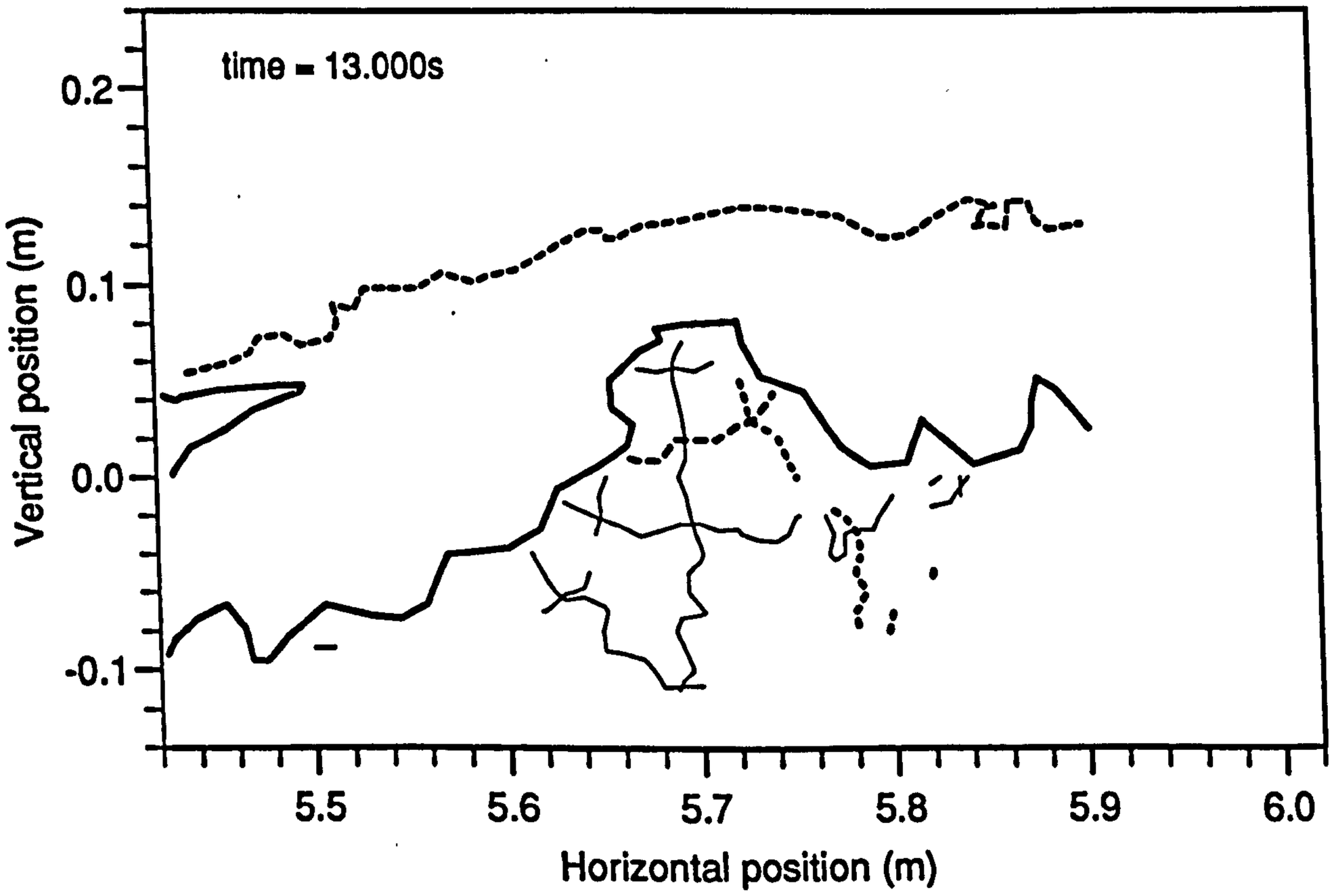

Figure 4.77: Experimentally derived isovelocity contours, $t = 13.000$s

In the preceding figures, a number of expected features of the wave's evolution can be identified. The maximum horizontal velocity increases in the early graphs. This can be followed by tracking the appearance of the $v_x = 1.0\text{ms}^{-1}$ contour, and its progress away from the crest up to about figure 4.32. Thereafter, the maximum velocity decreases.

The $v_z = 0.0\text{ms}^{-1}$ contour shows the line along which the velocity vectors are purely horizontal. In a steady wave this line should be vertical and directly beneath the crest. In these graphs this contour tends to lean to the right, is behind the crest of the wave as the wave grows, and in front as it collapses.

Regions of high acceleration can be identified by the closeness of the velocity contours. For example, in figure 4.63, the highest, recorded region of acceleration can be seen to be at the vertical face of the crest, about .04m down from the top of the wave. In figures 4.70 and 4.71, areas of high acceleration are apparent where the water has been forced up by the re-entering jet. In the first case this occurs at around $x = 5.30\text{m}$ and $z = .02\text{m}$.

Comparison of Experimental and Numerical Internal Kinematics

The same comparison between the numerically generated breaking sequence and the experimental data has been made, for the iso-velocity contour presentation as for the velocity vector plots. Figures 4.78 to 4.83 contain contour plots for the numerically generated kinematics and should be compared with the experimental data in figures 4.60 to 4.65.

The quality of the match has been quantified in section 4.6.3 for the numerical data plotted in figure 4.81 for the vertically-fronted phase compared to the experimental data in figures 4.63 and 4.62, and found to be 2.3% and 1.4% respectively.

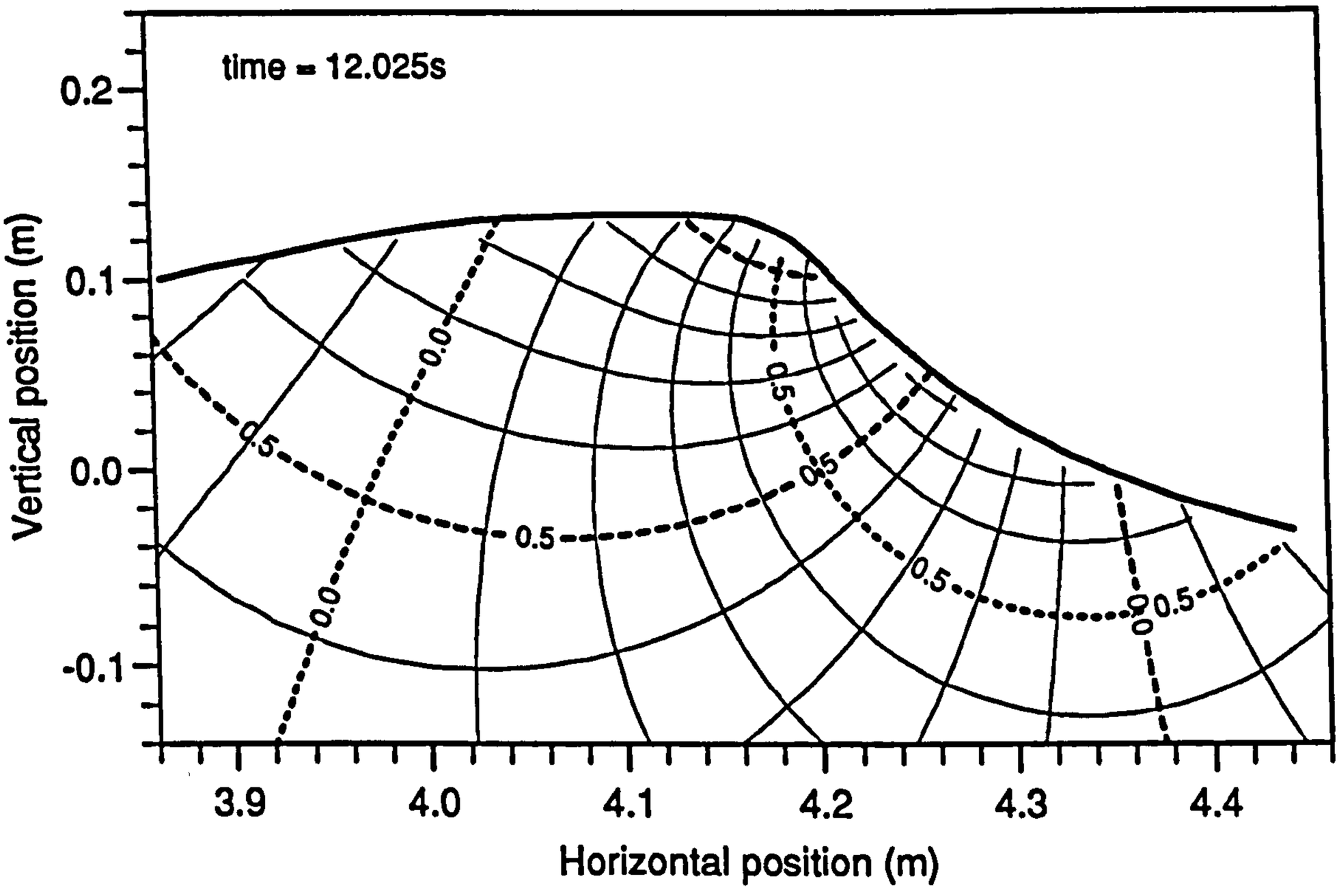

Figure 4.78: Numerical isovelocity contours, $t = 12.025$s (compare 12.150s)

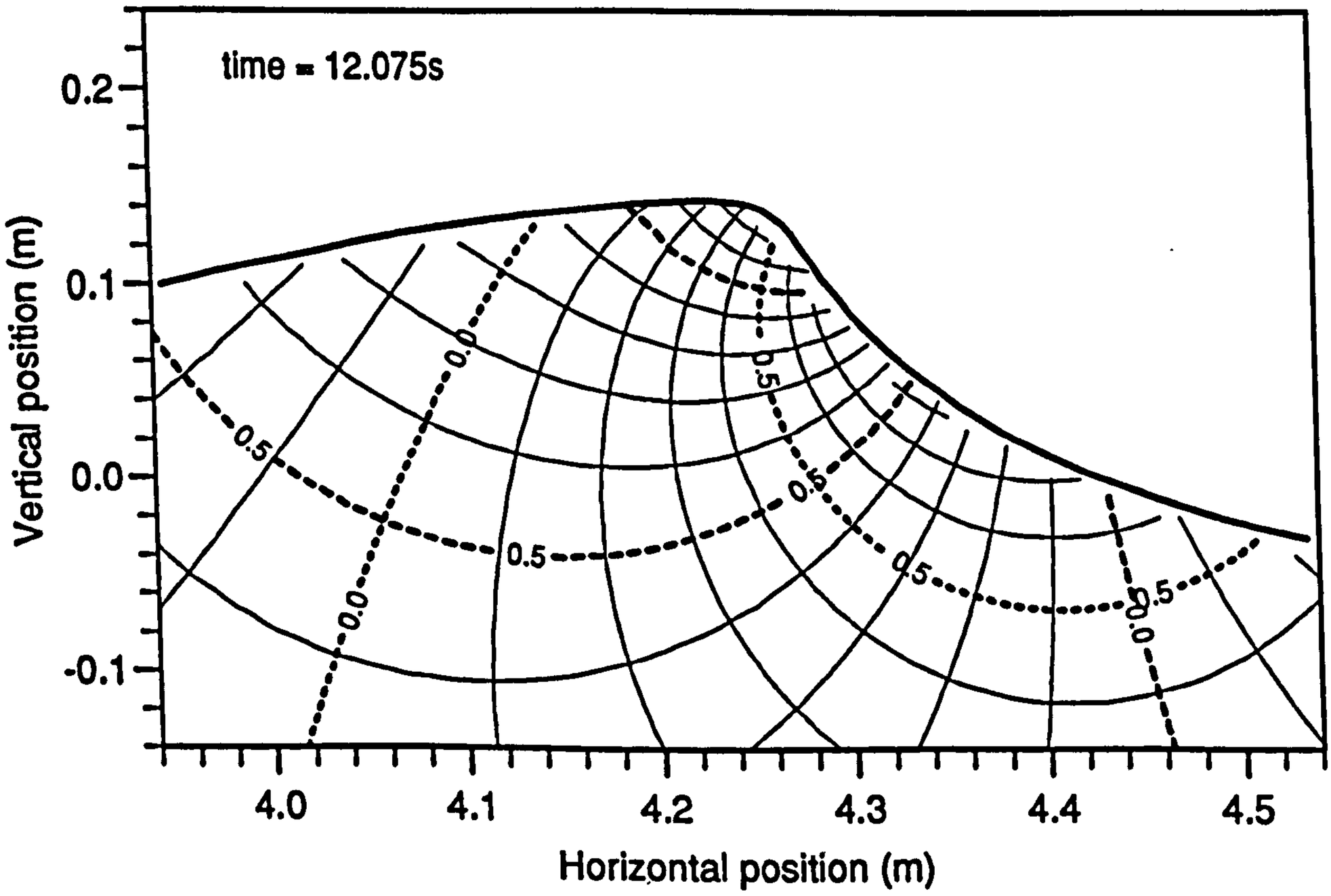

Figure 4.79: Numerical isovelocity contours, $t = 12.075$s (compare 12.200s)

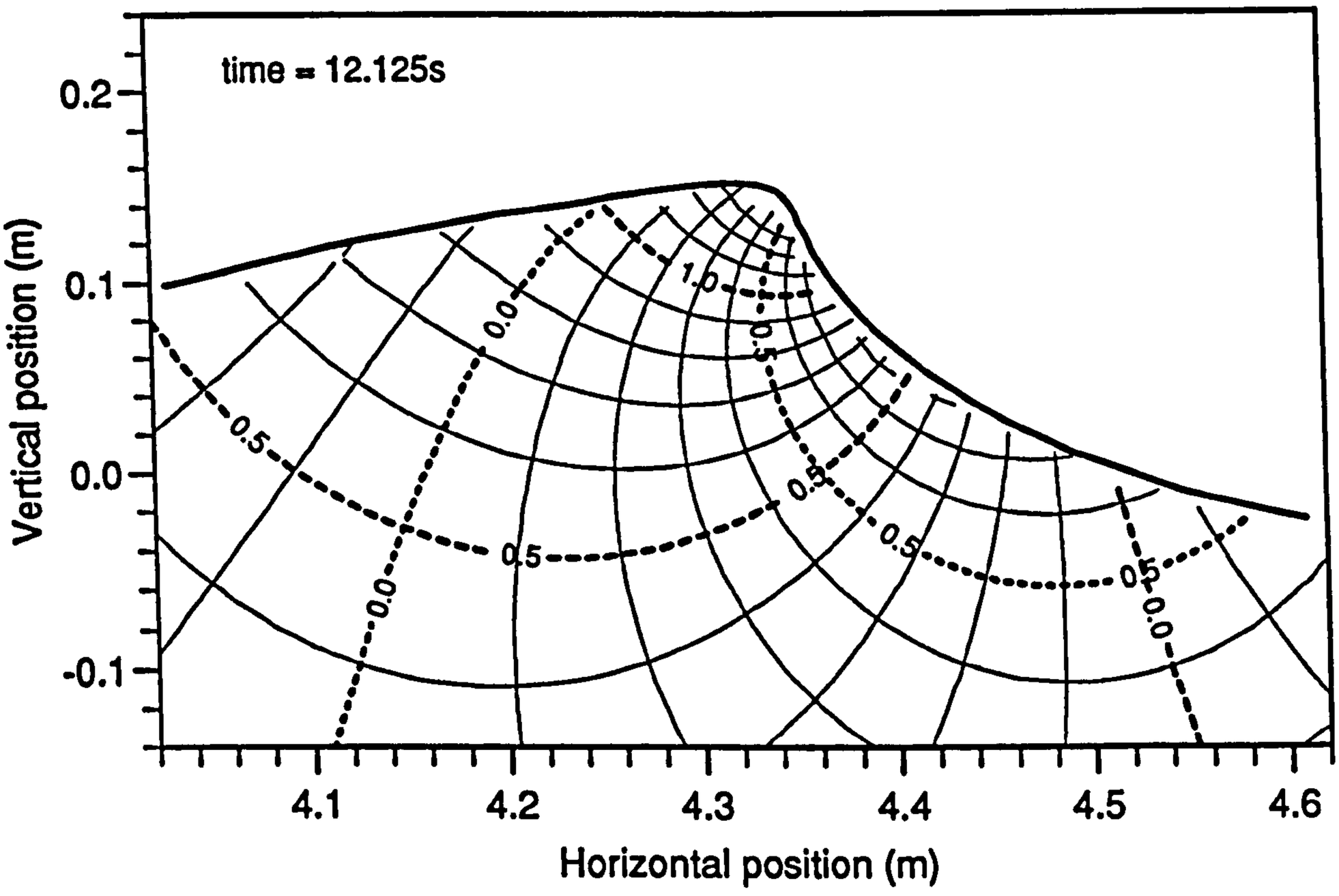

Figure 4.80: Numerical isovelocity contours, $t = 12.125$s (compare 12.250s)

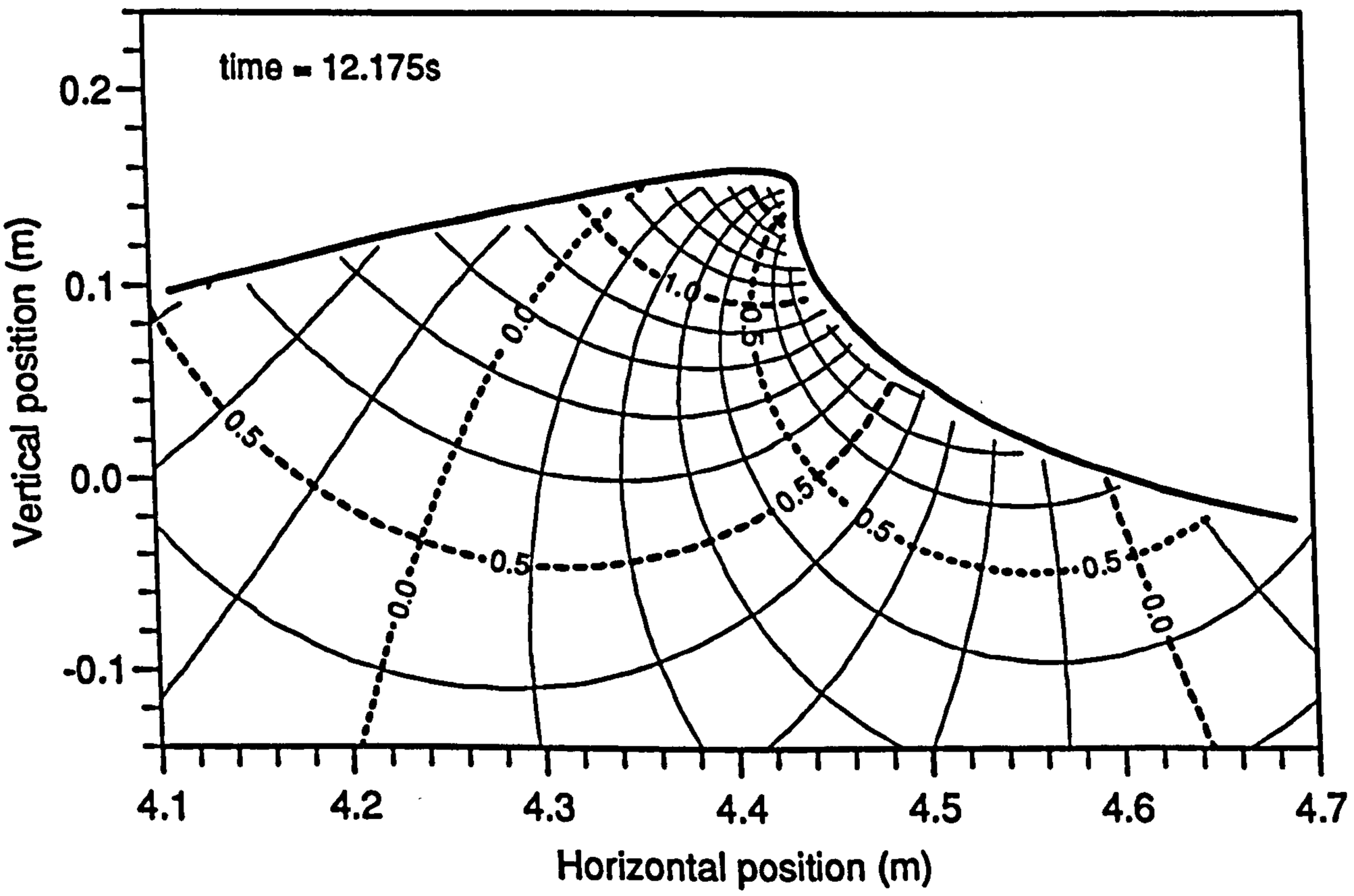

Figure 4.81: Numerical isovelocity contours, $t = 12.175$s (compare 12.300s)

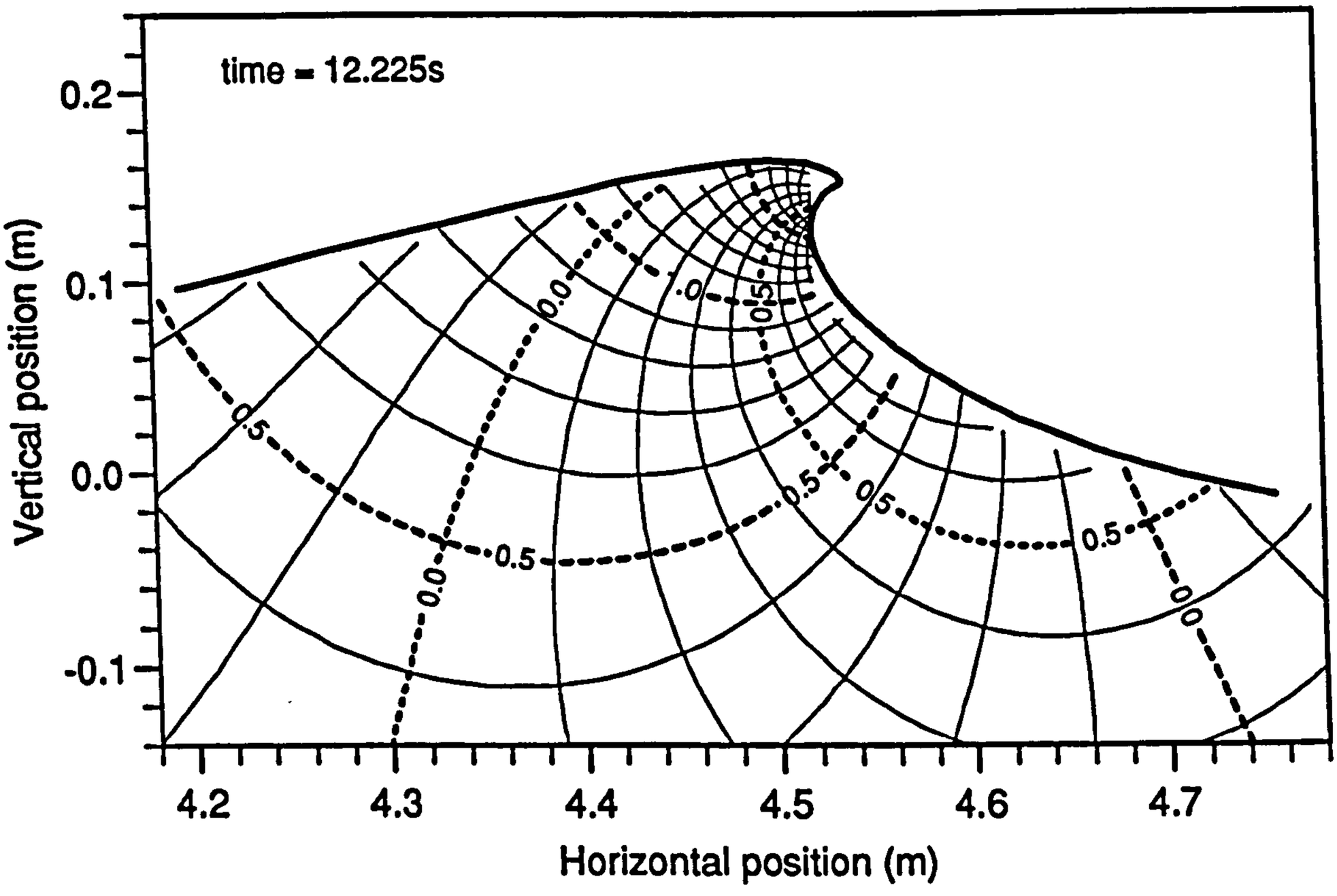

Figure 4.82: Numerical isovelocity contours, $t = 12.225$s (compare 12.350s)

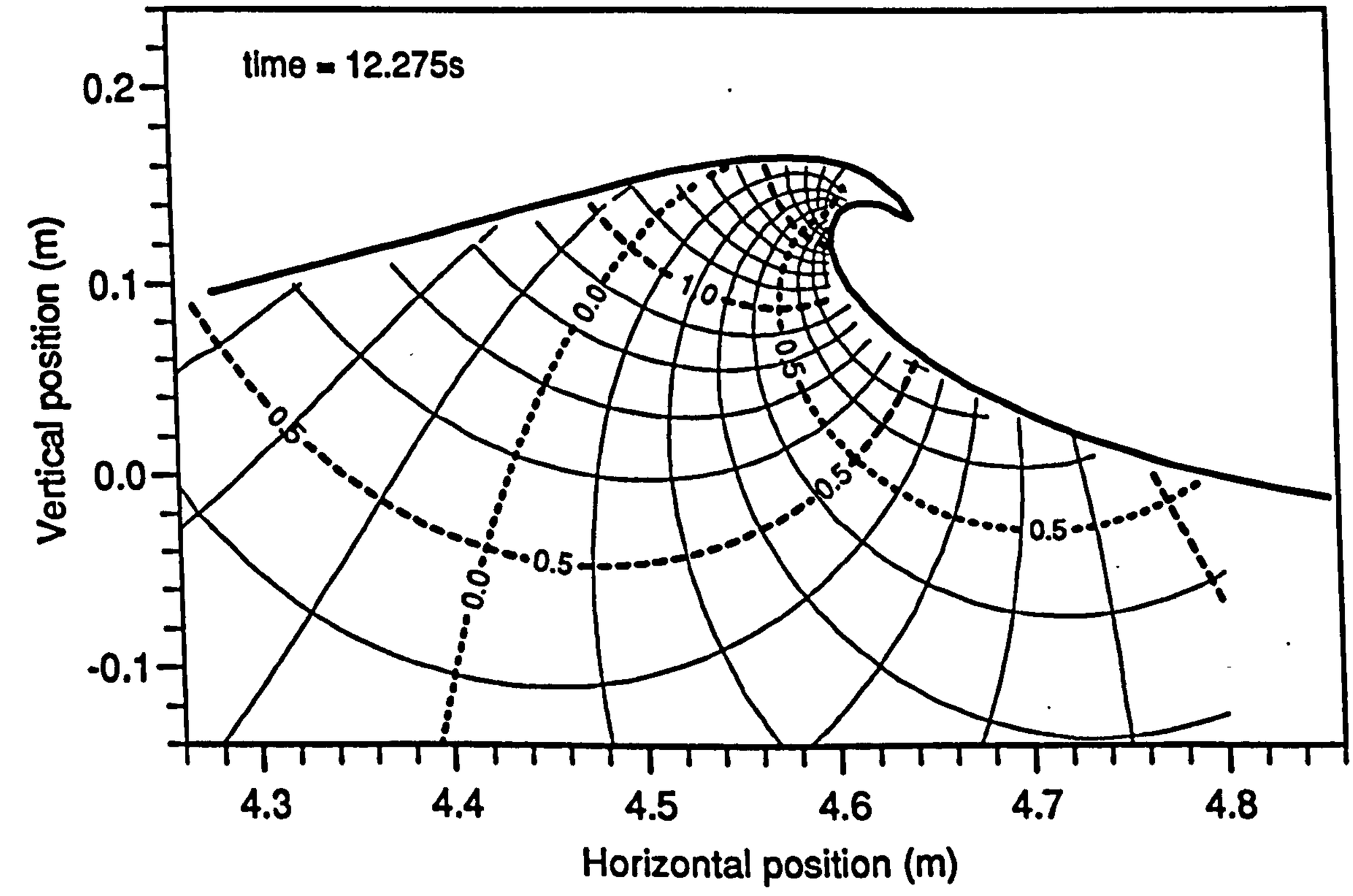

Figure 4.83: Numerical isovelocity contours, $t = 12.275$s (compare 12.400s)

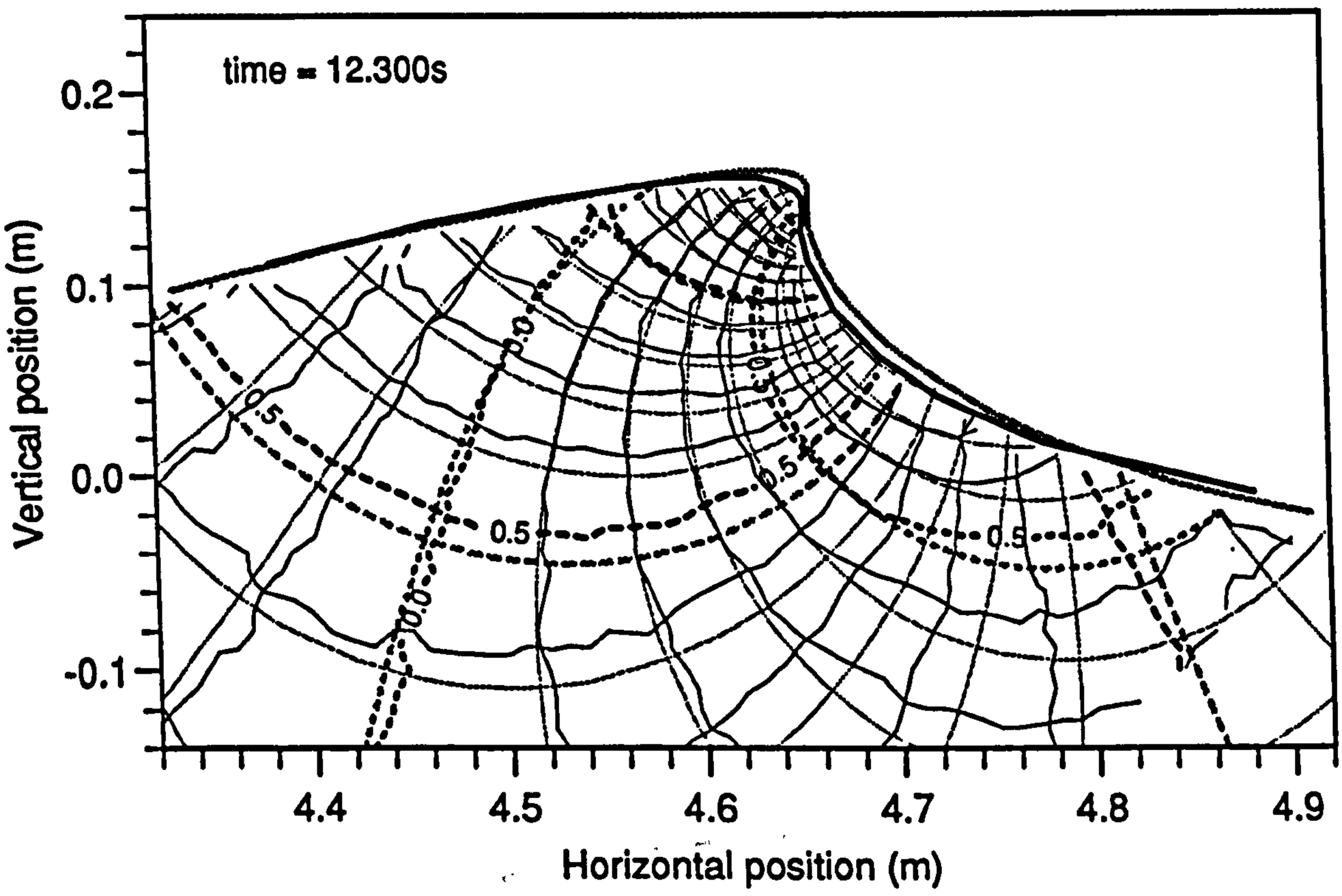

Figure 4.84: Experimental and numerical isovelocity contours for the vertically-fronted phase of the wave

In figure 4.84, the velocity contours from figures 4.81 and 4.63 are overplotted, in order to give a different view of the comparison. The numerical contours are plotted more faintly than those for the experimental data. The same features can be seen as in the plot of the vector differences, figure 4.50. The match in the crest region is very good, and the contour lines are very close to each other. Elsewhere, systematic differences are apparent.

Velocity Contours for the Plunging Phase

Figure 4.85 contains the same data as figure 4.52, this time plotted in iso-velocity contour form. While the effect of random errors in the measurement process can be seen in the lower contours, those higher up are quite smooth, and can be trusted even into the tip.

The repeated case, with the same experimental conditions, is shown in figure 4.86.

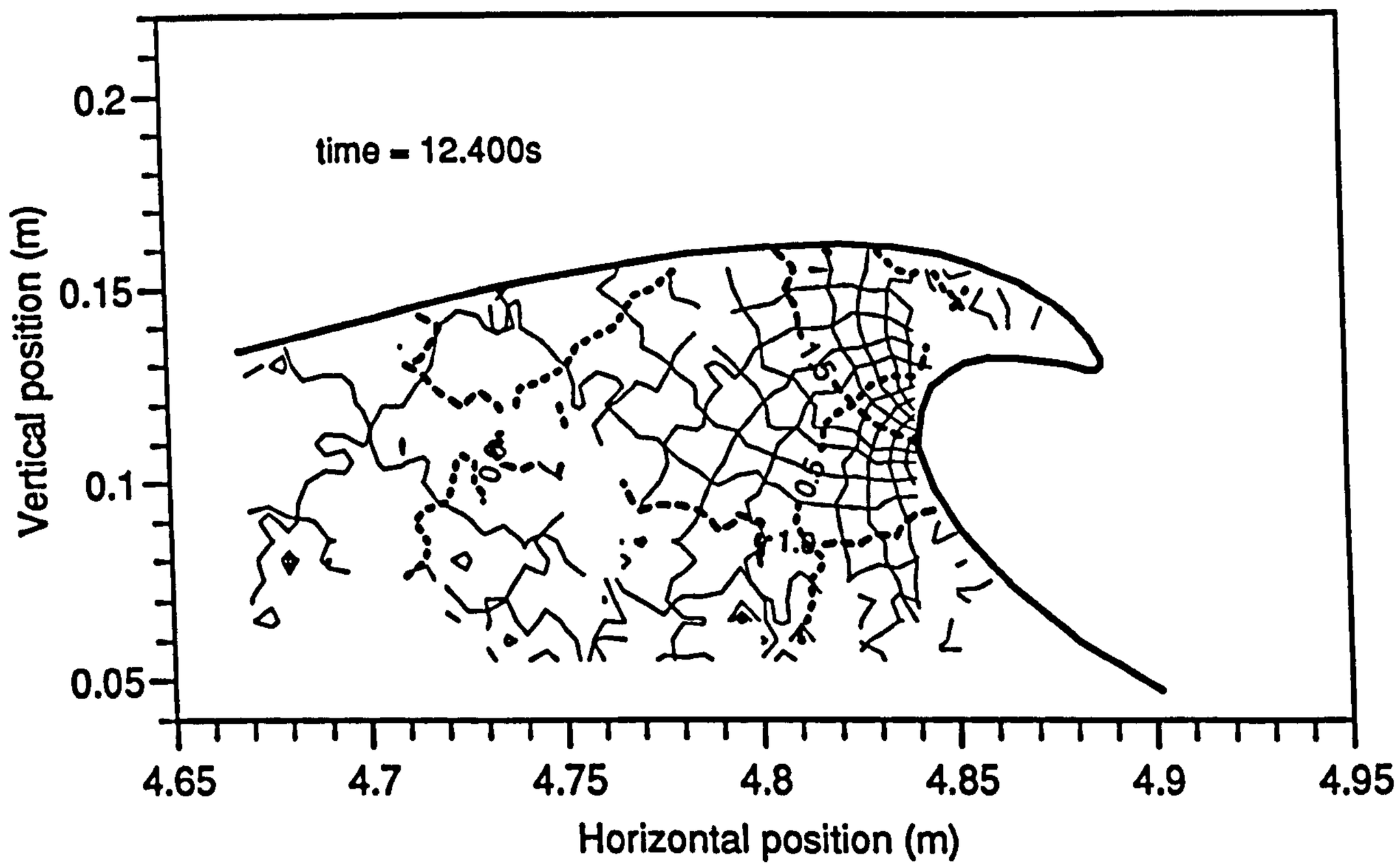

Figure 4.85: Experimentally derived isovelocity contours, plunging phase, $t = 12.4$s

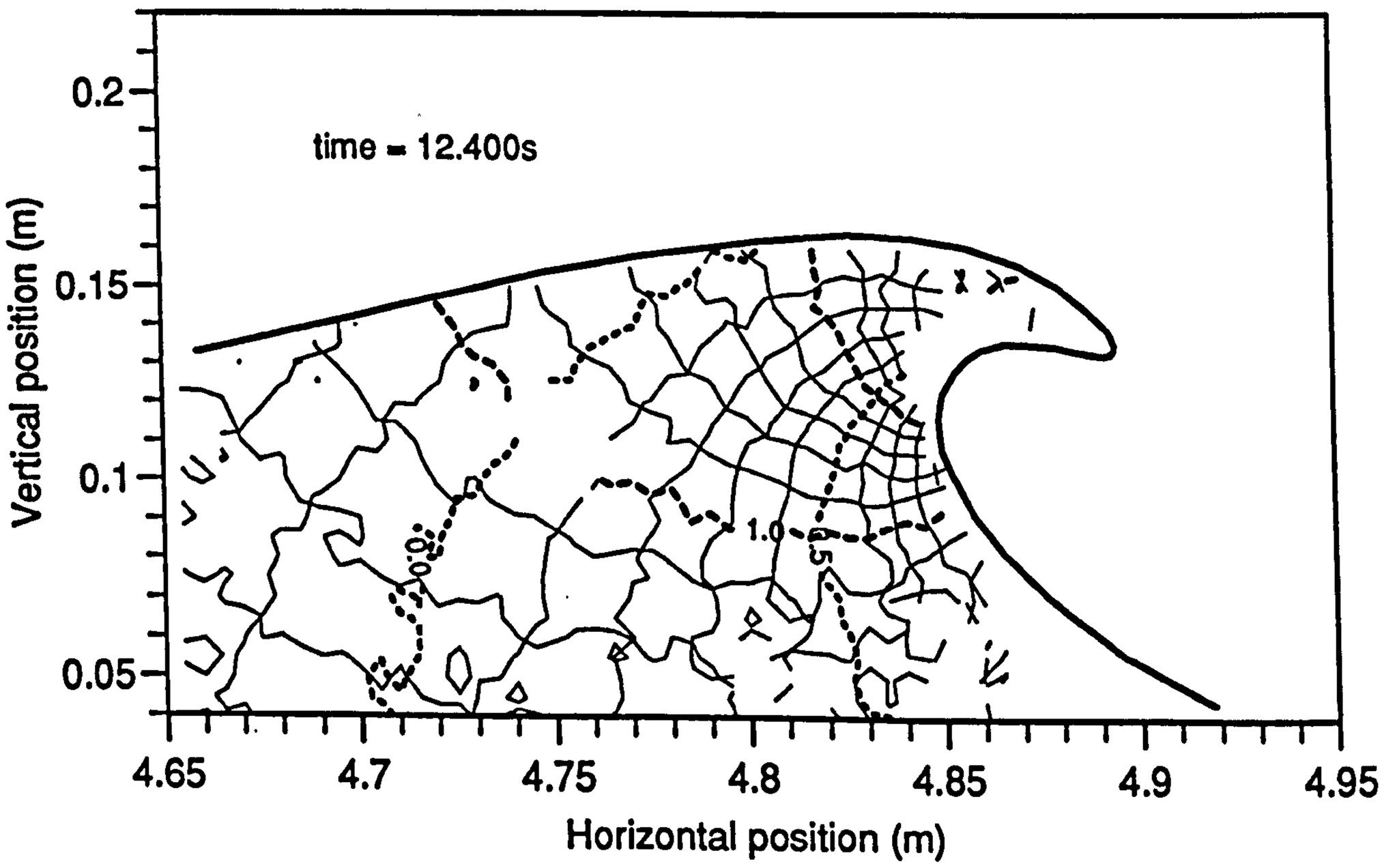

Figure 4.86: Experimentally derived isovelocity contours, plunging phase (repeat), $t = 12.4$s

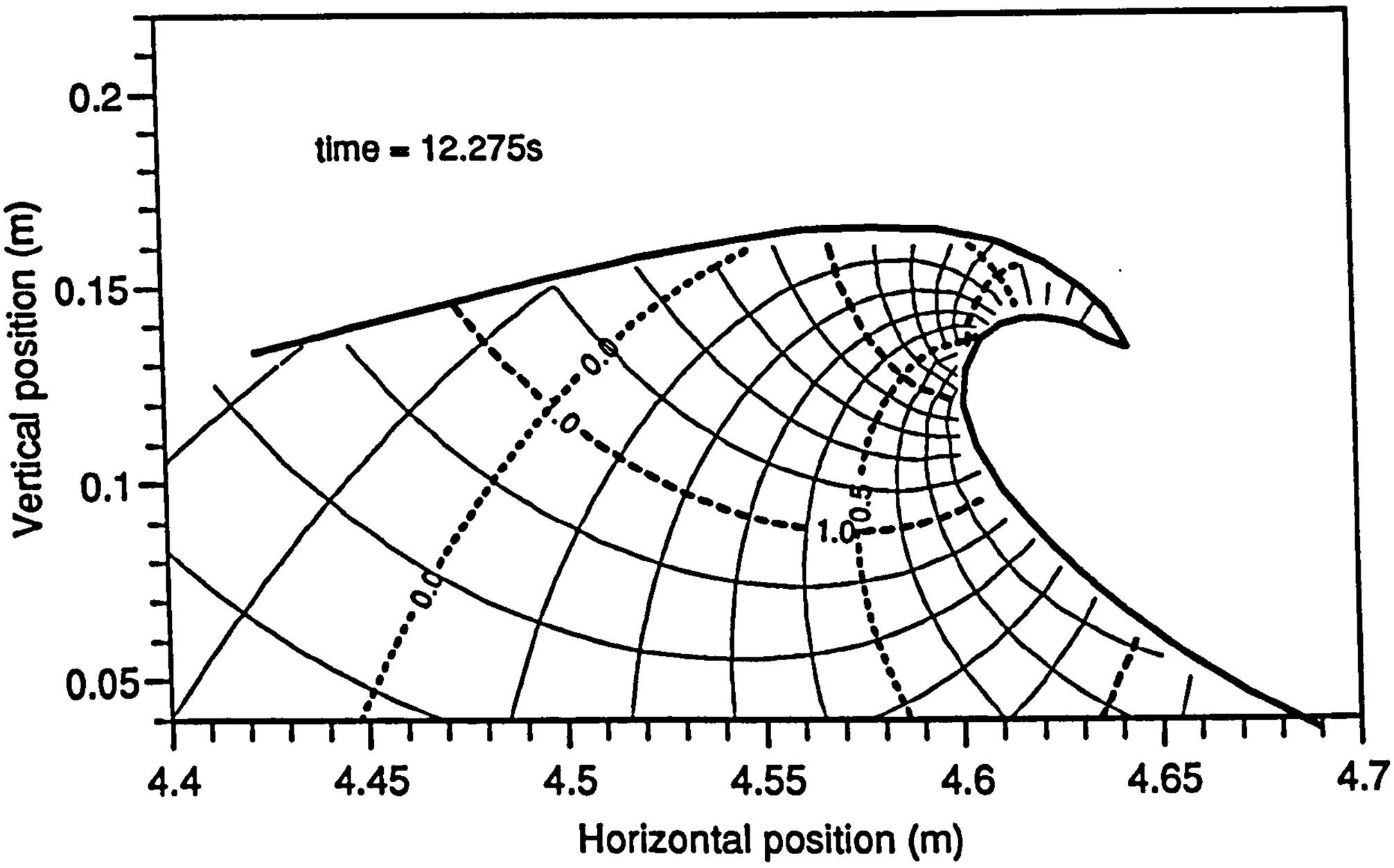

Figure 4.87: Numerical isovelocity contours, $t = 12.275$s (compare 12.4s)

Both the contours and the surface profiles can be seen to be very closely repeated.

In figure 4.87, the numerical data is plotted in contour form for the phase of the wave which can be compared to the experimental data. The same features are apparent as in the experimental case: there is a region of very high acceleration where the water surface is vertically-fronted [42] and less variation of velocity within the plunging tip.

To assess the quality of the match when the data is presented in this form, figure 4.88 contains an overplot of figures 4.85 and 4.87, again shifted sideways and slightly *upwards*. As expected from the earlier vector subtraction where the match was judged to be 1.7%, the experimental and numerical contours are extremely close. Given the experimental errors and uncertainties, and the differences between the surface profiles, the match is as good as could be hoped for in this type of study.

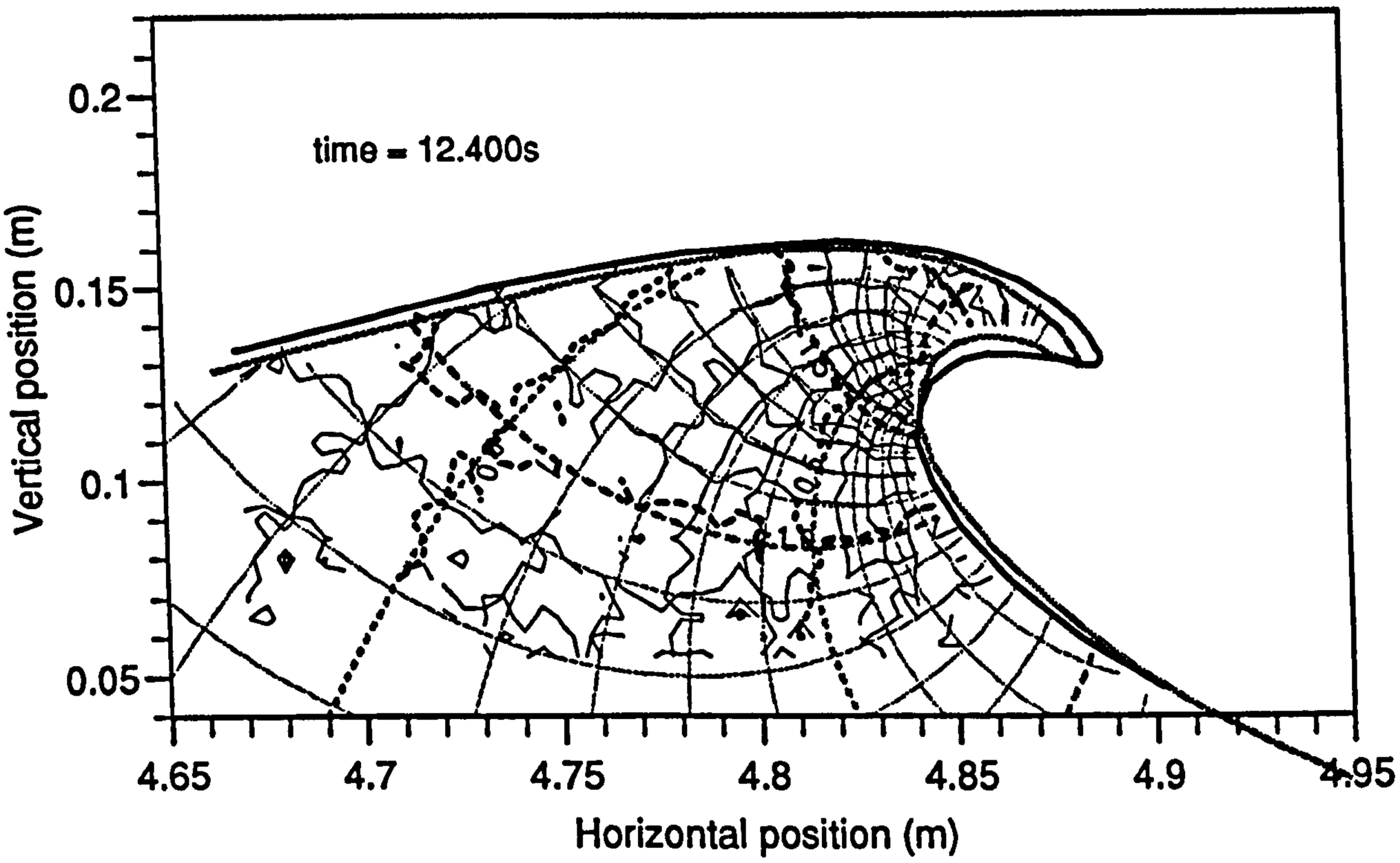

Figure 4.88: Experimental and numerical isovelocity contours for the plunging phase of the wave

4.8 Further Analysis of the Experimental Results

Examples of the experimental kinematics have been presented and shown to compare favourably with numerical predictions, up to the point of breaking, when assessed on a wave by wave basis. In this section, a preliminary attempt is made to reduce the experimental data, and derive other quantities.

4.8.1 Derived Quantities against Time

The experimental data consists of the main sequence of flow fields available for 1 second of the wave's evolution, and various other measurements at different magnifications and time. By extracting statistics from each phase of the sequence,

time-series of these quantities can be found.

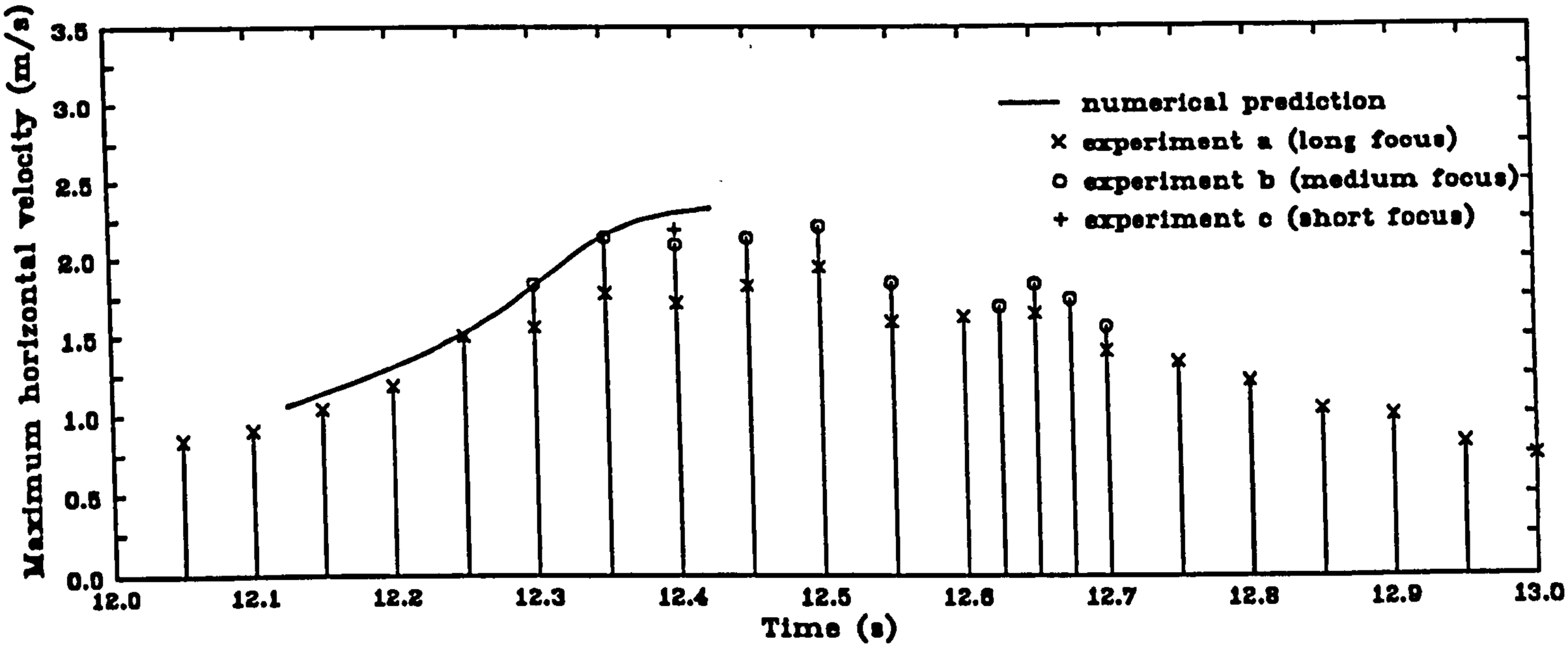

Figure 4.89: Maximum horizontal velocity component at each phase of the breaking wave

Perhaps the most obvious statistic to extract is the maximum horizontal velocity. Figure 4.89 contains the maximum horizontal velocity obtained from each flow field plotted against time. Results from the experiments at different magnifications are included, and compared to the maximum velocity predicted anywhere on the surface of the numerical wave.

As might be expected, the experiments at higher magnification yield the higher maximum velocities. This is because, in these cases it is possible to make measurements closer to the water surface, and even into the plunging spout. It can be seen that, where numerical predictions are available, the experimental values tend towards this limit. Again, it should be noted that the numerical values have been shifted in time, as discussed in section 4.6.1.

Of interest to the designer of offshore platforms and other structures, is the maximum horizontal velocity present at different vertical positions. Figure 4.90 contains the experimental values obtained by finding the maximum velocity present in each row of each flowfield, overlayed on the numerically derived quantities between 12.15s and 12.40s.

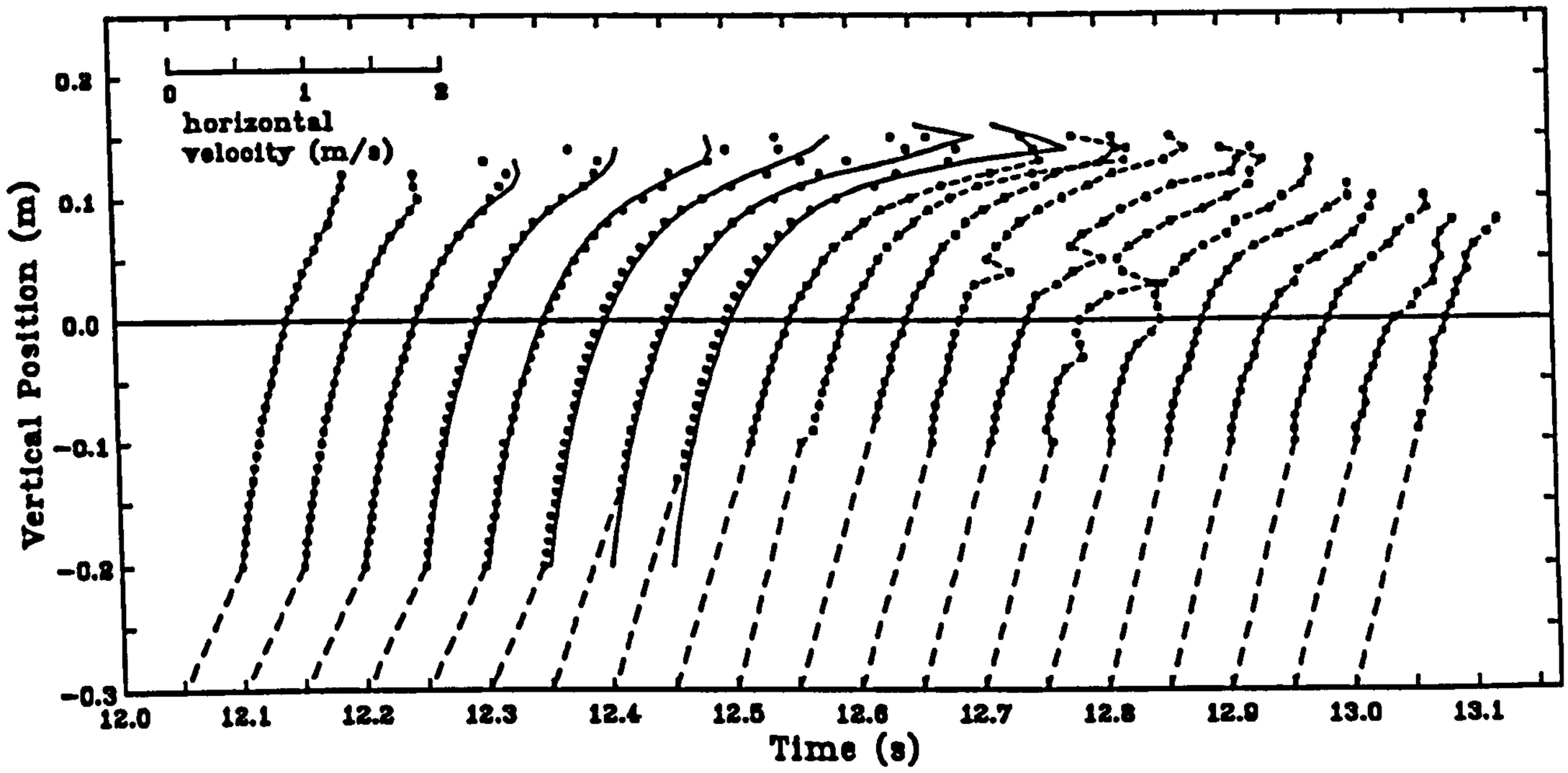

Figure 4.90: Horizontal velocity profiles at t=12.05,12.10,...13.00s. - • - • - experimental data, — numerical prediction

4.9 Concluding Remarks for the Breaking Wave Study

From the results of the breaking wave study presented in this chapter, the following concluding remarks are made:

It was found to be difficult to obtain an exact match between the surface profiles of the experimental and numerical waves, even by making fine adjustments to the parameters involved in the replication process. However, an acceptable match was obtained with a small shift of the numerical data in space and time.

High quality, full-field kinematic measurements were obtained until after the wave had broken, including the measurements into the spout and into the area of water forced up by the re-entry of the plunging tip.

After appropriate shifting of numerical data, the difference between the kinematics measured experimentally and predicted with the time-stepping numerical model was about 2%. This discrepancy can be accounted for by experimental errors, and

the imperfect match between the experimental and numerical conditions.

Chapter 5

Steep, Steady Waves on Sheared Currents

5.1 Summary

An experimental study of the interaction of steep, steady waves with sheared currents is described. Firstly, the selection of the test conditions is discussed and the experimental measurements outlined. The experimentally measured kinematics are presented in raw form, then averaged to reduce the effects of turbulence. Measurements of the wavelength and other parameters are presented and discussed. Vorticity is extracted from the full field velocity data, and an assessment made of the steadiness of the combined kinematics. Finally, the waves are assumed to be steady, and a comparison made with the predictions of an irrotational model combined with the stretched current profile, under the crest and for the whole wave.

5.2 Selection of the Test Conditions

The experimental programme was planned to cover a range of current and regular wave settings, and to concentrate mainly on measuring the combined kinematics. Ideally, such a study would include a large number of parameter combinations,

perhaps selected from several different current profiles and wave steepnesses, and a dozen or more wave frequencies. However, consideration of the time involved in the PIV measurement process, particularly the analysis of the negatives described in section 3.5.1, led to tests being conducted over a limited range of parameters.

The configuration of the wave flume for the study is illustrated in figure 5.1. The elements of the flume have been described in section 3.3.1. Here the tank has been drawn the opposite way round, so that waves would travel left to right, and a forward current is also in that direction. All results presented in this chapter assume this orientation.

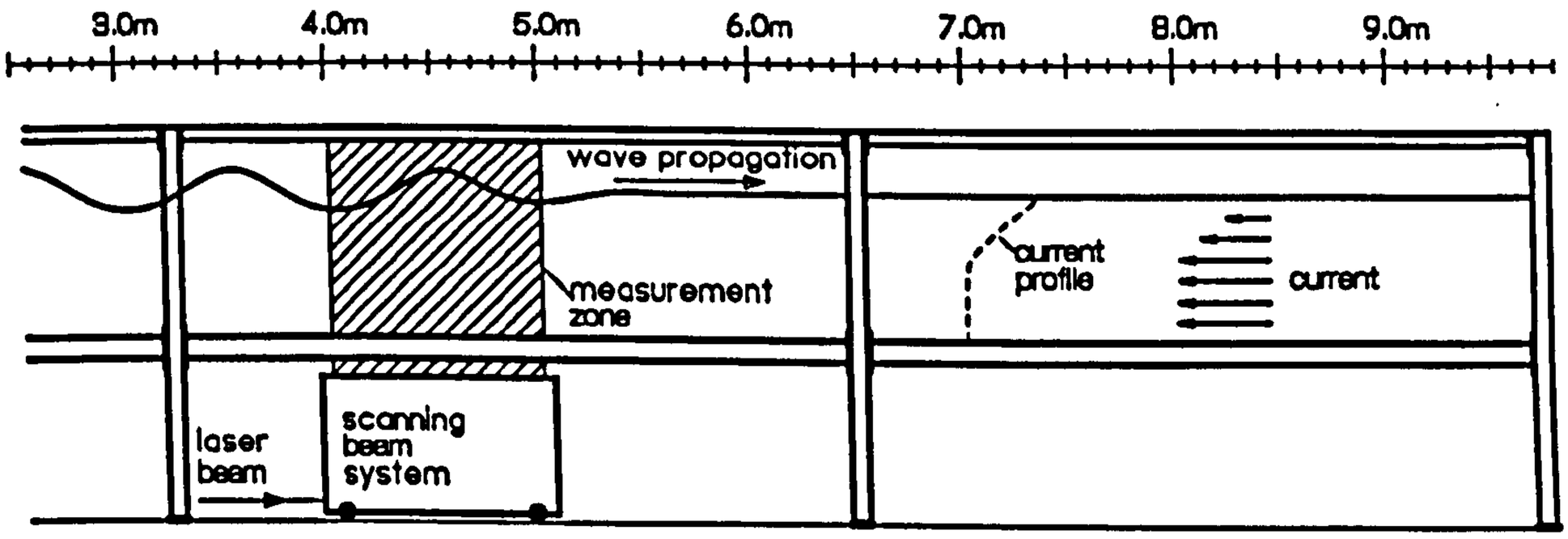

Figure 5.1: Wave flume used for the kinematic measurements of wave/current interaction, showing a reverse current with forward shear

5.2.1 Selection of the Current Profiles

The main current cases attempted were:

- No current
- Uniform, reverse current
- Uniform, forward current
- Weak shear, in the wave direction
- Strong shear, in the wave direction

For the sheared current cases, a decision was made at an early stage to generate the forward shear in combination with an overall reverse flow. This has two main experimental advantages: the current former and the wavemaker can be at opposite ends of the wave flume; and waves with limiting steepness can be generated on to an opposing current. The assumption implicit in this decision was that, in the analysis of the results, the kinematics could be view from different frames of reference, as necessary. Doppler shifting of the wave frequency, need to do this, has been described in section 2.2.2.

Since the research project was concerned primarily with the interaction of top-sheared currents with wave kinematics, only the top half of the current was assessed when trying to generate different current profiles.

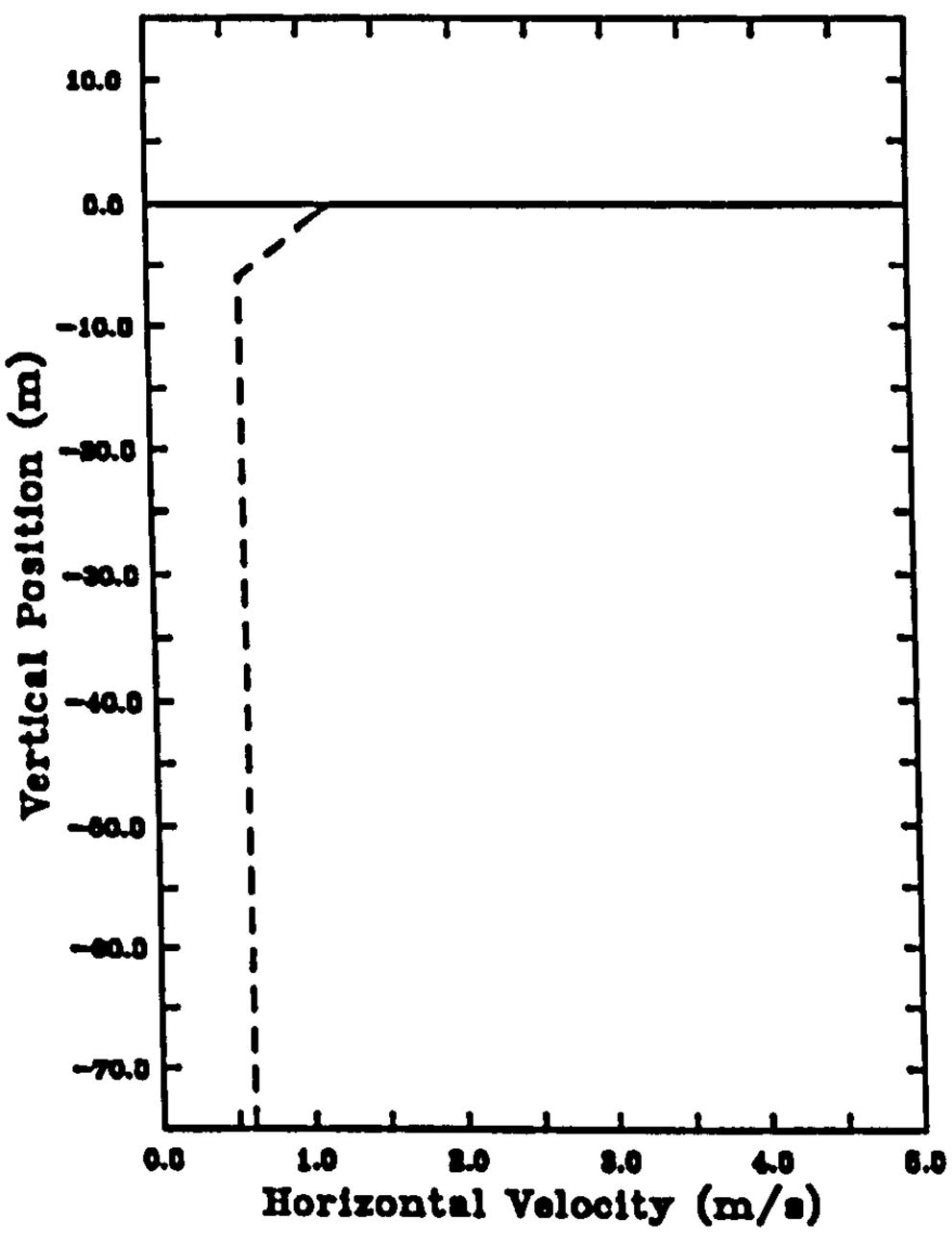

Figure 5.2: Sheared current profile obtained using Department of Energy Guidance notes

In the case of the sheared current, it was hoped to achieve a profile of the same form as the bilinear ones proposed by the Department of Energy [13]. Such a profile is shown in figure 5.2, obtained by assuming the wind speed to be 40 ms^{-1}, the storm surge current to be 0.6 ms^{-1}, and the water depth to be 75m. It was

not possible to obtain a profile in the tank with exactly this form. However, the bulk flow effects were expected to be described accurately with the use of Doppler shifting, and therefore the profile which gave the largest shear near the surface was sought.

Obtaining sheared profiles in the flume with roughly the desired, overall characteristics was found to be reasonably straightforward. The current inlet was baffled in different ways, and the effects noticed by eye in the illuminated measurement zone. Obtaining a more accurate measure of the profile was more involved, as the full PIV process had to be used each time. Because the technique uses photography, requires the tank to be regularly cleaned, and involves a lengthy analysis, it is not very well suited to the iterative task of obtaining a required profile.

It was found that very strong near-surface shears could be generated close to the current former, but they weakened as the current travelled down the tank. There were potential problems of reflection if waves were to be measured near the current former, and these currents had to be dropped, despite their promising form.

The four current profiles selected for the kinematic tests are shown in figure 5.3. In each plot the mean current profile is plotted along with error bars showing the turbulence level. The mean values were obtained from PIV measurements by averaging along each horizontal level in the 1m wide measurement zone for a number of repeats of each current condition. The turbulence level is shown as the standard deviation of the experimental data. The true mean of the current should lie within bounds an order of magnitude smaller than those shown.

The most important current profile, the strongly sheared case, can be seen to have an approximately linear profile in the top half of the water depth. The weakly sheared profile is somewhat less ideally behaved, and similar in form to the *uniform* reverse current case. The uniform, forward current has an almost constant profile in the top half of the flow. In each of the profiles, the boundary layer at the bed can be clearly seen, but this should be disregarded when assessing the general form of the profile.

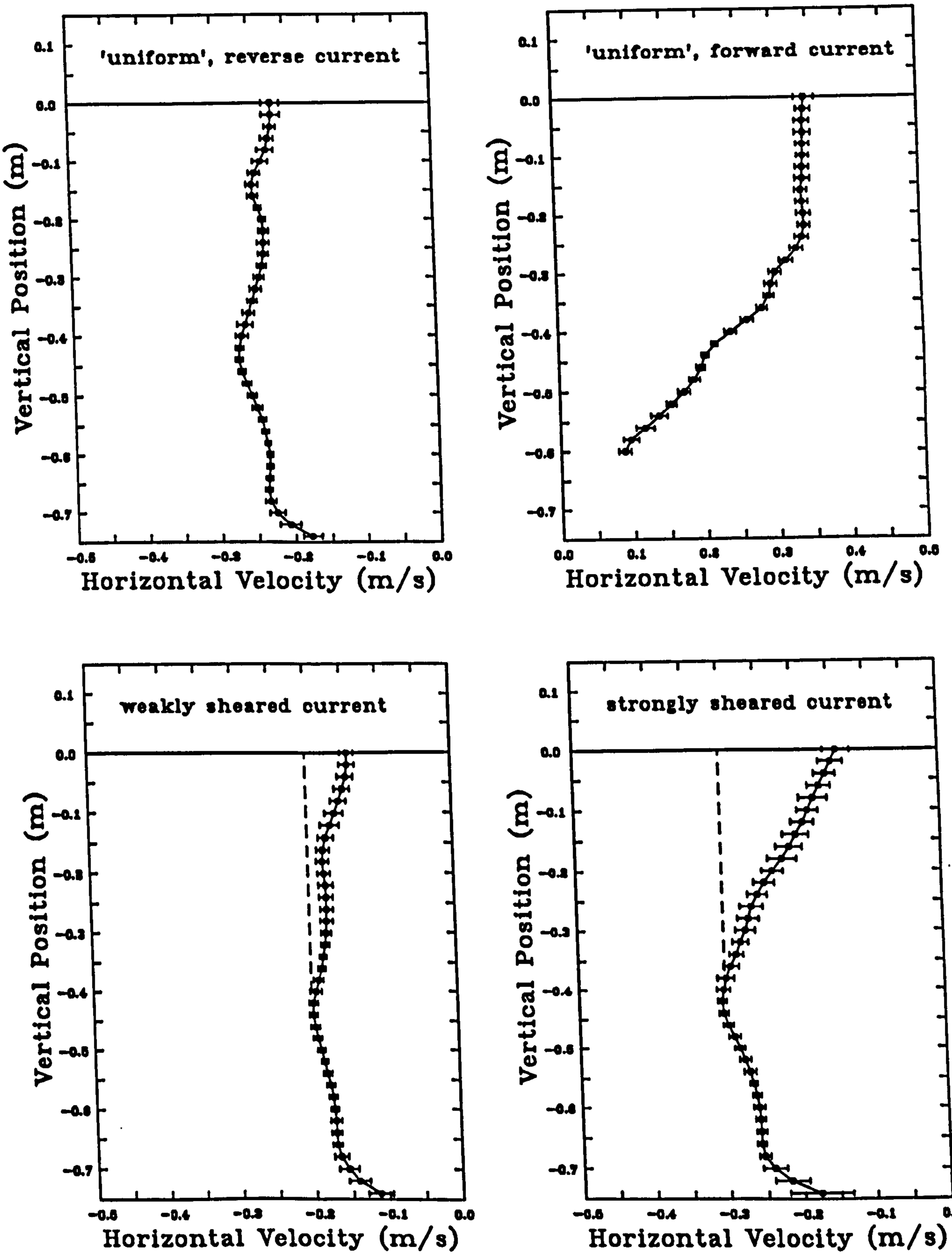

Figure 5.3: The four main current profiles used in the experiments

Current	Test Cases	Repeats	$\langle v_x \rangle$ (ms^{-1})	$\langle v_z \rangle$ (ms^{-1})	σ_{v_x} (ms^{-1})	σ_{v_z} (ms^{-1})	Turbulence level
Uniform, reverse	6	3	-.2395	-.0045	.0078	.0064	3.3%
Uniform, forward	7,8	3	.2695	.0030	.0088	.0094	3.3%
Weak shear	9-14	5	-.1720	-.0042	.0087	.0054	5.1%
Strong shear I	16,19	7	-.2498	-.0100	.0122	.0106	4.9%
Strong shear II	15,17,18,20	6	-.2421	-.0079	.0145	.0098	6.0%

Current	Top shear $z \geq -.14$ m (s^{-1})	Top shear $z \geq -.20$ m (s^{-1})	Top shear $z \geq -.40$ m (s^{-1})	Maximum velocity (ms^{-1})	Surface Current (ms^{-1})
Uniform, reverse	0.254		0.090	-0.272	-0.219
Uniform, forward		0.022		0.345	0.345
Weak shear	0.276		0.108	-0.198	-0.142
Strong shear I		0.622	0.425	-0.303	-0.139
Strong shear II		0.448	0.427	-0.304	-0.134

Table 5.1: Current statistics

Various current statistics are covered in table 5.1. Each case number corresponds to a set of test parameters, comprising the current form, the wave frequency and the wave steepness. Two *strong shear* rows are present, since, in the tests, some of measurements had to be redone and the current profile was found to be not quite repeatable.

5.2.2 Selection of the Wave Parameters

The main wave considered was one with frequency 1Hz, and height corresponding to 60% of limiting steepness. Six other cases were considered in addition to this central cases, by varying the frequency to 0.8Hz and 1.2Hz, and by changing the steepness to 40% and 80% of the limiting value. All of the wave conditions aimed for were selected from those indicated in table 5.2. The actual steepnesses achieved were all slightly less than those aimed for, as the wavelengths were estimated, at this stage, with linear theory.

	0.8Hz	1.0Hz	1.2Hz
40%	√	√	
60%	√	√	√
80%		√	√

Table 5.2: Wave parameters aimed for in the kinematic tests

In the planning of the experiments, it was thought desirable to attempt to achieve as closely as possible the same wave conditions for each of the current cases, in order that the waves travelling on the different currents could be directly compared with each other. This leads to an immediate difficulty: to match the wave conditions correctly, the wave frequency in the *appropriate* frame of reference should be the same. In the case of uniform currents the appropriate frame is the one travelling with the mean current, and the wavemaker frequency necessary to produce this frequency in the moving frame is given by the Doppler formula (equation 2.10). For the sheared current cases, the choice of appropriate reference frame was more difficult, and was estimated. In all cases, there was the additional problem that the current profile was not known exactly at the time of the experiment planning.

5.2.3 Obtaining the Combined Wave/Current Conditions in the Flume

Once the wavemaker frequency was decided upon, the wavelength was estimated and the corresponding wave height determined, given the required steepness. This was then achieved in the wave flume in an iterative manner: the drive signal to the wavemaker was estimated using the standard, current-free transfer function, then modified until the desired wave height was produced.

Since it was found to be impossible to use a conventional beach for the sheared current case, because it would interfere with the profile, all the testing was carried out once the wave train had become steady and before reflections had returned from the end of the tank. The available time window was estimated using the group velocity of the wave train, taking account of the estimated Doppler shifts and current velocity. It was found that, especially with the steeper waves, the leading wave in the train would break unless the drive amplitude was gradually ramped up to its steady value. This was done in software, and taken account of in the estimation of the available time window. To be on the safe side, the time window was reduced by 1 second at the start, and 2 seconds at the end.

Having gone through the procedure described above the waves were generated in the tank. The surface elevation timeseries was measured in the centre of the zone where the PIV pictures were to be taken, with wavegauges. Two wavegauges were placed across the flume, to reduce the spurious effect of cross waves, and their signals averaged. The gauges were sampled over the maximum, whole number of waves which passed during the available time window. In order that the signals might be processed with the Fast Fourier Transform (FFT), the sampling rate was selected in the range 40Hz to 80Hz, so that the integral number of waves corresponded to 2^N samples.

The average height of the waves in the train was obtained from the sum of the fundamental, and third and fifth harmonic amplitudes resulting from the FFT. The

phase of the waves relative to the start of sampling was also determined from the fundamental component, and the phase of the drive signal to the wavemaker adjusted accordingly, so that the correct phases could be captured in the subsequent photography.

The wave/current combinations selected for the kinematic measurements are summarised in table 5.3. The frequency in the moving frame is noted as approximate because the appropriate frame was not known at this time in all cases. Similarly, the steepness is uncertain because the wavelength had not yet been determined. In fact these values of the steepness tend to be over-estimates.

The wave height records are shown in figures 5.4 to 5.7. Each plot contains the traces of two wavegauges, positioned alongside each other. Any transverse unsteadiness of the waves shows up as differences between the two traces, and it can be seen that this is only detectable for the steep waves on the strongly sheared current (figure 5.7).

An important feature of the wave traces is an apparent lengthening of the period in some cases, compared to the period at the wavemaker. This manifests itself in some of the plots, for example case 19 in figure 5.7, by the number of waves in the sampling period being not quite integral, as it was specified to be. This suggests that the flow conditions were not steady, and that there was some time-evolving wave/current interaction. The same effect can be found in Swan [61] where the period of some of the waves is noticeably longer than the numerical waves with which they are compared.

5.3 Experimental Measurements

Having established a set of wave and current parameter combinations, experiments were then performed to measure the kinematics for these cases, and tests were also carried out to determine the wavelength for these and other wave parameters.

Case	Current	Frequency [Moving frame] (Hz)	%age of limiting steepness	Frequency [Wavemaker] (Hz)	Height [gauges] (m)
0	No current	~ 0.8	~ 60%	0.8000	0.2083
1	No current	~ 1.0	~ 40%	1.0000	0.0891
2	No current	~ 1.0	~ 60%	1.0000	0.1338
3	No current	~ 1.0	~ 80%	1.0000	0.1787
4	No current	~ 1.2	~ 60%	1.2000	0.0927
5	No current	~ 1.2	~ 80%	1.2000	0.1232
6	Uniform, reverse	~ 1.0	~ 60%	0.8336	0.1339
7	Uniform, forward	~ 0.8	~ 40%	0.9275	0.1343
8	Uniform, forward	~ 1.0	~ 40%	1.1929	0.0890
9	Weak shear	~ 0.8	~ 60%	0.7345	0.2080
10	Weak shear	~ 1.0	~ 40%	0.8976	0.0885
11	Weak shear	~ 1.0	~ 60%	0.8976	0.1341
12	Weak shear	~ 1.0	~ 80%	0.8976	0.1771
13	Weak shear	~ 1.2	~ 60%	1.0525	0.0935
14	Weak shear	~ 1.2	~ 80%	1.0525	0.1240
15	Strong shear	~ 0.8	~ 60%	0.7099	0.2074
16	Strong shear	~ 1.0	~ 40%	0.8592	0.0888
17	Strong shear	~ 1.0	~ 60%	0.8592	0.1326
18	Strong shear	~ 1.0	~ 80%	0.8592	0.1787
19	Strong shear	~ 1.2	~ 60%	0.9972	0.0932
20	Strong shear	~ 1.2	~ 80%	0.9972	0.1216

Table 5.3: Wave/Current conditions used for the PIV experiments

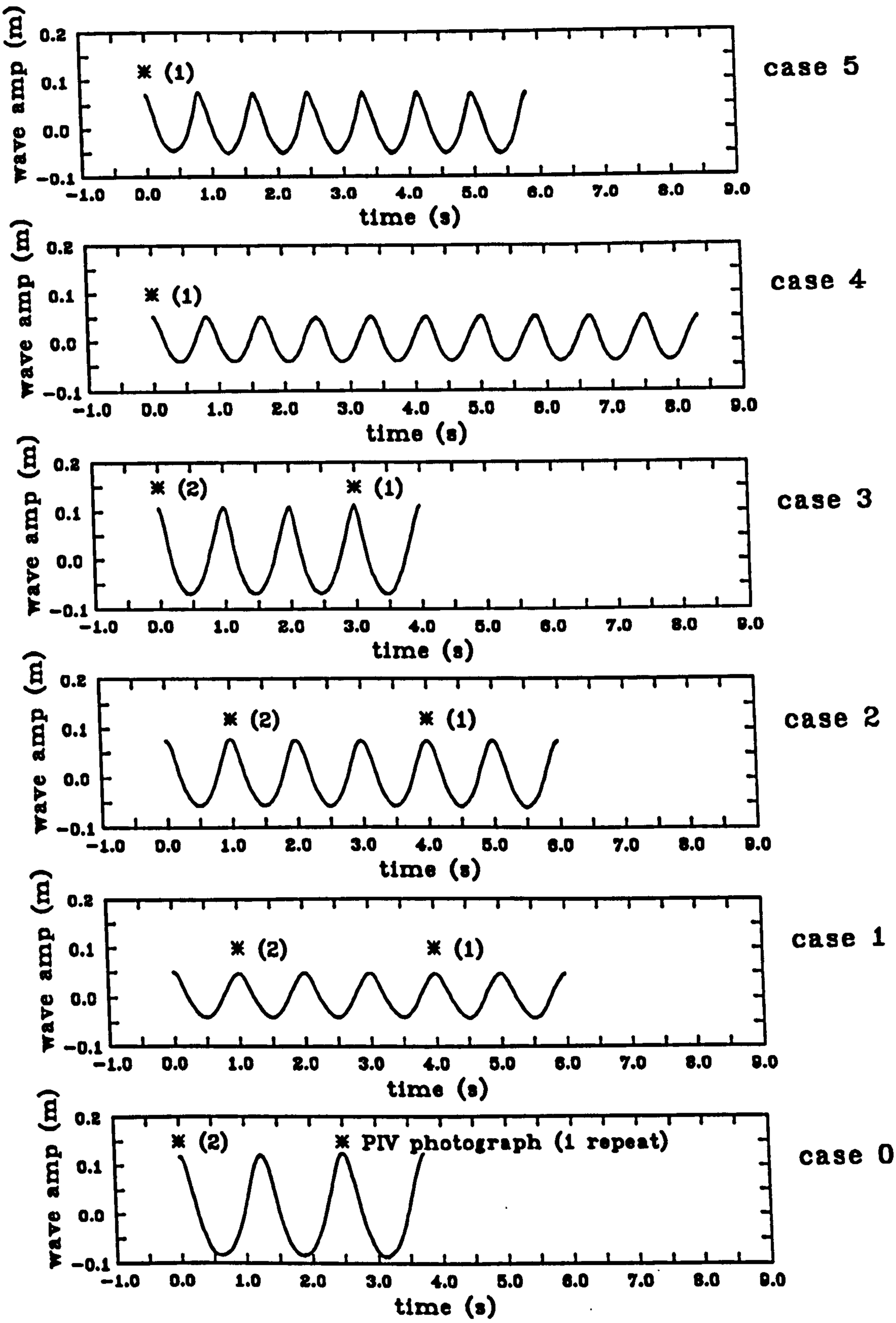

Figure 5.4: Wave height signals measured before the kinematic tests, no current

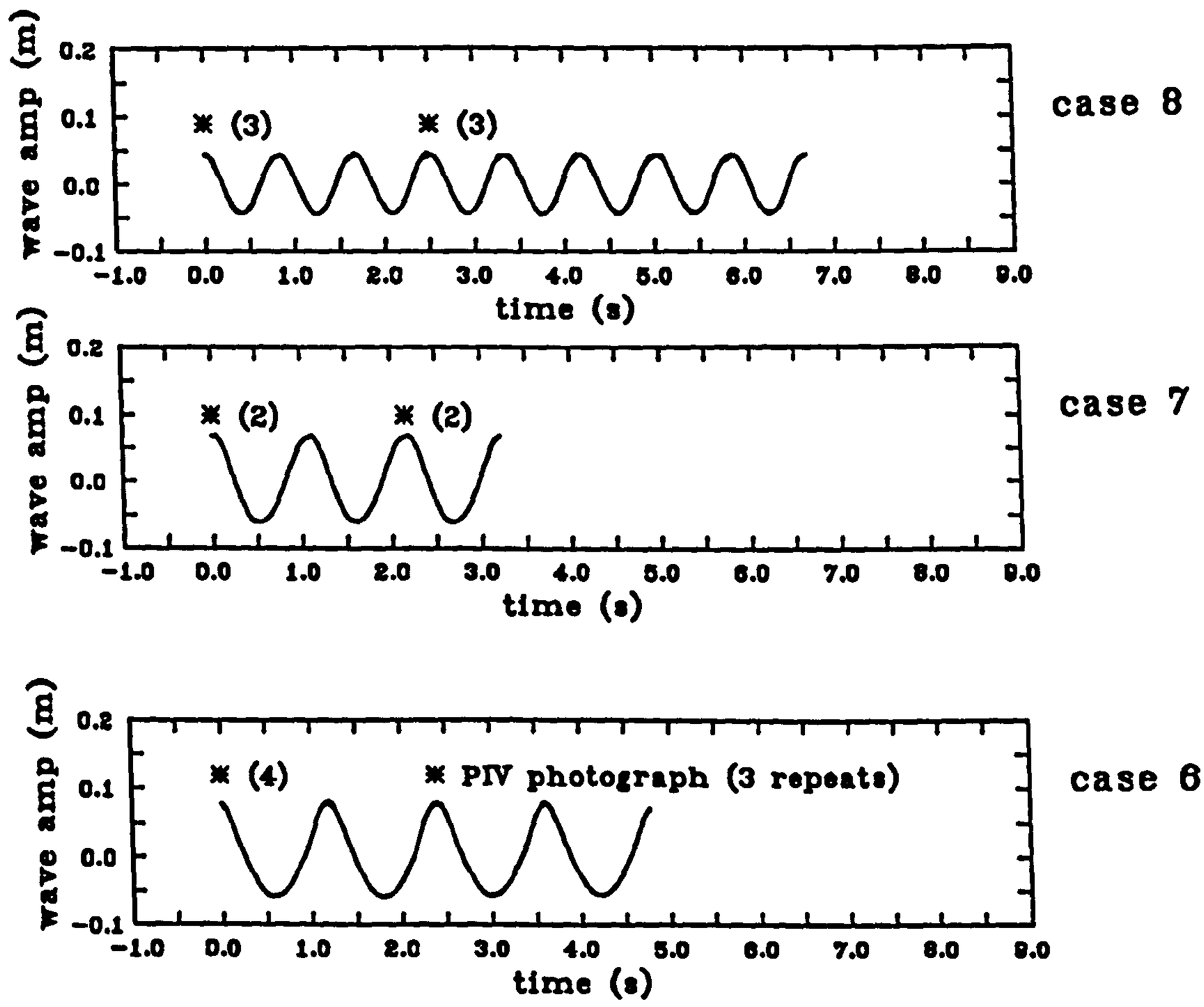

Figure 5.5: Wave height signals measured before the kinematic tests, uniform current

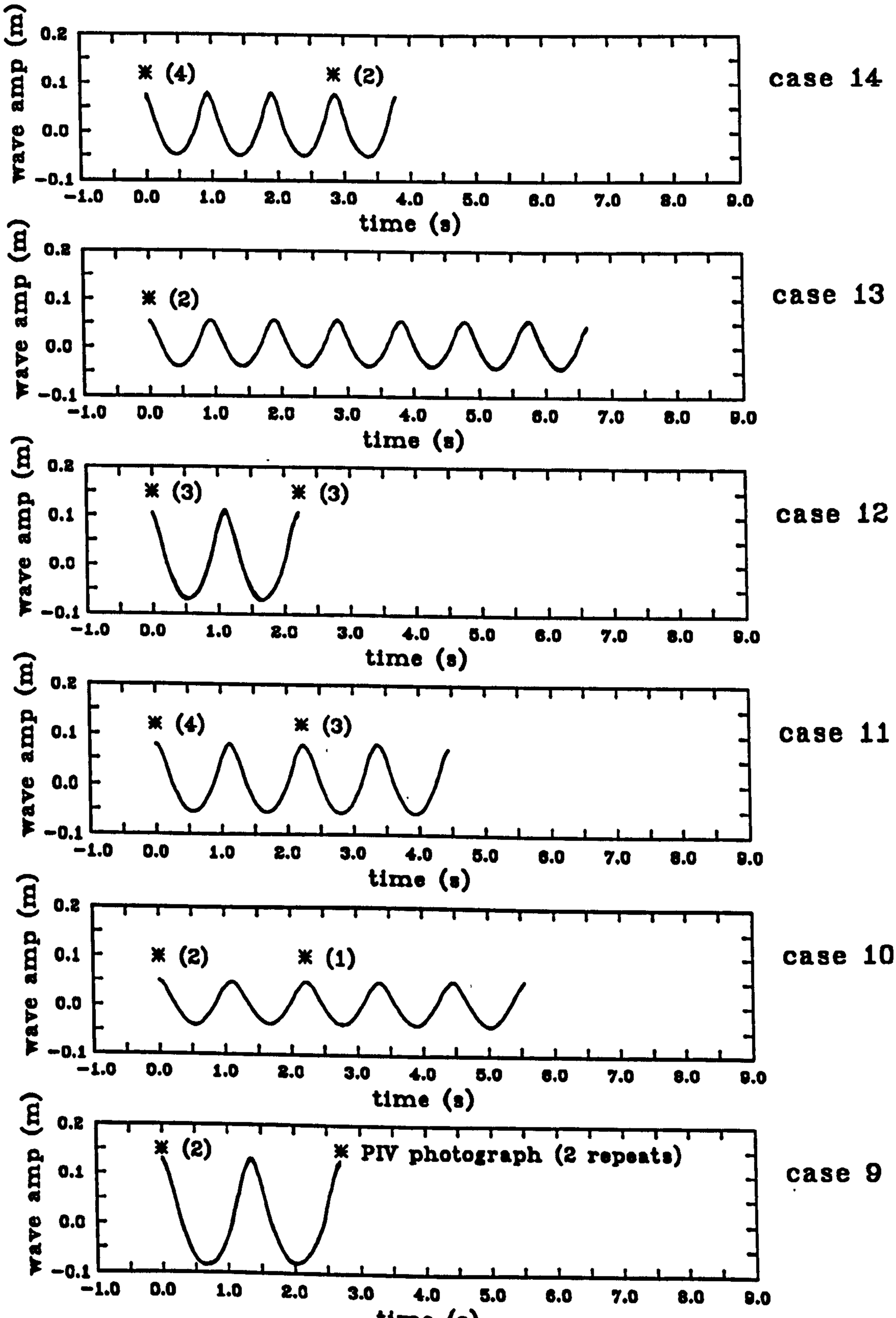

Figure 5.6: Wave height signals measured before the kinematic tests, weak shear

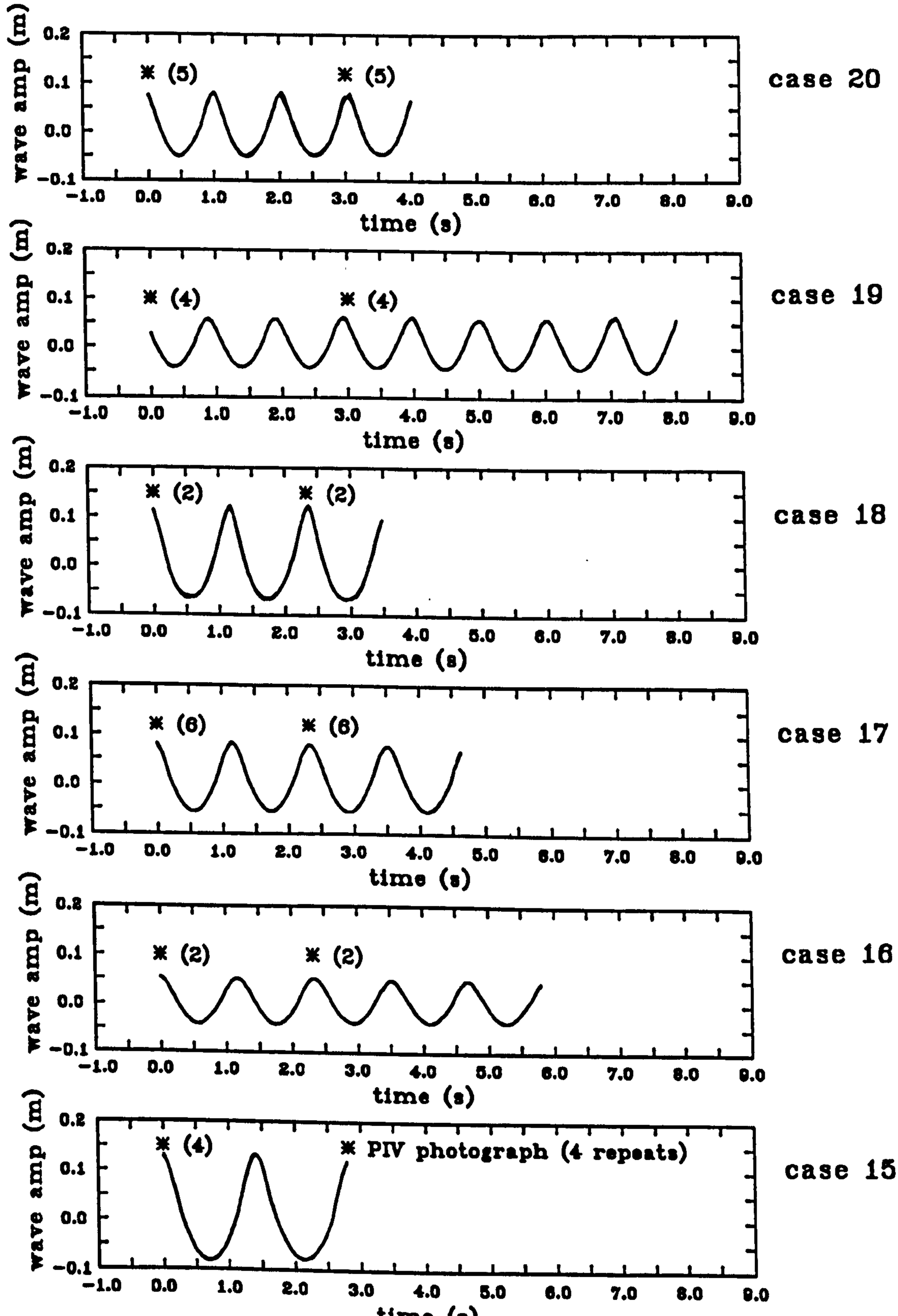

Figure 5.7: Wave height signals measured before the kinematic tests, strong shear

5.3.1 Experimental Procedures

The general experimental procedures used have been covered in chapter 3. However, there are some aspects of the acquisition on the PIV photographs which are particular to each set of experiments.

Acquisition on the PIV Photographs

A Hasselblad 500*EL/M* camera with an 80mm lens was used for all of the tests. This was positioned about 1.7m away from the illuminated plane, with the camera's view centred .2m below the water surface. In this way the whole of the 1m wide plane was imaged, from the bed to the water surface. In the majority of the tests the middle of the measurement plane was set up at a position 5m down from the wavemaker.

Parameter	Setting
Magnification	19.75:1
Aperture	f4
Shutter speed	1/30s
Laser power	12W
Film speed	400ASA

Table 5.4: Settings used in the PIV experiments

The optimal settings for the camera were found by a series of focussing and exposure tests. For the range of velocities covered in these tests, the optimal settings are summarised in table 5.4, along with other PIV parameters used in the study.

PIV has a limited dynamic range. If the particle images are too close on the film, they overlap and cannot be resolved. If they are too far apart, they are difficult to correlate. In order to make the most of the available dynamic range

it is necessary to estimate the maximum velocity, then calculate the illumination interval required so the resulting particle image separations are just resolvable.

For each of the wave/current combinations being tested, the maximum combined velocity and hence the best illumination interval was estimated. In some of the cases, the estimate was discovered, on analysing the photographs, to be too high. In such cases, in order to improve the minimum resolvable velocity, the experiments were redone with the improved knowledge of the maximum velocity.

Small velocities were present in interesting portions of the flow in some of the tests, due to the reverse current and the wave orbitals producing an instantaneous stagnation point. The difficulties associated with these zones could have been avoided with the use of a shifting technique, but a suitable implementation was not available.

5.3.2 The Kinematic Measurements Involving PIV

The PIV photographs were taken of the wave/current combinations summarised in table 5.3.

For each wave/current combination a number of photographs were taken at various times during the steady period of the wavetrain, in order to obtain measurements of the crest, trough, and still-water crossings. Measurements concentrated on the crests, and in all cases it was necessary to repeat the wave conditions a number of times to achieve the total number of pictures required, since the camera being used had a wind-on time of about 2 seconds. The times during the steady wave trains where the PIV photographs were taken have been marked with asterisks in figures 5.4 to 5.7, along with the number of repeats of the photographs at each of these times.

The sequence of tests was carried out under computer control, with a 150 second settling period programmed into the sequence to allow the flume to settle between

each run. The camera was operated in its mirror-cocked mode to avoid unnecessary vibrations, and was triggered 33ms before the required measurement time, to take account of the mechanical delays inherent in its operation.

Some manual intervention was required in the tests. The film had to be changed after every 12 frames, and the scanning rate of the illumination system was set to the required value for each wave/current combination. Due to the presence of the current, it was not necessary to stir-up the seeding periodically, just to ensure that the overall level was satisfactory. The actual illumination used was measured when appropriate, and the laser was continually adjusted to ensure high light levels during the long running period.

Analysis of the PIV Photographs

The general points concerning the analysis of PIV negatives have been covered in section 3.5.1.

Given the time taken to process a complete negative, it was impossible to analyse all of the pictures taken, about 200, over the full frame. However, the most interesting part of the combined flow fields is under the crest, so many of the photographs were analysed over a thin strip in this region. The wave/current cases judged to be the most important were analysed over the full field.

All of the negatives obtained in the present study were analysed in the standard manner on a grid whose spacing was equivalent to 20mm steps in the measurement zone. Given the photographic magnification, this corresponded to steps of just over 1mm on the negatives. The magnification also implies that each velocity vector obtained was the average over an area in the flow with diameter 20mm. The absolute positioning of the vector maps was ensured by making use of the registration marks present on the negative, resulting from the positioning crosses on the tank.

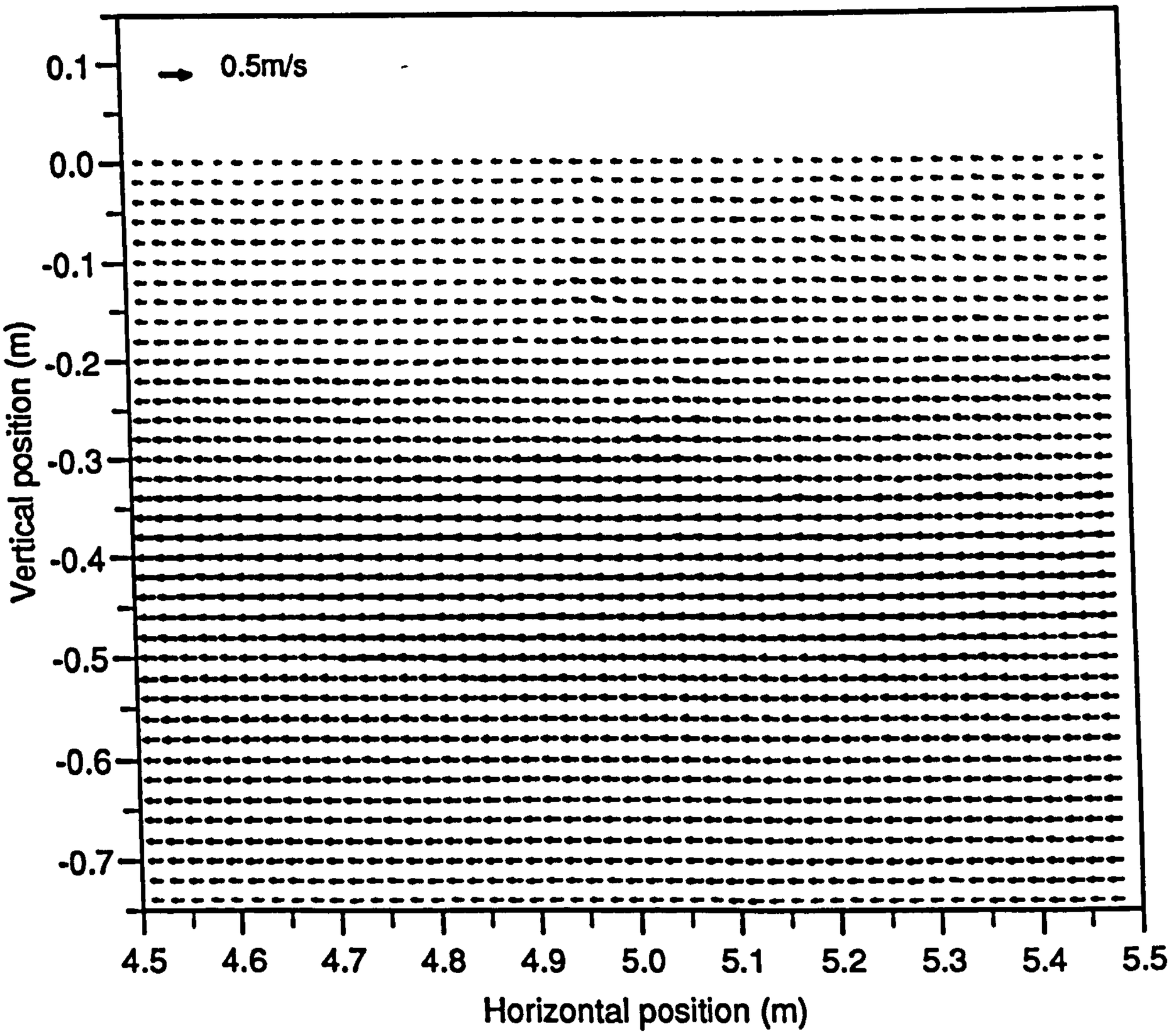

Figure 5.8: Example of the results of a typical PIV analysis, for a strongly sheared current

Having obtained velocity fields from each negative, spurious vectors were eliminated. This was done by removing vectors whose magnitude was less than a preset minimum value, whose reliability level was too low, and those which were inconsistent with their neighbours. The directional sense of each vector was set making use of an a-priori knowledge of the fluid flow, and by ensuring that continuity applied through the velocity field.

Figure 5.8 shows an example PIV vector plot of the strongly sheared current in the absence of waves. Because the velocity gradients are small and the magnitude of all the velocities is comfortably within the dynamic range, all points within the field have been accurately recorded. The direction of all the velocity vectors is readily set as it is known, a-priori, to be towards the wavemaker.

Figure 5.9 shows a vector plot obtained for a wave riding on the strongly sheared current, whose bulk flow was opposed to the waves. The resulting stagnation zone, under the crest, can be seen in the centre of the plot. PIV measurements were not possible here, as the particle images were overlapping. Around the stagnation point, the direction of the velocity vectors can be seen to change smoothly. The sense of all the vectors was set by ensuring that this happened, and by knowing the direction of the velocity under the crest, or near the bed. Other features of this typical plot include odd missing vectors due to high velocity gradients, low seeding density or other noise problems.

Extraction of the Wave Surface

The wave surfaces were obtained from the PIV negatives using the procedure described in section 3.5.2. However, in the cases when the current was present, the surface was often difficult to identify, because the seeding on the surface drifted away. In the graphs which follow, lines marking the wave's surface should be regarded as approximate.

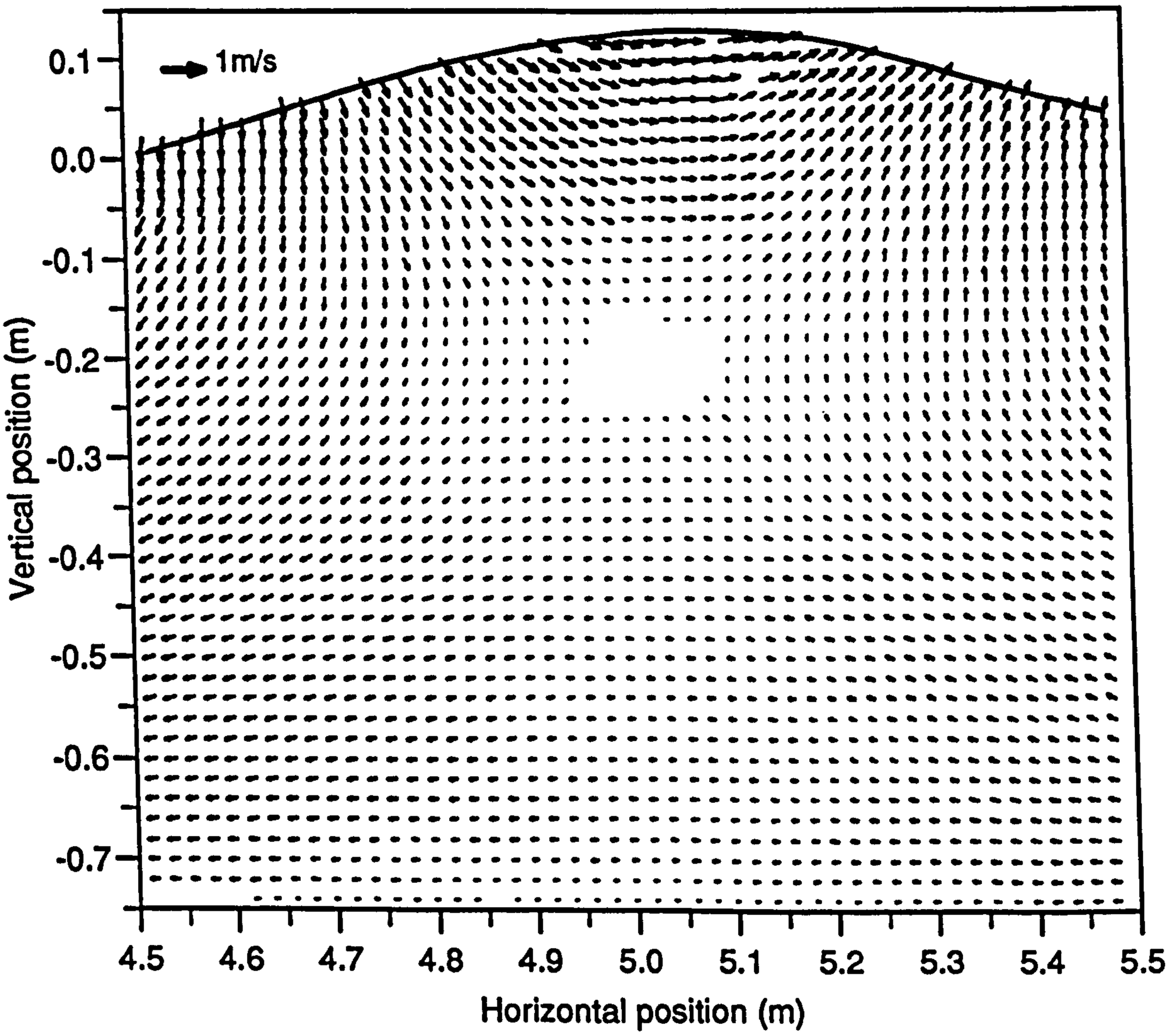

Figure 5.9: Example of the results of a typical PIV analysis, for a wave on a strongly sheared current (case 15)

5.3.3 Measurement of Wavelength

The wave frequency is readily known with some accuracy, but the wavelength is more difficult to measure. While a value of the wavelength can be obtained from the photographic images, its was deemed desirable to obtain another estimate by an independent means. This was done with the use of wavegauges.

If the wavetrain is steady, of known frequency, with no unbound harmonics and with no reflections present, then it is possible to obtain a value of the wavelength from the phase difference between the surface elevation at different places along the tank. An array of four gauges was constructed, consisting of two pairs separated by 188mm. Pairs were used in order to obtain an average value of the wave height across the tank.

A matrix of tests was conducted for each current case, covering wave frequency (wavemaker frame) and driving amplitude. In addition, all the wave/current cases listed in table 5.3 were repeated, and the wavelength discovered in this way. Again, with the matrix of tests, care was taken to ensure that the waves were steady, and the drive signal was ramped up in order that the leading crest of the group did not break. In one case, the set of wave conditions were randomised in case the heating of the water was causing systematic errors.

5.3.4 Experimental Errors

In all experiments of this type there are a number of sources of error, and a variety of ways in which the experimental conditions vary from the assumptions usually made in any mathematical modelling.

Turbulence

The current profiles generated contained some turbulence. For the *uniform*, reverse current, this amounted to a rms level of about 3% of the bulk flow. More turbulence was inevitably produced with the strongly sheared flows, up to 6% for the large shear case. Note that if the current is viewed from a different frame of reference, for instance one moving with the maximum velocity, where it represents a wind-sheared current, then the apparent turbulence calculated in the same manner is higher.

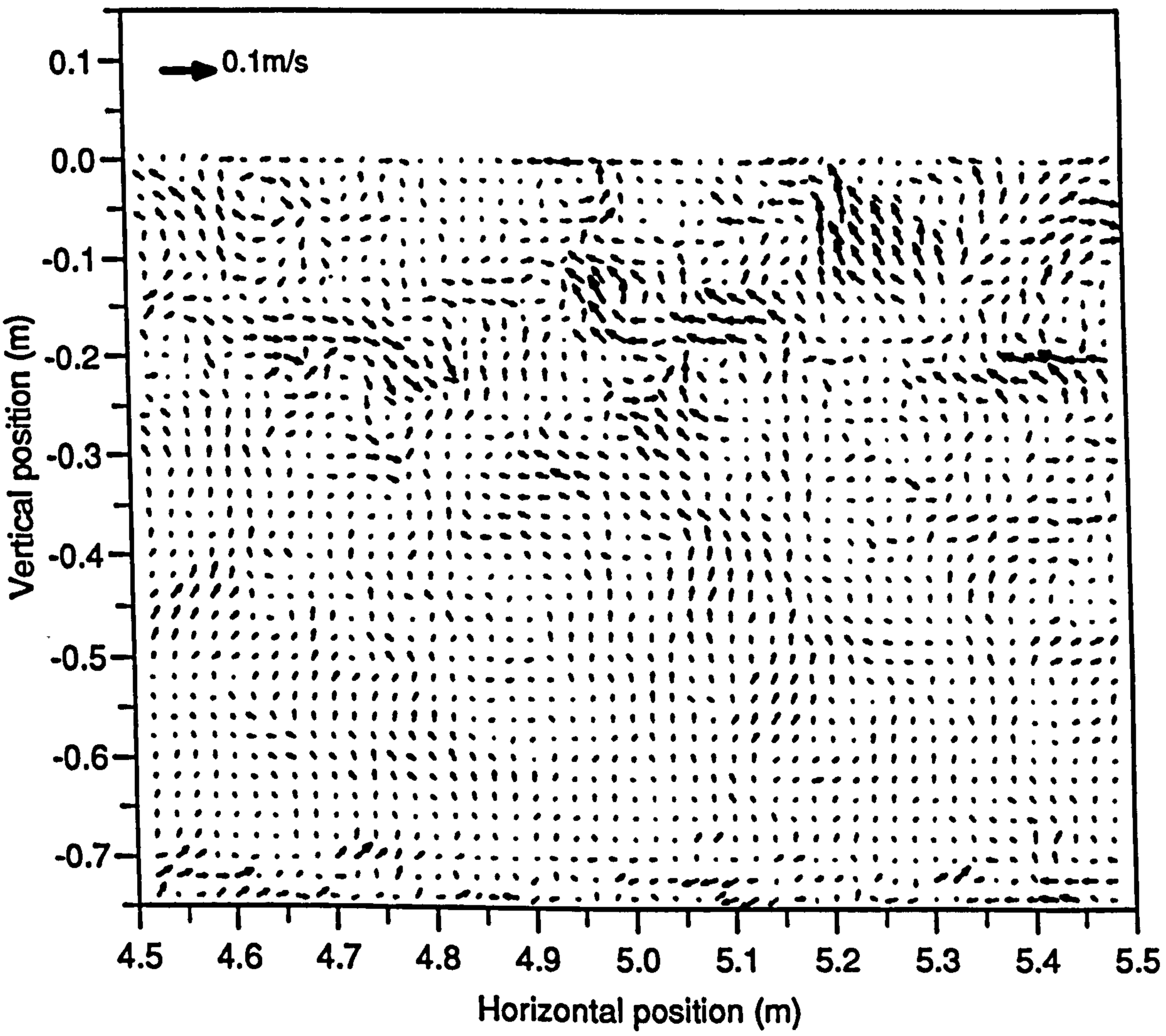

Figure 5.10: Residual turbulence in one of the current cases, strong shear

The turbulence was initially regarded as random noise, on top of any measurements made. Therefore, in the PIV experiments, tests were repeated to allow

subsequent averaging to reduce the effect of the turbulence.

The turbulent structure present in one of the currents is emphasised in figure 5.10, by subtracting from each row of vectors the mean velocity at that level. Coherent turbulent structures are clearly seen and their intensity is greatest in the regions of largest shear. These structures are likely to be 3-dimensional, and this property can be identified in the regions where sizable vectors are surrounded by little activity. Determining the divergence of the field would show up these effects.

PIV Errors

The errors and limitations inherent in PIV have been discussed in section 3.4.2. In this study, the dominant error was that associated with the local averaging of the flow. In some of the cases, non-negligible velocity gradients were present, which can be expected to lead to an increased error [19]. It was estimated that for all of the tests conducted the error in the maximum measurable velocity was about 1%.

Reflections and Wave Steadiness

The experimental procedure relied on the waves being steady, with no reflections. The wave traces plotted in figures 5.4 to 5.7 show that this was a reasonable assumption. However, a little unsteadiness is apparent in the steeper wave cases, manifesting itself by the difference between the two wavegauge signals. In addition, it can be seen in the strongly sheared cases, particularly, that the period of the waves is slightly longer than that expected, as the waves do not fit in to the sampling period an integral number of times. This may be due to an interaction, evolving with time between the sheared layer and the wave kinematics.

During observation of the tests, some unsteady effects were noticed. Particularly with the strongly sheared cases and the high frequencies, some unsteadiness across

the tank was noted. With the higher frequencies, the waveform became a little distorted later during the sampling window, due to spurious, unbound harmonics being generated at the wavemaker and travelling slowly along the tank.

Only during the testing of the longest period waves were any effects due to early reflections suspected.

Repeatability

The inherent repeatability of the wavemaking system, described in section 3.3.2, is excellent. From the PIV photographs of the waves travelling on currents, it was found that the surface profiles of the waves were repeatable to within about 20mm, or about 2% of the wavelength. This amounts to a slight decrease in system repeatability from that which is normally expected and can probably be ascribed to the turbulence present in the currents.

The repeatability of the current after removing, then replacing the profile forming baffles to a previous configuration, was not good. It was anticipated in the testing that this might be a problem, so all measurement of the kinematics of the wave/current combinations were interlaced with measurements of the undisturbed current, without modifying the baffles during that period.

Current Steadiness over Space and Time

Most of the current profiles were formed by the baffles at the end of the flume. The current profile will alter as it flows along the tank, with any shear at the surface reducing, and boundary layers growing from the bed and the walls. In order to obtain a measure of the spatial evolution of the profile, profiles for the strongly sheared current were determined by obtaining averages for the left and right hand sides of the measurement zone.

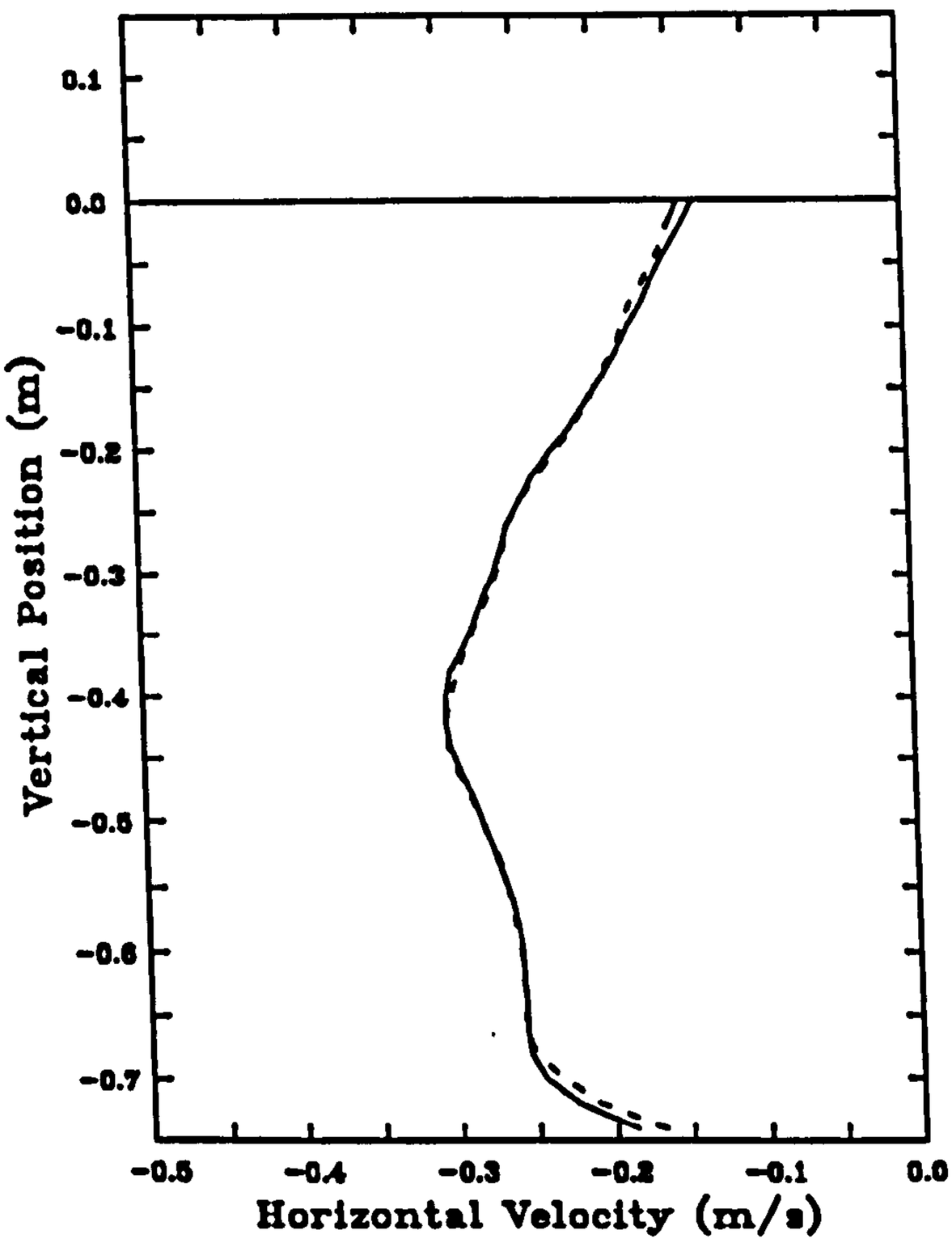

Figure 5.11: Evolution of the averaged, strongly sheared current profile over .5m of the flume, - - - - profile at $x = 5.25$m, —— profile at $x = 4.75$m

Figure 5.11 shows the average profile for the strongly sheared current obtained at two places along the tank, separated by .5m. The variation is very small, and for the purposes of the present study the spatial variation was assumed to be negligible.

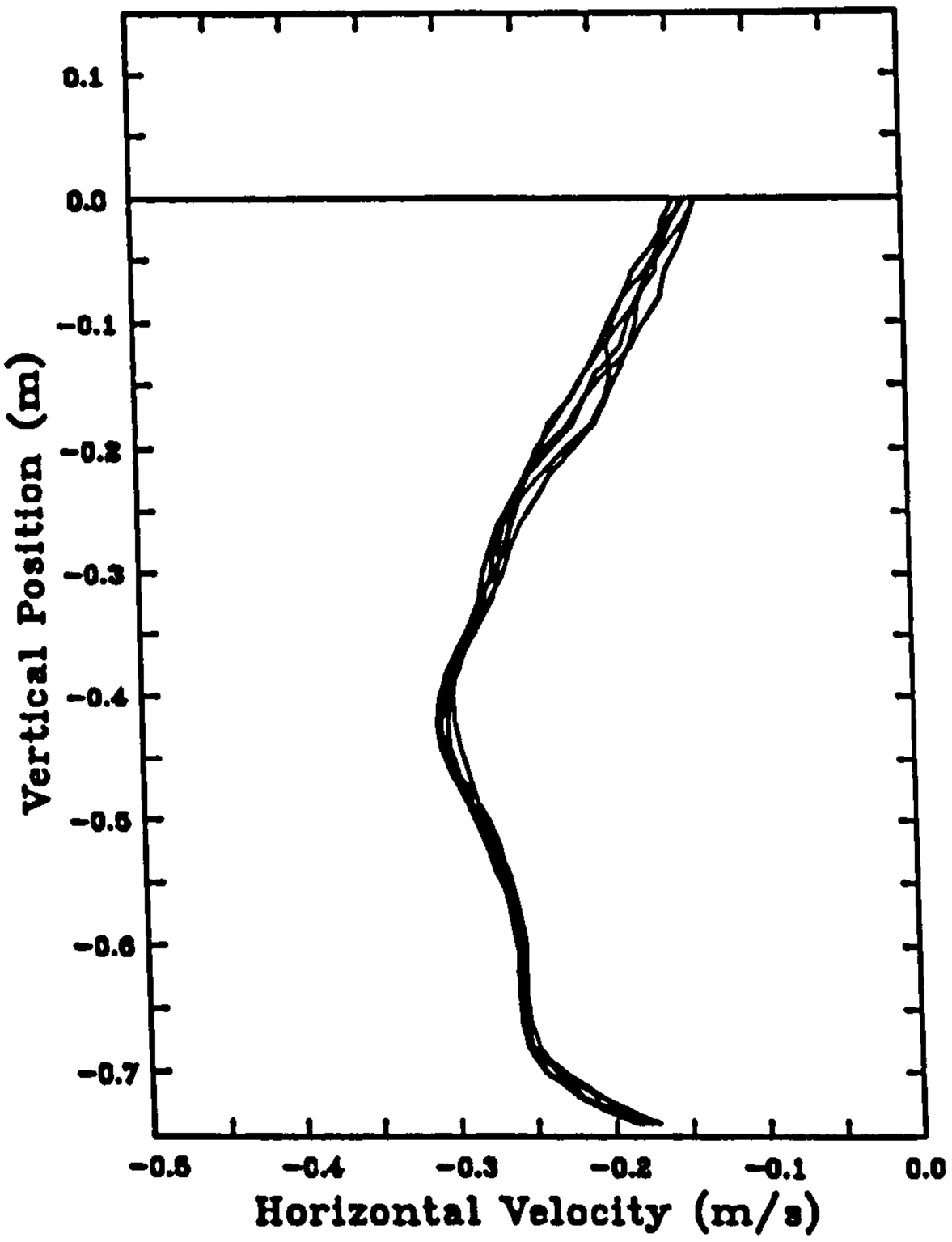

Figure 5.12: Profiles of the strongly sheared current, measured during the sequence of experiments to obtain the wave/current kinematics

It might be expected that the current profiles would show some variation with time. The turbulence in the currents contains some coherent structures with length scales comparable, though smaller, to the size of the 1m wide measurement zone, and averages over the measurement zone may be subverted by these coherent structures. Over a period of time, the mean current profiles might also change due to the build-up of large scale circulations. After running the pump for several hours the water temperature was found to rise dramatically, which might lead to trends which varied slowly with time.

Figure 5.12 shows undisturbed current profiles obtained from individual PIV photographs interspersed with the wave/current measurements. The variation of these mean profiles is a little larger than would be expected if the turbulence was a truly random, steady process. However, the variations are not large compared with the overall shear.

5.4 Experimental Results

Results are presented of the combined wave/current kinematics from some of the PIV test cases, and of the experimentally determined wavelengths.

5.4.1 Kinematic Results

The data produced by the PIV process consists of two-component velocity vectors available on a spatial grid. A typical vector plot of this data has been illustrated in figure 5.9. While this means of presentation is useful in the data validation stage of the PIV process, a better way of displaying the flow field information is by means of iso-velocity plots of the velocity components.

In the iso-velocity plots that follow, the contour interval is $0.1ms^{-1}$, with the contours at $0.5ms^{-1}$ intervals labelled and drawn dashed. The contours of constant horizontal velocity component appear like arcs centred on the top of the crest, with their maximum value at the top. Contours of constant vertical velocity component cross at right angles, and increase in the same direction as the wave propagation, from left to right.

Only a few of the experimental results are presented in this section. In each instance, the test case number is given, and further information about the wave parameters can then be found by referring back to table 5.3 and forward to table 5.5. When information about the wave crest number is given, the timing of

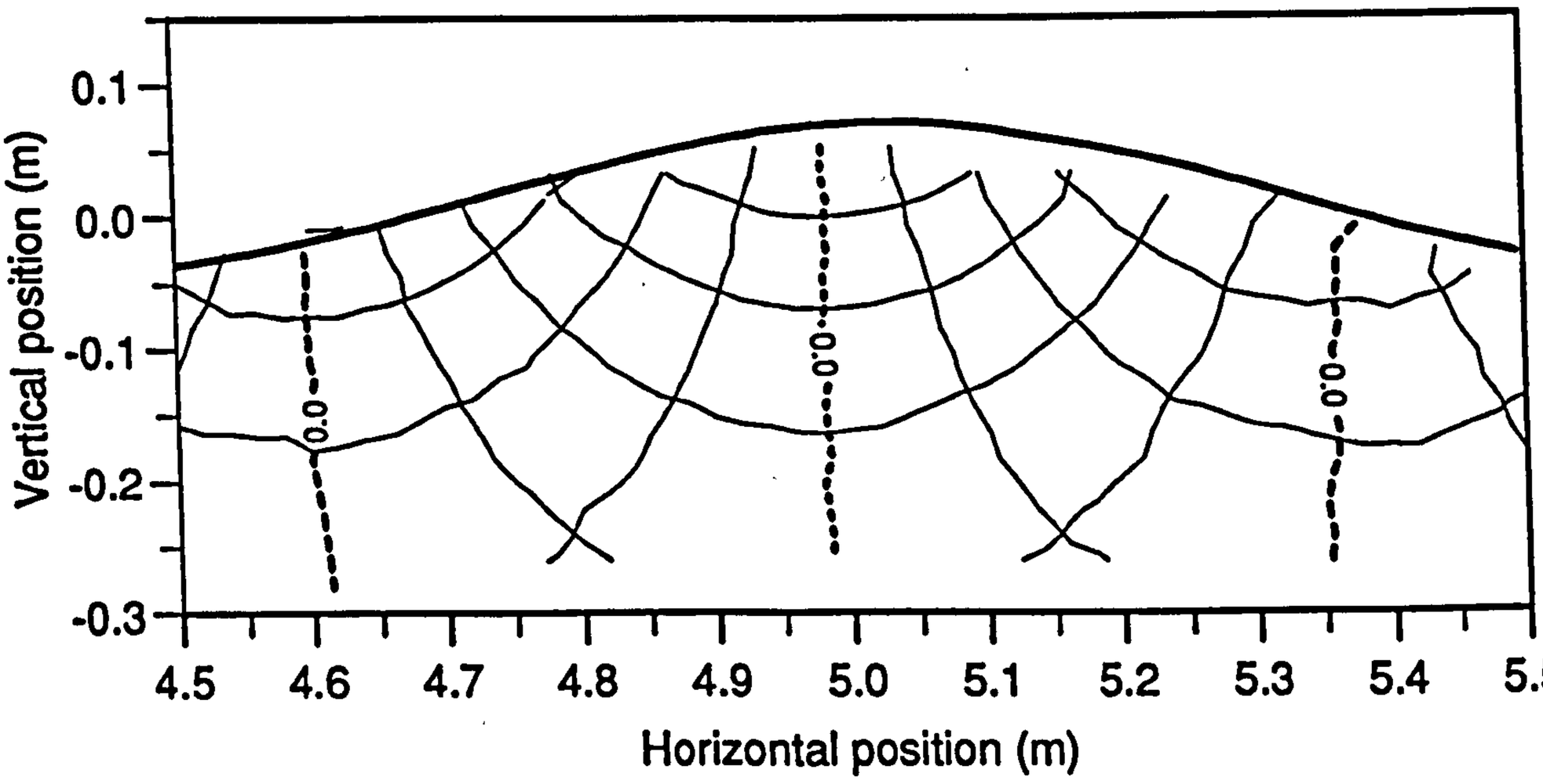

Figure 5.13: Iso-velocity contours for a 1.0Hz wave (case 2), in the absence of current, *second* wave crest. Contour interval: $0.1 ms^{-1}$

the wave within the train can be found by referring back to figures 5.4 to 5.7.

Figure 5.13 shows iso-velocity contours for case 2, a 1.0Hz wave, in the absence of current. As expected for a steady wave, the plot is very symmetrical about the crest. In particular, the $v_x = 0$ line, beneath the crest is almost exactly vertical. This also suggests that the seeding used was sufficiently close to being neutrally buoyant and that no rotational alignment errors arose in the PIV analysis. The $v_x = 0$ lines (the heavy dashed lines to the left and the right of the figure) are not vertical, as expected, possibly due to optical distortion which is greatest at the edge of the field.

The flowfield obtained from a later crest in the same wave train is plotted in figure 5.14. It should be noted that all the contours, with the exception of that for the highest v_x values, are almost exactly the same as those in figure 5.13, again as expected if the wavetrain is steady.

Data from another wave case in the absence of current is plotted in figure 5.15. Again the symmetry of the wave is apparent. Another feature of this graph along with figures 5.13 and 5.14 is the smoothness of the contour lines, indicating a lack

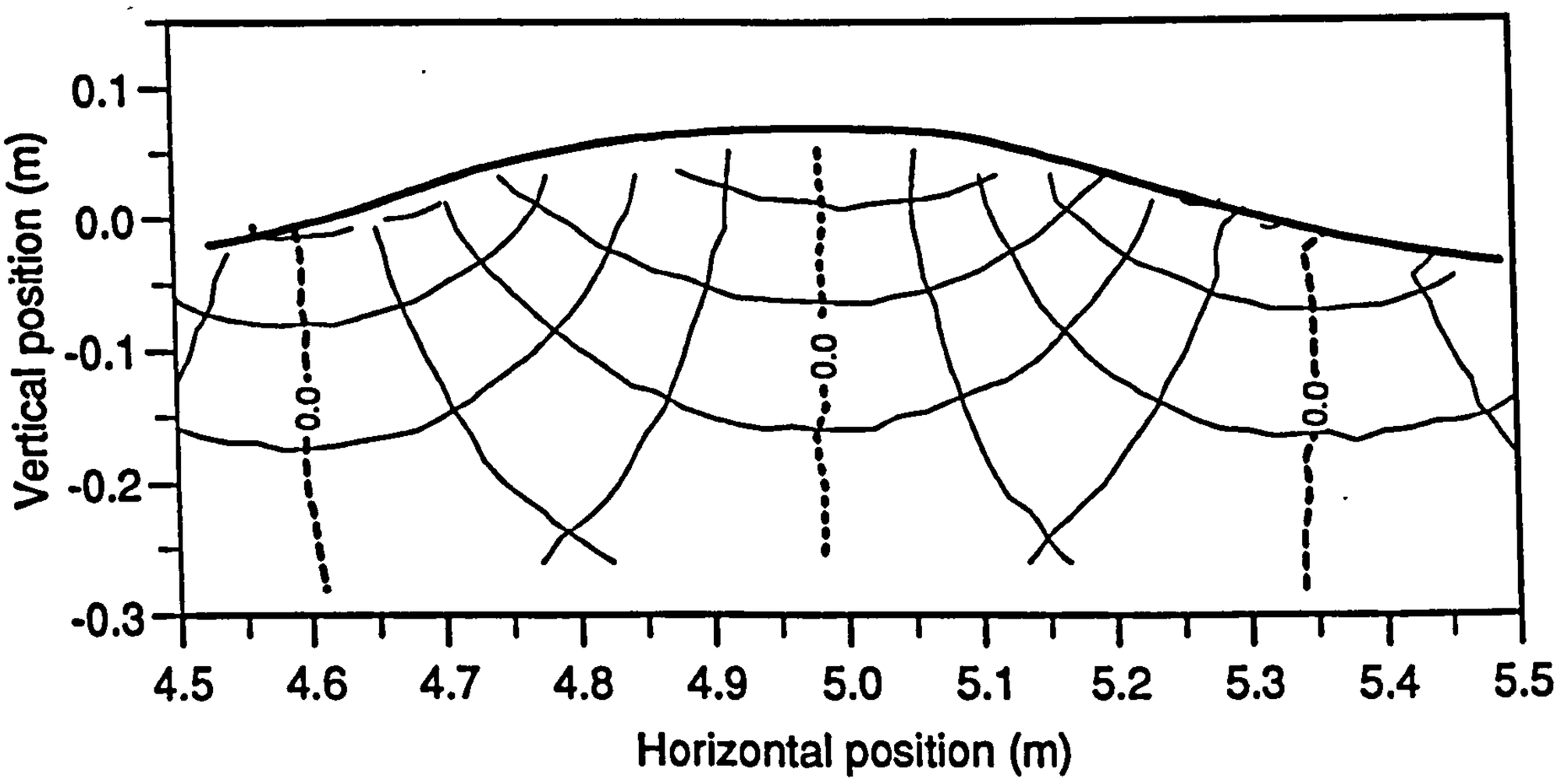

Figure 5.14: Iso-velocity contours for a 1.0Hz wave (case 2), in the absence of current, *fifth* wave crest. Contour interval: $0.1 ms^{-1}$

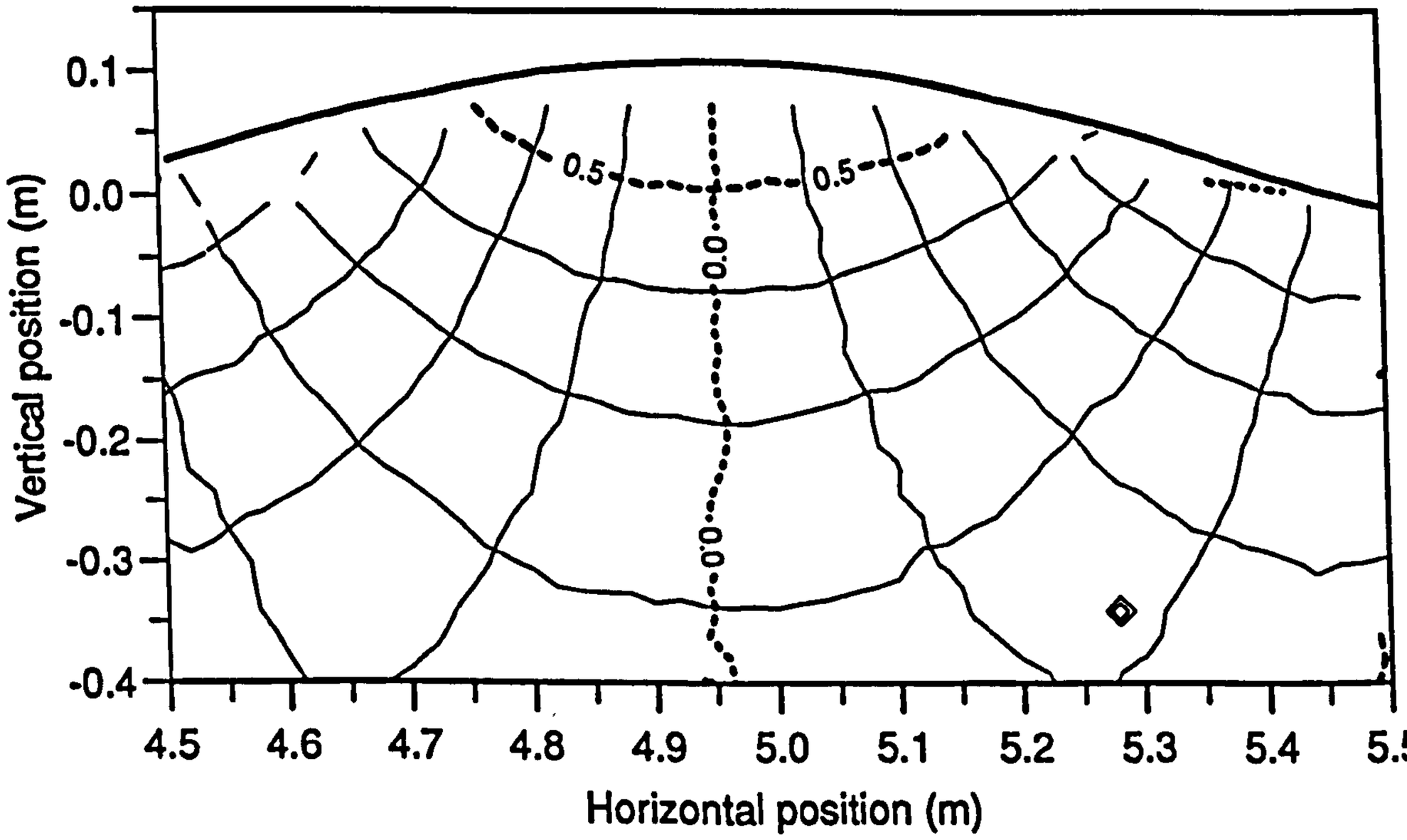

Figure 5.15: Iso-velocity contours for a 0.8Hz wave (case 0), in the absence of current, first wave crest. Contour interval: $0.1 ms^{-1}$

of turbulence in the flow and of random errors in the measurement technique. In addition, the fact that the v_x and v_z contour lines are orthogonal indicates that the flow is relatively irrotational.

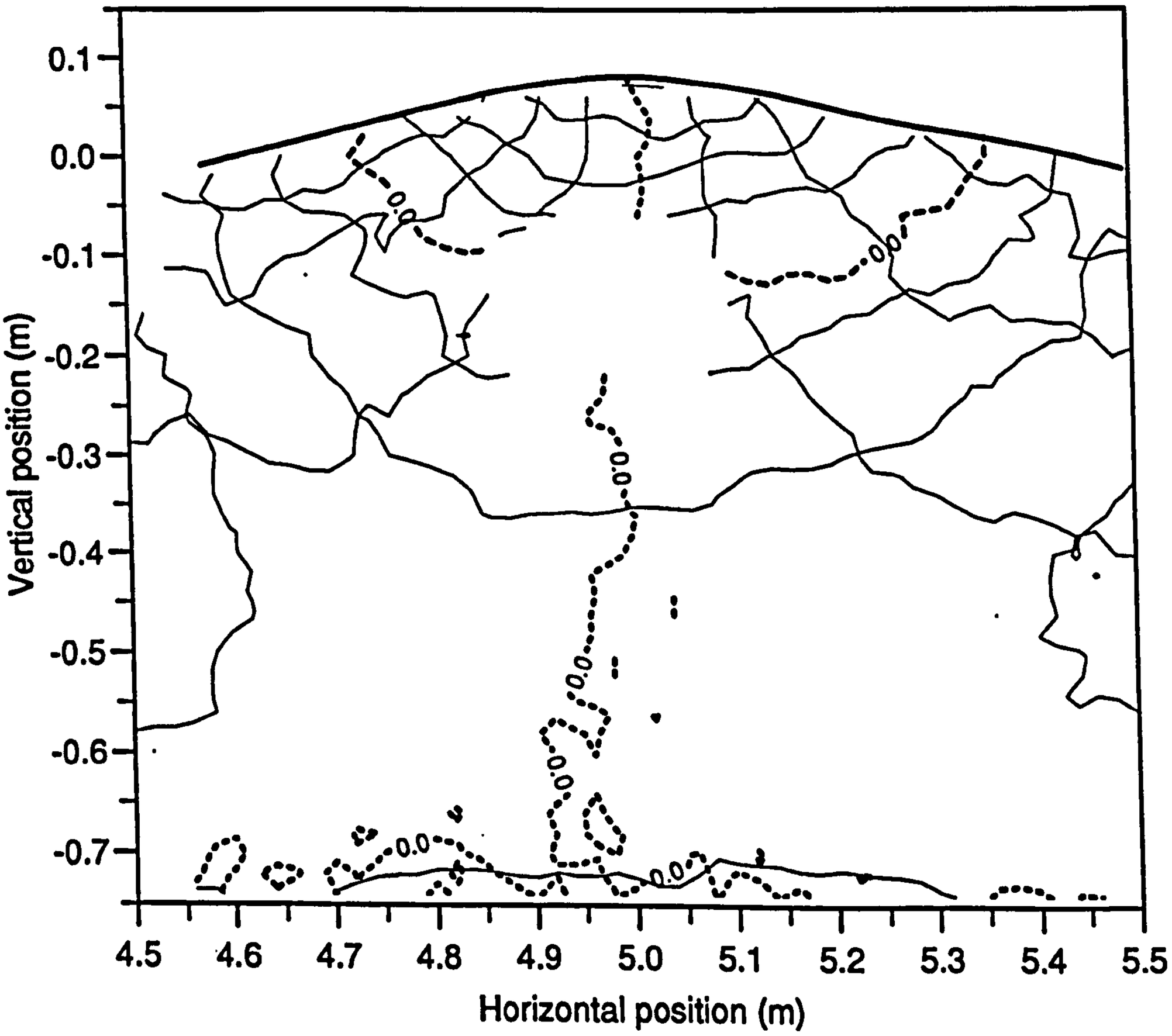

Figure 5.16: Iso-velocity contours for a medium amplitude wave (case 17), on the strongly sheared current, *first* wave crest. Contour interval: $0.1 ms^{-1}$

Figure 5.16 illustrates flow field data from the central wave case, 17, propagating on the strongly sheared current. A number of differences can be seen from the current-free cases. The contours are not so smooth, indicating small scale turbulence. The areas formed by the contours are no longer square in some regions, most noticeably near the crest, due to the sheared current. Finally, the wave is not as symmetrical as those illustrated in figures 5.13 to 5.15.

The missing contours in the centre of the plot for the wave/current case are due

to missing data in this region. While this area could have been interpolated, it was considered better to leave it blank, especially as the turbulence may have distorted the interpolation.

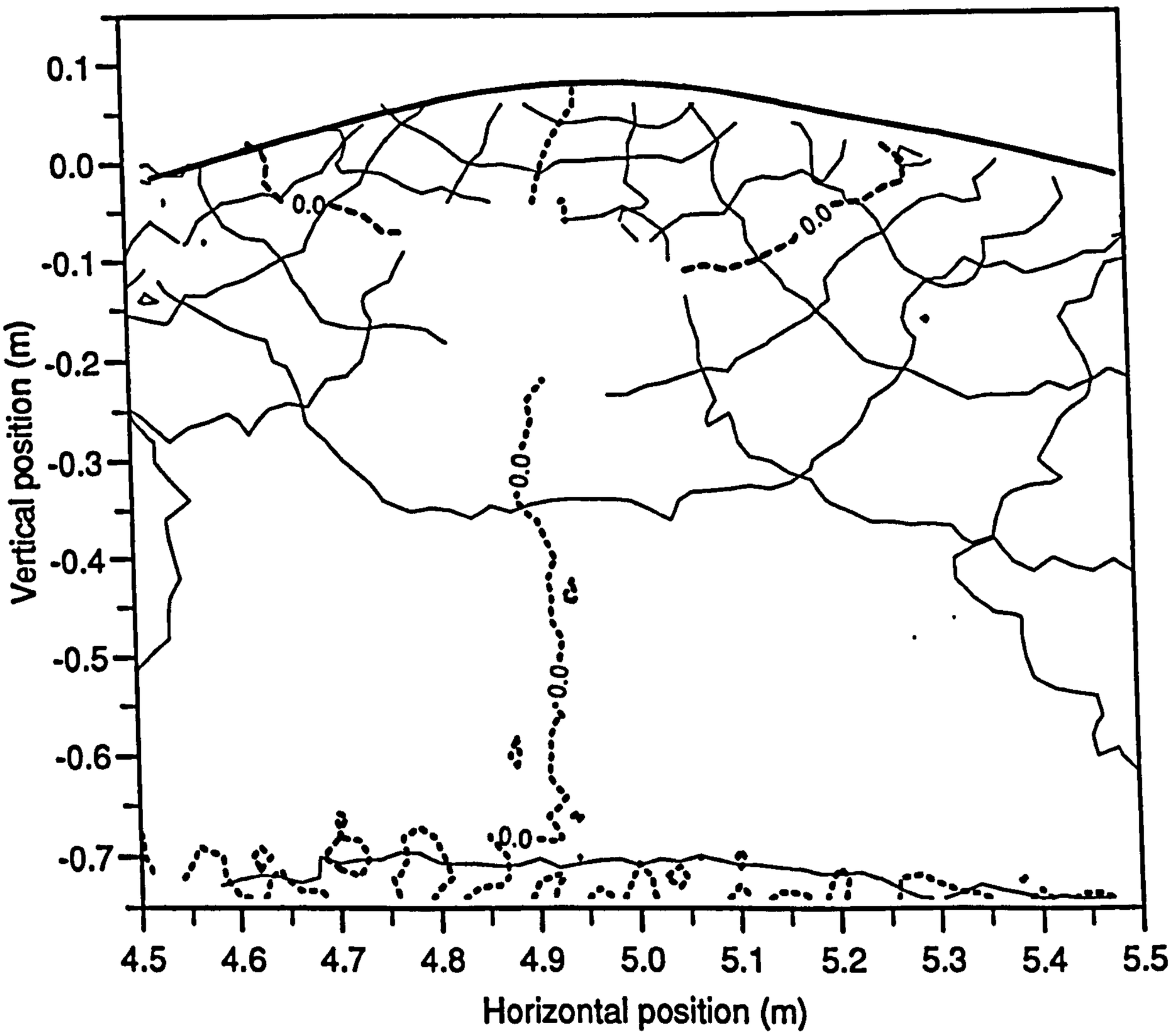

Figure 5.17: Iso-velocity contours for a medium amplitude wave (case 17), on the strongly sheared current, *third* wave crest. Contour interval: $0.1 ms^{-1}$

In order to assess the steadiness of the wave/current combinations, velocity data is plotted in figures 5.17 and 5.18, corresponding to the same wave case as in figure 5.16, but at successively later crests in the wave train.

A general trend is apparent in figures 5.16 to 5.18, and is especially noticeable in the $v_x = 0$ contours near the crest which lean more to the right in each plot. In addition the position of the crest moves left, despite the careful triggering of the camera, synchronised with the wavemaking frequency. Both these effects suggest

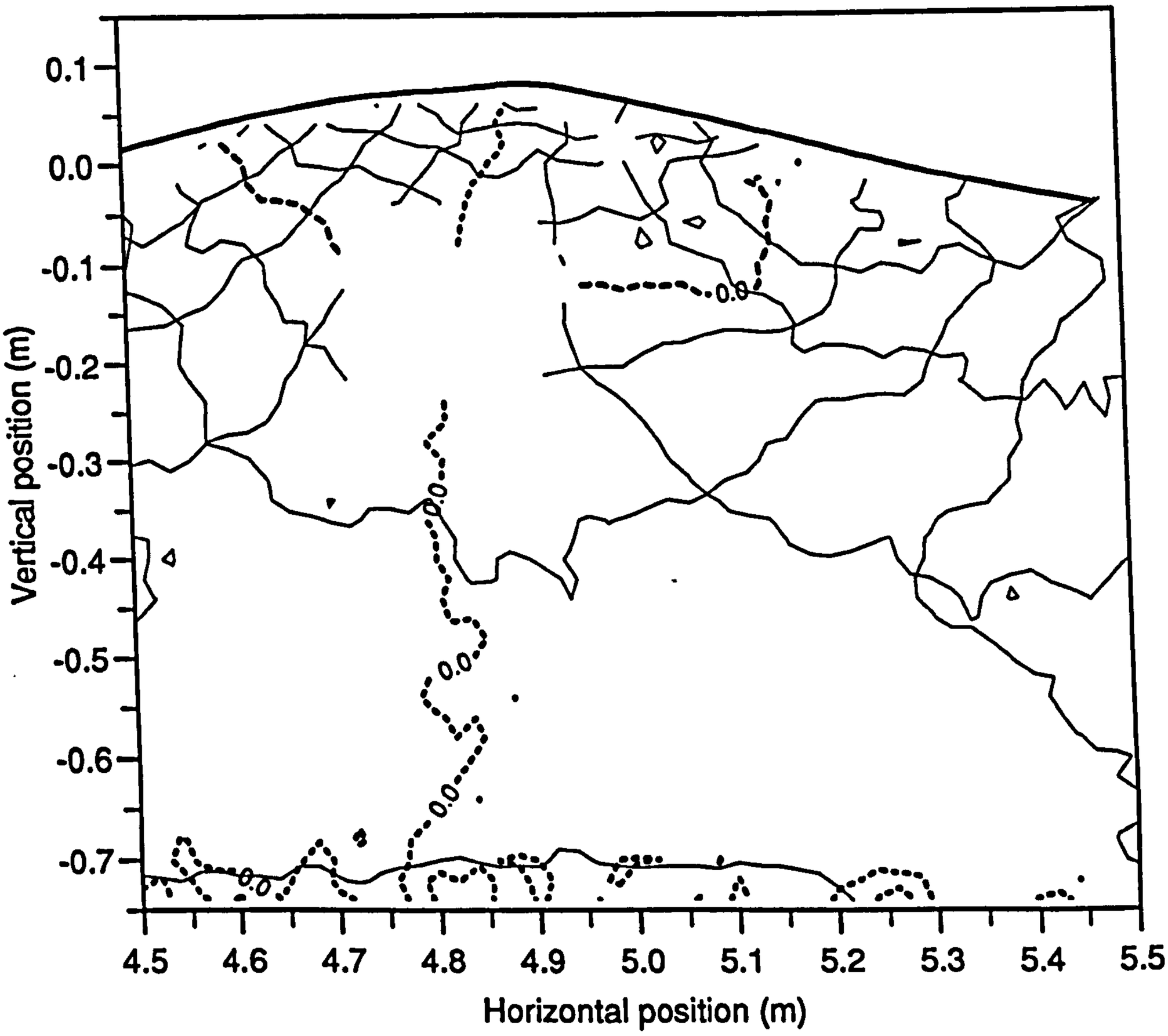

Figure 5.18: Iso-velocity contours for a medium amplitude wave (case 17), on the strongly sheared current, *fifth* wave crest. Contour interval: $0.1 \mathrm{ms}^{-1}$

that the combined conditions are not as steady as might be expected from the independent steadiness of the wave and current components.

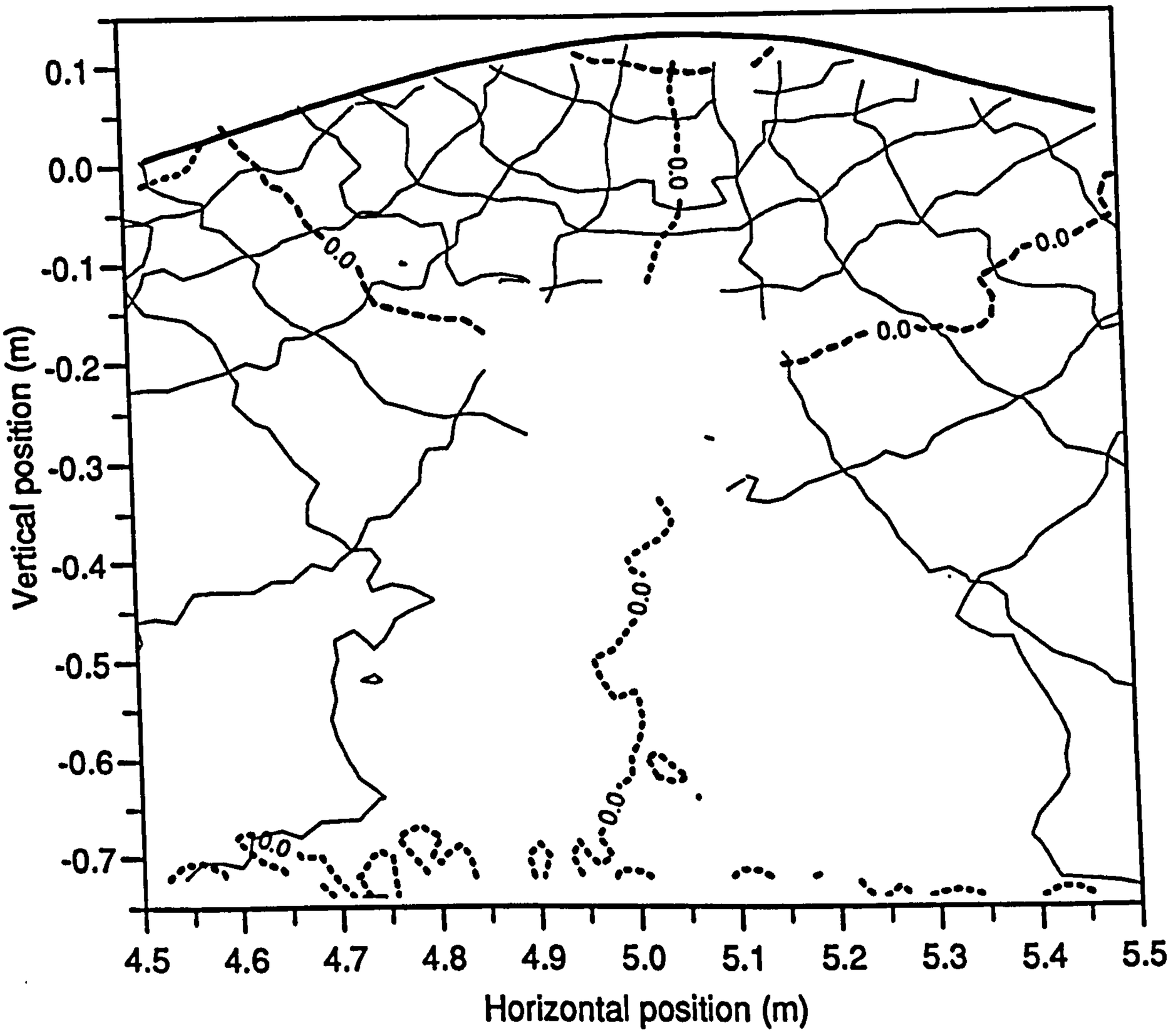

Figure 5.19: Iso-velocity contours for a medium amplitude wave (case 15), on the strongly sheared current. Contour interval: $0.1 ms^{-1}$

Other examples of the kinematics results are contained in figures figure 5.19 to 5.22. In the first, figure 5.19, the measurements are again on the strongly sheared current, this time with a wave of lower frequency (case 15). Similar features are noticeable as in the earlier cases, with the stagnation zone lower due to the slower decay of the wave orbitals with depth.

In figure 5.20, velocity contours are plotted for a wave on the reverse *uniform* current. While the form of the contours is reminiscent of the waves in the absence of current, some turbulence is apparent.

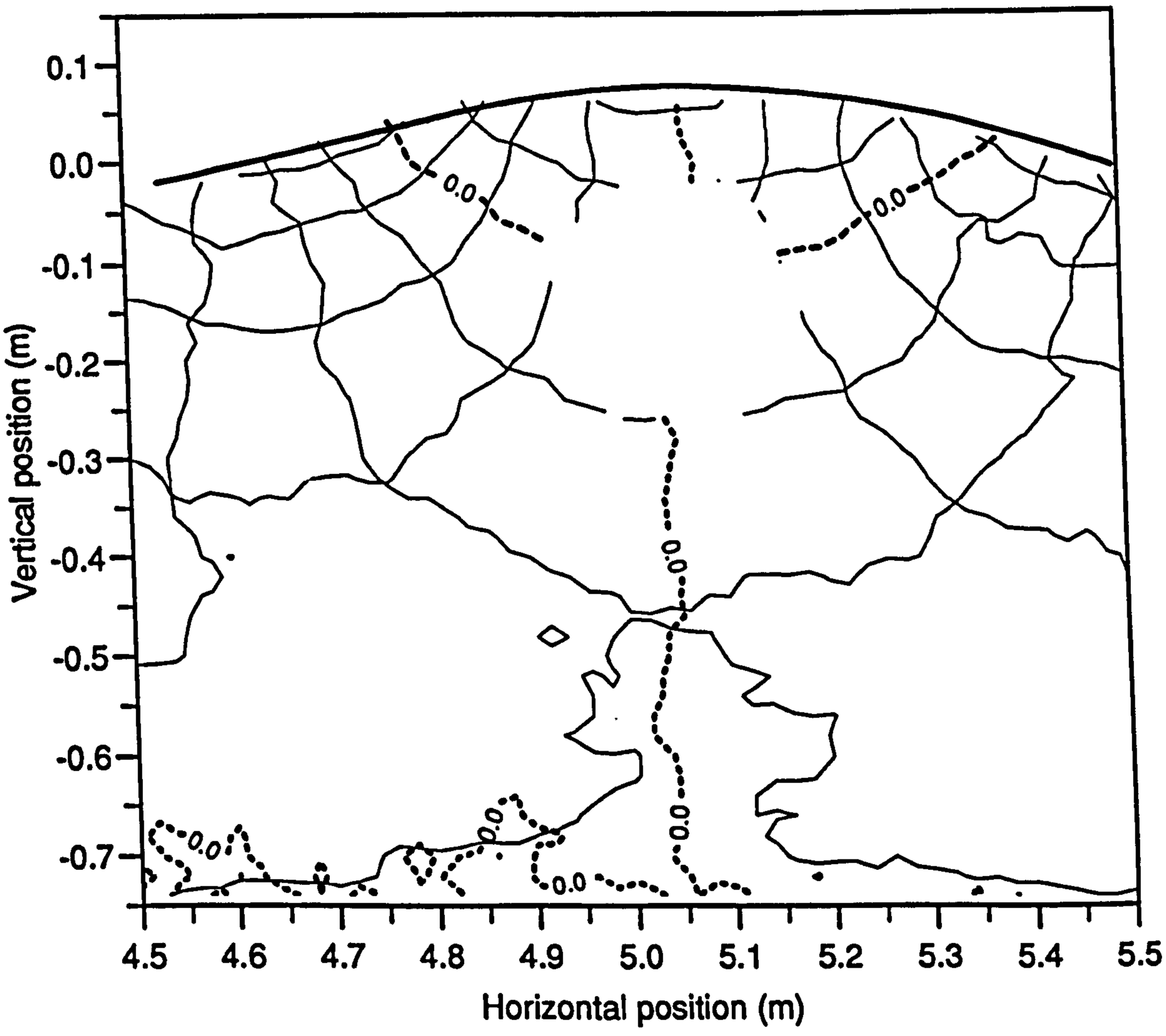

Figure 5.20: Iso-velocity contours for a medium amplitude wave (case 6), on the reverse, uniform current. Contour interval: $0.1 ms^{-1}$

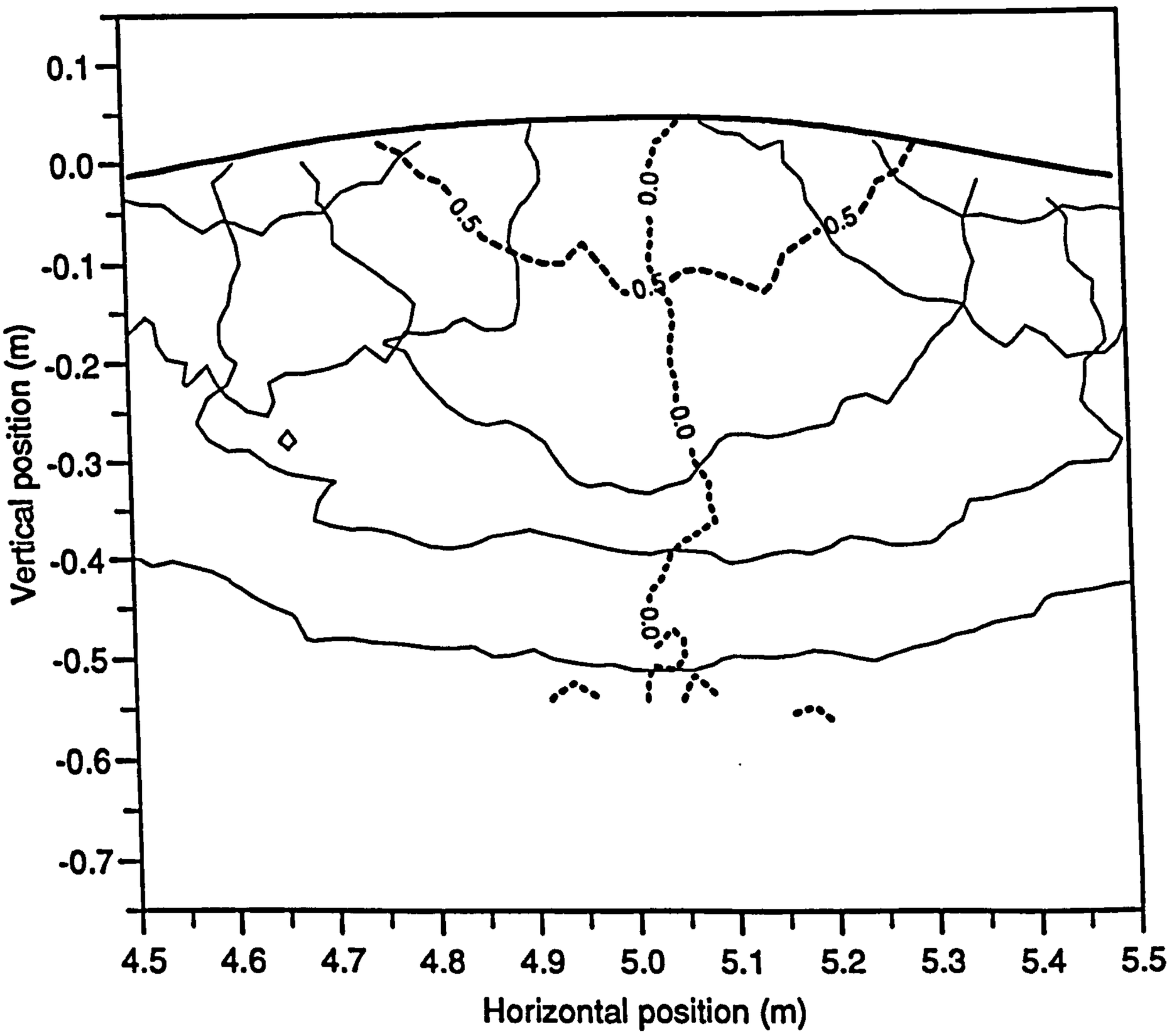

Figure 5.21: Iso-velocity contours for a medium amplitude wave (case 8), on the forward, uniform current. Contour interval: $0.1 ms^{-1}$

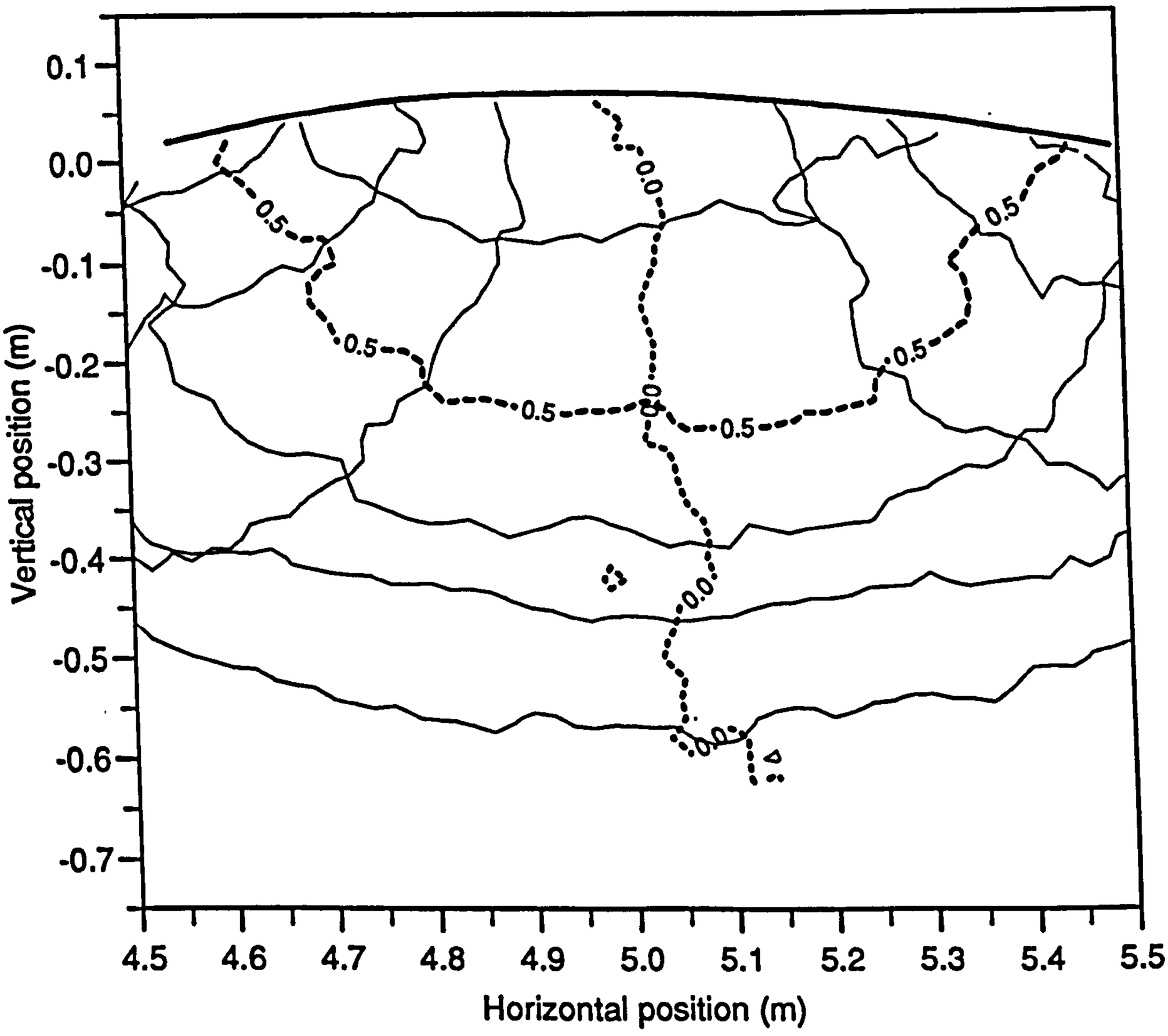

Figure 5.22: Iso-velocity contours for a medium amplitude wave (case 7), on the forward, uniform current. Contour interval: $0.1 ms^{-1}$

In figures 5.21 and 5.22 result are plotted for the forward *uniform* current. This current could only be regarded as uniform in the top half of the flow, which shows up in the contours below about $z = -.3$m. Some interesting effect on the contours can be seen near the crest, but it was suspected, in this forward case, that the current generation may have been affected by the arrival of the wave group, so conclusions for these cases should be drawn with caution.

5.4.2 Wavelength Results

The wavelengths determined in the absence of current are plotted in figure 5.23 against steepness for each frequency. The experimental values are well predicted by third order theory [67], giving confidence in the experimental method. Significant discrepancies are only apparent at very low frequency, where it was suspected that some reflected waves may have returned to the measurement position during the sampling period.

The wavelengths determined in the presence of the strongly sheared current are plotted in figure 5.24 against frequency. Again, the sets of points are annotated with the driving frequency of the wavemaker. In this case, on the strongly sheared current, no theoretical prediction has been attempted.

It was apparent in the tests that, at higher frequencies where the wavemaker could produce limiting waves, steeper waves were possible in the absence of current, than, for example, in the presence of the strongly sheared current. This can be seen by comparing the maximum steepness obtained at the shorter wavelengths in figures 5.23 and 5.24. However, conclusions should be drawn from these observations with great caution, as a number of factors may lead to the reduction in limiting steepness, especially the turbulence level.

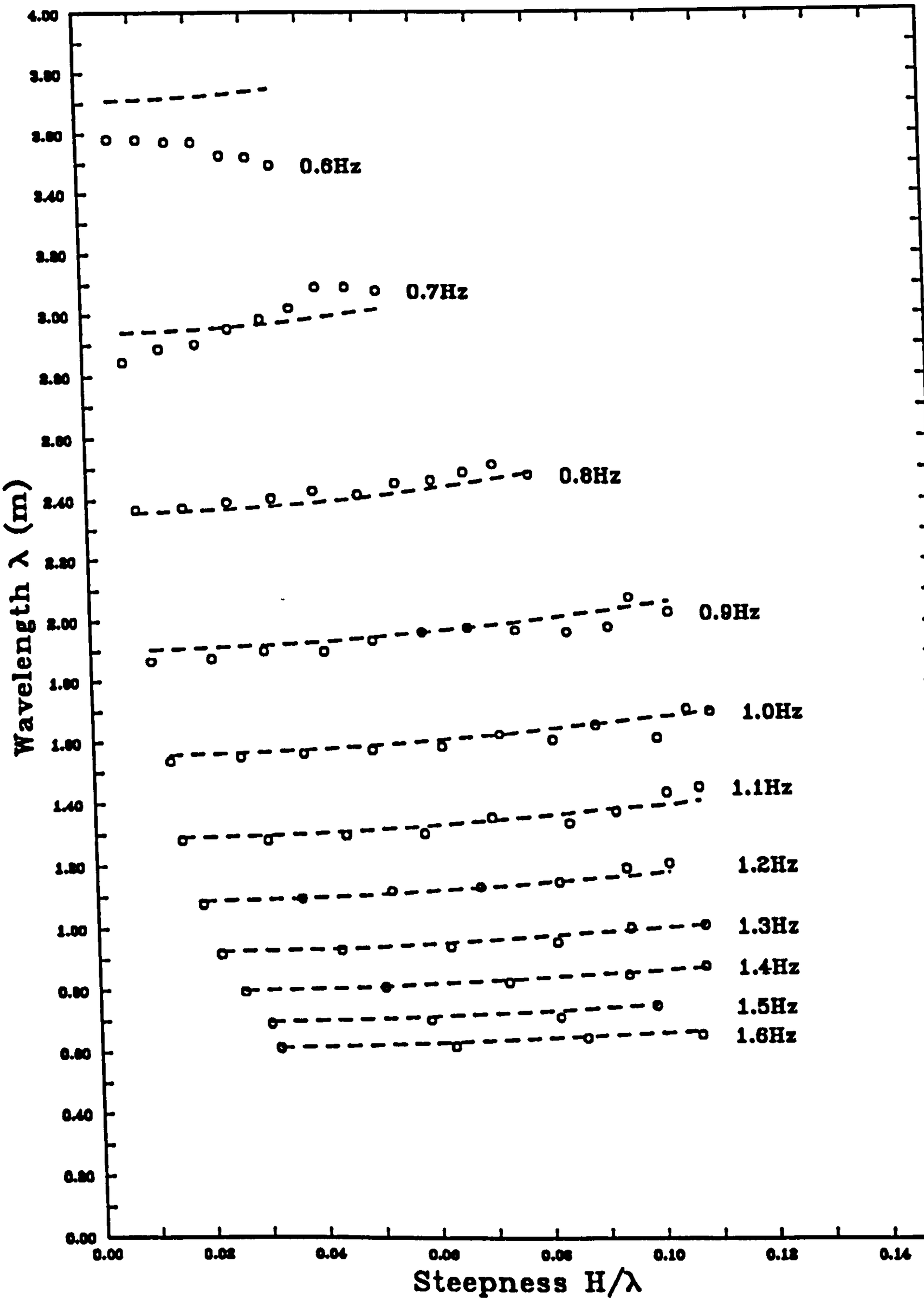

Figure 5.23: Wavelengths determined from wavegauge measurements, no current, o experimental data, - - - - 3rd order theory

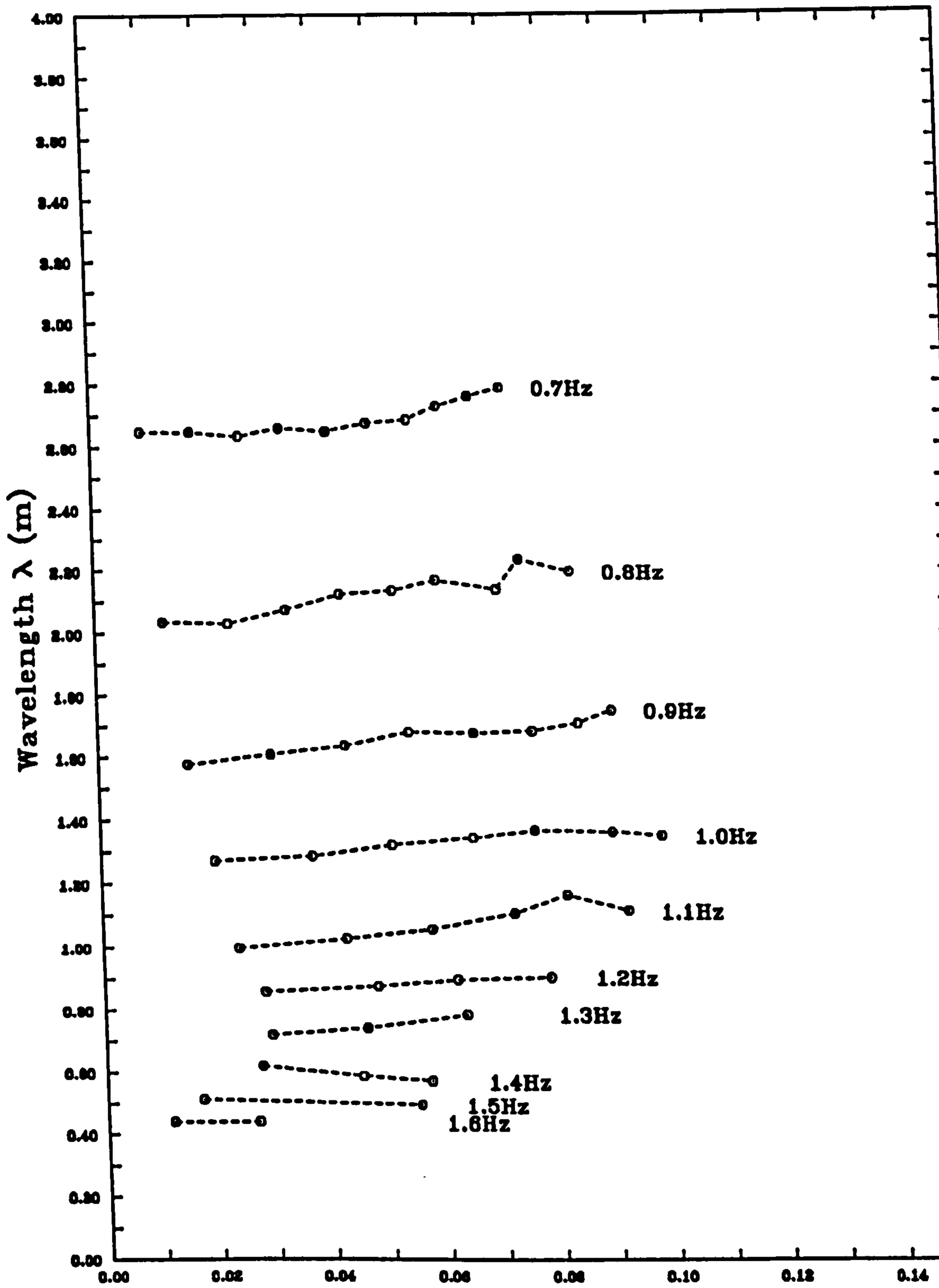

Figure 5.24: Wavelengths determined from wavegauge measurements, strong shear, - - o - - experimental data, labelled with wavemaker frequency

5.5 Further Analysis of Experimental Results

Details of the methods used to assess and further manipulate the experimental data are described. The whole field operations performed on the experimental data, including averaging, are detailed. The measured wavelengths are summarised and from them the *effective* slab current is implied. Vorticity is extracted from the data and a method of using vorticity to estimate the underlying sheared current is proposed.

5.5.1 Whole Field Velocity Field Data

The raw experimental results presented in section 5.4.1 require some further processing before they can be made use of. In particular, the data may be averaged to limit the effect of turbulence, and the internal flow fields from different phases of the wave combined to yield information over a full wavelength.

Averaging to Reduce the Effect of Turbulence

It is apparent from figures 5.16 to 5.22 that the turbulence level may be significant in comparing the experimental results with numerical predictions. In order to reduce the effect of the turbulence, repeats of the same phase of each wave were averaged. The number of repeats used for each average was variable, and has been indicated in figures 5.4 to 5.7. The number of repeats was necessarily limited by the time it takes for each PIV analysis.

Figures 5.25 and 5.27 show iso-velocity contours obtained from the flow field present under the crest in case 17, obtained by averaging 6 repeats of the wave. In the averaging process, missing vectors were rare and any effect on the mean was therefore ignored. The resulting data can be seen to be much smoother, aiding the assessment of trends in the flow.

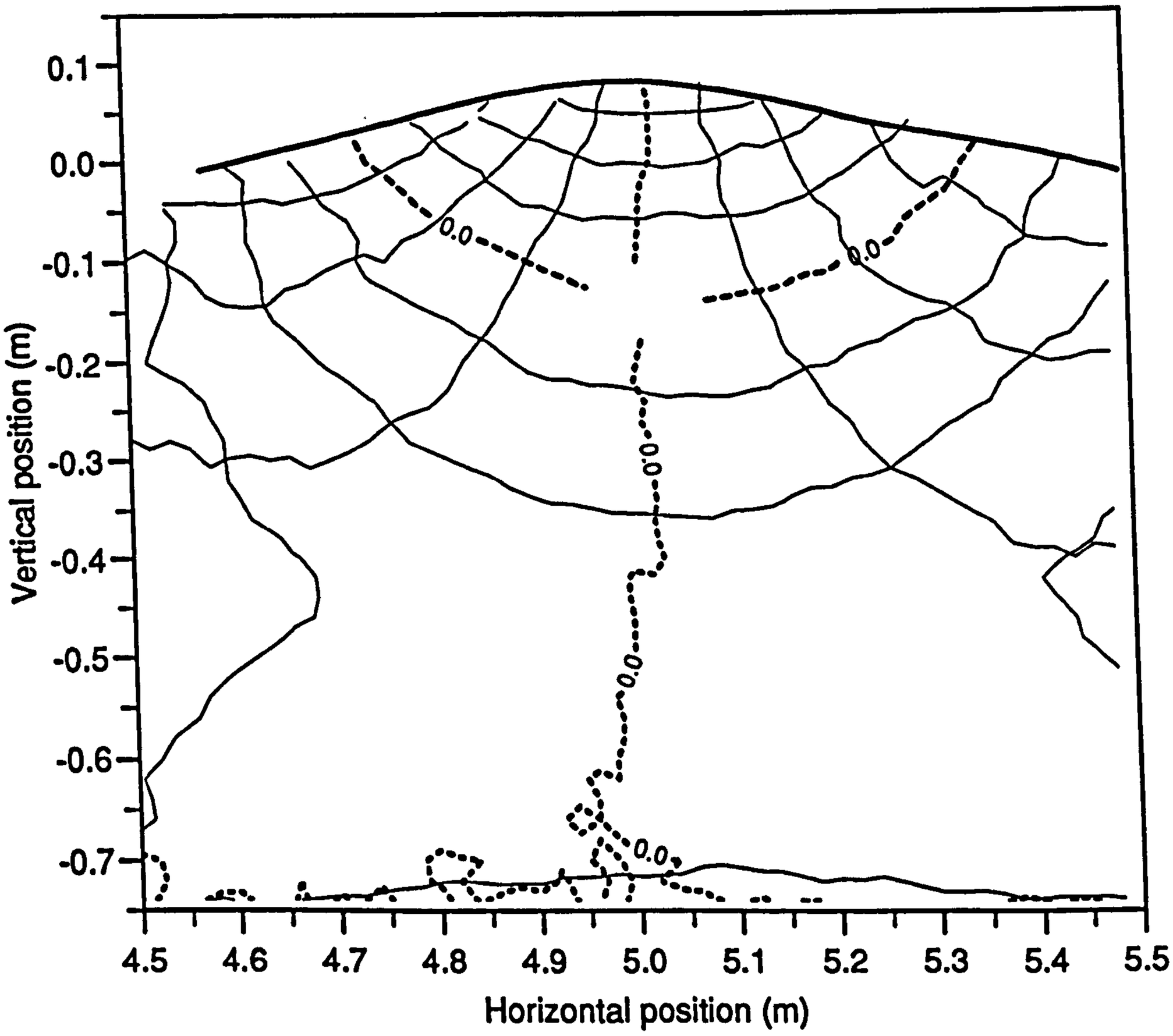

Figure 5.25: Iso-velocity contours for the average of 6 repeats of a medium amplitude wave (case 17), on the strongly sheared current, *first* wave crest. Contour interval: $0.1 ms^{-1}$

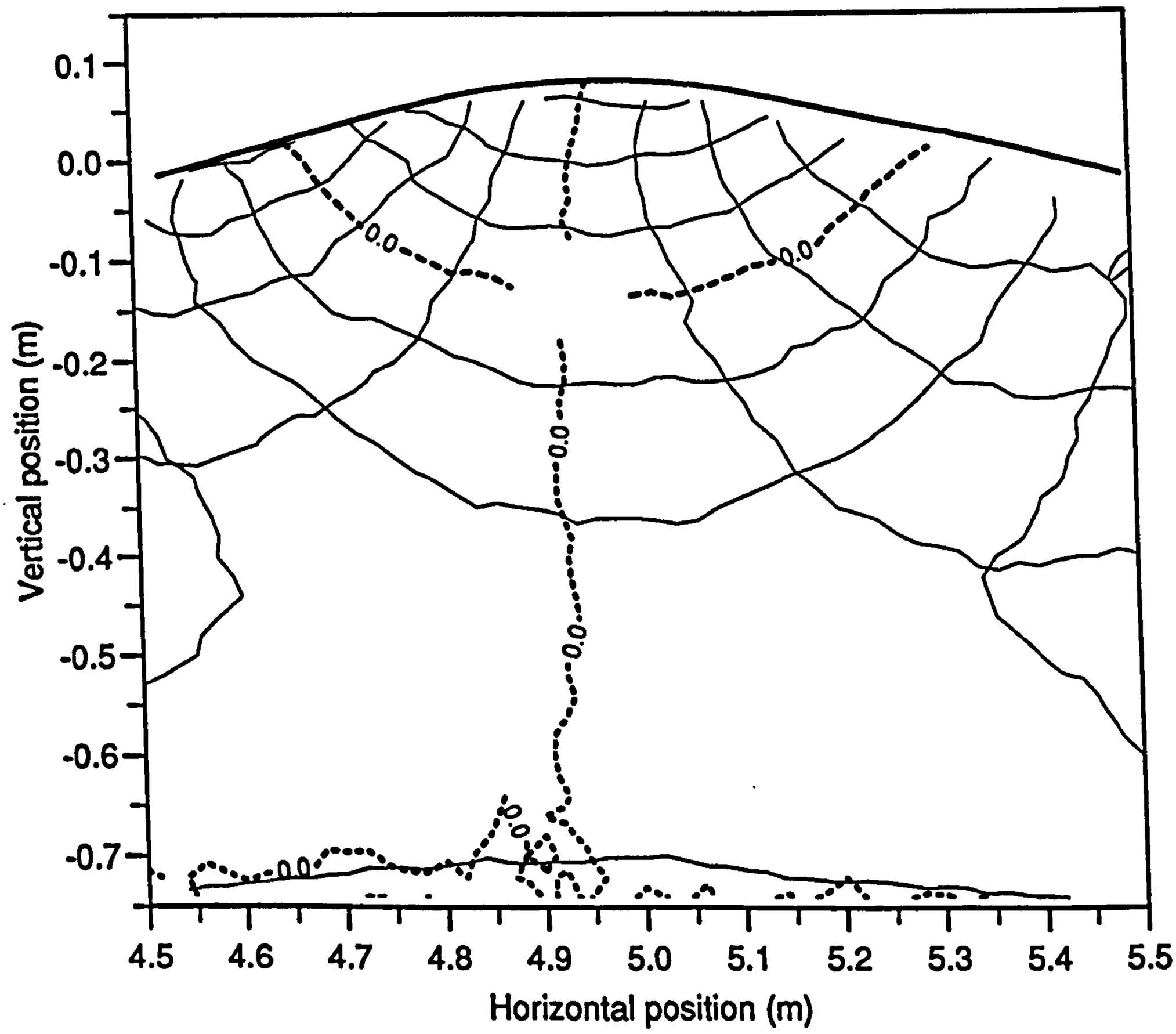

Figure 5.26: Iso-velocity contours for the average of 6 repeats of a medium amplitude wave (case 17), on the strongly sheared current, *third* wave crest. Contour interval: $0.1 ms^{-1}$

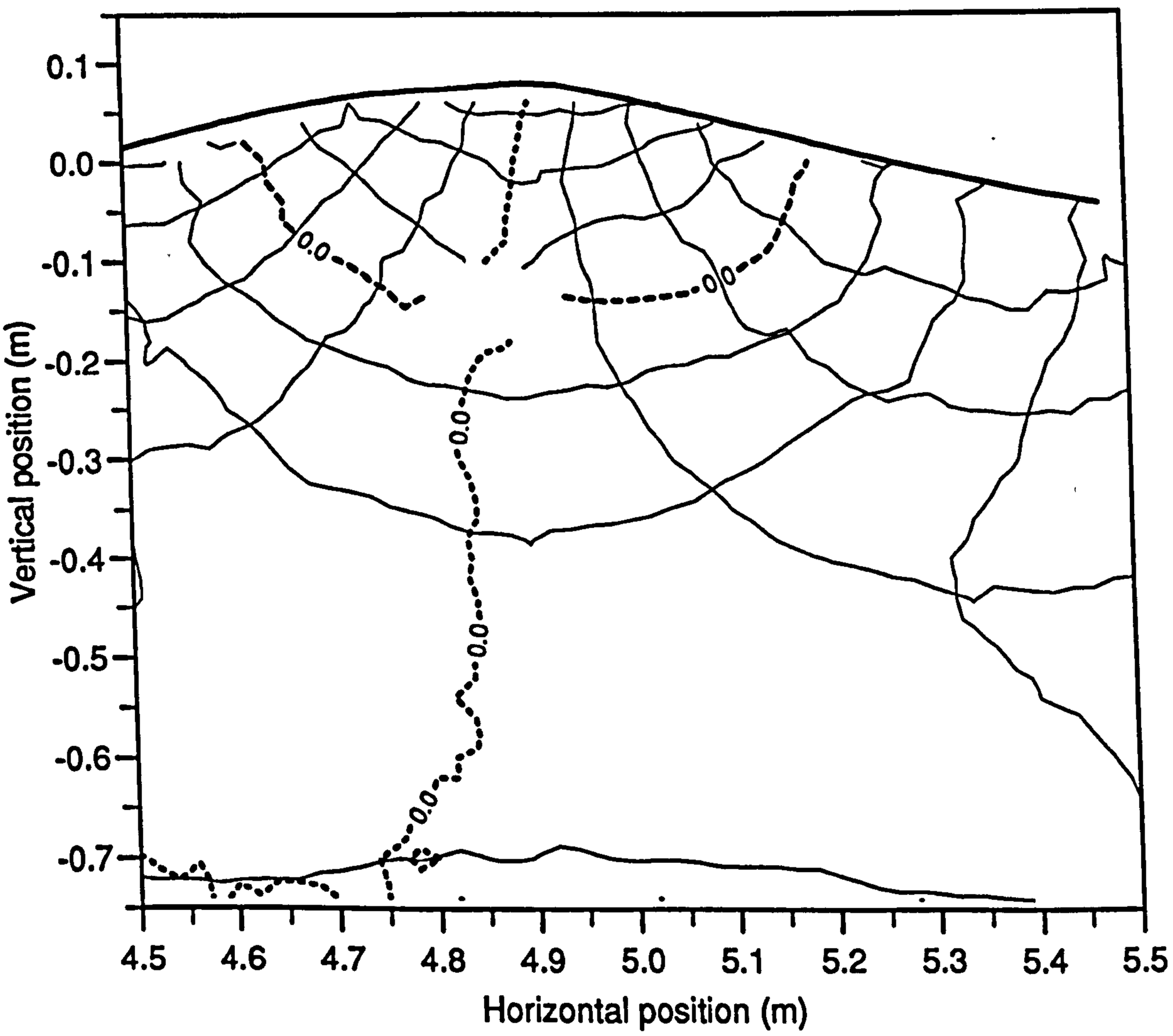

Figure 5.27: Iso-velocity contours for the average of 6 repeats of a medium amplitude wave (case 17), on the strongly sheared current, *fifth* wave crest. Contour interval: $0.1 ms^{-1}$

As can be seen in figures 5.16 to 5.18, there is a slight trend for the flow field to lean right in both cases, with an increased tendency from the early crest to the later. This feature is not expected for steady, irrotational waves, and its presence indicates either a lack of steadiness or some effect of the strong shear. The same effect was noticed in all of the wave cases on the strongly sheared current.

Combining of the Velocity Fields to Make a Complete Wave

A number of the wave/current combinations were analysed in sufficient detail to obtain reliable velocity data over a whole wavelength. Case 2, from the waves in the absence of current, and cases 15, 17 and 19, from the waves travelling on the strongly sheared current, were selected for this treatment. Each of these waves is moderately steep. As the PIV measurement area is 1m wide, corresponding to about half a wavelength of all the waves considered, constructing velocity maps to cover the complete wave requires care if the resulting data is to be free from discontinuities.

Composite velocity maps were constructed for each case by matching up vector maps from various phases of the waves, ensuring that the total wavelength was consistent with the values listed in table 5.5. The positions of the crests and trough were estimated manually.

An example of the composite flow field obtained in this way is shown in figure 5.28. It should be noted that while the flow beneath the crest was obtained by averaging six separate measurements of the wave, that beneath the trough resulted from just two, and is noticeably more turbulent. The data arrived at in this way assumes that the combined kinematics are steady, and should be treated with some caution. The crest kinematics were obtained from the third wave cycle, and those for the trough from between the passing of the second and third crests.

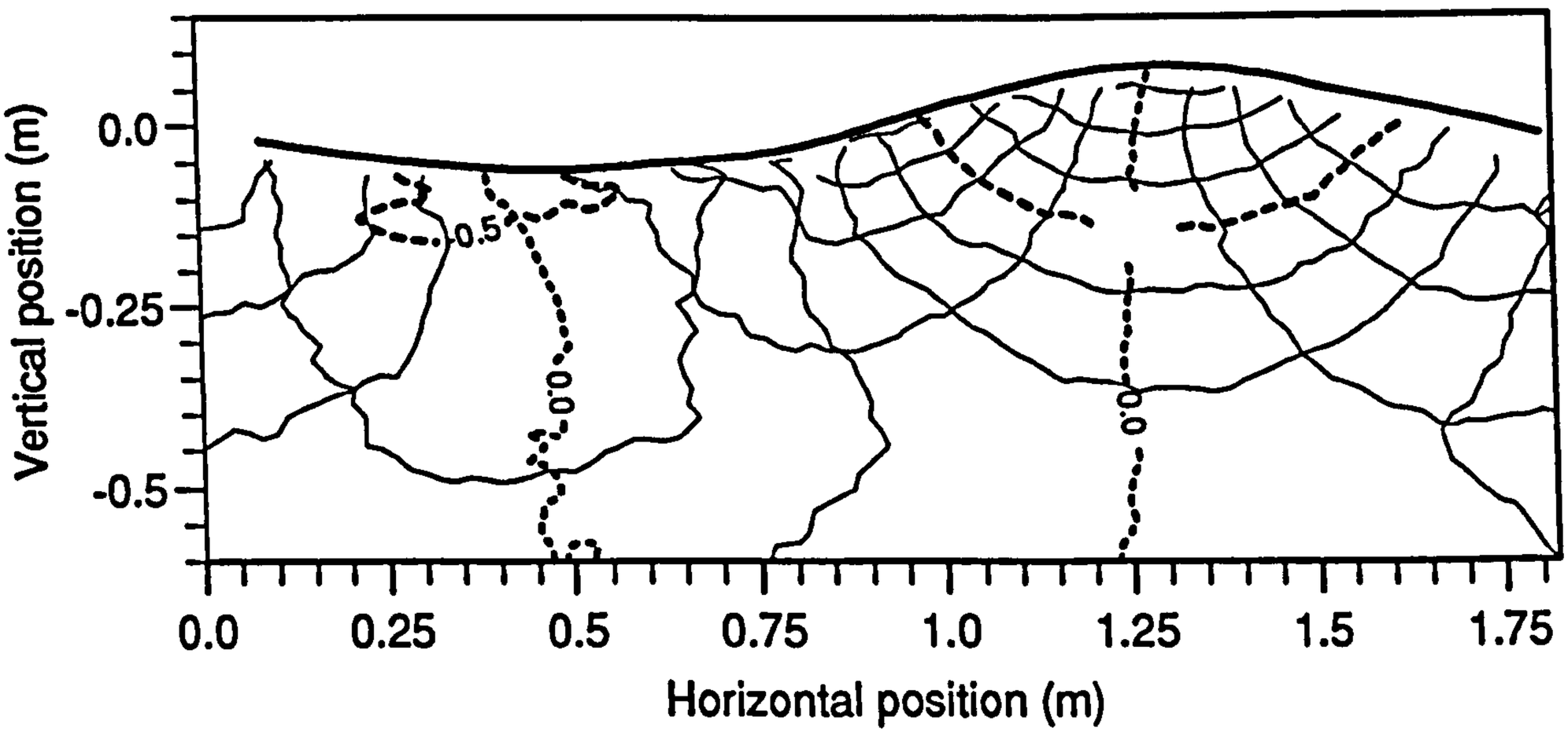

Figure 5.28: Iso-velocity contours for the composite flow field for case 17, a medium amplitude wave on the strongly sheared current. Contour interval: $0.1 ms^{-1}$

5.5.2 Vorticity

It is possible to extract vorticity from the data obtained with PIV, because the velocity field is known throughout the measurement area. The definition of vorticity is

$$\Omega = \nabla \times \underline{u} \tag{5.20}$$

So that the component perpendicular to the measurement plane is

$$\Omega_y = \frac{\partial u_z}{\partial x} - \frac{\partial u_x}{\partial z} \tag{5.21}$$

A reasonable estimate of the vorticity can be obtain from the measured flow field by approximating equation 5.21 to

$$\Omega^{i,j} = \frac{u_z^{i+1,j} - u_z^{i-1,j} - u_x^{i,j+1} + u_x^{i,j-1}}{2\delta} \tag{5.22}$$

where i and j are the column and row numbers, respectively, and δ the grid

spacing, when the continuous flow field is approximated by a two-dimensional array.

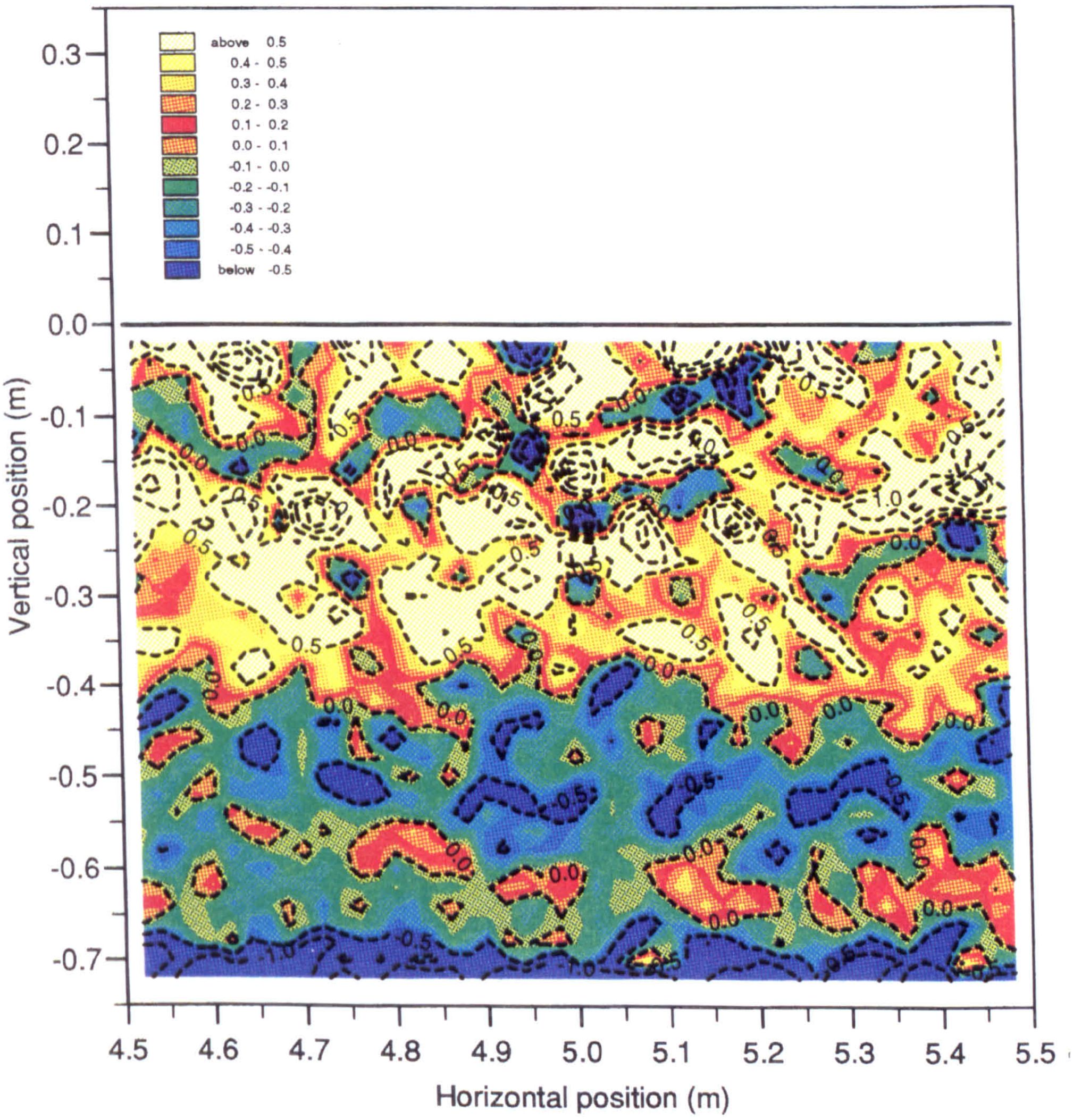

Figure 5.29: Vorticity contours for a strongly sheared current. Contour line interval: $.5s^{-1}$

Figure 5.29 contains a contour plot of vorticity for one realisation of the strongly sheared current, obtained by applying equation 5.22 to the data. In this, and subsequent vorticity plots, colour is used to highlight the different values of vorticity. Shades between red and yellow correspond to positive vorticity, so that the areas of forward sheared current show up with these colours. Greens and blues indicate

negative vorticity, the bottom boundary layer containing the strongest of these shades.

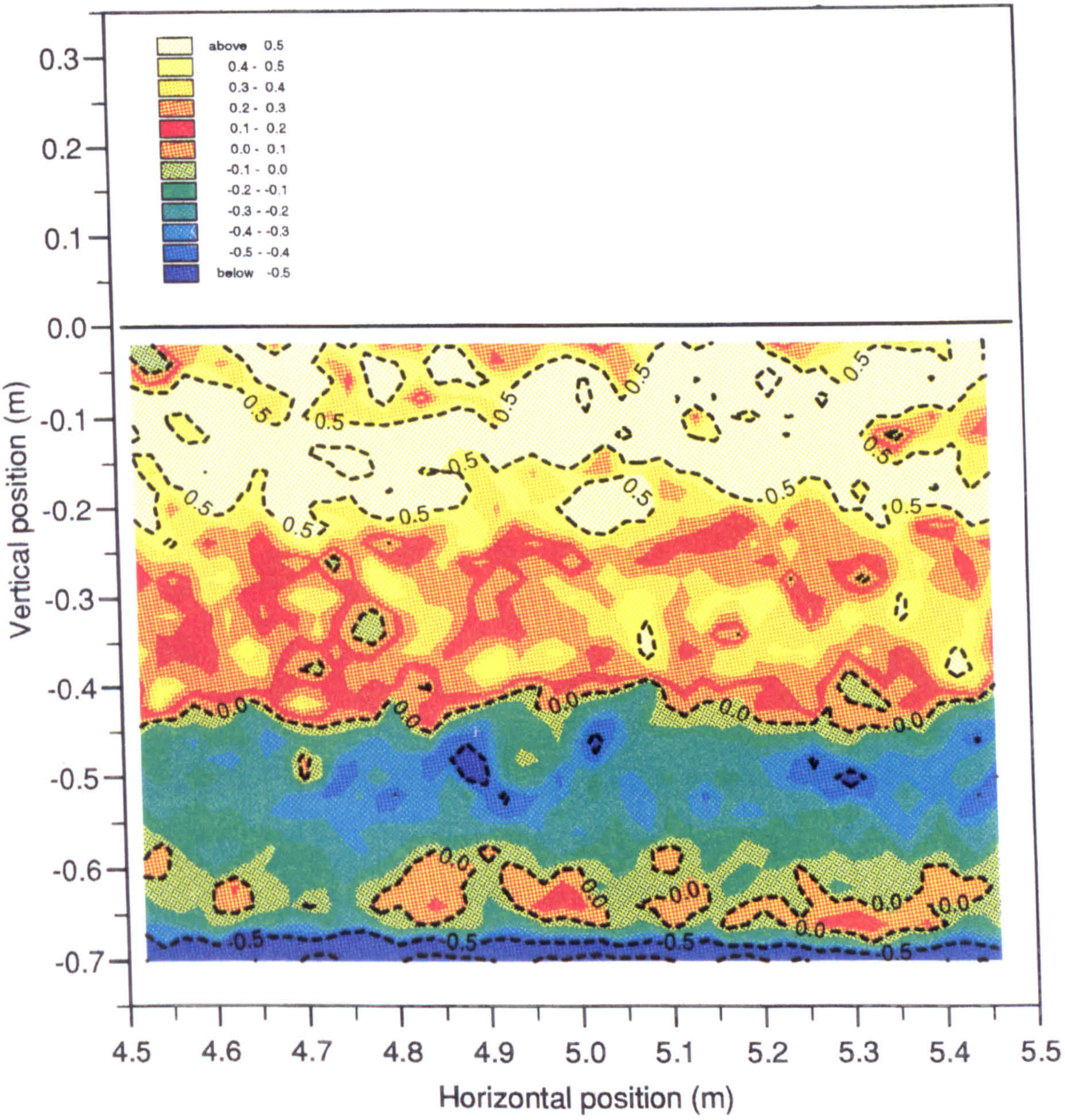

Figure 5.30: Vorticity contours for the average of 8 repeats of the strongly sheared current. Contour line interval: $.5s^{-1}$

In figure 5.29 two features are most apparent. Firstly, the transition from negative to positive vorticity around $z = -.4$m. This is to be expected from the form of the strongly sheared profile previously illustrated in figure 5.3. Secondly, a lot of small scale turbulence can be identified, manifesting itself as local peaks and troughs of vorticity. This is just a different representation of turbulence from that

illustrated in figure 5.10.

To aid later assessment of the wave/current combinations, figure 5.30 contains a vorticity plot for the strongly sheared current, this time averaged from 8 measurements of the current. As expected, the apparent turbulence is reduced and the trends are more clearly seen.

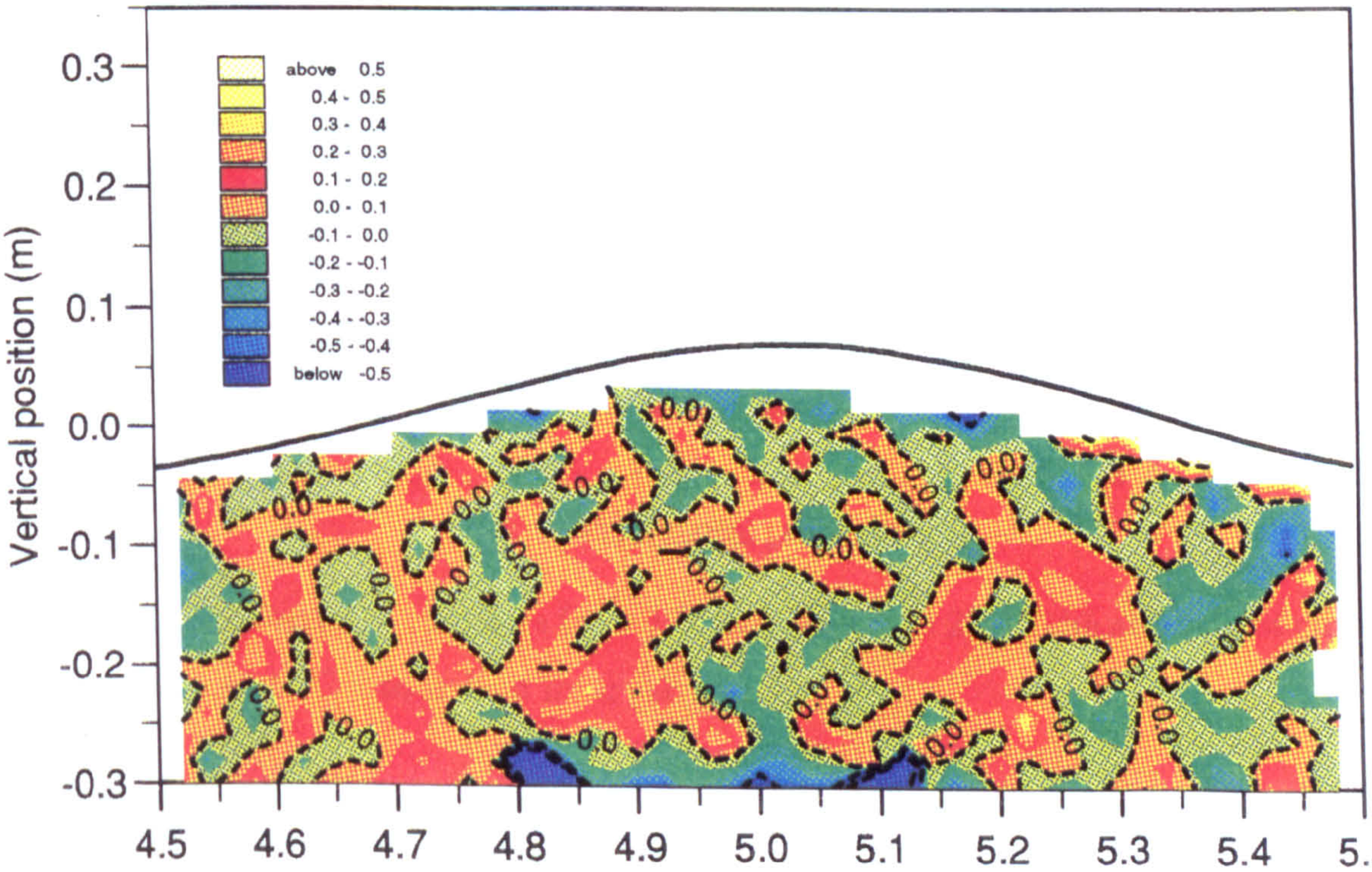

Figure 5.31: Vorticity contours for a 1.0Hz wave (case 2), in the absence of current, *second* wave crest. Contour line interval: $.5s^{-1}$

In order to gauge the variations of vorticity within the combined flows, figure 5.31 is presented which contains a vorticity contour plot for a wave in the absence of current. While the overall level is small, there appears to be negative vorticity on average. Figure 5.32 shows to vorticity distribution for a later wave crest in the same wave train. Little change in the overall level is apparent in this representation of the data.

Vorticity was calculated for some of the wave/current combinations, concentrating, as previously, on case 17. In figure 5.33 vorticity contours are plotted for a single realisation of this wave, at an early crest in the wave train. The hole in the centre

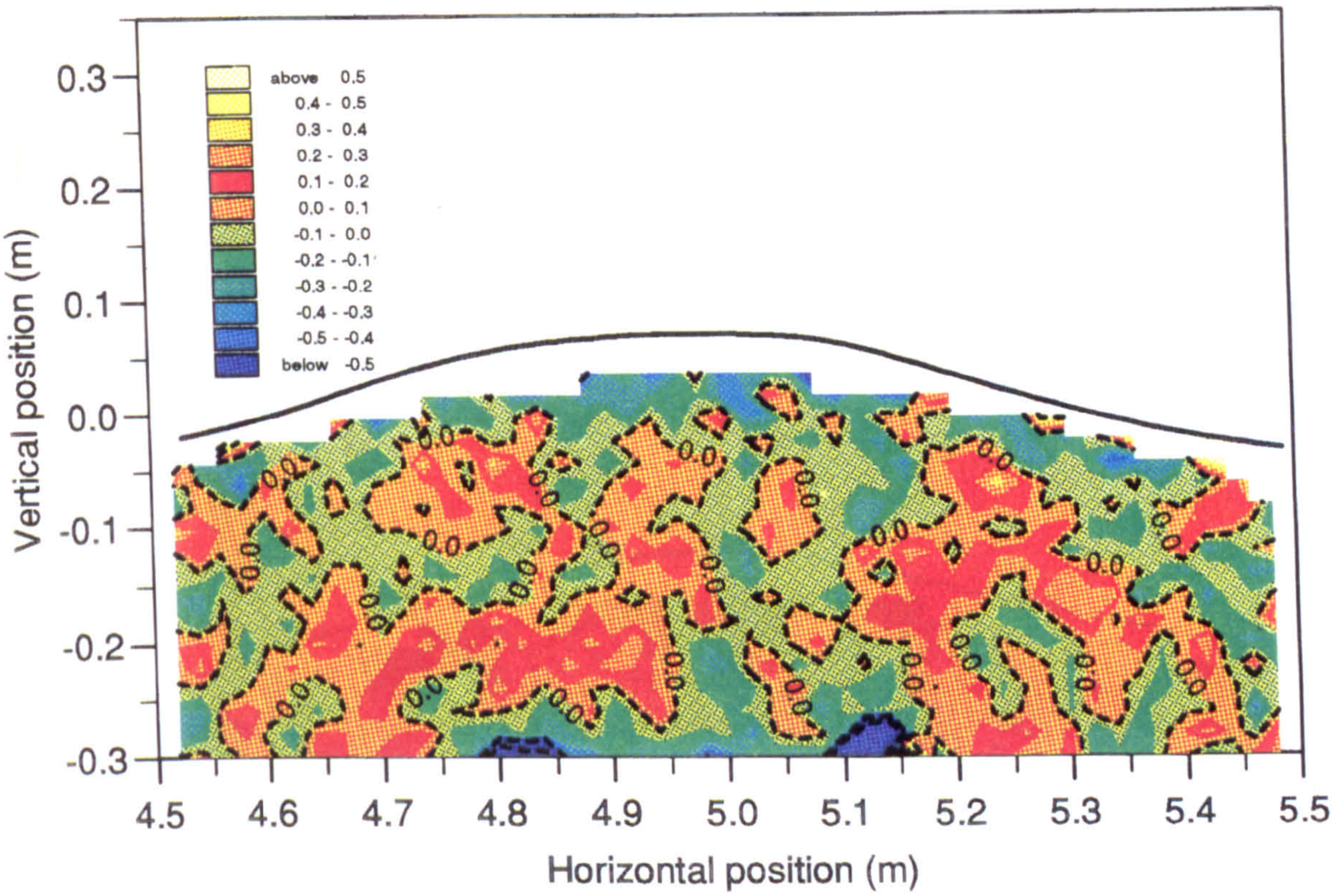

Figure 5.32: Vorticity contours for a 1.0Hz wave (case 2), in the absence of current, *fifth* wave crest. Contour line interval: $.5s^{-1}$

of the plot is just due to missing data, no attempt being made to interpolate.

Figures 5.34 to 5.36 show vorticity contours for averages of three of the wave crests in the wave train. The averaged kinematics have been shown in figures 5.25 to 5.27, and trends noted. Here, the most noticeable trend is the appearance of some negative vorticity near the surface of the crest, with an increasing amount in subsequent plots.

The reduction of the overall vorticity in the upper half of the waves, as time goes on, is extremely interesting. Swan [62] has suggested that negative vorticity will diffuse down from the wave surface over time, in the absence of current, and Klopman [33] has noted that this will happen much more quickly when a turbulent current is present.

In order to obtain a rough estimate of the change in vorticity with time, spatial averages were calculated from the vorticity fields already presented. Ideally, this

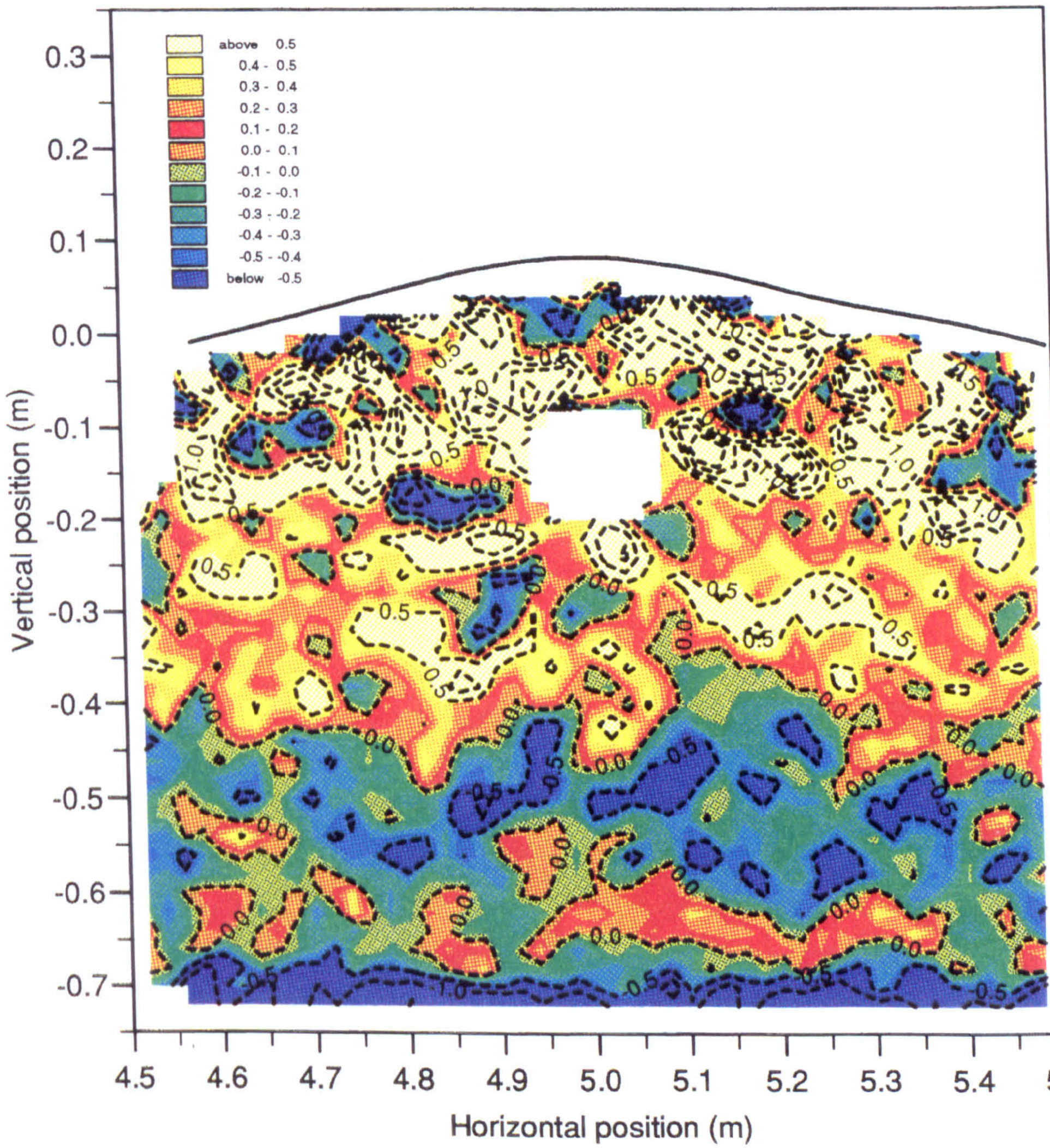

Figure 5.33: Vorticity contours for a medium amplitude wave (case 17), on the strongly sheared current, first wave crest. Contour line interval: $.5s^{-1}$

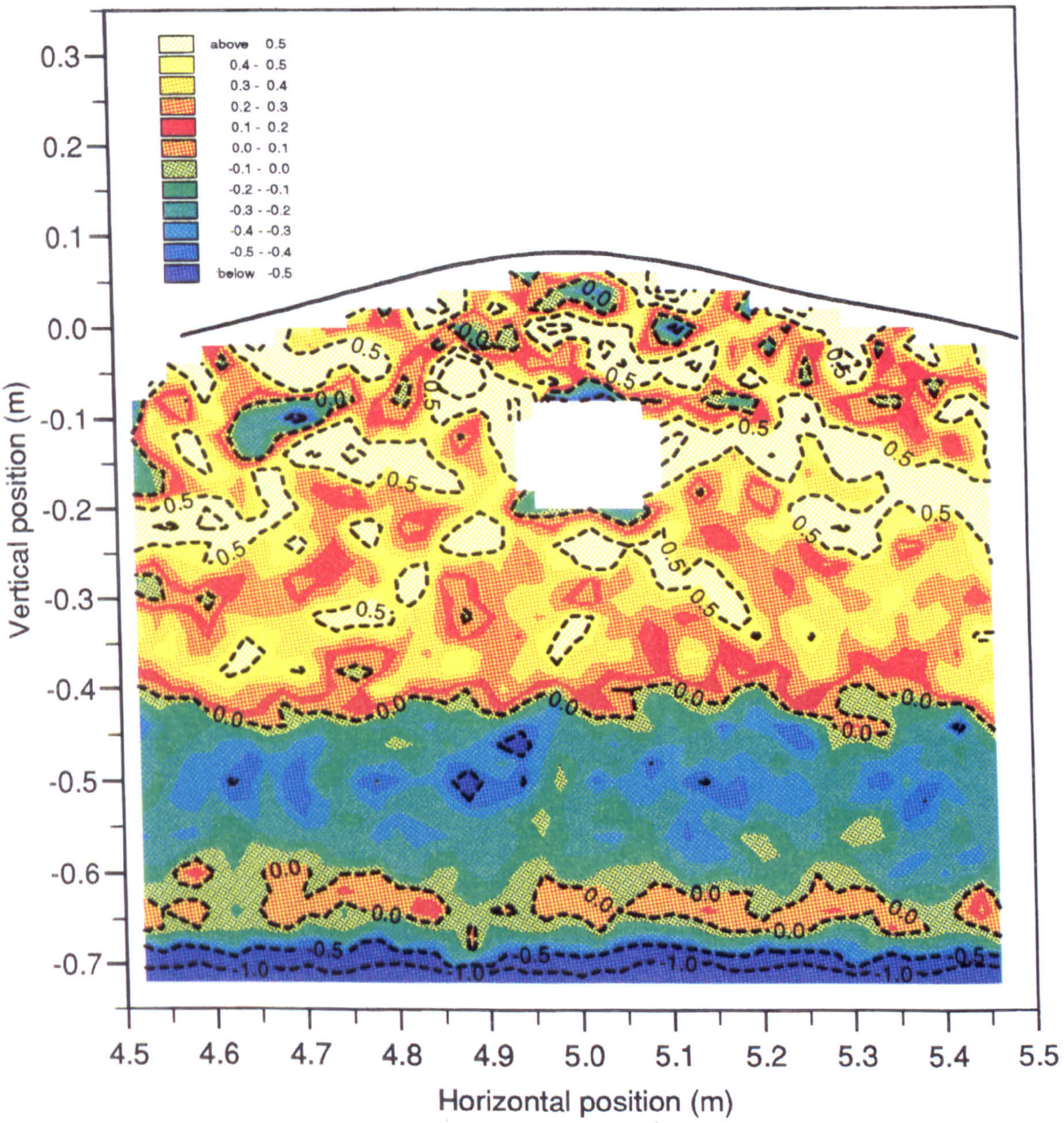

Figure 5.34: Vorticity contours for the average of 6 repeats of a medium amplitude wave (case 17), on the strongly sheared current, *first* wave crest. Contour line interval: $.5s^{-1}$

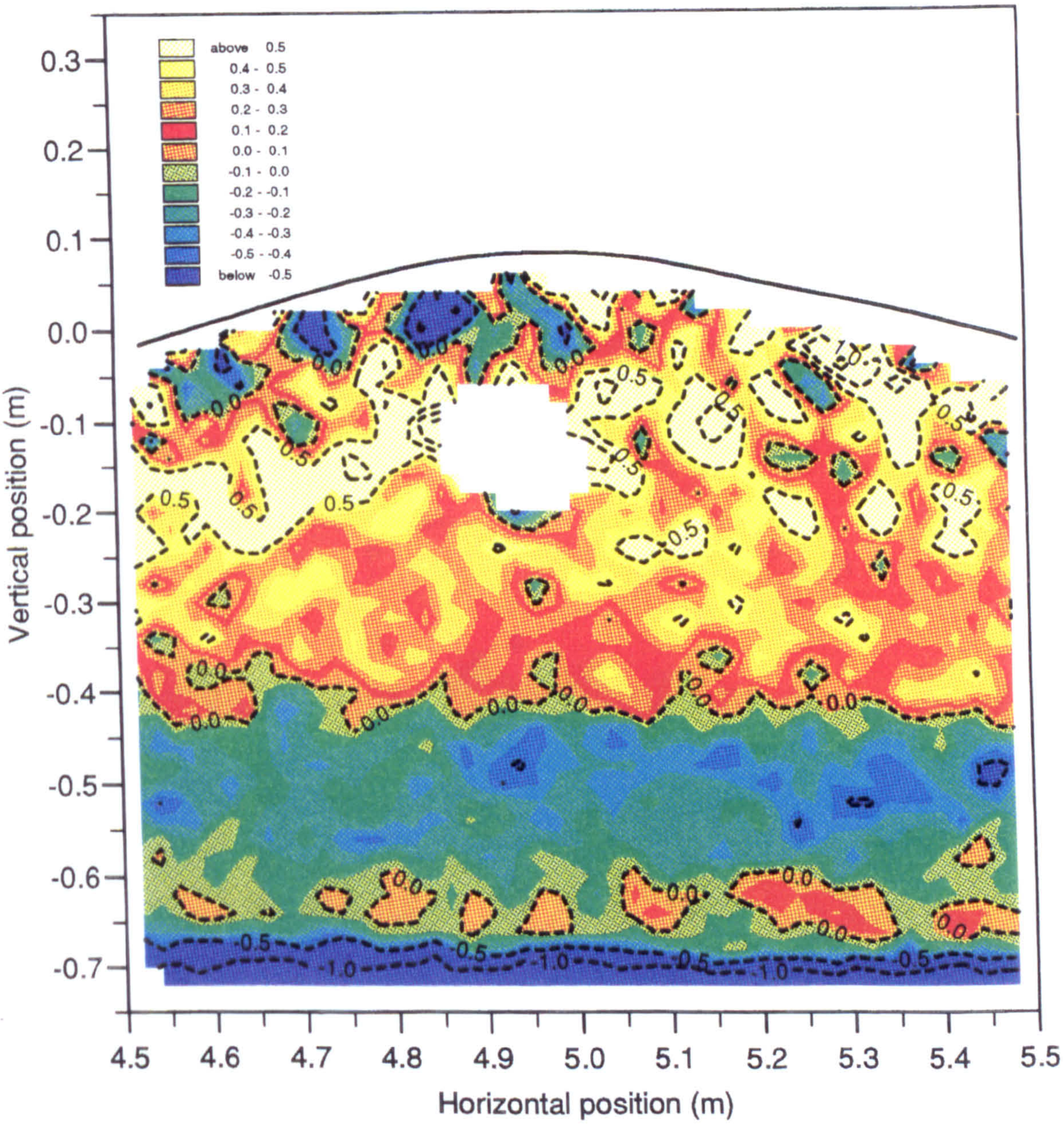

Figure 5.35: Vorticity contours for the average of 6 repeats of a medium amplitude wave (case 17), on the strongly sheared current, *third* wave crest. Contour line interval: $.5 s^{-1}$

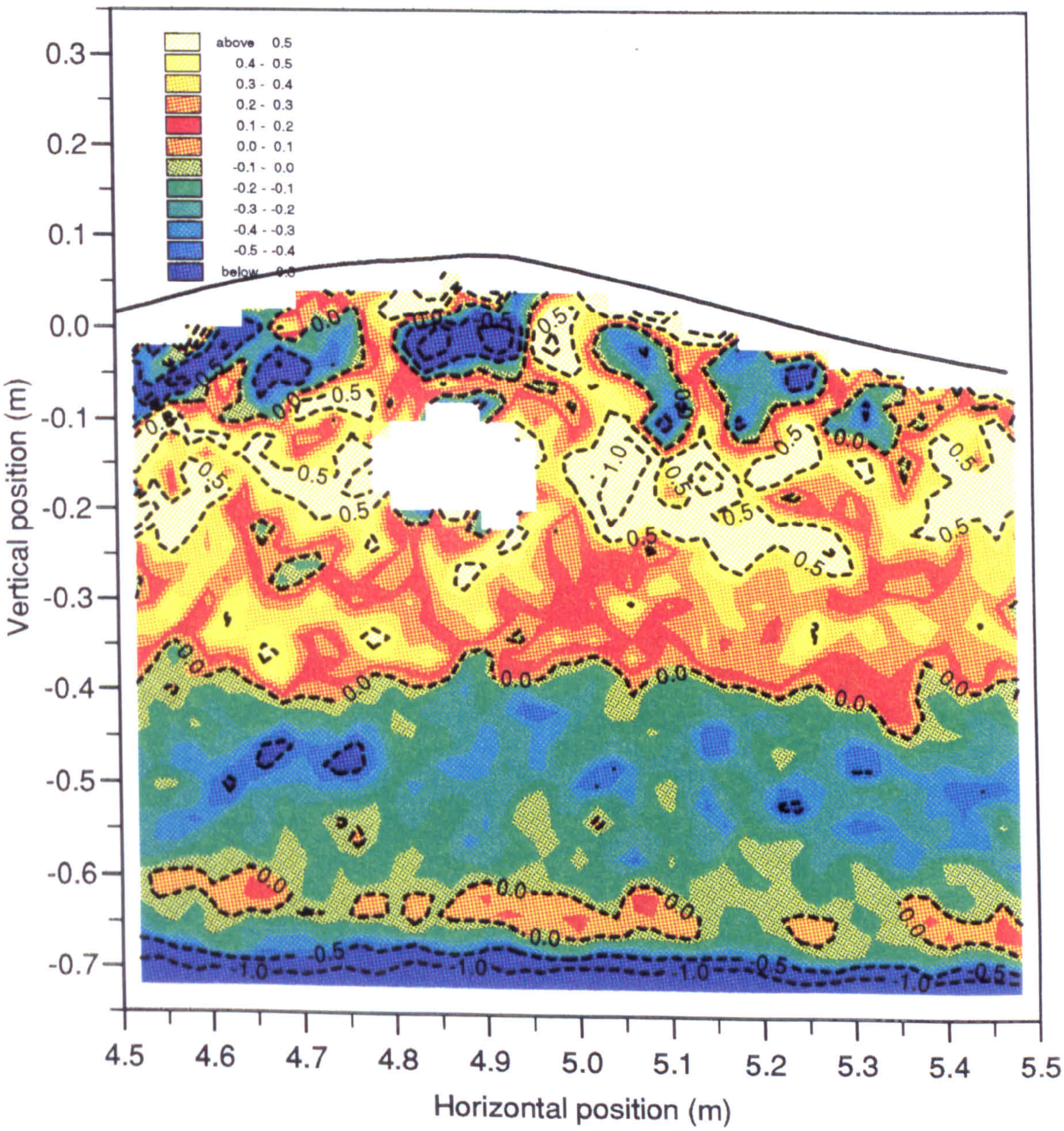

Figure 5.36: Vorticity contours for the average of 6 repeats of a medium amplitude wave (case 17), on the strongly sheared current, *fifth* wave crest. Contour line interval: $.5 s^{-1}$

would be done by integrating over a complete wavelength and right up to the surface. However, a crude estimate was obtained by simply averaging the vorticity above a given level and across the measurement zone, with no attempt to interpolate or extrapolate the data. If the vorticity was uniform, the average would not be affected by missing values.

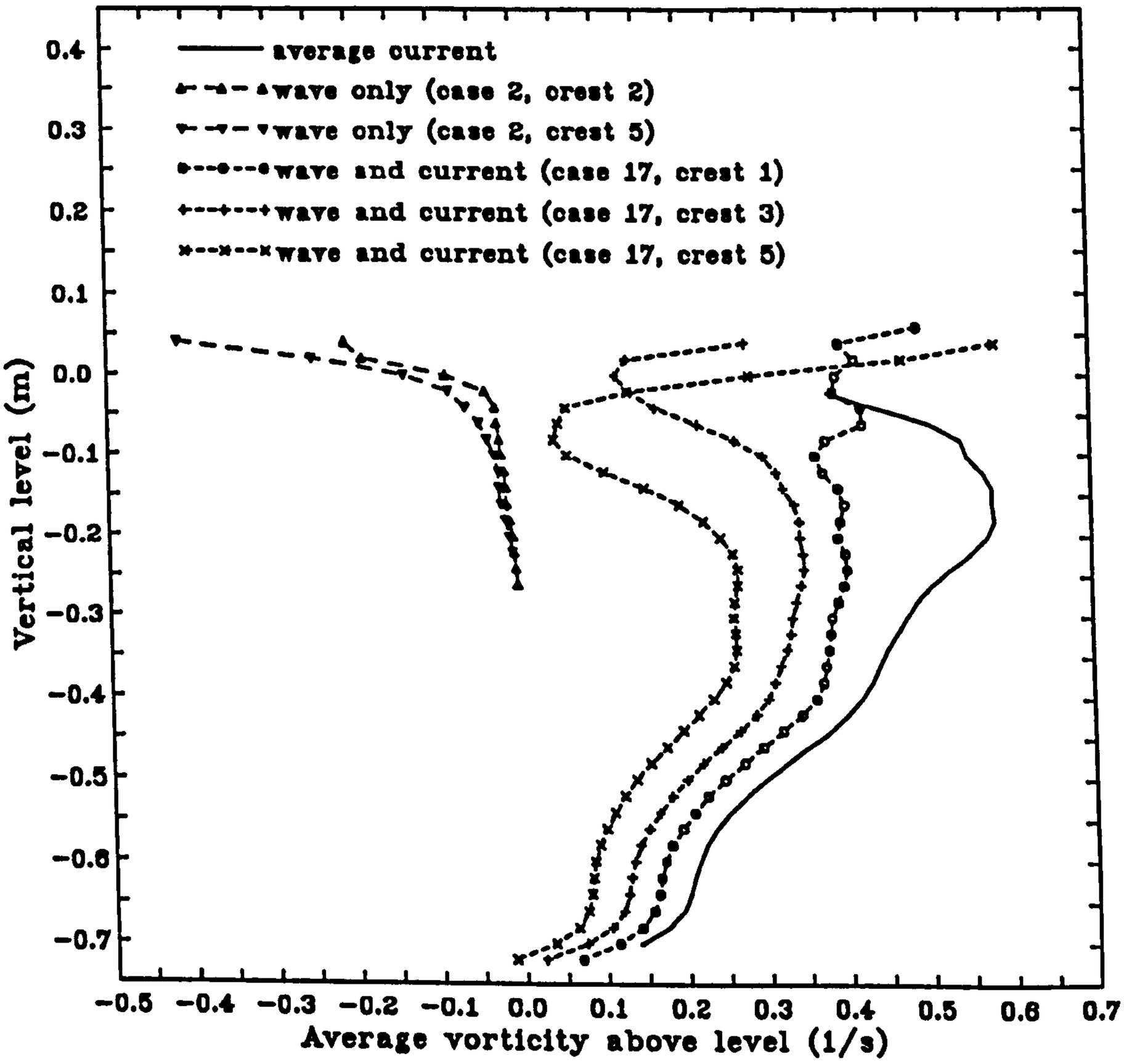

Figure 5.37: Average vorticity obtained above given level

Figure 5.37 shows the average vorticity obtained above given levels. The graph contains averages from the mean strongly sheared current, waves in the absence of current, and averages of the wave/current combination (case 17). Because the data was obtained by summing from the given level to the surface, turbulence has a larger effect higher in the graph.

A clear trend is apparent in all the curves, below $z = -.1$m. Those for the wave

in the absence of current, at different times in the wave train are very similar, but the later one has more negative vorticity. In the combined cases the trend is more striking — there is a steady, and substantial decrease in vorticity with time, and the value for the first wave crest in the group is similarly less than the corresponding value for the current by itself.

The effects near the surface are harder to identify. In the wave-only case, there seems to be a formation of a boundary layer, growing down from the surface with time. In the combined case, no trend is apparent.

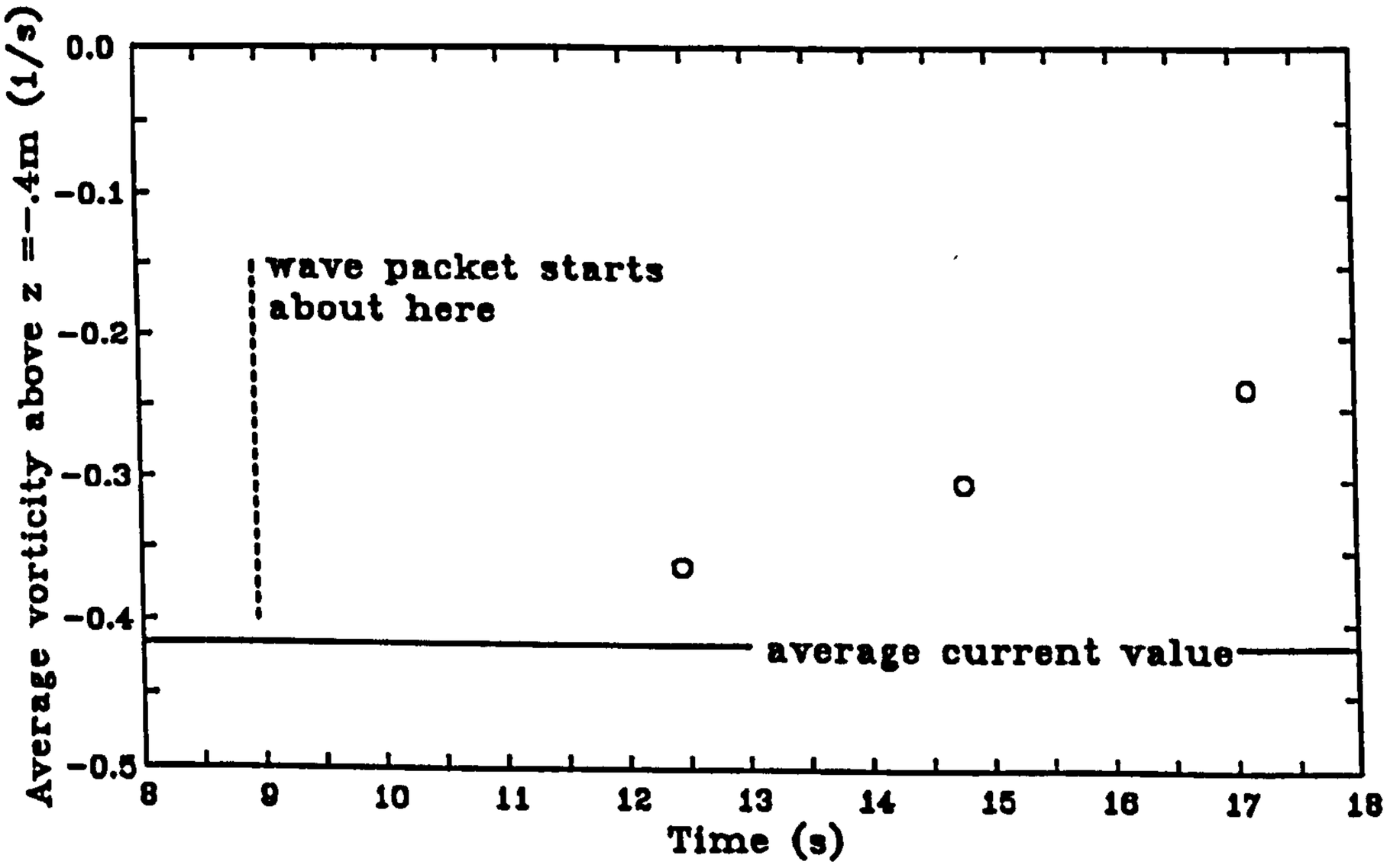

Figure 5.38: Average vorticity against time

From figure 5.37, the average vorticity values above $z = -.4$m, have been extracted, for cases 17, and are plotted in figure 5.38 against time. While it should be possible to predict the form of this curve, given the wave steepness and turbulence level, no such prediction is available at the time of writing.

For completeness, vorticity is plotted in figure 5.39 for the composite kinematics data. The trough was obtained for the average of two flow fields, compared with six for the crest, and the transition between these two regions is readily identified.

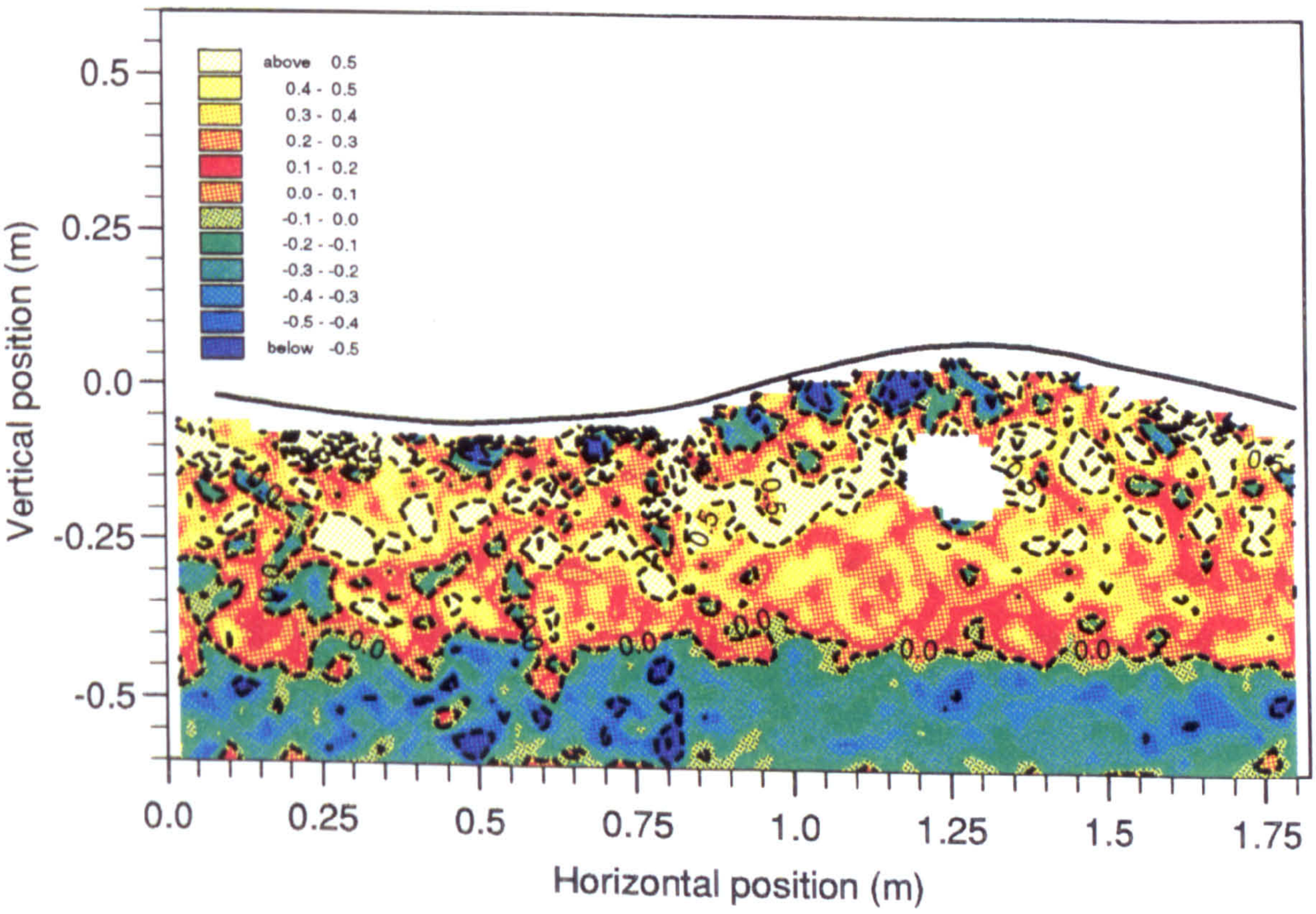

Figure 5.39: Vorticity contours for the composite flow field for case 17, a medium amplitude wave on the strongly sheared current. Contour line interval: $.5s^{-1}$

Underlying Current Calculated from Vorticity

If the vorticity is attributed to a current underlying the wave, then the shape of the current can be deduced from the vorticity obtained from a combined wave/current flow field.

From the vorticity, plotted previously in figure 5.39, the underlying current was estimated, by integrating the vorticity from the bed for each column. The data obtained in this way was then averaged into bands beneath various portions of the wave cycle.

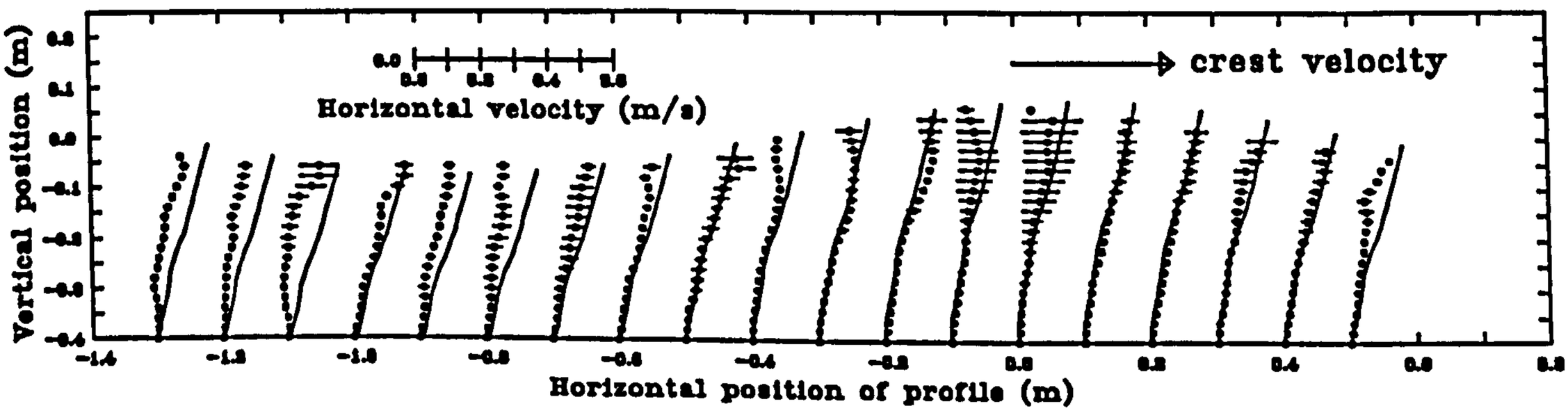

Figure 5.40: The underlying current obtained for case 17 from the vorticity. -•- underlying current obtained from experimentally measured vorticity, —— stretched current profile.

Figure 5.40 shows the estimated underlying current, derived from the vorticity, at various positions with the wave cycle, for case 17. For comparison, the stretched current profile, obtained in the way described in section 2.5.1, is also plotted for each position. The large amount of scatter around the crest region is due to the missing data in this region.

The estimated underlying current shows similar form to the stretched current profile in the half wavelength around the crest, but tends to be less sheared in the trough region. In fact, a constant value of about $.3s^{-1}$ for the shear of the current, compared to $.427^{-1}$ for the undisturbed current, fits the data better.

5.5.3 Averages from the Whole Wave

Complete vector maps under the waves were produced for wave/current cases 15, 17 and 19, with an example of the velocity fields obtained in this way plotted in figure 5.28. From each of these velocity fields the mean Eulerian velocity, or overall current, was estimated by summing the vectors over the complete wavelength, including the crest, and over the full depth. The mean velocities obtained in this way differed from those present in the undisturbed current by .01ms^{-1} to .02ms^{-1}. These discrepancies are quite small and are most likely to be accounted for by the missing vectors in the area under the crest and near the surface.

For each case where velocity data was available over the full wavelength, averages of the horizontal velocity component were obtained at each level, by averaging the vectors over the complete wave. The mean horizontal velocities obtained in this way are plotted in figure 5.41 along with the undisturbed current profiles for comparison. The estimated mean Eulerian velocity due to the wave has been subtracted from all the experimental data, in order that the true residual mean current should be revealed.

In each of the graphs the same trend can be seen — the shear found by averaging over a complete wave is less than that present in the undisturbed current, the reduction being in the opposite direction to the wave propagation. This effect has been measured by Kemp and Simons [30] and is predicted by Klopman [33]. However, the presented graphs should be treated with some caution. If the flows are not steady, the mean values will have a dubious meaning.

5.5.4 Wavelength and Implied Current

While the measured period or frequency of a wave depends upon the frame of reference from which the wave is viewed, the measured wavelength is independent of any change of reference frame. Moreover, if it is known that the wave is riding on a uniform current, then the magnitude of the current can be deduced from

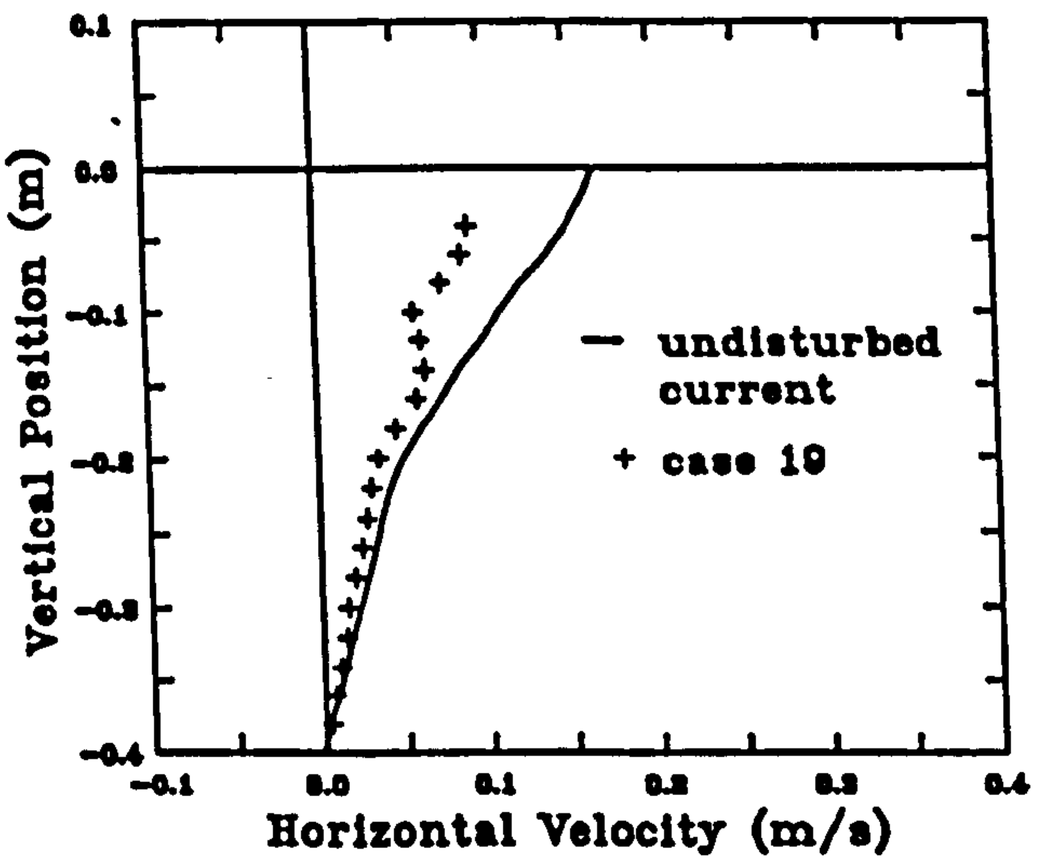

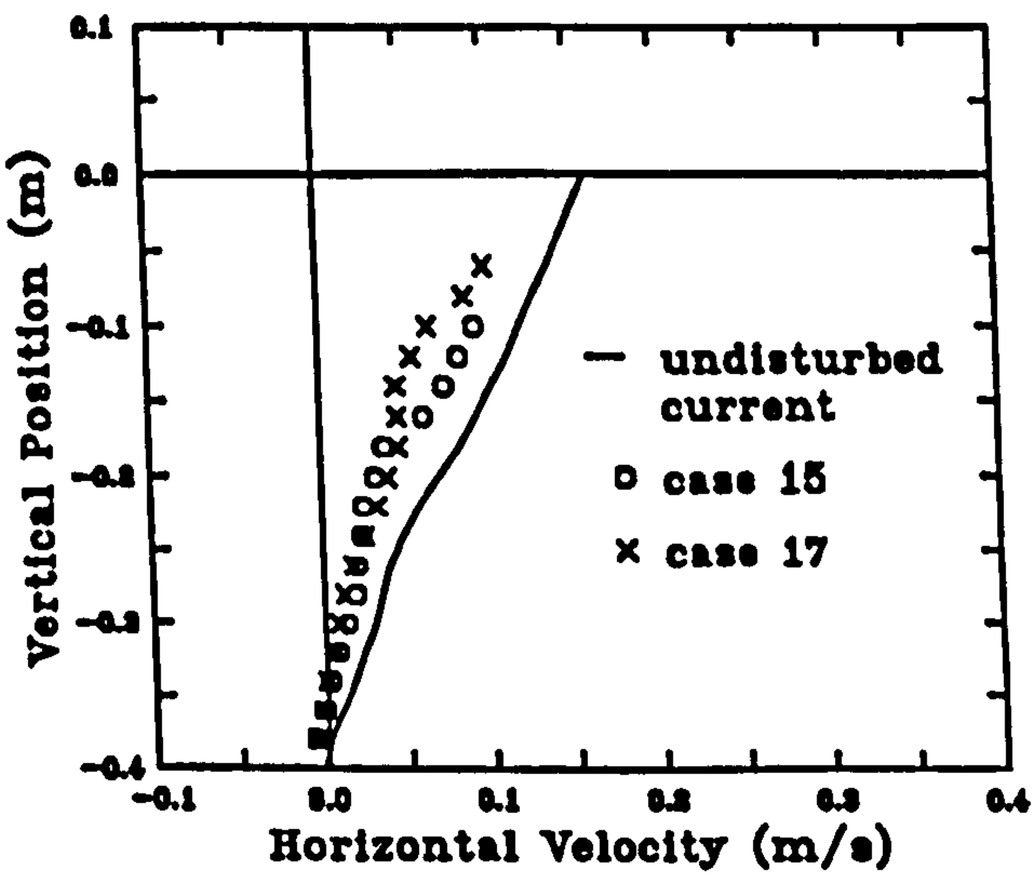

Figure 5.41: Mean horizontal velocities for medium steepness waves on a strongly sheared current.

the wavelength, waveheight and the associated frequency. If the current is not uniform, the effective current implied in this way may still have some physical significance.

Implied Current from the Wavelength for Small Amplitude Waves

In the section 5.3.3, tests were described in which the wavelength was measured with wavegauges over a range of frequencies and steepnesses for each current condition. The wavelengths obtained in this way were in good agreement with 3rd order theory in the current-free case.

For each wave frequency, the small steepness limit of the wavelength was estimated by fitting a quadratic function of steepness to the data. The constant term was taken to be the small amplitude limit of the wavelength. From this value the effective current was estimated by making use of equations 2.10 and 2.3.

The currents deduced in this way are shown for each current condition against frequency in figure 5.42. Also shown, for each current, is the value of its velocity at the surface, in the absence of waves. In the cases where there was no current, the implied current is zero as expected, within experimental error, except at low frequency, where there may have been some problems due to reflections. For the *uniform* currents, forward and reverse, the agreement is not quite as good as might be expected. In the sheared-current cases, the deduced slab current values are very close to the surface values of the current.

It is perhaps surprising that there is not more variation with frequency for the strongly sheared current cases, given that the orbital decay with depth is very dependent on frequency.

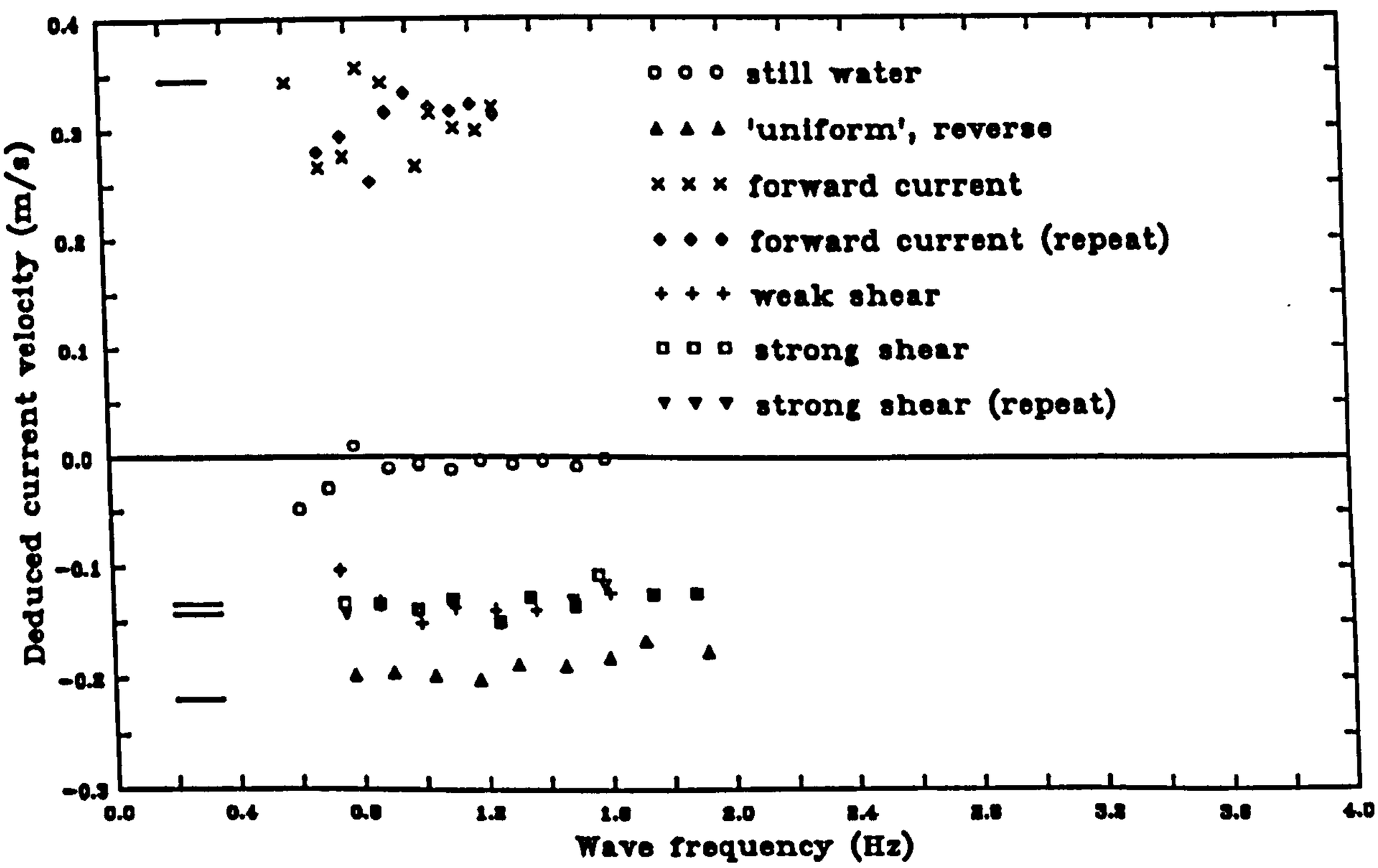

Figure 5.42: Currents implied from measured wavelengths for small amplitude waves

Wavelengths Obtained for the PIV Cases

The wavegauge measurements of wavelength described in section 5.3.3 also covered the 21 wave/current cases selected for kinematic measurement with PIV and summarised in table 5.3. In addition to the values of wavelength obtained in this way, various estimates could also be made from the PIV pictures themselves, and great care was taken to check the consistency of these different estimates and to select, objectively, the best value if there was a conflict.

For all the PIV cases, an estimate of the wavelength was obtained by enlarging and tracing the surface profiles present on the photographic negatives. Since each picture only covers a portion of a wavelength, it was necessary to build up a complete wavelength by matching together each part of the surface. Apart from cases 15 and 17, the estimates for λ obtained in this way differed from those measured with the wavegauges by between $\frac{1}{2}\%$ and 5% in all circumstances. It was therefore decided to use the values obtained with the wavegauges in all cases except 15 and 17, which differed by about 10% and would be investigated further. Since these two wave/current cases corresponded to medium steepness waves on a strongly sheared current, the most interesting circumstances, it was important to track down any inconsistencies.

Because they were amongst the more important flows, cases 15 and 17 were subjected to more PIV analysis than the other wave/current combinations. The matching of the surface profiles was found to be a not very accurate way of discovering the wavelength, as quite large changes in the amount of overlap between neighbouring portions of the surface could still be judged acceptable. However, once the velocity fields were measured, it was found that the various portions of the wave could be overlapped by matching up the vector angles, with greater sensitivity than the surface profiles. The wavelengths determined in this manner were much closer to those obtained with the wavegauges and were the ones used.

Case	Current	Surface Current (m/s)	Frequency [lab] (Hz)	Measured Wavelength (m)	Implied Frequency (Hz)	Implied Current (m/s)	Frequency difference
0	No current	0.000	0.8000	2.525	0.7833	0.042	2.1%
1	No current	0.000	1.0000	1.582	1.0016	-0.003	-0.2%
2	No current	0.000	1.0000	1.625	1.0001	0.000	0.0%
3	No current	0.000	1.0000	1.679	0.9993	0.001	0.1%
4	No current	0.000	1.2000	1.159	1.1889	0.013	0.9%
5	No current	0.000	1.2000	1.210	1.1813	0.023	1.6%
6	Uniform, reverse	-0.219	0.8336	1.780	0.9493	-0.206	1.0%
7	Uniform, forward	0.345	0.9275	2.360	0.8059	0.287	-2.4%
8	Uniform, forward	0.345	1.1929	1.550	1.0127	0.279	-3.1%
9	Weak shear	-0.142	0.7345	2.390	0.8111	-0.183	-2.5%
10	Weak shear	-0.142	0.8976	1.650	0.9788	-0.134	0.6%
11	Weak shear	-0.142	0.8976	1.690	0.9780	-0.136	0.4%
12	Weak shear	-0.142	0.8976	1.790	0.9602	-0.112	2.0%
13	Weak shear	-0.142	1.0525	1.200	1.1666	-0.137	0.4%
14	Weak shear	-0.142	1.0525	1.260	1.1539	-0.128	1.2%
15	Strong shear	-0.134	0.7099	2.760	0.7399	-0.083	2.7%
16	Strong shear	-0.139	0.8592	1.660	0.9757	-0.193	-4.1%
17	Strong shear	-0.134	0.8592	1.820	0.9369	-0.141	-0.5%
18	Strong shear	-0.134	0.8592	1.830	0.9479	-0.162	-1.9%
19	Strong shear	-0.139	0.9972	1.360	1.0886	-0.124	1.2%
20	Strong shear	-0.134	0.9972	1.310	1.1262	-0.169	-2.9%

Table 5.5: Wave parameters on the different currents, along with the implied current velocity

Table 5.5 contains a summary of the selected wavelength along with the implied velocity. The *implied frequency* was obtained from the measured wavelength and waveheight using code due to Klopman based on the Fourier approximation method [48], mentioned in section 2.4.1. These calculations were carried out in the frame of reference where there is no overall mass flux, which is the most natural physical frame. The final column of the table shows the percentage difference between the wave frequency deduced from the surface current velocity (using Doppler Theory), and that obtained from the wavelength, given also the wave heights. This difference never amounts to more than a few percent, and is very small for the central waves cases in the absence of current.

5.5.5 Lengthening of the Wave Period

An apparent lengthening of the wave period was noticed in some of the plots in figures 5.4 to 5.7. If the waves are steady, then the period at any location in the flume must be the same as that at the wavemaker.

The period of a steady wave can be found by measuring the times between still water crossings at a chosen location. From the wave traces measured in the determination of the wavelength, the wave period was established by measuring the time between still water crossings at the start and end of the sampled wave train. In this way the average period of the wave train was established and compared to the wavemaker period.

Figure 5.43 contains the relative increase in wave period found for the case of waves on the strongly sheared current, against wave steepness. A strong trend can be seen for the wave period to increase, roughly linearly with steepness, for most of the wavemaker periods attempted. Each point on the graph represents the average period over a number of cycles. The period was also extracted from the first cycle in the wave trains and similar trends found, although the results were more noisy.

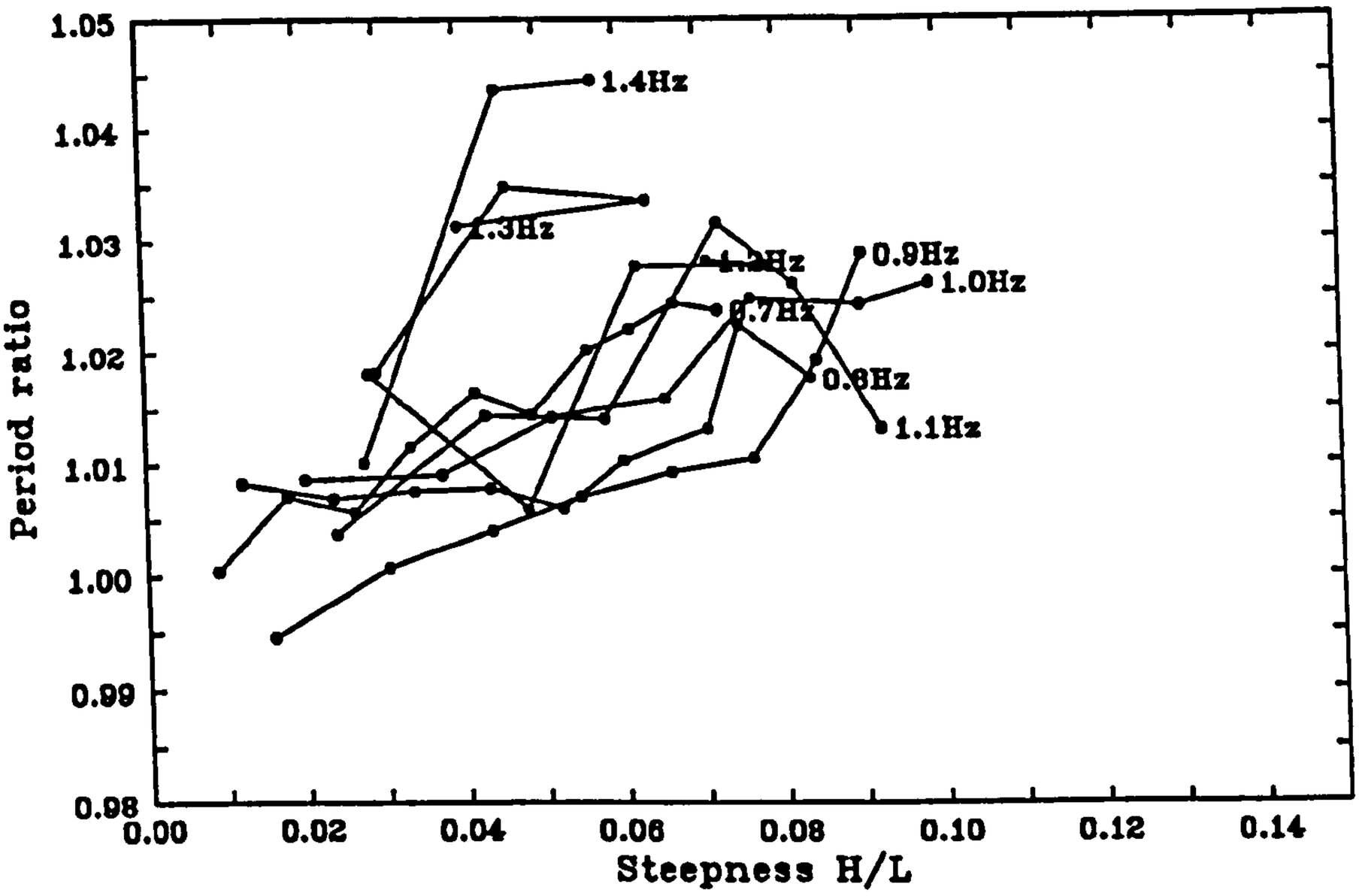

Figure 5.43: Wave periods measured on the strongly sheared current compared to the wavemaker period

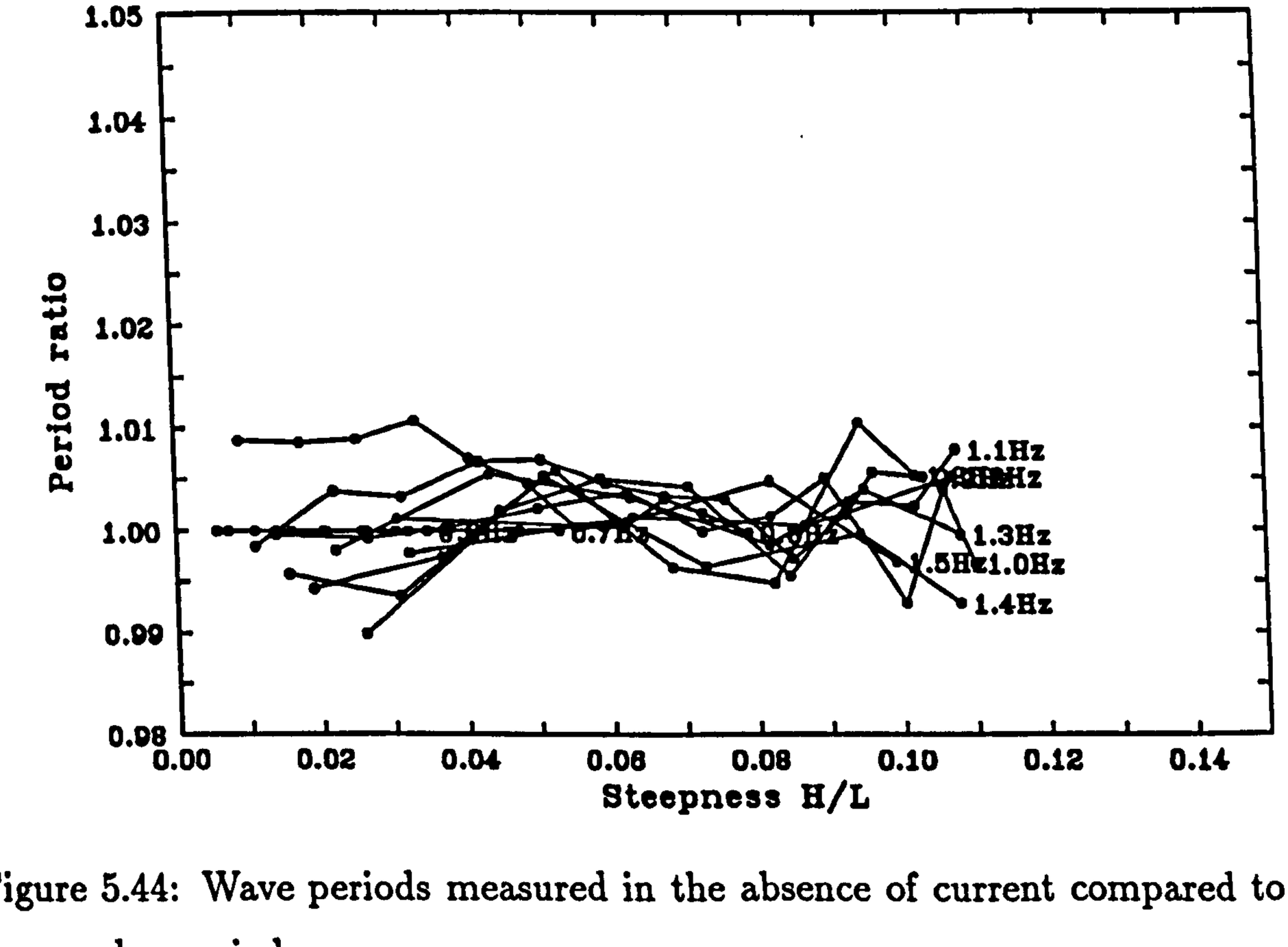

Figure 5.44: Wave periods measured in the absence of current compared to the wavemaker period

For comparison, figure 5.44 contains similar data obtained for waves in the absence of current. No period change is expected in this graph, and any variation is most likely to be due to experimental errors.

5.6 Comparisons with Steady Numerical Waves Predictions

In section 5.5 it has become apparent that the measured combination of waves and turbulent currents are not steady: the vorticity has been found to decrease with time, and the wave period to increase. Nevertheless, it is useful to compare the experimental results with steady wave predictions, in order to gauge the significance of the differences. In this section, it is assumed that the waves are steady and an assessment is made of how well the kinematics are predicted with current design practice.

In this section the velocity data is mainly compared with irrotational numerical models combined with the stretched current, as present design practice is normally based on this approach. While it would have been possible to compare the results with those of a model taking account of vorticity, this was not pursued as a predicted value for the reduced vorticity was not available.

Initially, the experimentally obtained kinematics of steep waves, in the absence of a current, are checked for consistency against a high-order steady wave model. Then the kinematics measured with waves riding on a uniform current are compared with numerical predictions after suitable shifting of the frequency. Next the combined kinematics of steep waves and strongly sheared currents are plotted along with the results of adding the predictions from the irrotational model to the stretched current profile. Such comparisons are present under the crest in all cases, and under the whole wave in a case which was studied in more detail.

5.6.1 Generation of Numerical Data

Irrotational numerical models were available from Chaplin and from Klopman, and a constant vorticity model from the University of Bristol. These models have been outlined in section 2.4.1.

Klopman's program was able to calculate velocity vectors in the frame of reference where there is no net mass flux, given the wave height and wavelength from table 5.5. Because there is an upper limit on the number of points at which velocities can be calculated, this program was just used for the crest profiles and wave parameters, not for the full velocity field. For each of the wave cases, the program was run for the measured wavelength and the wavelength obtained from Doppler theory using the surface current value.

Chaplin's model was used when data was required over the whole wave. The wave height was set, and the wavelength matched to the appropriate value from table 5.5 by iteration. The waves were calculated to 11th order, and velocity vectors evaluated on the same 20x20mm grid on which experimental velocity data had been gathered. The calculations in this model are carried out in the frame of reference where the mean Eulerian velocity is zero. In order to compare with the experimental results, data is required in the frame of reference where there is zero mass flux, so the numerical data was moved to this frame by adding the mean Eulerian velocity, calculated with Klopman's program.

The Bristol model required a constant value for the vorticity. Although it was known that the vorticity was reducing with time, this was obtained, for the strongly sheared case, from the slope of the current in the top half of the flow

Use of the Numerical Data

The numerical velocity data was to be used in two ways. For comparison with the crest kinematics, the results from the irrotational computations were added

Case	Current	Top shear $\frac{\partial u}{\partial z}\sqrt{\frac{\lambda}{g}}$	h/λ	H/λ	$\frac{h}{gT^2}$	%age of limiting steepness
0	No current		0.2970	0.0825	0.0489	58.8%
1	No current		0.4741	0.0563	0.0764	34.9%
2	No current		0.4615	0.0823	0.0765	52.4%
3	No current		0.4467	0.1064	0.0764	70.0%
4	No current		0.6471	0.0800	0.1101	51.0%
5	No current		0.6198	0.1018	0.1101	67.7%
6	Uniform, reverse	(0.094)	0.4213	0.0752	0.0703	48.6%
7	Uniform, forward	(0.028)	0.3178	0.0569	0.0474	37.2%
8	Uniform, forward	(0.022)	0.4839	0.0574	0.0738	33.7%
9	Weak shear	0.053	0.3138	0.0870	0.0503	59.7%
10	Weak shear	0.044	0.4545	0.0536	0.0732	33.3%
11	Weak shear	0.045	0.4438	0.0794	0.0731	50.4%
12	Weak shear	0.046	0.4190	0.0989	0.0705	64.4%
13	Weak shear	0.038	0.6250	0.0779	0.1040	48.7%
14	Weak shear	0.039	0.5952	0.0984	0.1018	63.3%
15	Strong shear	0.226	0.2717	0.0751	0.0419	53.7%
16	Strong shear	0.175	0.4518	0.0535	0.0728	33.2%
17	Strong shear	0.183	0.4121	0.0729	0.0671	46.4%
18	Strong shear	0.184	0.4098	0.0976	0.0687	63.6%
19	Strong shear	0.159	0.5515	0.0686	0.0906	42.8%
20	Strong shear	0.156	0.5725	0.0929	0.0970	59.4%

Table 5.6: Non-dimensionalised wave parameters. Note that T has been obtained from H and λ using irrotational theory

to the current profile, which was stretched to the surface. For comparison with the kinematics over the whole wave, the numerical data was subtracted from the experimental values, point by point, to yield the underlying current.

In undertaking these comparisons for the sheared current cases, the frame of reference from which the waves were viewed was shifted so that the current profile best represented a wind-sheared current. This is justifiable, as the parameters used for the numerical calculations, λ and H, do not change with change of reference frame. In doing this, there is an implicit assumption that the physics of the flow is the same in different inertial reference frames, and effects due to turbulence and side wall friction have been ignored.

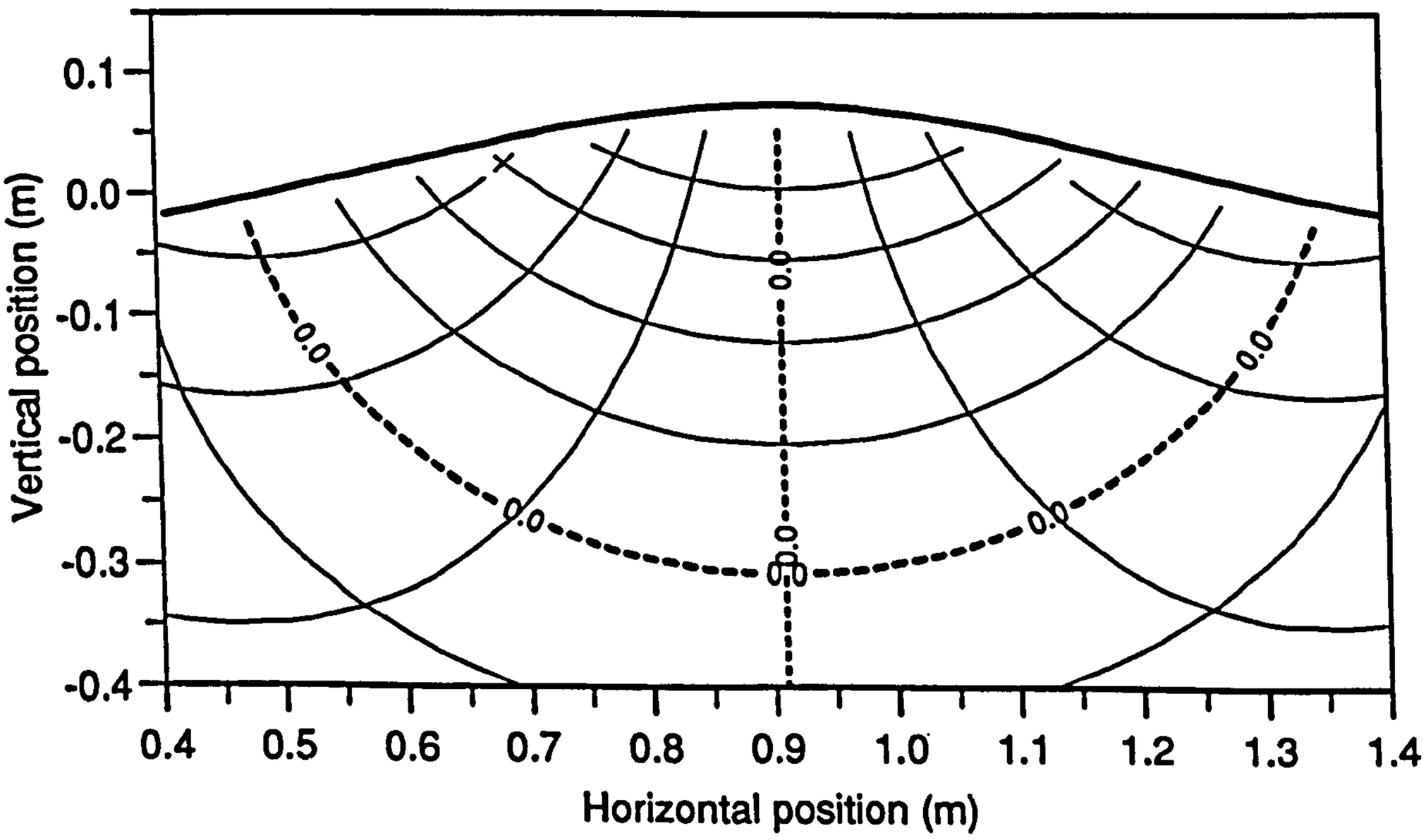

Figure 5.45: Iso-velocity contours for numerically generated flowfield (Bristol constant vorticity model), parameters as case 17. Contour interval: $0.1 ms^{-1}$

For direct comparison with the previously presented experimental results, figure 5.45 shows iso-velocity contours plotted from predictions of the Bristol model. This data should be compared to figures 5.25, 5.26 and 5.27. While the overall form of these graphs is similar, they should be compared with caution, as the assumed value of the average vorticity in the model has been obtained from

the undisturbed current. There is a shift between the absolute values of the v_x contours, corresponding to different frames of reference.

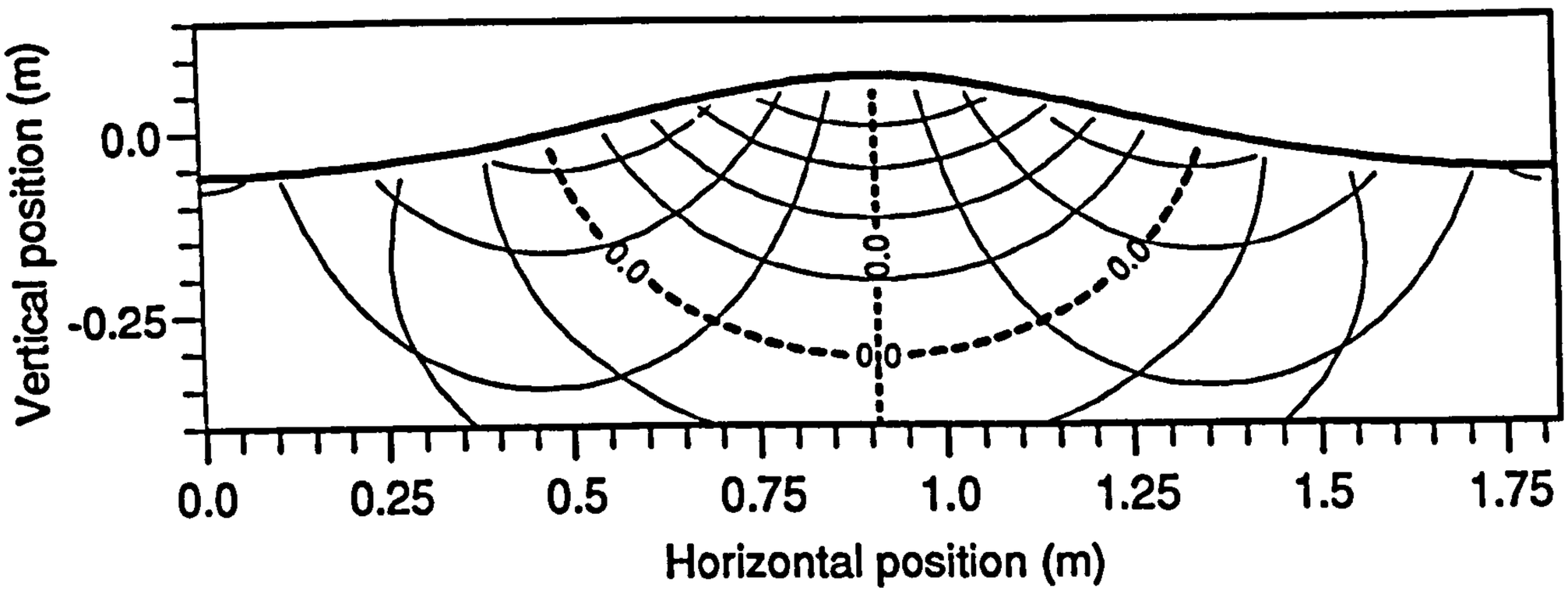

Figure 5.46: Iso-velocity contours for numerically generated flowfield (Bristol constant vorticity model), parameters as case 17. Contour interval: $0.1 ms^{-1}$

For comparison with the combined experimental data plotted in figure 5.28 for a whole wavelength, the numerical data from the Bristol model is replotted in figure 5.46, also for a full wavelength.

5.6.2 Comparison between Experimental and Numerical Kinematics in the Absence of Current

Before attempting comparisons for the cases of waves combining with currents, the experimental measurements of steep, steady waves, in the absence of current, were checked against numerical predictions. This has a major benefit: if the two approaches are found to be consistent then some confidence in the quality of the experiments and the correctness of the assumptions in applying the model is gained. In the tests, care was taken to ensure that the measurements were accurate, and that the waves were as steady as possible and free from reflection. An overall assessment of these effects is obtained by checking against a suitable numerical model.

The kinematic measurements were conducted, in the absence of current, for six waves with similar parameters, of height and wavelength, to those used in the tests with currents. The main parameters of the waves are summarised in dimensionless form in table 5.6, for these six waves, together with the wave & current combinations.

The experimental measurements of the horizontal velocity component under the crest are plotted in figure 5.47 for the wave cases in the absence of current, along with the numerical predictions. The plots for cases 0 to 3 are the averages of two repeats of the same wave cycle in the wavetrain. The variation between the repeats is smaller than the symbols marking the data points. The position of the wave crests in the respective wavetrains can be found by referring to figure 5.4. Of the cases for which measurements were also made later in the wavetrain the agreement for case 3 was better, and for case 0 worse, probably due to reflection.

The discrepancies range from about 1% for the central waves case, to about 4% in the worst case, with these errors being defined from the differences and absolute velocities near the crest. These discrepancies should be borne in mind when assessing the later comparisons.

Along with the horizontal velocity profiles, the wavelengths of these irrotational waves were measured. The discrepancy between the measurements and that expected from theory ranged from less than .1% to 3%, being greatest at the lowest and highest frequencies. The measured wavelengths and their differences from prediction have been covered in table 5.5.

5.6.3 The Checking of Doppler Shifting on a Uniform Current

Doppler theory has been covered in section 2.2.2. Experiments were performed on currents whose profiles were approximately uniform in the top half of the water depth. Horizontal velocity profiles beneath the crest are plotted for the reverse

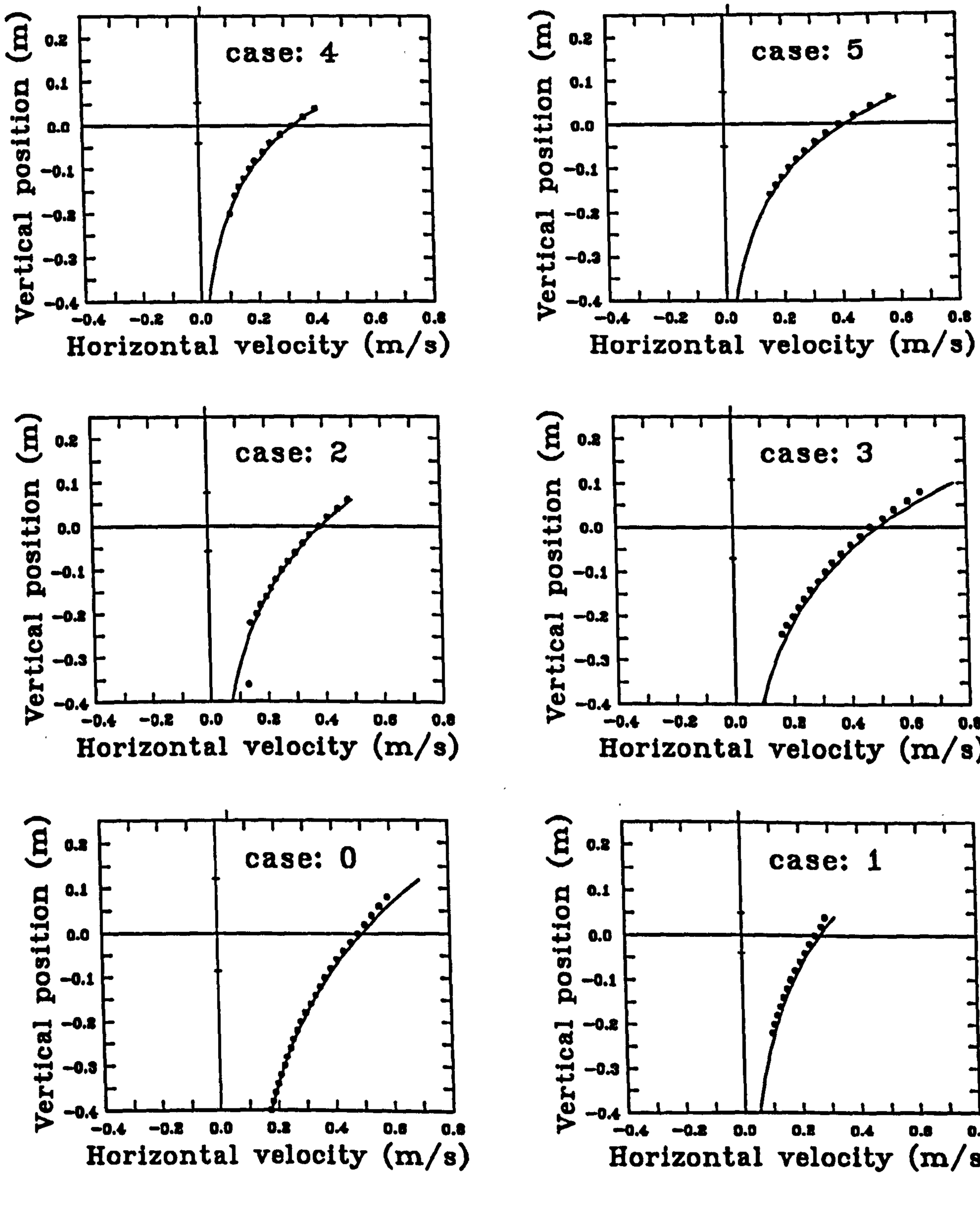

Figure 5.47: Horizontal velocity profiles under the crest, in the absence of current. -•- experimental data, with scatter, —— prediction from irrotational numerical model. Water depth = .75m

current cases in figure 5.48 and the forward current cases in figure 5.49. Each plot shows the experimental measurements, the *almost* uniform current profiles and velocity profiles generated numerically by Doppler shifting the frequency to the frame of reference moving with the current. Also shown is the combined profile obtained by adding the numerical values to the (stretched) current profile.

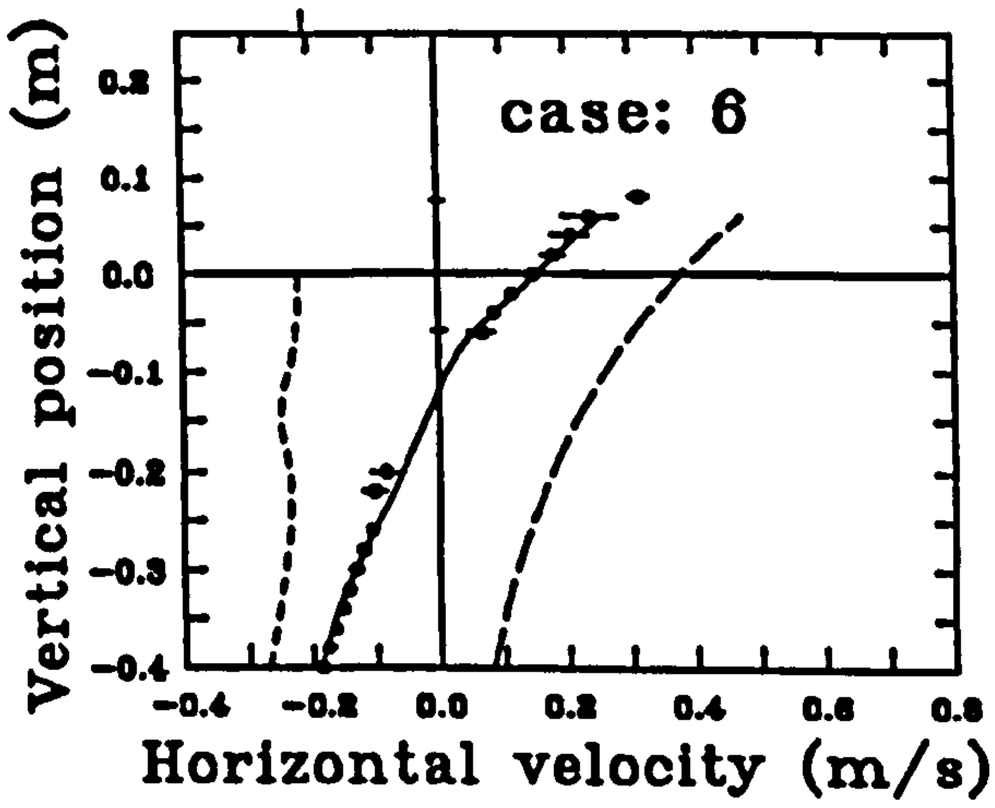

Figure 5.48: Horizontal velocity profiles under the crest, for waves on a uniform, reverse current. -•- experimental data, with scatter, - - - - undisturbed current, — — irrotational numerical model, —— prediction from numerical model and stretched current profile

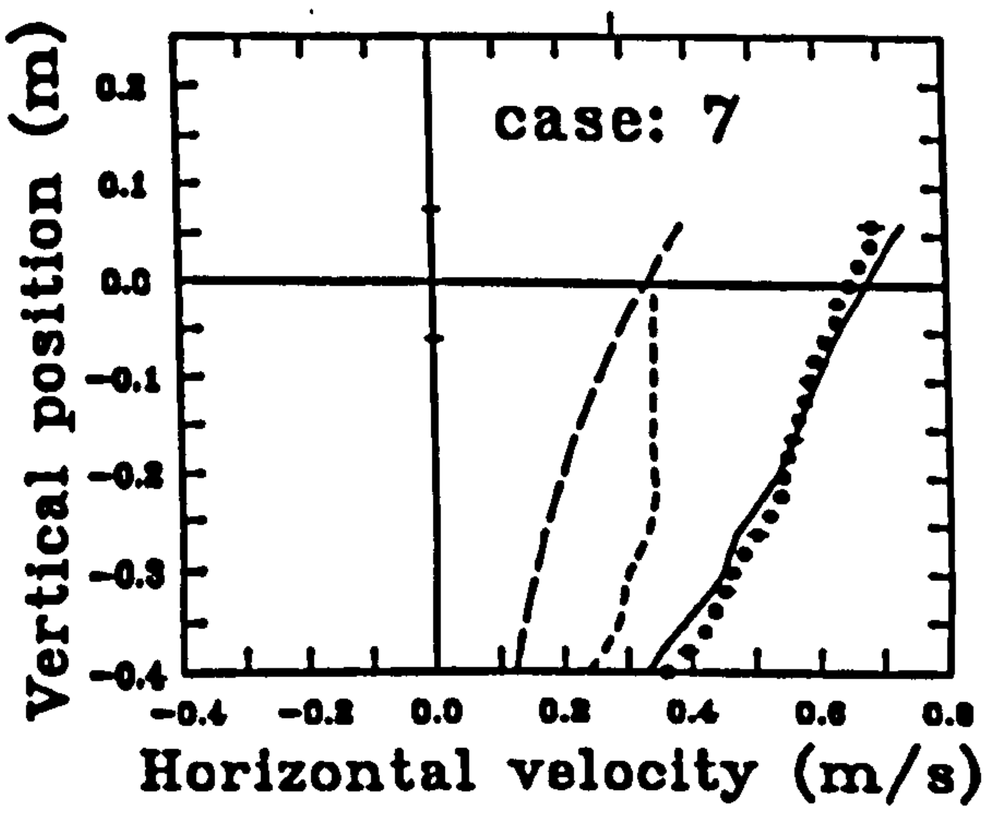

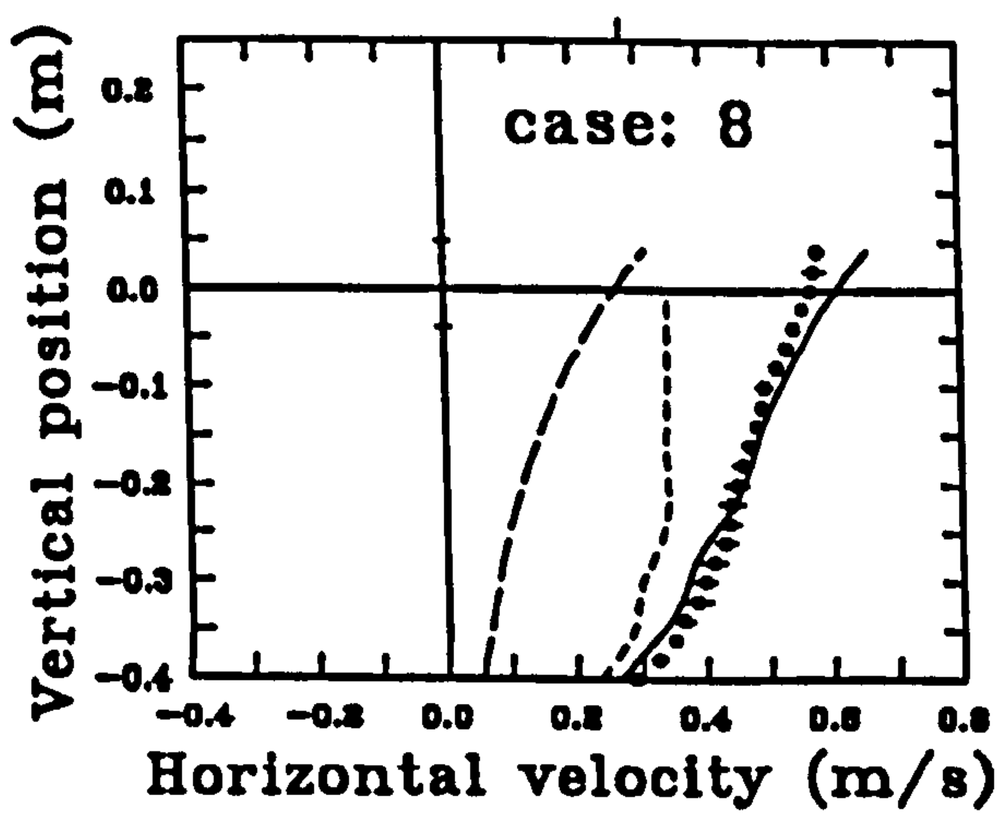

Figure 5.49: Horizontal velocity profiles under the crest, for waves on a uniform, forward current. -•- experimental data, with scatter, - - - - undisturbed current, — — irrotational numerical model, —— prediction from numerical model and stretched current profile

The horizontal lines in the plots represent the scatter found between repeats of the same cycle of the wave in each wavetrain and between earlier and later cycles. Refer to figure 5.5 for the number of repeats and the timing of the photographs within the wave packet.

It can be seen that the crest kinematics are reasonably well predicted within the value of the experimental errors, for the reversing current. The agreement is less good for the forward current cases, particularly above the trough level. This may be due to interaction between the wave and current generation being advected down to the measurement zone, or may be due to the turbulence present in the current.

5.6.4 Waves on Sheared Currents

Tests where conducted with lightly sheared and strongly sheared currents, over similar ranges of wave frequency and wave steepness to those used in the earlier, shear-free cases. The dimensionless parameters of the wave/current cases studied have been summarised in table 5.6.

Effect of Sheared Currents on Velocity Profiles Under the Crest

The experimentally measured velocity profiles under the crest for lightly sheared and strongly sheared current conditions are plotted in figures 5.50 and 5.51, along with numerical predictions. Each graph contains the undisturbed current profile, the velocity profile under the crest for the combined flow, a numerically generated profile for an irrotational wave with the same height and wavelength, and the numerical data combined with the stretched current profile. The results presented in figures 5.50 and 5.51 have been shifted by $.2ms^{-1}$ for the weakly sheared current, and by $.3ms^{-1}$ for the strongly sheared current.

The experimental values were obtained by averaging over repeats of the same

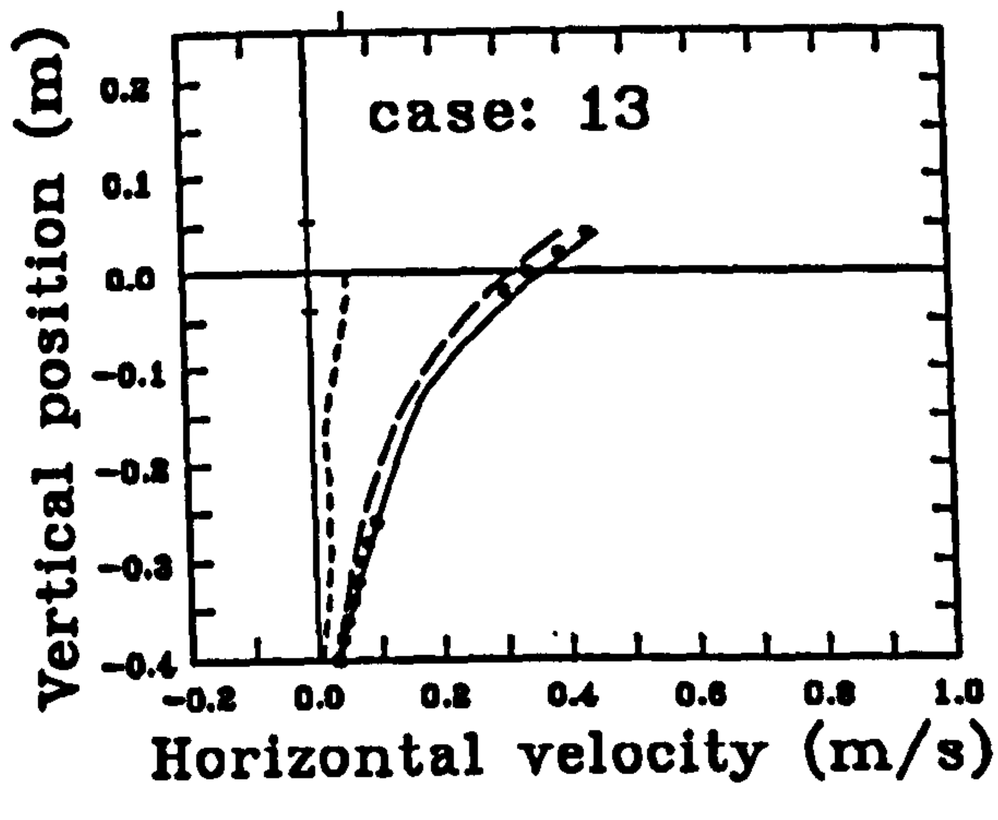

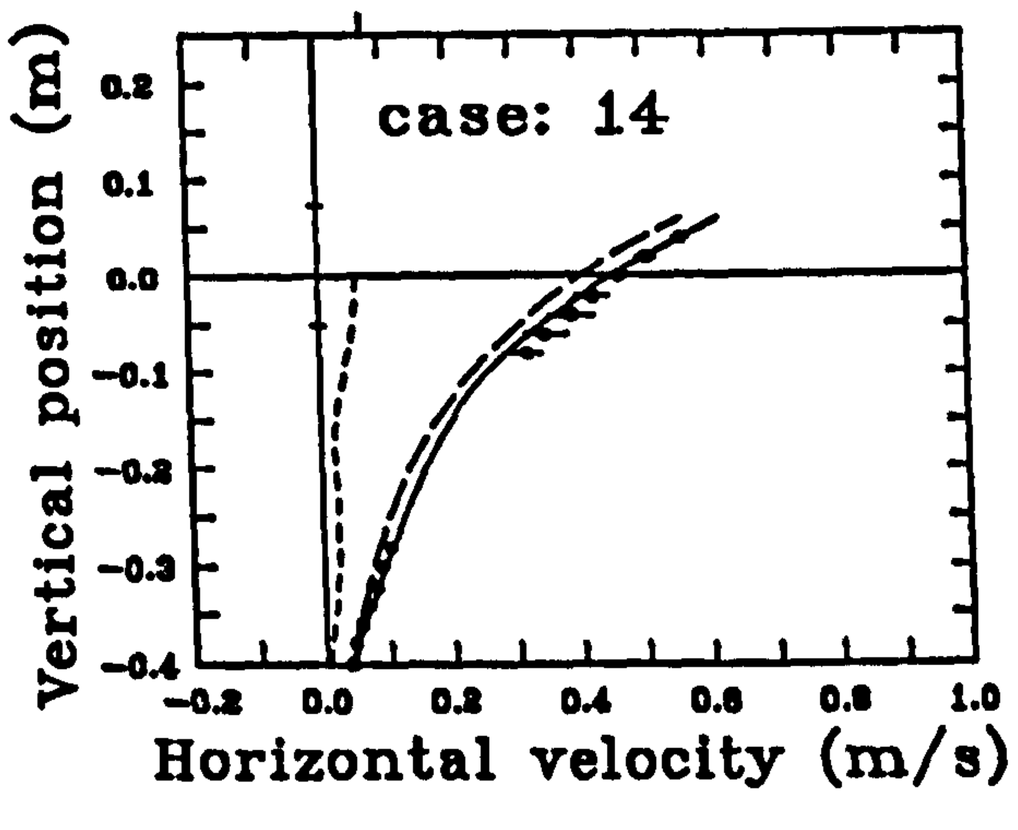

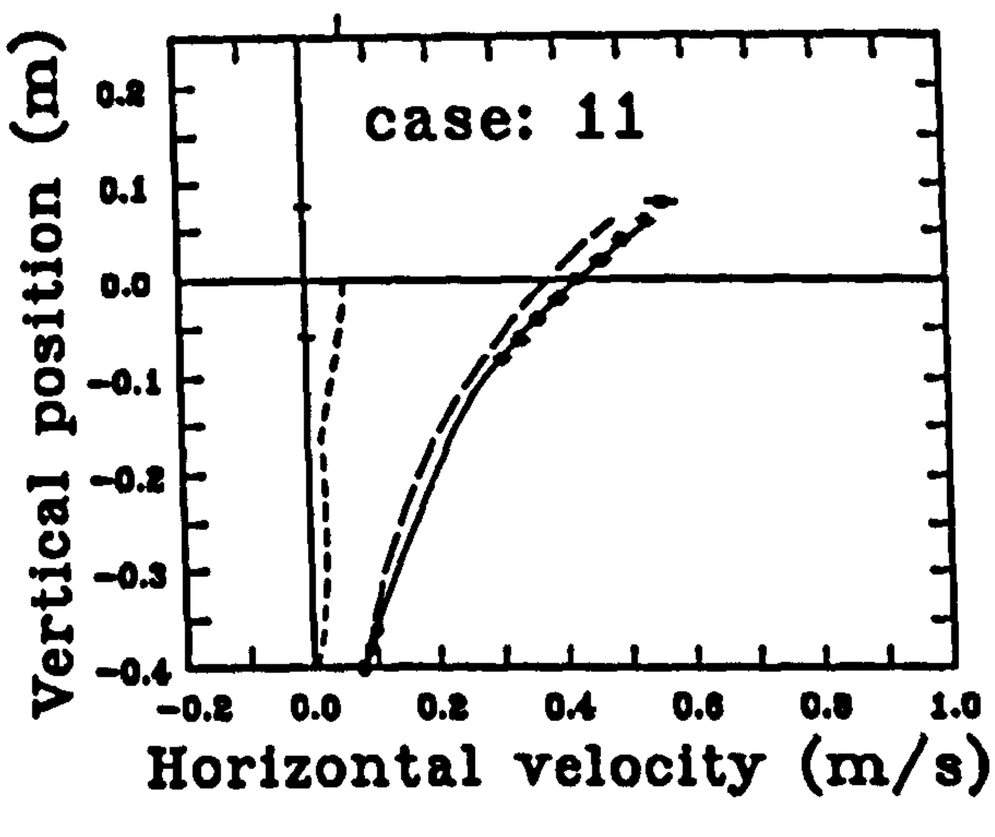

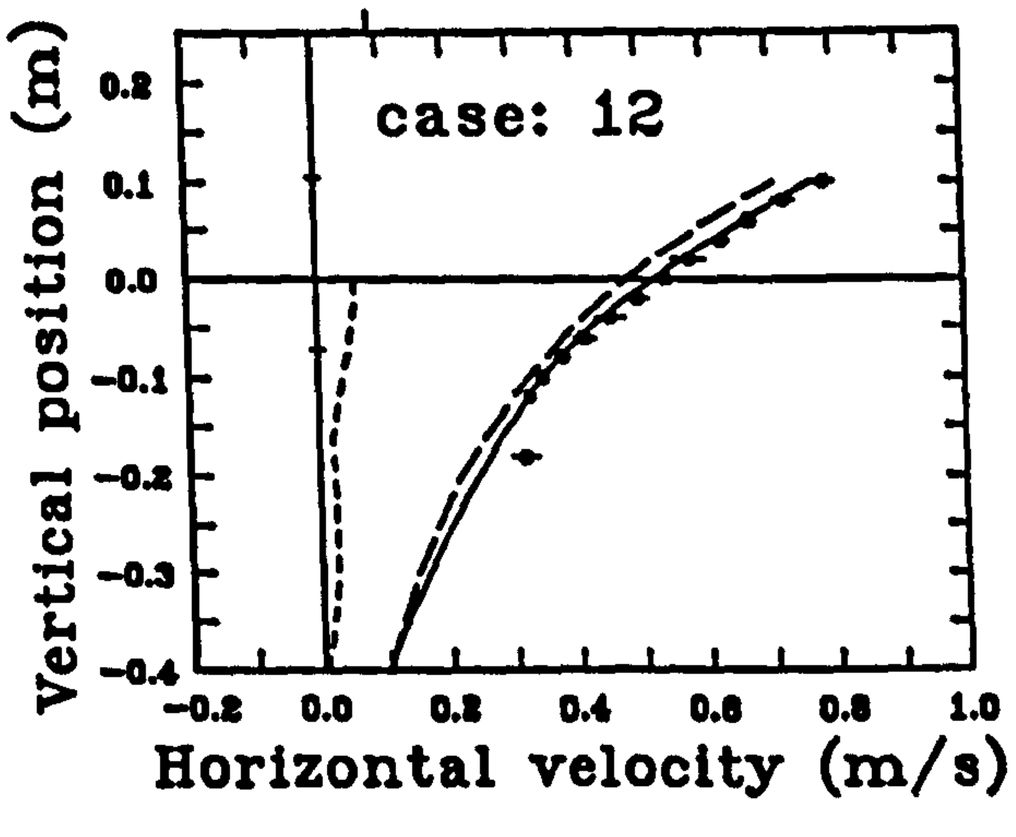

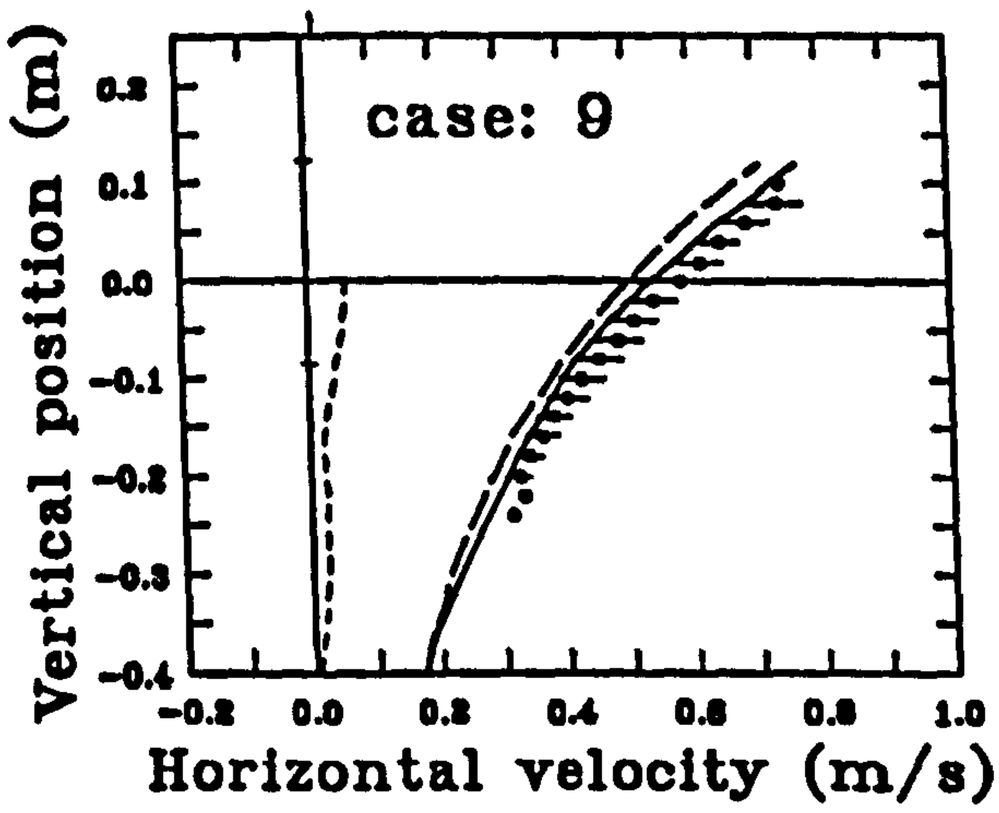

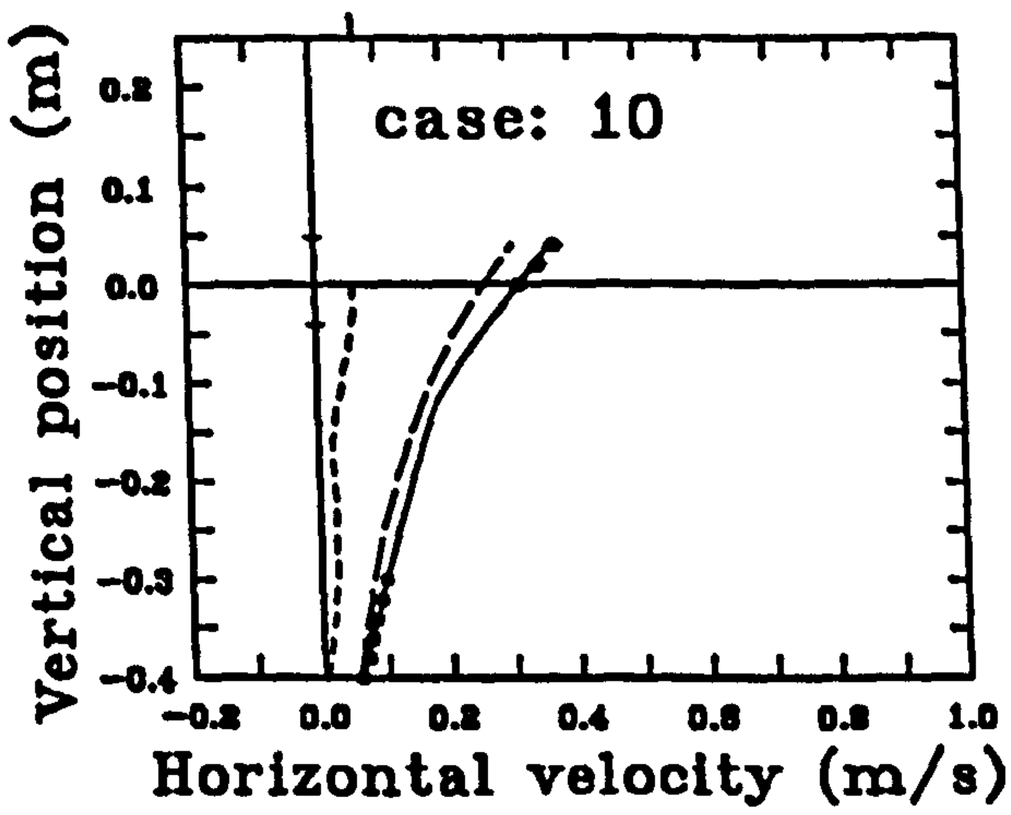

Figure 5.50: Horizontal velocity profiles under the crest, for waves on a weakly sheared current. -•- experimental data, with scatter, - - - - undisturbed current, — — irrotational numerical model, ——— prediction from numerical model and stretched current profile

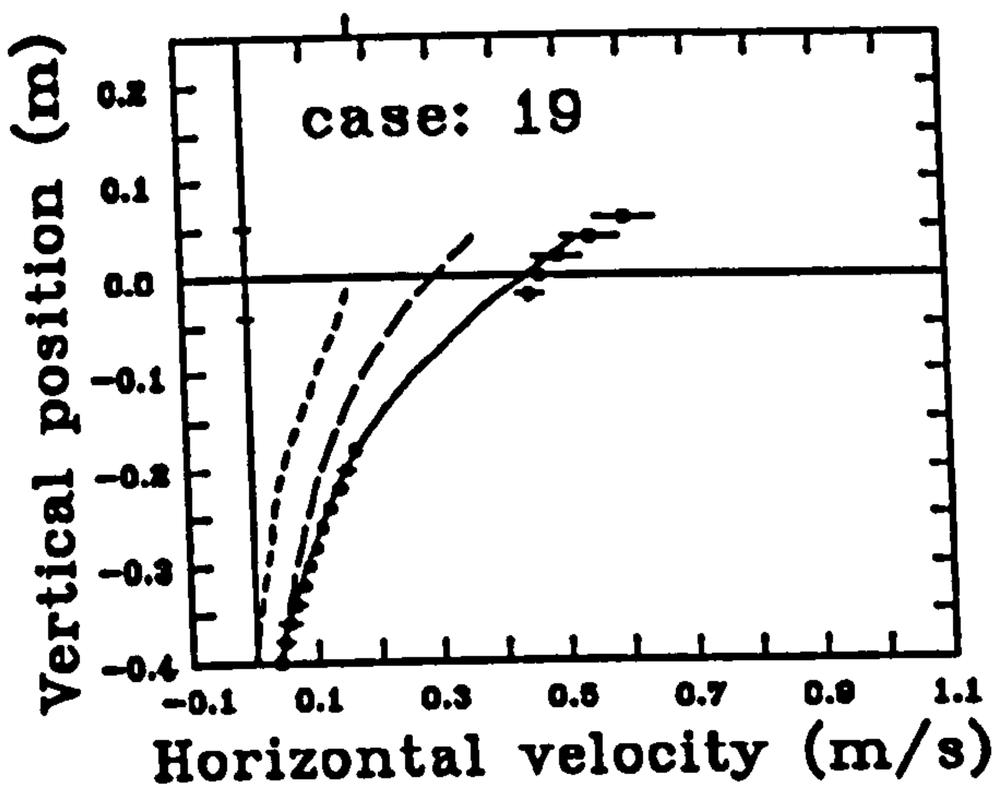

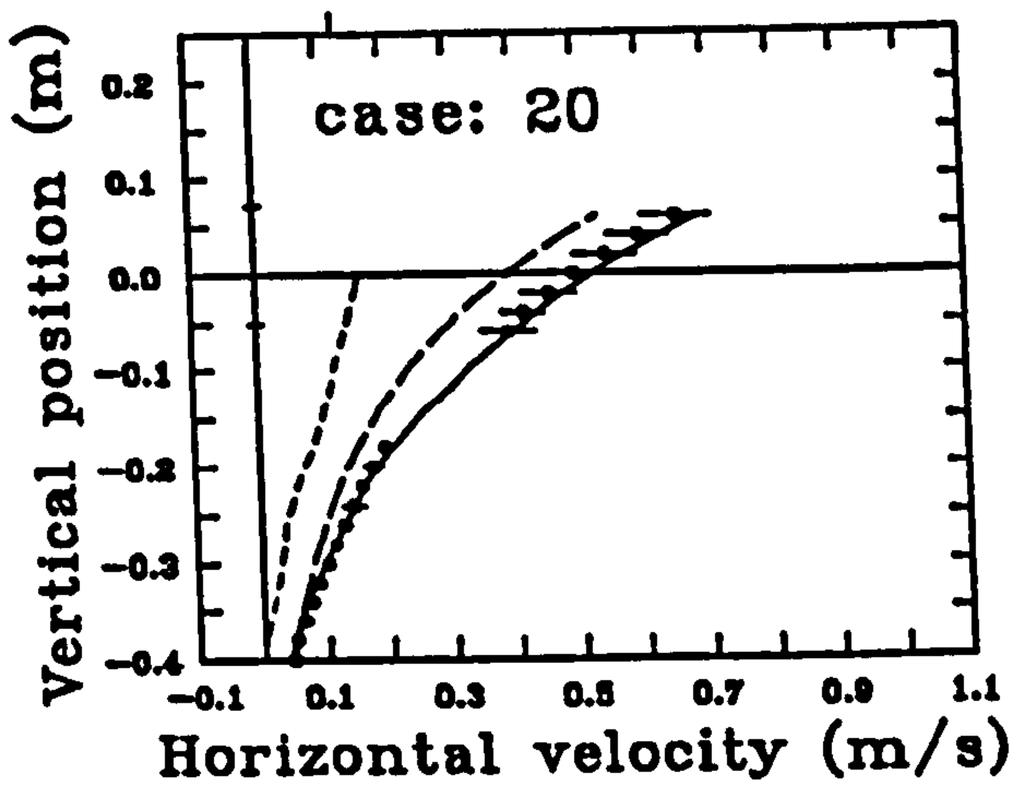

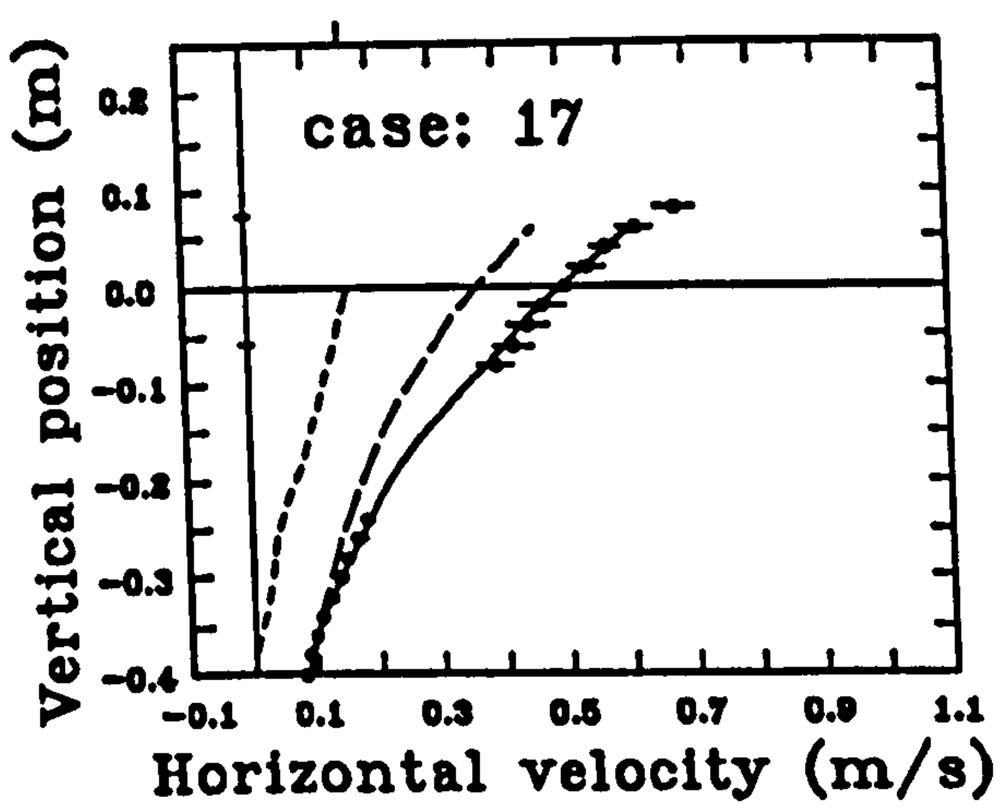

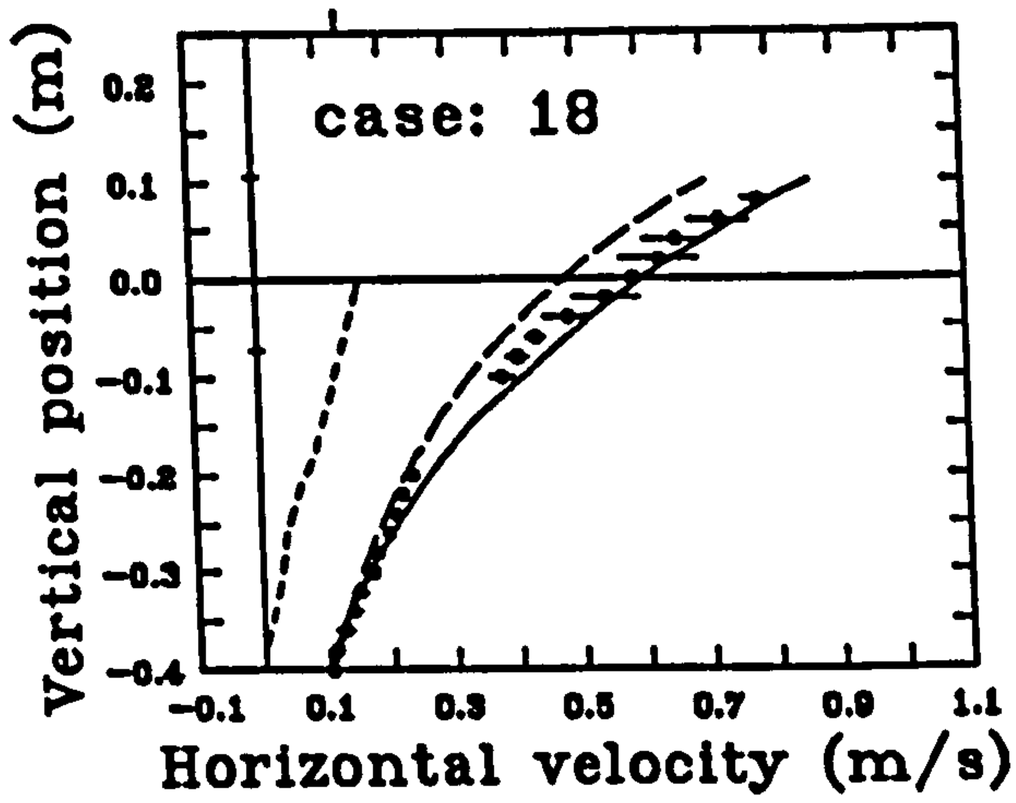

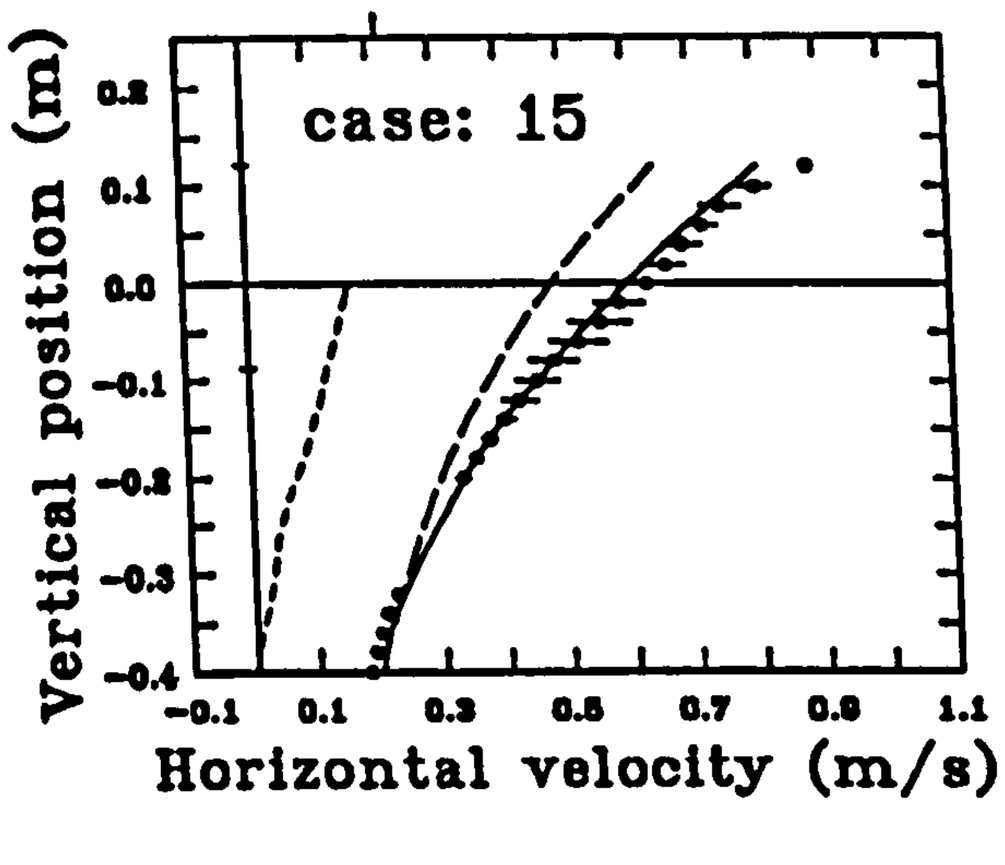

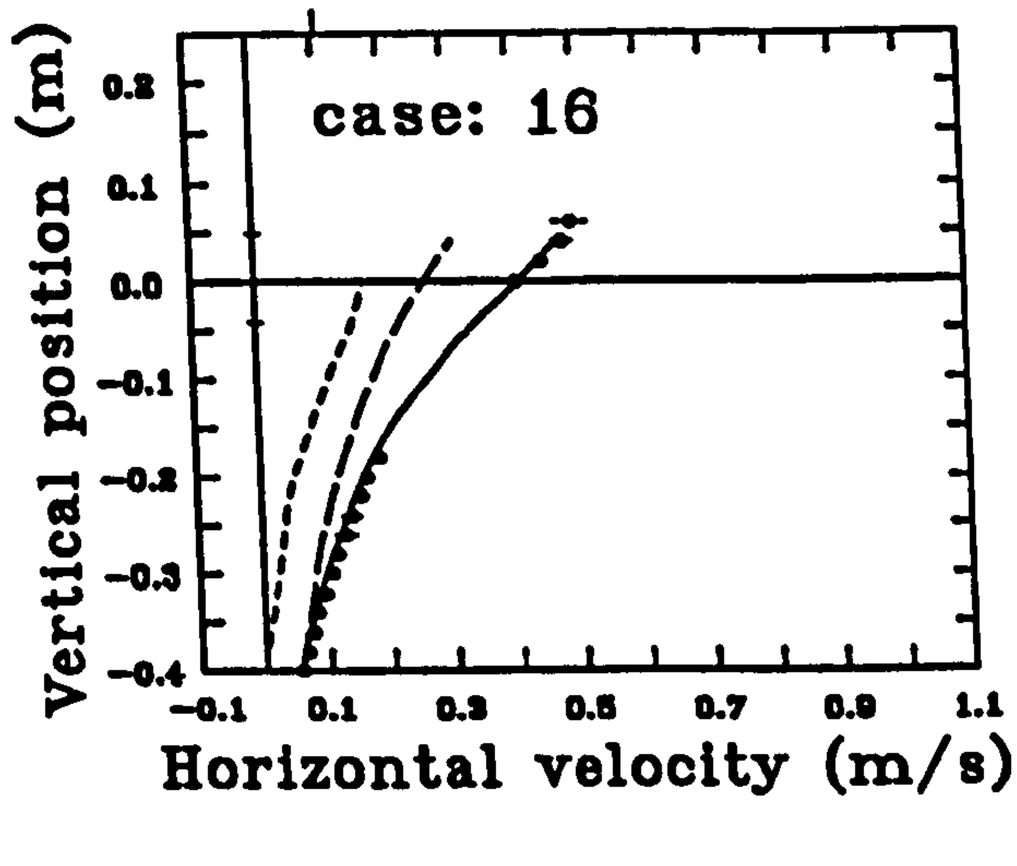

Figure 5.51: Horizontal velocity profiles under the crest, for waves on a strongly sheared current. -•- experimental data, with scatter, - - - - undisturbed current, — — irrotational numerical model, ——— prediction from numerical model and stretched current profile

waves in the train, at each of two different cycles in the progression, as described in section 5.5.1. The number of repeats for each plot can be discovered from figures 5.6 and 5.7. The horizontal lines in each plot represent the experimental scatter.

The numerically generated velocity data was for waves with the same height and wavelength as those measured experimentally. This approach is slightly different from that adopted for the cases in the absence of current and on uniform currents, where the current velocity was used to obtain the appropriate wave parameters, given the wave frequency and height in the laboratory frame of reference. The approach differs because the velocity value which should be used for the Doppler shift on a sheared current is not known. A treatment using the value of the current at the surface for the Doppler shifting was attempted for the sheared current cases, yielding plots which are almost identical to those shown in figures 5.50 and 5.51.

The current profile under the crest was obtained by linearly stretching the undisturbed current profile to the surface, in the way described in section 2.5.1. No modification to conserve mass has been applied. A slightly less arbitrary scheme for stretching the current profile, based on the water orbital excursions at each level was attempted, but the difference from the linear stretching was negligible.

In the graphs there is good agreement in all cases, with the predicted values for the combined wave and current velocities lying within the experimental scatter.

Effect of Sheared Currents on Velocity Profiles Under the Whole Wave

While the horizontal velocities near the crest lead to the highest loadings and are therefore the most important for design purposes, the velocity field throughout a complete wave cycle or wavelength is also of interest. For the more central wave/current cases, the wave kinematics were analysed in greater detail, and composite velocity fields constructed over a complete wavelength. Velocity data was then generated with a Chaplin's irrotational numerical model, with the same

wave height and wavelength as those measured experimentally. This numerical data was then subtracted, point by point, from the experimental values to yield the underlying current.

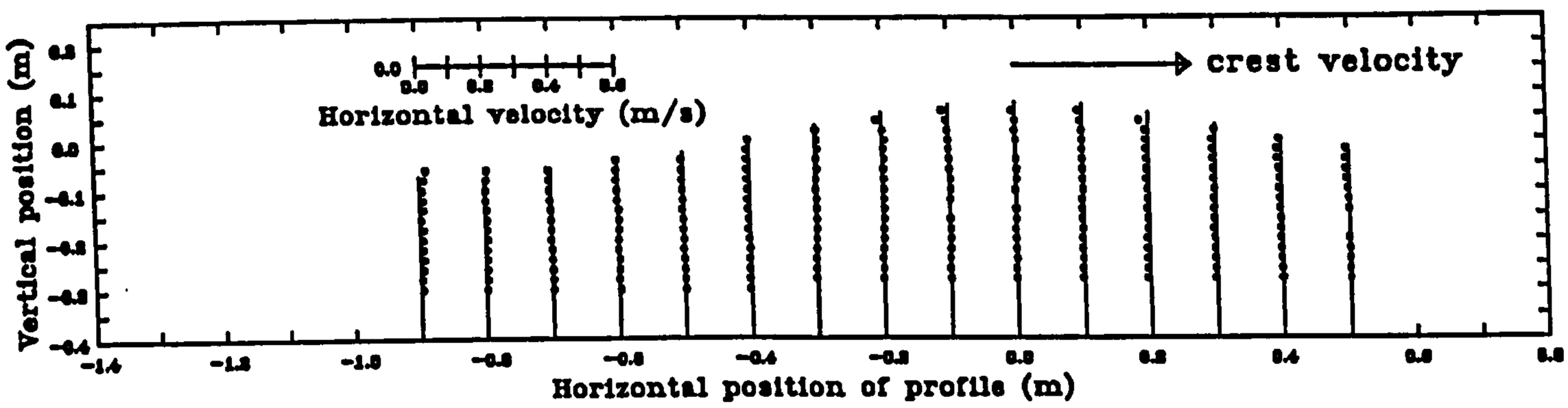

Figure 5.52: Underlying current at various phases of a wave, in the absence of current. -•- experimental data, with predictions from irrotational numerical model subtracted, —— stretched current profile.

In order to check the sensitivity of this method, the procedure was first tried for one of the waves in the absence of current (case 2), where the underlying current should be zero. The residual current obtained after subtracting the numerical data is plotted in figure 5.52 at various positions within the wave. In this case experimental data was only available over three-quarters of a wavelength, but since this includes both trough and crest, and the wave is expected to be symmetric, there is no loss of information.

The agreement between the experimental and numerical velocity data in this irrotational case is good, except very near the water surface where some overprediction is apparent. The maximum velocity in the crest is plotted for comparison with these small discrepancies.

Figure 5.53 shows the results for a similar treatment to one of the wave cases on the strongly sheared current (number 17). Again the numerical data has been subtracted to leave the residual current, which is plotted by averaging bands within the wavelength. For comparison, the stretched current profile is also plotted at each position.

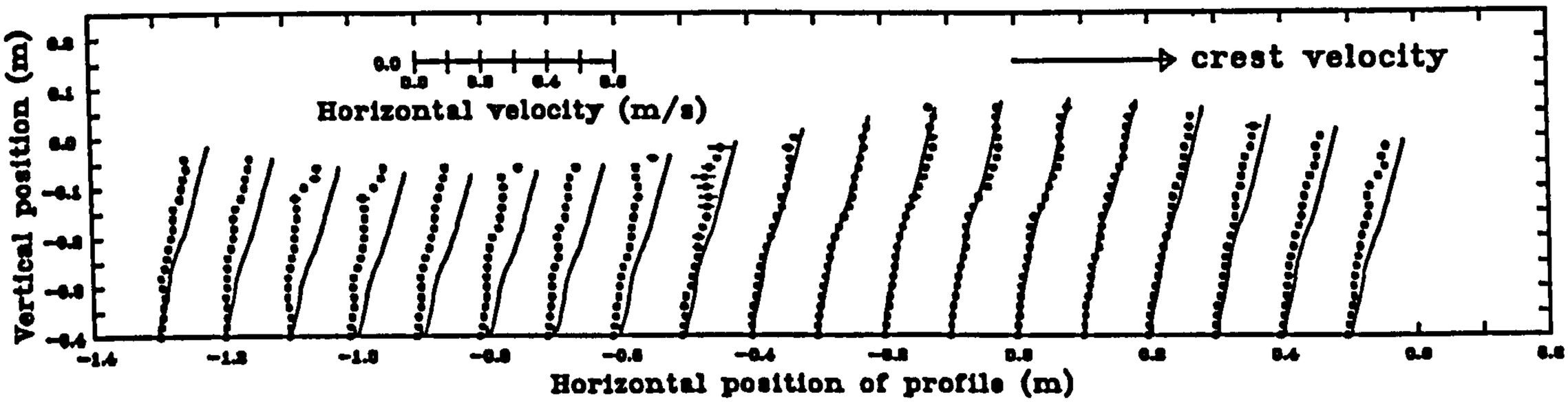

Figure 5.53: Underlying current at various phases of a wave, on a strongly sheared current. -•- experimental data, with predictions from irrotational numerical model subtracted, —— stretched current profile.

In the whole of the crest region, the estimated residual current matches the stretched current profile, as expected from the crest profiles shown earlier. However, in the trough, stretching predicts an increase in shear, which is not supported by these experimental results. If anything, the shear is reduced in the trough compared to the value in the undisturbed current. Similar trends were found for the wave/current cases with similar steepness at higher and lower frequency. In addition, the residual current estimate from the vorticity field in section 5.5.2 is very consistent with the trends shown in figure 5.53.

The success of current stretching in the crest seems a little fortuitous. No combination of current profile stretching and mass conservation can predict the experimental values satisfactorily over the whole wave, although the good agreement near the crest may be adequate for design purposes. The behaviour presented through the wave cycle should be predictable by the full numerical treatments.

5.7 Concluding Remarks for the Wave/Current Study

From the results of the wave/current study presented in this chapter, the following concluding remarks are made:

a) **Prediction of the crest kinematics**

There was good agreement for the crest kinematics of the waves in the absence of currents. In the presence of uniform currents, the kinematics were reasonably well predicted by the irrotational numerical model, after Doppler shifting the wave frequency. When sheared currents were present, there was fair agreement between the measured crest kinematics and the estimate obtained by combining the stretched current profile with the prediction of the irrotational model.

b) **Internal kinematics of the whole wave**

While the kinematics of a medium amplitude wave, in the absence of current, were well predicted over a complete wavelength, in the strongly sheared case the predictions obtained using current stretching were poor in the trough region. The was some evidence that the underlying current had constant shear throughout the wavelength.

c) **Wavelengths on the sheared currents**

It was found that, even for the strongly sheared current profile, the wavelength was determined adequately by assuming Doppler shifting of the wave frequency with the current value at the surface.

d) **Evidence of unsteadiness of the combined kinematics**

Strong evidence that the combined kinematics were not steady was found for the strongly sheared current case, suggesting that the good agreement obtained with current stretching for the crest kinematics might be fortuitous.

The main evidence for the unsteadiness of the combined kinematics was the trend found in one case, studied in detail, for the average vorticity in the crest region to decrease with time. Other evidence included an apparent lengthening of the wave period, in the interval when the wavetrain was assumed to be steady, and the reduction in shear between the undisturbed current and averages obtained from complete wavelengths.

Chapter 6

Main Conclusions

6.1 Summary of the Main Results

The following main results have come out of the present work:

a) Kinematics of the deep-water long-crested breaking wave

There was very good agreement between the velocity fields measured experimentally and predicted numerically for the breaking wave, within about 2%, after a small spatial shift of the numerical data.

New high-quality measurement of the internal kinematics of the breaking process were obtained throughout the breaking wave's evolution.

b) Kinematics of steep, steady waves on sheared currents

While irrotational predictions combined with the stretched current profile were found to give reasonable predictions of the crest kinematics, this approach does not satisfactorily explain the interaction of waves with a turbulent current.

There was strong evidence that wave/current interaction was evolving with time, manifesting itself most strongly in the measured reduction of the vorticity with time.

c) **Measurement of internal kinematics with Particle Image Velocimetry**

A versatile new wave flume has been constructed, allowing measurements of the internal kinematics of water waves with Particle Image Velocimetry (PIV). PIV has been established as a reliable technique for this purpose, able to generate measurements at the rate demanded by the the needs of the research project.

6.2 Suggestions For Future Work

The following suggestions are made for future work:

a) **The mechanics of breaking waves**

A more detailed analysis should be performed on the measured internal velocity fields in order to derive quantities such as the rate of energy dissipation and the accelerations present in the flows.

Further measurements should be made of the turbulence present after breaking, with the use of image-shifting to allow the measurement of near-zero velocities.

Use could be made of the PIV illumination system to make estimates of the aeration present after breaking and measurements of the motion of the spray.

Numerical modelling of the breaking process could be supported with the measured kinematics presented in the current work.

Detailed measurements should be made of other types of two-dimensional breaking waves, such as spilling, and of three-dimensional breaking.

b) **The mechanics of waves combined with currents**

More measurements are required of the change in vorticity with time as a wave group establishes itself on a turbulent current, including a measurement after the wave group has passed.

Measurement of the interaction with different current profiles would be desirable, particularly a case which was more strongly sheared.

c) The measurement of water wave kinematics with PIV

A CCD based PIV system would be very useful if it could deliver almost *real-time* velocity fields, even if the resolution was lower than that for the film-based system.

Bibliography

[1] Adrian, R.J. *Scattering Particle Characteristics and Their Effect on Pulsed Laser Measurement of Fluid Flow: Speckle Velocimetry vrs Particle Image Velocimetry.* 1984. Applied Optics, 23(11).

[2] Adrian, R.J. *Image Shifting Technique to Resolve Directional Ambiguity in Double Pulsed Velocimetry.* 1986. Applied Optics, 25(21).

[3] Barker, D.B. and Fourney, M.E. *Measuring Fluid Velocities with Speckle Patterns.* 1977. Applied Optics, 1(4), 135-137.

[4] Barltrop, N.D.P. 1990. Water Wave Kinematics, 233-46, Eds. Torum, A. and Gudmestad, O.T, Kluver Academic Publishers.

[5] Basco, D.R. *A Qualitative Description of Wave Breaking.* 1985. J. Waterway, Port, Coastal and Ocean Eng, ASCE 111, 2, 171-88.

[6] Bellamy, N.W. *Development of the Sea Clam Wave Energy Concept.* 1982. Wave Energy Utilisation Symposium, Trondheim.

[7] Chaplin, J.R. *Developments of Stream Function Wave Theory.* 1980. Coastal Engineering 3, 179-205.

[8] Chaplin, J.R. *The Computation of Non-Linear Waves on a Current of Arbitrary Non-Uniform Profile.* 1990. OTH 90 327, HMSO.

[9] Cokelet, E.D. *Steep Gravity Waves in Water of Arbitrary Uniform Depth.* 1977. Phil. Trans. Roy. Soc., Ser. A., 286, 183-230.

[10] Dalrymple, R.A. and Heidemanm, J.E. *Non-linear Water Waves on a Vertically-Sheared Current Wave and Current Kinematics and Loading.* 1989. E&P Forum, Report No. 3.12/156, 69-92.

[11] Dean, R.G. *Stream Function Representation of Non-linear Ocean Waves Journal of Geophysical Research.* 1965. 70(18), 4561-72.

[12] Department of Energy. *Metocean Parameters — Parameters other than Waves, Supporting document to Offshore Installations: Guidance on Design, Construction and Certification — Environmental Considerations.* 1990. OTH 89 299, HMSO.

[13] Department of Energy. *Offshore Installations: Guidance on Design, Construction.* 1990. 4th Edition, Section 11, Environmental considerations, 11.31-11.61, HMSO.

[14] Dold, J.W. and Peregrine, D.H. *An Efficient Boundary-integral Method for Steep Unsteady Water Waves.* 1986. In Numerical Methods for Fluid Dynamics II, Eds. Morton, K.W. and Baines, M.J., Oxford University Press, 671-9.

[15] Dommermuth, D.G., Yue, D.K.P., Lin, W.M., Rapp, R.J., Chan, E.S. and Melville, W.K. *Deep-water Plunging breakers: a Comparison Between Potential Theory and Experiments.* 1988. J. Fluid Mech., 189, 432-42.

[16] Eastwood, J.W. and Watson, C.J.H. *Implications of Wave-Current Interaction for Offshore Design Wave and Current Kinematics and Loading.* 1989. E&P Forum, Report No. 3.12/156, 93-112.

[17] Fenton, J.D. *A Fifth Order Stokes's Theory for Steady Waves.* 1985. J. Waterways, Port, Coastal and Ocean Eng., 111, 216-34.

[18] Grant, I., Liu, A., Qin, J. and Dong, S. *An Experimental Investigation of Wave-Current Interaction by Particle Image Velocimetry (Speckle) and Laser Doppler Velocimetry.* 1989. MTD S05.

[19] Gray, C. *The Development of Particle Image Velocimetry for Water Wave Studies.* 1989. PhD thesis, the University of Edinburgh.

[20] Gray, C. *The Evolution of Particle Image Velocimetry.* 1992. Optical Methods and Data Processing in Heat and Fluid Flow, City University, 2-3 April, 19-36.

[21] Gray, C., Greated, C.A., McCluskey, D.R. and Easson, W.J. *An Analysis of the Scanning Beam PIV Illumination System.* 1991. J. Phys. Measurement Science and Technology 2, 717-24.

[22] Greenhow, M., Vinje, T., Brevig, P. and Taylor, J. *A Theoretical and Experimental Study of the Capsize of Salter's Duck in Extreme Waves.* 1982. J. Fluid Mech, 118, 221-39.

[23] Griffiths, G. *Near Surface Current Shear in the Open Sea.* 1990. OTO-90-024.

[24] Griffiths, M.W.P., Easson, W.J. and Greated, C.A. *Measured Internal Kinematics for Shoaling Waves with Theoretical Comparisons.* 1992. J. ASCE, 118(3), 280-99.

[25] Grilli, S. and Svendsen, I.A.. *Computation of Nonlinear Wave Kinematics During Propagation and Runup on a Slope.* 1990. Water Wave Kinematics, 387-412, Eds. Torum, A. and Gudmestad, O.T, Kluver Academic Publishers.

[26] Grousson, R. and Mallick, S. *Study of the Flow Pattern in a Fluid by Scattered Laser Light.* 1977. Applied Optics, 16(9), 2334-6.

[27] Hyun, J.M. *Theory for Hinged Wavemakers of Finite Draft in Water of Constant Depth.* 1976. J. Hydronautics, 10(1), 2-7.

[28] Jakobsen, M.L., Hossack, W.J., Greated, C.A. and Easson, W.J. *PIV Analysis Using an Optically Addressed Spatial Light Modulator.* 1992. Applied Optics and Opto-Electronics, Leeds.

[29] Keane, R.D. and Adrian, R.J. *Optimisation of Particle Image Velocimeters.* 1990. Meas. Sci. Technol., 1, 1202-15.

[30] Kemp, P.H. and Simons, R.R. *The Interaction of Waves and a Turbulent Current: Waves Propagating against the Current.* 1983. Journal of Fluid Mechanics, 130, 73-89.

[31] Kjeldsen, S.P. *2- and 3-Dimensional Deterministics Freak Waves.* 1980. NHL Trondheim Norway, Pub. R-149.83.

[32] Kjeldsen, S.P. *Breaking Waves.* 1990. Water Wave Kinematics, 453-473, Eds. Torum, A. and Gudmestad, O.T, Kluver Academic Publishers.

[33] Klopman, G. *Private communication.*

[34] Lamarre, E. and Melville, W.K. *Air Entrainment and Dissipation in Breaking Waves.* 1991. Nature, 351, 469-72.

[35] Longuet-Higgins, M.S. and Cokelet, E.D. *The Deformation of Steep Surface Waves in Water. A Numerical Method of Computation.* 1976. Proc. Royal Soc. London,, 350, 1-26.

[36] Miller, R.L. *The Role of Vorticies in Surf Zone Prediction: Sedimentation and Wave Forces,.* Soc. Econ. Paleontol. Mineral., Spec. Pub. 24, 92-114.

[37] Morison, J.R., O'Brien, M.P., Johnson, J.W., Scaaf, S.A. *The Force Exerted by Surface Waves on Piles.* 1950. Petrol. Trans., AIME, 189, 149-154.

[38] Nakagawa, T. *On Measurements of the Water-Particle Velocity under Breaking Waves over the Horizontal Step in a Laboratory Tank.* 1991. Int. J. Offshore and Polar Eng., 1(2), 108-21.

[39] Peregrine, D.H. *Breaking Waves on Beaches.* 1983. Ann. Rev. Fluid Mech., 15, 149-78.

[40] Peregrine, D.H. *Computations of Breaking Waves.* 1990. Water Wave Kinematics, 475-490, Eds. Torum, A. and Gudmestad, O.T, Kluver Academic Publishers.

[41] Peregrine, D.H. *Theory versus Measurement.* 1990. Water Wave Kinematics, 89-101, Torum, A. and Gudmestad, O.T, Kluver Academic Publishers.

[42] Peregrine, D.H., Cokelet, E.D. and McIver, P. *The Fluid Mechanics of Waves Approaching Breaking.* 1980. Proc. Int. Conf. Coastal Eng. 17th., 521-28.

[43] Pickering, C.J.D. and Halliwell, N.A. *Speckle Photography in Fluid Flows: Signal Recovery with Two Step Processing.* 1984. Applied Optics, 23(8), 1128-9.

[44] Pierson, W.J. and Moskowitz, L. *A Proposed Spectral Form for Fully Developed Wind Seas Based on the Similarity Theory of S.A. Kitaigorodsku.* 1964. J. Geophys Res.

[45] Prasthofer, P.H. *Issues in Wave and Current Kinematics and Loadings — the Structural Designer's Perspective.* 1990. Wave and Current Kinematics and Loading, E&P Forum, Report No. 3.12/156, 3-7.

[46] Quinn, P.A., Skyner, D.J., Gray C., Greated, C.A. and Easson, W.J. *A Critical Analysis of the Particle Image Velocimetry Technique as Applied to Waves on Beaches.* 1992. Applied Scientific Research.

[47] Richman, J.G. and de Szoeke, R.A. *Measurements of Near Surface Shear in the Ocean.* 1987. Journal of Geophysical Research, 92, No C3, 2851-2858.

[48] Rienecker, M.M, and Fenton, J.D. *A Fourier Approximation Method for Steady Water Waves.* 1981. Journal of Fluid Mechanics, 104, 119-37.

[49] Roark. 1999. Formulas for Stress and Strain.

[50] Salter S.H. *Wave Power.* 1974. Nature, 239, No 5459, 720-724.

[51] Salter S.H. *Absorbing Wave Makers and Wide Tanks.* 1982. Proc. Conf. Directional Wave Spectra Applications, ASCE, 185-200.

[52] Sand, S.E., Hansen, N.E.O., Klinting, P., Gudmestad, O.T. and Sterndorff, M.J. *Freak Wave Kinematics.* 1990. Water Wave Kinematics, 535-549, Eds. Torum, A. and Gudmestad, O.T, Kluver Academic Publishers.

[53] Sarpkaya, T. and Isaacson, M. *Mechanics of Wave Forces on Offshore Structures.* 1981. Van Nostrand Reinhold Company, ISBN 0-442-25402-4.

[54] She, K., Greated C.A. and Easson, W.J. *Development of a Two-dimensional Numerical Wave Tank.* 1992. Proc. 2nd Conf. Int. Offshore & Polar Eng., 3, ISBN 1-880653-03-6, 102-13.

[55] Simpkins, P.G. and Dudderar, T.D. *Laser Speckle Measurement of Transient Benard Convection.* 1978. J. Fluid Mechanics, 89(4), 665-71.

[56] Skyner, D.J. *Solo Duck Linear Analysis.* 1987. Dept. of Energy Report.

[57] Skyner, D.J. and Greated, C.A. *The Evolution of a Long-crested Deep-water Breaking Wave.* 1992. Proc. 2nd Conf. Int. Offshore & Polar Eng., 3, ISBN 1-880653-03-6, 132-8.

[58] Skyner, D.J, Easson, W.J. and Greated C.A. *The Internal Kinematics of Steep Waves on Sheared Currents — An Experimental Study.* 1992. OTH 92 366.

[59] Skyner, D.J., Gray, C. and Greated, C.A. *A comparison of Time-stepping Numerical Predictions with Whole-field Measurements in Breaking Waves.* 1990. Water Wave Kinematics, 491-508, Eds. Torum, A. and Gudmestad, O.T, Kluver Academic Publishers.

[60] Sutherland, J., Greated, C.A. and Easson, W.J. *Crest Kinematics in Wave Groups.* 1991. Proc. 1st Conf. Int. Offshore & Polar Eng., 3, 97-103.

[61] Swan, C. *An Experimental Study of Waves on a Strongly Sheared Profile.* 1990. Proc. 22nd Int. Conf. on Coastal Eng., ASCE, 1, 489-502.

[62] Swan, C. *A Viscous Modification to the Ocsillatory Motion Beneath a Series of Progressive Gravity Waves.* 1990. Water Wave Kinematics, 313-29, Torum, A. and Gudmestad, O.T, Kluver Academic Publishers.

[63] Tallent, J.R., Yamashita, T. and Tsuchiya, Y. *Transformation Characteristics of Breaking Water Waves.* 1990. Water Wave Kinematics, 509-23, Eds. Torum, A. and Gudmestad, O.T, Kluver Academic Publishers.

[64] Teles Da Silva, A.F. and Peregrine, D.H. *Steep, Steady Surface Waves on Water of Finite Depth with Constant Vorticity.* 1988. Journal of Fluid Mechanics, 195, 281-302.

[65] Thomas, G.P. *Wave-current Interactions: an Experimental and Numerical Study, Part2: Non-Linear waves.* 1990. Journal of Fluid Mechanics, 216, 505-536.

[66] Toumazis, A.D. and Anastasiou, K. *Scale Effects in Breaking Waves.* 1990. Proc. 22nd Int. Conf. on Coastal Eng., ASCE, 1, 973-985.

[67] Weigel R.L. *Oceanographical Engineering.* 1964. Prentice-Hall.

[68] Wheeler, J.D. *Method for Calculating Forces Produced byb Irregular Waves.* 1970. J. Petroleum Tech., 119-37.